Building galaxy models with self-consistent prescriptions for stellar and nebular emission

Eleanor Beryl Byler

A dissertation
submitted in partial fulfillment of the
requirements for the degree of

Doctor of Philosophy

University of Washington

2017

Reading Committee:

Julianne J. Dalcanton, Chair

Emily Levesque

Jessica Werk

Richard Wright, GSR

Program Authorized to Offer Degree:
Astronomy

University of Washington

Abstract

Building galaxy models with self-consistent prescriptions for stellar and nebular emission

Eleanor Beryl Byler

Chair of the Supervisory Committee:
Professor Julianne J. Dalcanton
Department of Astronomy

A galaxy's spectrum is simply the sum of light emitted by its constituent parts; it contains light emitted by stars and gas, modulated by intervening dust. Translating between the observed flux from galaxies and meaningful astrophysical quantities relies on "stellar population synthesis" (SPS) models. These models include descriptions for the light produced by stars and dust in galaxies, but most neglect the nebular emission from ionized gas. Accounting for nebular emission is important, as both line and continuum emission can contribute significantly to the total observed flux. The goal of this thesis is to include and exploit a proper accounting of emission from ionized gas in widely-used galaxy models. I have integrated a fully self-consistent treatment of nebular line and continuum emission into the SPS code Flexible Stellar Population Synthesis (FSPS; Conroy et al., 2009), using the photoionization code Cloudy (Ferland et al., 2013). This model, `CloudyFSPS`, successfully reproduces observed properties of galaxies in the UV and optical wavelength regimes, and galaxies with young and old stellar populations. This thesis contains three main efforts. The first describes the development and validation of the `CloudyFSPS` package. The second uses `CloudyFSPS` to assess UV emission and absorption line diagnostics. The third uses `CloudyFSPS` to explore the origin of LIER-like emission and the UV-upturn in early-type galaxies.

TABLE OF CONTENTS

LIST OF FIGURES

LIST OF TABLES

ACKNOWLEDGMENTS

To the UW astronomy graduate students, thank you for filling my time here with happiness. It has been an absolute privilege to be classmates and colleagues. Special thanks to my graduate cohort, Michael Tremmel, Russell Dietrick, and Ben Vega-Westhoff. Special thanks to Kristen Garofali, my former roommate and constant partner in crime for all things related to astronomy outreach.

Thank you to the extragalactic group at UW, including Grace Telford, Alexia Lewis, Yumi Choi, Lori Beerman, Cliff Johnson, Morgan Fouesneau, and Ben Williams. It has been a pleasure working with each and every one of you.

I have been fortunate to share office B329 with truly awesome humans. Thank you Adrienne Stilp and Phil Rosenfield, for your wisdom, patience, and emergency desk chocolate. To the later inhabitants of B329, the dream team: Diana Windemuth and Phoebe Upton Sanderbeck you are my dearest friends and I am forever grateful for the constant encouragement and advice you've provided, both professionally and personally. I am certain that Din Tai Fung, karaoke, and crossroads therapy has kept me sane these last few years.

Thank you to Dan Weisz, your scientific support and professional encouragement came at a time when I needed it the most. Thank you to Charlie Conroy, your research mentorship has expanded my scientific horizons in uncountable ways.

Thank you to the UW astronomy department and every faculty member that I have had the honor of interacting with during my time here. Special thanks go to Suzanne Hawley, my first research mentor at UW, I am a better scientist because of you.

Thank you Jessica Werk and Emily Levesque, for serving on my reading committee and for the invaluable research support and career advice.

Thank you to Richard Wright, for serving as the graduate school representative for both my general exam and my final exam.

To my fantastic superhero of an adviser, Julianne Dalcanton, thank you. You are an inspirational scientist, writer, mentor, and human, and I am eternally grateful for your tireless support and enthusiastic encouragement. Thank you for cultivating "bossy boots" Nell.

Thank you to my family, Tess, Eric, Nick, and Rebecca Byler, Chuck, Kathryn and James Reeves, and Jordyn Jones, who have loved me every day of this journey.

Above all, thank you to my partner, husband, and best friend, Oliver Byler. Thank you for picking me up every time I fell, and for cheering me on in every success, large or small. You have helped me find the confidence I needed to accomplish this.

DEDICATION

To Beta Trombone Reeves Byler, the queen bee and pug of all pugs. You are my star.

Chapter 1
INTRODUCTION

"Do not look at stars as bright spots only. Try to take in the vastness of the universe." [attributed to Maria Mitchell]

Galaxy light is a tangled combination of emission from billions of stars and networks of gas, all modulated by complex distributions of intervening dust. The exact properties of the emergent galaxy spectrum therefore reflect the past star formation, chemical enrichment of elements, the structure and phase of the gaseous interstellar medium (ISM), and the composition and distribution of dust. Translating between the observed flux from galaxies and meaningful astrophysical quantities relies on "stellar population synthesis" (SPS) models. These models are broadly applied throughout extragalactic astronomy, at both high and low redshifts and to both photometric and spectroscopic spectral energy distributions (SEDs).

SPS models include robust descriptions for the ultra-violet (UV), optical, and infrared (IR) light produced by stars and dust in galaxies, but most neglect the nebular emission from ionized gas, or include it in an *ad hoc* fashion (see reviews in Walcher et al., 2011; Conroy, 2013). In star forming regions, the young, hot, stars emit copious ionizing photons into their surrounding natal gas cloud. In galaxies with active star formation, nebular emission can contribute as much as 20-60% of broadband fluxes and is responsible for nearly all of the optical emission lines present in the spectra of star-forming galaxies (e.g., Anders & Fritze-v. Alvensleben, 2003; Reines et al., 2010). The strength of nebular line and continuum emission depends on both the ionizing radiation field and the metallicity of the gas. The amount of nebular emission thus varies from galaxy to galaxy, and can evolve with cosmic time.

On their own, nebular emission lines are a powerful diagnostic of the ISM of galaxies.

Emission lines are routinely used at low and high redshift to measure key physical properties of entire galaxies, such as the star formation rate (SFR) and metallicity (e.g., Brinchmann et al., 2004; Tremonti et al., 2004; Kewley & Ellison, 2008). Emission lines are used to identify galaxies where the gas is ionized by young massive stars, by hot evolved stars, or by an active galactic nuclei (AGN), primarily through diagnostic diagrams using ratios of emission lines (e.g., Baldwin et al., 1981; Dopita et al., 2000; Kewley et al., 2006; Levesque et al., 2010).

Despite its importance, nebular emission is rarely accounted for when modelling galaxy SEDs. Amongst the most widely used SPS models, only a handful include the effects of nebular emission. The goal of this thesis is to include and exploit a proper accounting of emission from ionized gas in widely-used galaxy models. In this thesis I have integrated a full, self-consistent treatment of nebular line and continuum emission into the SPS code Flexible Stellar Population Synthesis (FSPS; Conroy et al., 2009), using the photoionization code Cloudy (Ferland et al., 2013). My model, `CloudyFSPS`, provides a straightforward means of coupling the local gas physics with the starlight model for a galaxy, and produces self-consistent predictions for the nebular line and continuum emission from a stellar population as a function of age and metallicity. `CloudyFSPS` successfully reproduces observed properties of galaxies in the UV and optical wavelength regimes, and galaxies with young and old stellar populations.

1.1 Outline of this thesis

The outline for the remainder of my thesis is as follows. In Chapter 2, I present a new nebular emission model integrated within the Flexible Stellar Population Synthesis code that computes the line and continuum emission for complex stellar populations using the photoionization code Cloudy. The self-consistent coupling of the nebular emission to the matched ionizing spectrum produces emission line intensities that correctly scale with the stellar population as a function of age and metallicity. Chapter 2 focuses on introducing the model and its ability to reproduce the location of observed galaxies in various optical

diagnostic diagrams.

In Chapter 2, I present a new nebular emission model integrated within the FSPS code. This model computes the line and continuum emission for complex stellar populations using the photoionization code CLOUDY. The self-consistent coupling of the nebular emission to the matched ionizing spectrum produces emission line intensities that correctly scale with the stellar population as a function of age and metallicity. This more complete model of galaxy SEDs will improve estimates of global gas properties derived with diagnostic diagrams, star formation rates based on Hα, and physical properties derived from broadband photometry. Chapter 2 focuses on the development and validation of the `CloudyFSPS` package.

Next, in Chapter 3, we extend the `CloudyFSPS` nebular model to include predictions for UV emission and absorption lines. UV diagnostics are critical for the study of higher redshift galaxies, given that commonly-used optical emission line diagnostics become observationally unavailable as they redshift out of wavelength regimes accessible from the ground. In this chapter we assess the diagnostic potential of both absorption and emission features in the UV and evaluate the diagnostics against observations of local galaxies and galaxies at high redshift.

Then, in Chapter 4, we use the `CloudyFSPS` model to characterize the Low Ionization Emission Regions (LIERs) in early type galaxies (ETGs). I present the first prediction of LIER-like emission that is based on the fully self-consistent photoionization modelling available with `CloudyFSPS`. These models are able to reproduce the observed nebular emission signature of LIER-like objects while simultaneously matching the optical color and absorption line properties of the general ETG population.

Finally, in Chapter 5, I provide a short discussion on the current and future context of my thesis research, and important directions this work will take in the next few years.

Chapter 2

NEBULAR CONTINUUM AND LINE EMISSION IN STELLAR POPULATION SYNTHESIS MODELS

In this chapter, I present a new nebular emission model integrated within the Flexible Stellar Population Synthesis code that computes the line and continuum emission for complex stellar populations using the photoionization code Cloudy. The self-consistent coupling of the nebular emission to the matched ionizing spectrum produces emission line intensities that correctly scale with the stellar population as a function of age and metallicity. This more complete model of galaxy SEDs will improve estimates of global gas properties derived with diagnostic diagrams, star formation rates based on Hα, and physical properties derived from broadband photometry. Our models agree well with results from other photoionization models and are able to reproduce observed emission from H II regions and star-forming galaxies. Our models show improved agreement with the observed H II regions in the Ne III/O II plane and show satisfactory agreement with He II emission from $z = 2$ galaxies when including rotating stellar models. Models including post-asymptotic giant branch stars are able to reproduce line ratios consistent with low-ionization emission regions (LIERs). The models are integrated into current versions of FSPS and include self-consistent nebular emission predictions for MIST and Padova+Geneva evolutionary tracks.

Material from this chapter was previously published in collaboration with Julianne J. Dalcanton, Charlie Conroy, and Benjamin D. Johnson, in the May 2017 edition of the Astrophysical Journal (Byler et al., 2017). The American Astronomical Society grants back to authors the non-exclusive right of republication with appropriate credit to the journal in which the article was published.

2.1 Introduction

The light emerging from galaxies is a complex combination of emission from stars and gas, processed by any intervening dust. For star-forming galaxies, the UV and optical flux is dominated by the light produced by young, luminous stars and the surrounding networks of ionized gas. The latter produces nebular emission, which can contribute as much as 20-60% of UV-IR broadband fluxes and which is responsible for nearly all the optical emission lines present in the spectra of star-forming galaxies (Anders & Fritze-v. Alvensleben, 2003; Reines et al., 2010). Emission lines are routinely used at low and high redshift to measure key physical properties of entire galaxies, such as the star formation rate (SFR) and metallicity (e.g., Tremonti et al., 2004; Kewley & Ellison, 2008).

Nebular emission is comprised of two components: (1) the nebular continuum, which is a continuous emission spectrum that consists of free-free (bremsstrahlung), free-bound (recombination continuum), and two-photon emission; and (2) nebular line emission, which is primarily produced by radiative recombination processes and emission from forbidden and fine structure line transitions. The strength of emission from these two components depends on both the ionizing radiation field and the metallicity of the gas. The amount of nebular emission thus varies from galaxy to galaxy, and can evolve with cosmic time.

Stellar Population Synthesis (SPS) models used to interpret galaxy observations account for the light emitted by stars and the reprocessing of that light by dust, but only a handful of current SPS codes include nebular emission, despite its important effects on the output spectrum (see reviews in Walcher et al., 2011; Conroy, 2013). The contribution from nebular emission can be calculated with varying levels of sophistication. The simplest approach computes the line and continuum emission analytically, using the number of photons in the Lyman continuum to calculate the strength of emission as a function of wavelength. The most complex and accurate approach uses photoionization models to compute the transfer of ionizing photons exactly.

The SPS codes PÉGASE (Fioc & Rocca-Volmerange, 1999), POPSTAR (Mollá et al.,

2009), and STARBURST-99 (Leitherer et al., 1999) all include analytic prescriptions for nebular emission, where it is assumed that all stellar photons with energies greater than 13.6 eV are converted into nebular emission. Continuum emission is calculated based on emission coefficients for free-free, bound-free, and two-photon transitions. Hydrogenic line intensities are similarly computed by translating the number of photons in the Lyman continuum directly into a line intensity based on Case-B approximations. If line intensities for other elements are included, they are usually based on empirical line strengths, as in PÉGASE. In STARBURST-99, line emission is computed from a normalized library of stellar UV spectra, with absolute fluxes derived from the stellar SED. While these prescriptions are computationally efficient, they cannot account for temporal or chemical evolution.

For a more detailed analysis of the stellar and nebular energy distributions, population synthesis models can be coupled with photoionization models. Photoionization models have proven to be essential in interpreting the emission-line properties of H II regions in terms of the properties of the stars and gas (e.g., Dopita et al., 2000) and the nebular emission from galaxies in terms of macroscopic star formation parameters (e.g., Brinchmann et al., 2004). Popular photoionization codes include CLOUDY (Ferland et al., 2013) and MAPPINGS-III (Groves et al., 2004), both of which compute the full radiative transfer through a gas cloud and predict the resultant emission spectrum. Most implementations model the total nebular emission as the sum of emission from multiple H II regions with different ages and physical properties, though at the cost of being much more computationally expensive (e.g., Kewley et al., 2001; Moy et al., 2001; Charlot & Longhetti, 2001; Dopita et al., 2006).

We present a nebular emission model within the Flexible Stellar Population Synthesis code (FSPS[1], Conroy et al., 2009) that adopts the best features of the realistic photoionization models and implements them within a more flexible stellar population framework. Nebular emission is included in current versions of FSPS, with line and continuum emission predictions that scale correctly with age and metallicity. The nebular emission model is

[1]available on GitHub `https://github.com/cconroy20/fsps`

self-consistently applied to stellar populations generated with different stellar evolutionary tracks.

We couple the ionizing spectrum and stellar metallicity with the gas phase metallicity to compute the total line and continuum emission. Following the process of Charlot & Longhetti (2001), we use simple stellar populations (SSPs) as the ionizing source for the gas clouds using the photoionization code CLOUDY. The resultant nebular line and continuum emission are embedded within FSPS as pre-computed tables. We can then combine the results from the SSPs to produce self-consistent spectra for arbitrary star formation histories (SFHs). This strategy maintains the flexibility of FSPS without the need to rerun the computationally expensive photoionization models for each output stellar population.

The self-consistent implementation of the nebular model is two-fold: First, the nebular line and continuum emission predicted by CLOUDY is added to the *same* spectrum that was used to produce the emission lines, and is thus directly tied to the ionizing continuum of each SSP as a function of age, metallicity, and ionization parameter. Second, by linking the stellar metallicity in FSPS with the gas-phase abundances in CLOUDY we couple the metallicity dependent changes in the ionizing EUV spectral shape to the changes in the gas coolants, which is reflected in both the temperature and ionization structure of the nebula. This is a particularly important feature, as it allows us to more accurately model the simultaneous signature of stars, gas, and dust in the integrated spectra of galaxies, as discussed below.

In §2.2 we introduce the nebular emission model and our means of coupling FSPS and CLOUDY. We first discuss broad trends in the ionizing spectra in §2.3, before moving on to discuss the results of the nebular model in §2.4. We begin §2.4 by discussing the ionization structure of individual H II regions as a function of age and metallicity (§2.4.1). We then use these results to discuss the origin of common optical and NIR lines and their variation in line strength (§2.4.2). In §2.5 we generate model grids of line ratios and showcase their ability to reproduce lines observed in H II regions and star-forming galaxies. We consider several complicating features in §2.6, including alternate evolutionary tracks and dust, followed by our conclusions in §2.7.

2.2 Methods and Implementation

In the following sections we discuss the parametrization of the nebular emission model and our means of embedding it within FSPS. We highlight broad trends in the ionizing spectra and identify parameters which most influence the properties of the nebular model.

2.2.1 CLOUDY *Model Parametrization*

To calculate photoionization models, we use version 13.03 of CLOUDY[2], last described by Ferland et al. (2013). CLOUDY simulates physical conditions within a gas cloud to predict the thermal, ionization, and chemical structure of the cloud and the resultant spectrum of the diffuse emission. Users must describe the physical properties of the gas cloud and provide an external source of radiation to photoionize the cloud. Each model must specify (1) the geometry and (2) the chemical content of the gas cloud, and (3) the spectrum and (4) the intensity of the ionizing radiation source. Our choices for these parameters are as follows.

Assumed Geometry

We adopt a spherical shell cloud geometry and assume that the ionizing radiation is produced by a point source at the center of the spherical shell of gas. The distance from the central ionizing source to the inner face of the gas cloud, $R_{\rm inner}$, is fixed at 10^{19} cm ($\sim$ 3pc) and we assume a constant gas density of $n_{\rm H} = 100$ cm^{-3}.

We note that density is the fundamental parameter in CLOUDY simulations, whereas pressure is the fundamental parameter in MAPPINGS-III. We compared CLOUDY models run with a constant density law (which keeps the sum of protons in atomic, ionized, and molecular forms constant throughout the gas) to those run with an isobaric density law (which dictates that the gas pressure follows $P_{\rm gas} = n_{\rm tot} \cdot k \cdot T_{\rm e}$) and found that our results did not change by more than a few percent. Differences between MAPPINGS-III and CLOUDY

[2]available at `https://nublado.org/`

models are therefore unlikely to be due solely to the different application of density and pressure laws.

Gas Chemical Content

We adopt the gas phase abundances specified by Dopita et al. (2000), which are based on the solar abundances from Anders & Grevesse (1989). We assume that the gas phase metallicity scales with the metallicity of the stellar population, given that the metallicity of the most massive stars should be identical to the metallicity of the gas cloud from which the stars formed. Metal abundances are solar-scaled, with the exception of nitrogen, which has a known secondary nucleosynthetic contribution. For the scaling of nitrogen with metallicity, we follow the piecewise relationship between nitrogen and oxygen specified by Dopita et al. (2000).

Elements like carbon and nitrogen are observed to be heavily depleted onto dust grains in H II regions. This alters the chemical composition of the nebula, but also the thermal properties of the nebula, since these elements are important gas coolants. To account for this, the relative abundances used in this work include the effect of depletion onto dust grains derived from observations as defined in Dopita et al. (2000). The applied depletion factors are constant factors applied to specific elements and do not scale with the metallicity of the model. The depletion factors are applied regardless of whether the model nebula includes dust grains, due to their important effect on the temperature structure of the cloud. A complete description of the elemental abundances and depletion factors used in this work can be found in 2.1. In 2.2 we compare the abundances used in this work with those used in other nebular emission models.

We produce two separate nebular models, one that includes grains within the nebula and one that does not. The majority of the models discussed hereafter do not include dust grains within the nebula. For the dusty models, we use a dust grain model with a size distribution and abundances pattern appropriate for the ISM of the Milky Way. The grain prescription includes both a graphite and silicate component and generally reproduces the

Table 2.1. Solar Metallicity (Z_{aa}) and Depletion Factors (D) adopted for each element

Element	$\log_{10} Z/Z_\odot$	log (D)
H	0	0
He	-1.01	0
C	-3.44	-0.30
N	-3.95	-0.22
O	-3.07	-0.22
Ne	-3.91	0
Mg	-4.42	-0.70
Si	-4.45	-1.0
S	-4.79	0
Ar	-5.44	0
Ca	-5.64	-2.52
Fe	-4.33	-2.0

observed extinction properties for a ratio of extinction per reddening of $R_{\rm v} \equiv A_{\rm v}/E(B-V) = 3.1$. We note that in real galaxies $R_{\rm v}$ will not necessarily equal the canonical Milky Way value and depletion patterns may differ from the ones adopted in this work, which could in turn significantly alter the physical properties of the model H II region.

Ionizing spectra

We use the stellar population synthesis code FSPS via the python interface, `python-fsps`[3], to generate spectra from coeval clusters of stars, each with a single age and metallicity (SSPs). The spectra from FSPS are used as the central radiation field responsible for ionizing the surrounding gas cloud in the CLOUDY model. For each SSP (t, Z), the SED dictates the spectrum of ionizing photons and the metallicity fixes the nebular abundances. This couples the age and metallicity-dependent changes in the shape and intensity of the ionizing spectrum with the coolants in the gas cloud, both of which regulate cloud temperature and ionization structure. We do not vary the gas-phase abundances in CLOUDY for a given SSP. We caution users that the current implementation in FSPS allows the user to specify different stellar and gas-phase metallicities, which will break some of the self-consistency of the model, since emission lines will be added to an SSP that is different from the one used to ionize the gas.

The SSPs are generated assuming a Kroupa IMF (Kroupa, 2001) and a fully sampled mass function. We adopt the BaSeL 3.1 stellar library, a theoretical library of stellar spectra based on Kurucz models, re-calibrated using empirical photometric data (Westera et al., 2002). The Wolf-Rayet (WR) stellar spectra are from M. Ng, G. Taylor & J.J. Eldridge (priv. comm) using WM-Basic (Pauldrach et al., 2001), and the O-star spectra are from Smith et al. (2002) using CMFGEN (Hillier & Lanz, 2001). Post asymptotic giant branch (post-AGB) stellar isochrones are from Vassiliadis & Wood (1994) with post-AGB spectra from Rauch (2003). If the user adjusts the IMF or the stellar library used in FSPS, the precomputed CLOUDY output will no longer be self-consistent.

[3]available at `http://dan.iel.fm/python-fsps/`

Table 2.2. Abundances of important gas coolants in various nebular emission models

Abundance Set	Solar Abundance Set	log (C/H)	log (D)	log (N/H)	log (D)	log (O/H)	log (D)
CLOUDY <Orion Nebula>	Anders & Grevesse (1989)	-3.52	···	-4.15	···	-3.40	···
Dopita et al. (2013)	Grevesse et al. (2010a)	-3.87	(-0.30)	-4.65	(-0.05)	-3.38	(-0.07)
Dopita et al. (2000)	Anders & Grevesse (1989)	-3.74	(-0.30)	-4.17	(-0.22)	-3.29	(-0.22)
Charlot & Longhetti (2001)	Grevesse & Noels (1993)	-3.45	···	-4.30	(-0.27)	-3.18	(-0.05)
Levesque et al. (2010)	Anders & Grevesse (1989)	-3.70	···	-4.22	···	-3.29	···

Note. — Values in table reflect absolute abundance at solar metallicity and include the indicated depletion factors.

The SSPs use the 2007 Padova isochrones (Bertelli et al., 1994; Girardi et al., 2000; Marigo et al., 2008) which do not include evolutionary tracks for massive stars. Geneva isochrones are adopted for $M > 70 M_{\odot}$, using the high mass-loss rate evolutionary tracks from (Schaller et al., 1992; Meynet & Maeder, 2000) as recommended by Levesque et al. (2010).

In §2.3 we discuss how changing various aspects of the applied SPS model affects the ionizing spectrum and the resultant nebular emission. We include an analysis of the ionizing spectra produced by the MESA Isochrones & Stellar Tracks (MIST, Dotter, 2016; Choi et al., 2016), which include stellar rotation. The nebular model included in FSPS includes self-consistent nebular emission predictions for stellar populations generated using either MIST or Padova+Geneva evolutionary tracks.

We include a comparison between FSPS and Starburst-99 models in Appendix A.

Ionizing Spectrum Intensity

For photoionization models, we care primarily about the intensity of the ionizing spectrum blueward of 912Å, the ionization threshold for hydrogen. We quantify the intensity of each ionizing spectrum with $Q_{\rm H}$, the total number of photons emitted per second that are capable of ionizing hydrogen:

$$Q_{\rm H} \equiv \int_{\nu_0}^{\infty} \frac{f_\nu}{h\nu} d\nu = \frac{1}{hc} \int_0^{\lambda_0} \lambda f_\lambda d\lambda \, . \tag{2.1}$$

$Q_{\rm H}$ can be calculated directly from the SSP ionizing spectra from FSPS, which assume the formation of one solar mass of new stars. Over the full range of SSP ages and metallicities used in this work, $Q_{\rm H}$ calculated from the 1 $\rm M_{\odot}$ spectra varies from $10^{43} - 10^{47}$ ($\rm s^{-1}$). However, $1\,\rm M_{\odot}$ SSPs do not provide enough ionizing photons to reproduce the ionizing photon rates observed massive H II regions. A single O7V star with $M_{\rm i} \sim 25\,\rm M_{\odot}$ produces $Q_{\rm H} \sim 10^{48.75}$, while a young star cluster with $M \sim 3 \times 10^4\,\rm M_{\odot}$ produces $Q_{\rm H} \sim 10^{51}$. Thus, to achieve values of $Q_{\rm H}$ consistent with observed massive H II regions, we must increase the intensity of the ionizing spectra by increasing the total stellar mass of the SSPs. We

first describe how we specify the intensity of the ionizing spectra within CLOUDY, and then describe the relation to SSP stellar mass.

When running CLOUDY, we set the intensity of the ionizing spectrum using the ionization parameter, $\mathcal{U}$, a dimensionless quantity that gives the ratio of hydrogen ionizing photons to total hydrogen density:

$$\mathcal{U} \equiv \frac{Q_{\rm H}}{4\pi R^2 \cdot n_{\rm H} \cdot c}, \tag{2.2}$$

where R is radius of the ionized region, $n_{\rm H}$ is the number density of hydrogen ($\rm cm^{-3}$), and c is the speed of light. The ionization parameter used in this work, $\mathcal{U}$, differs from the ionization parameter q ($\rm cm \cdot s^{-1}$) used by Levesque et al. (2010) and Dopita et al. (2013) by a factor of c, the speed of light: $q = \mathcal{U} \cdot c$.

In its derivation, $\mathcal{U}$ is computed at $R = R_{\rm S}$, the Strömgren radius, the location where ionization and recombination rates are balanced in thermal equilibrium, which can only be calculated after a photoionization model is computed. CLOUDY defines $\mathcal{U}$ at $R = R_{\rm inner}$, the distance from the ionizing source to the illuminated inner face of the cloud. To avoid confusion, we define $\mathcal{U}_0$ as the ionization parameter calculated at the inner radius of the gas cloud. The distinction does not matter for a thin spherical shell, the geometry assumed in this work (for details see Charlot & Longhetti, 2001).

$\mathcal{U}_0$ conveniently folds in both the intensity of the ionizing source ($Q_{\rm H}$) and the geometry of the gas cloud ($R_{\rm inner}$, $n_{\rm H}$), which allows us to make a simplification to reduce the dimensionality of our model grid. For a fixed EUV shape and metallicity, any combination of $Q_{\rm H}$, $R_{\rm inner}$, and $n_{\rm H}$ that produces the same value of $\mathcal{U}_0$ will produce the same nebular spectrum, a simplification which holds at typical H II region densities and sizes ($n_{\rm H} \sim 10 - 1000$, $R_{\rm inner} \sim 0.1 - 10$ pc).

Each model is run through CLOUDY at 7 different ionization parameters, $-4 \leq \log_{10} \mathcal{U}_0 \leq -1$ in steps of 0.5, a range consistent with ionization parameters observed in local starburst galaxies (Rigby & Rieke, 2004). To produce the various values of $\mathcal{U}_0$, we choose to fix $R_{\rm inner}$ and $n_{\rm H}$ and only vary $Q_{\rm H}$. Other groups have taken different approaches: Moy et al. (2001) fix $R_{\rm inner}$, $n_{\rm H}$, and $Q_{\rm H}$ and produce different ionization parameters by varying the filling factor

of the surrounding gas cloud[4]. Levesque et al. (2010) fix the total mass of the instantaneous bursts at 10^6 $M_\odot$ and vary the inner radius of the cloud to produce different values of $\mathcal{U}_0$.

We note that running models at different values of $\mathcal{U}_0$ and fixed $R_{\rm inner}$ and $n_{\rm H}$ by varying $Q_{\rm H}$ implicitly varies the effective mass of the SSPs. Older SSPs produce fewer ionizing photons and must be more massive than a younger SSP to achieve the same value of $\mathcal{U}_0$. To distinguish the $Q_{\rm H}$ input to CLOUDY from the one measured from the 1 $M_\odot$ ionizing spectrum, we define $\hat{Q}_{\rm H}$ as the ionizing photon rate *per solar mass*: $\hat{Q}_{\rm H} \equiv Q_{\rm H}/M_\odot$. To account for the different intensities required to produce the desired range in $\log_{10}\mathcal{U}_0$, we simply normalize the output from CLOUDY by the total stellar mass, $\hat{Q}_{\rm H}/Q_{\rm H}$.

The range in total stellar mass required to produce ionization parameters in the range of $-4 \leq \log_{10}\mathcal{U}_0 \leq -1$ varies from 10^1 to 10^8 $M_\odot$ depending on the age and metallicity of the SSP. For a 1 Myr solar-metallicity SSP, $-4 \leq \log_{10}\mathcal{U}_0 \leq -1$ implies variation in stellar mass from 10^1 to 10^4 $M_\odot$ at the assumed $R_{\rm inner} = 10^{19}$ cm and $n_{\rm H} = 100$ cm^{-3} of our model. At 7 Myr, the oldest SSP used in our model, this requires larger masses, 10^5 to 10^8 $M_\odot$.

Other Model Specifications

The CLOUDY models are radiation-bounded, and all relevant radiative transfer effects are included in the treatment of line formation, which requires several iterations per model to establish a well-defined optical depth scale. We set a temperature floor of 100K, and stop the radiative transfer calculation when the ionized fraction of the cloud drops to 1%; resultant line ratios do not qualitatively change for simulations that are stopped at slightly different fractions.

We record 128 emission lines for each model, which includes emission lines from the UV to the far-IR (for a full list of included emission lines, see §B). Roughly 60% of the lines included are in the optical wavelength regime, with $\sim$ 20% in the UV and $\sim$20% in the IR.

[4]The volumetric fill factor is a measure of how clumpy the surrounding gas is, and alters the effective path length of the ionizing photons. It is different from the covering factor, $\frac{\Omega}{4\pi}$, which specifies the fraction of the ionizing flux that is "seen" by the gas.

CLOUDY reports air wavelengths for any wavelength over 2000Å, and we convert these to vacuum wavelengths using the IAU standard formalism from Morton (1991). Note that many wavelengths for the reported emission lines from CLOUDY were inaccurate by 0.1-0.5Å, due to a combination of the limited number of significant figures that could be recorded in legacy versions of CLOUDY and the use of outdated line databases. To remedy this, the lines were matched to the appropriate lines from the NIST atomic line database, and their wavelengths set to the true vacuum value.

We integrate the FSPS model spectra into CLOUDY using its support for "user-defined" atmosphere grids. We have generated CLOUDY-formatted ascii files that supply the FSPS spectrum for stellar populations that span the full range of available ages and metallicities; these files have been made publicly available for anyone to use within CLOUDY. The publicly available ASCII files include a standard, single-burst version and a version for populations with constant star formation; both use the IMF, evolutionary tracks, and spectral libraries as specified above. However, `CloudyFSPS`[5] provides a python interface between FSPS and CLOUDY that can be used to generate ASCII files for arbitrarily complex stellar populations as input to CLOUDY.

2.2.2 Integration of Nebular Emission into FSPS

The nebular emission model samples the following values for SSP age, SSP metallicity, and ionization parameter, $\mathcal{U}_0$:

$\log_{10} \mathcal{U}_0$: -4.0, -3.5, -3.0, -2.5, -2.0, -1.5, -1.0

$\log_{10} Z/Z_\odot$: -2.0, -1.5, -1.0, -0.6, -0.4, -0.3, -0.2, -0.1, 0.0, 0.1, 0.2

Age: 0.5, 1, 2, 3, 4, 5, 6, 7, 10 million years (Myr)

The nebular model has one "free" parameter, $\log_{10} \mathcal{U}_0$. For each SSP of age t and metallicity Z, we run photoionization models at each ionization parameter, $\mathcal{U}_0$. We normalize the

[5]available on GitHub `https://github.com/nell-byler/cloudyfsps`.

line and continuum emission by $Q_{\rm H}$ input to CLOUDY. The normalized line and continuum emission are recorded into separate look-up tables.

For a given SSP (t, Z) and specified $\mathcal{U}_0$, FSPS returns the associated line and continuum emission associated with that grid-point from the look-up table. This maintains the model self-consistency, such that the nebular emission is added to the same spectrum that was used to ionize the gas cloud.

The normalized line and continuum emission are rescaled by $Q_{\rm H}$ calculated from the SSP's spectrum; FSPS then removes the ionizing photons from the SED to enforce energy balance. FSPS includes a parameter, `frac_obrun`, which allows some fraction of the ionizing luminosity to escape from the H II region, however, in this work we assume an ionizing photon escape fraction of zero.

The nebular model is implemented for SSPs with age $t < t_{\rm esc}$, a parameter within FSPS that specifies the time a given SSP is surrounded by its birth cloud. For complex stellar populations, the total nebular contribution is the sum of emission from all SSPs that contribute to the SFH with age $t < t_{\rm esc}$. In practice, the emission from H II regions surrounding star clusters is a relatively short-lived phenomenon ($\lesssim 10^7$ years), with most of the contribution coming from SSPs 3 Myr and younger, though deviations from this are discussed in §2.6.1. In general, we neglect the contribution from old planetary nebula and hot intermediate-aged stars. In §2.6.2, however, we assess the importance of the contribution from post-AGB stars. We do not consider the contribution from AGN.

2.3 Properties of the Model Ionizing Spectra

The ionizing spectrum is the link between FSPS and the nebular emission model, and the emission line spectrum is critically dependent on the adopted ionizing radiation field. Important parameters like the number of ionizing photons and the slope of the spectrum blueward of 912Å vary with the age and metallicity of the SSP. In this section we present basic properties of the ionizing spectra used in the nebular emission model and demonstrate the effects that age and metallicity have on the intensity and shape of the input spectrum.

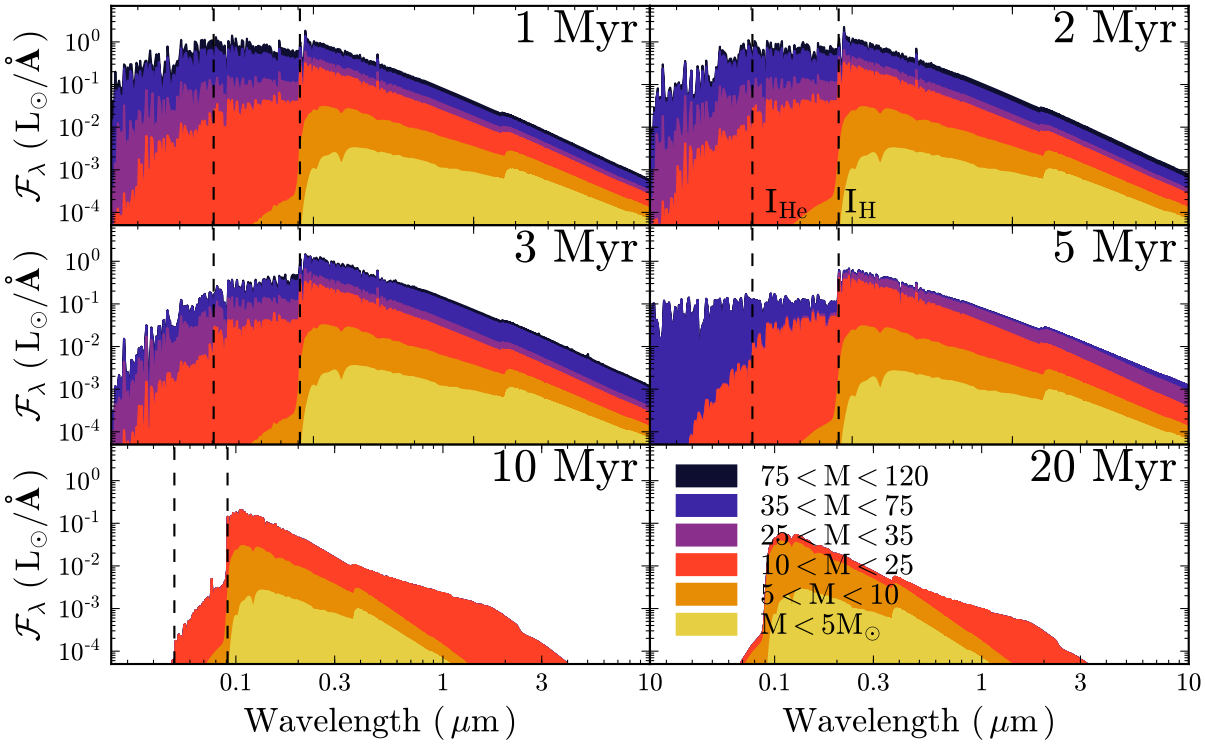

Figure 2.1 The time evolution of a solar-metallicity SSP, showing the relative flux contribution from stars of different masses. The ionization threshold for hydrogen, $I_{\rm H}$, and helium, $I_{\rm He}$, are shown as dashed lines. Massive stars ($M > 10\,{\rm M}_\odot$, shown in blue, purple, and orange) are responsible for producing most of the radiation capable of ionizing hydrogen. These stars are short lived, and most of the ionizing radiation is gone by ~ 10 Myr.

2.3.1 Time evolution of the ionizing spectra

For giant H II regions, the ionization is provided by groups of rapidly evolving massive stars. The ionizing spectrum will thus change with time, with stars of different masses dominating the spectrum at different times. For H II regions, we are primarily concerned with the evolution of flux at wavelengths shorter than 912Å, as these are the photons with energies high enough to ionize hydrogen in the surrounding gas cloud.

2.1 shows the relative flux contribution of stars in different mass ranges to the ionizing spectrum at solar metallicity as a function of time. In all panels, the radiation capable of ionizing hydrogen is produced by the most massive stars: those with initial masses $\gtrsim 10\,\mathrm{M}_\odot$. At 1 Myr, stars with initial mass $\gtrsim 35\,\mathrm{M}_\odot$ dominate the ionizing spectrum. These stars are extremely short-lived and by 3 Myr the spectrum is dominated by stars with initial masses $\gtrsim 25\,\mathrm{M}_\odot$. O-type stars ($> 25\,\mathrm{M}_\odot$) have evolved off of the main sequence by 5 Myr, and stars with masses $10 - 25\,\mathrm{M}_\odot$ (B-type stars) dominate the spectrum from $6 - 20$ Myr. By 10 Myr there are not enough stars left with sufficiently high temperatures to produce significant amounts of ionizing radiation.

2.3.2 Ionizing photon production rate

2.1 shows the evolution in the intensity of ionizing photon production with age. We quantify this in 2.2, where we show typical values of $\hat{Q}_\mathrm{H}$, the production rate of photons that are capable of ionizing hydrogen ($\lambda \geq 912$Å) as a function of the age and metallicity of the stellar population. As expected, the youngest stellar populations produce the most ionizing photons and have the highest values of $\hat{Q}_\mathrm{H}$. As the population ages, cooler stars dominate the SED, producing less light at higher energies and decreasing the overall ionizing photon rate.

The SSP metallicity has a second-order effect on the ionizing photon rate, attributed to (1) metallicity-dependent changes in the stellar atmospheres and (2) metallicity-dependent changes in stellar evolution. First, metals in stellar atmospheres absorb heavily, diminishing

the UV flux for high-metallicity SSPs, lowering $\hat{Q}_{\rm H}$. Second, low-metallicity stellar populations have longer main sequence lifetimes, and can thus produce photons capable of ionizing hydrogen for longer.

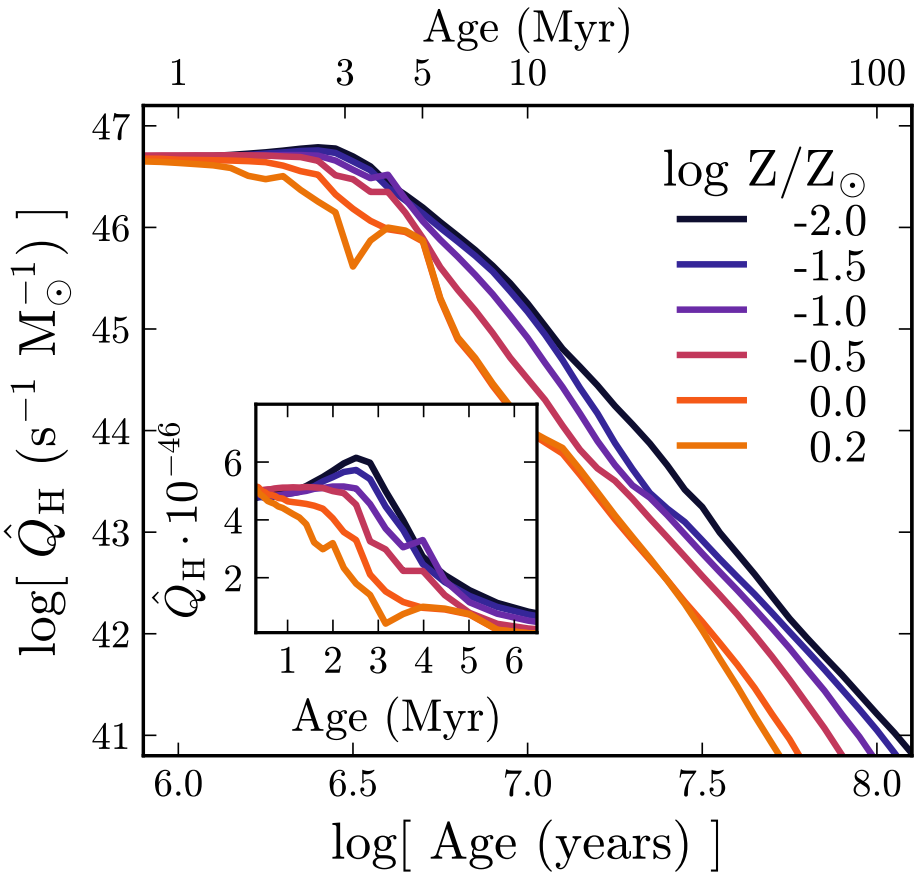

Figure 2.2 The time evolution of the ionizing photon production rate ($\hat{Q}_{\rm H}$, see 2.1) for single-burst populations at different metallicities. $\hat{Q}_{\rm H}$ decreases with time as the stellar population ages and cooler stars dominate the flux. Metallicity affects $\hat{Q}_{\rm H}$ in two separate ways. At high-metallicity, line-blanketing in stellar atmospheres reduces UV flux, lowering $\hat{Q}_{\rm H}$. Low metallicity populations have longer main sequence lifetimes, enhancing $\hat{Q}_{\rm H}$ at later times.

2.3.3 EUV spectrum

Not only is the absolute *number* of ionizing photons important, but the exact distribution of ionizing photon energies is important as well. Photoionization ejects an electron with kinetic energy proportional to the energy of the ionizing photon, and thus the spectrum of initial electron velocities in the nebula reflects the spectrum of ionizing photons. The more high energy photons are present, the "harder" a spectrum is, which ultimately affects the temperature and ionization structure of the H II region. To quantify the hardness of the SSPs in our models, we calculate the slope of the extreme-ultraviolet (EUV) portion of the SED, as measured between the ionization threshold for helium (HeI, 24.6 eV or 505Å) and hydrogen (13.6 eV or 912Å). A large slope implies relatively few high-energy photons (a "soft" ionizing spectrum) and a smaller, flatter slope implies relatively more high-energy photons (a "hard" ionizing spectrum).

We show the time evolution of the EUV slopes in 2.3. To first-order, the slope of the EUV spectrum is a function of SSP age. The youngest populations have spectra dominated by hot stars, which emit relatively more high-energy photons. Older populations have spectra dominated by cooler stars, which emit relatively fewer high-energy photons. Thus as the population ages, the slope gradually steepens, or "softens." The abrupt change in spectral slope at $\log t \sim 6.5$ (~ 3 Myr) roughly corresponds to the lifetime of an O-type star; once the O-type stars have evolved off of the main sequence the slope suddenly becomes much "softer."

The EUV-slope is also a function of metallicity, since metallicity affects stellar evolutionary time scales and mass loss rates. Low-metallicity populations are generally hotter, which hardens the EUV spectrum. Low-metallicity populations have weaker line-driven winds and experience less mass-loss, affecting main sequence lifetimes. The low-metallicity models produce a more gradual softening of the EUV spectrum, maintaining hard ionizing spectra for 1-2 Myr longer than the most metal-rich population.

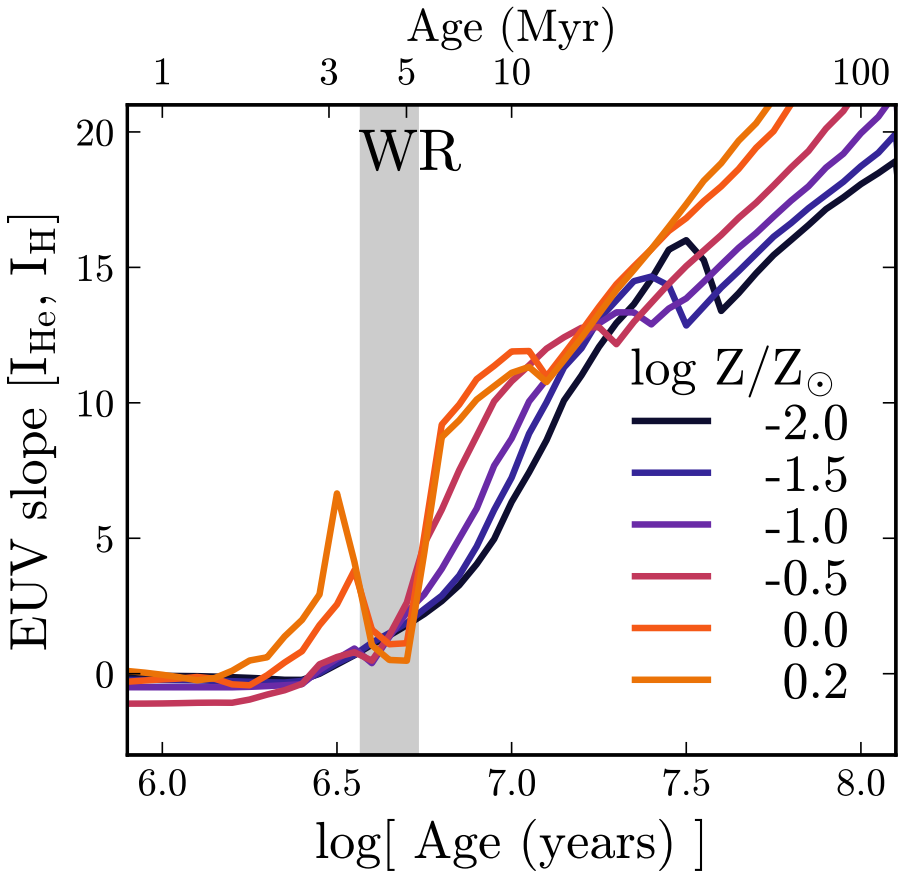

Figure 2.3 The time evolution of the EUV slope of ionizing spectra for single-burst populations at different metallicities. The slope is measured between the ionization energy of helium (505Å) and hydrogen (912Å); a smaller slope indicates a "harder" ionizing spectrum with relatively more high energy photons. The ionizing spectra soften with time as the SSP ages. The metal-poor populations produce harder ionizing spectra at all ages. The sudden hardening of the spectra near $\log t \sim 6.7$ is due to the onset of the WR phase, which does not occur for very metal-poor populations.

2.3.4 Massive Star Evolution

Flux in the EUV portion of the spectrum is primarily produced by stars with $M > 10\,\mathrm{M}_\odot$, and is thus closely tied to massive star evolution. As such, the reliability of the photoionization models is tied to the reliability of evolutionary models of massive stars. Although the ionizing spectrum tends to become both softer and less intense with time, there are noticeable departures from these trends at ∼5 Myr. These fluctuations are due to Wolf-Rayet (WR) stars, which are massive stars (initial mass $\gtrsim 30\,\mathrm{M}_\odot$; highlighted as $\sim 35 - 75\,\mathrm{M}_\odot$ in 2.1) that have evolved off of the main sequence. WR stars are stellar cores exposed from extreme mass loss, and their hot temperatures significantly harden the ionizing spectrum of the stellar population, seen clearly at $\log t \sim 6.7$ in 2.3. While the affect of the WR phase appears huge in 2.3, it occurs on such short timescales that it will likely not be detectable compared with the predictions of classical models of massive stars.

We note, however, that models of WR evolution are extremely uncertain, and that the exact masses and evolutionary pathways are not well-constrained. The extreme non-LTE nature of their atmospheres make WR stars challenging to model, and variations in mass loss and the strength of stellar winds make it difficult to predict ionizing fluxes (see review by Crowther, 2007, and references within). This limitation likely imparts significant uncertainties into the evolution of the ionizing spectrum, particularly at late (∼5 Myr) times.

The Padova+Geneva isochrones used in this work do not include the effects of stellar rotation or binarity, both of which have important effects on the ionizing spectrum and main sequence lifetimes of massive stars (e.g., Levesque et al., 2012; Eldridge, 2012; Stanway et al., 2016). We discuss this issue in detail in §2.6, and in §2.6.1 we include an analysis of the ionizing spectra produced by the MESA Isochrones & Stellar Tracks (MIST, Dotter, 2016; Choi et al., 2016), which include stellar rotation.

2.3.5 Constant Star Formation Rate

Ionizing spectra from single bursts may be a good approximation for a single massive H II region, but real galactic stellar systems can show more complexity. Star clusters do not form instantaneously, and may be better modeled by a population with a range of ages spanning a few million years. Likewise, galaxies are subject to prolonged bursts of star formation involving many clusters, and their integrated spectra may be better represented with even more extended, complex SFHs.

We illustrate the effect of extended star formation by comparing the instantaneous burst models to models generated with a constant star formation rate (CSFR) of 1 $M_\odot$ per year. In this analysis, the constant SFR spectra are generated with FSPS and then fed as input to Cloudy. To calculate the total emission spectrum for complex or extended SFHs, FSPS adds the nebular emission from contributing SSPs from the nebular look-up tables generated by instantaneous bursts.

In the top panel of 2.4 we compare the time evolution of $\hat{Q}_{\rm H}$ for instantaneous bursts and constant SFR populations. For instantaneous burst models, $\hat{Q}_{\rm H}$ decreases steadily with age as the massive star population evolves off the main sequence. In models with constant SFR, however, the rate of stars forming and the rate of stars dying eventually reach an equilibrium, after which there is little evolution in the ionizing spectrum. The constant SFR models reach an equilibrium around 4 Myr, after which the ionizing photon rate is essentially constant.

The bottom panel of 2.4 shows the time evolution of the EUV slope. The slope of the constant-SF model reaches equilibrium around 6 Myr, with a slope that is roughly equivalent to that of a 2 Myr instantaneous burst. We note that these identified equilibrium ages correspond to a specific IMF and set of evolutionary tracks and may be different for stellar populations generated with different properties.

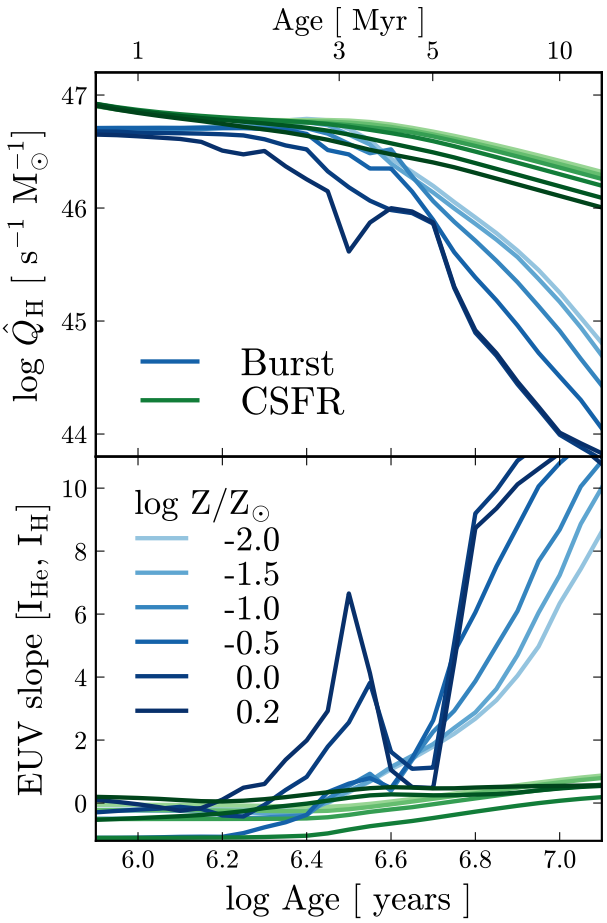

Figure 2.4 The time evolution of ionizing spectra for instantaneous bursts (blue) and populations with constant SFRs (green). The color intensity shows different metallicities, where darker colors correspond to lower metallicities. **Top:** Time evolution of $\hat{Q}_H$, as in 2.2 for the instantaneous bursts. The constant SFR models eventually reach an equilibrium where the birth rate of stars balances the rate of stars leaving the main sequence. This occurs at ∼4 Myr, after which the ionizing spectrum shows little variation. **Bottom:** Time evolution of the EUV slope, as in 2.3 for the instantaneous bursts. The slope of the constant SFR model reaches equilibrium near 7 Myr, with a slope consistent with that of a ∼2 Myr instantaneous burst.

2.4 Nebular Models

For the models described in §2.2, we use CLOUDY to calculate the physical properties of the gas and the emergent emission line and continuum spectrum. In this section, we discuss each of these features in turn.

2.4.1 Broad Physical Trends in Model HII Regions

CLOUDY calculates the full radiative transfer through the gas cloud, so each individual H II region model has internal structure, with radial variations in ionization state and temperature, which in turn affect the location within the nebula where various emission lines are produced. Before discussing the emission properties of the model H II regions, we first explore their internal structure to better understand the physical conditions driving the global spectrum.

Model HII Region Temperatures

The emergent emission spectrum is sensitive to the kinetic temperature of the free electrons, T_e, since collisions between electrons and metal ions are responsible for producing some of the most prominent emission lines observed in H II region spectra. In this section, we describe how the equilibrium temperature of model H II regions is affected by the input ionizing spectrum and gas-phase metallicity. Our model links the metallicity-dependent changes in the ionizing spectrum with the coolants in the gas cloud, which drive the bulk trends in cloud temperature and ionization structure.

The equilibrium temperature of an H II region is set by the balance of heating and cooling processes. Photoionization of hydrogen is the dominant source of heating in an H II region. The net heating from photoionization is determined by (1) the photoionization rate and (2) the average energy of the liberated electrons, both of which depend on the intensity and shape of the ionizing radiation field by means of the number of incident ionizing photons and the energy injected per photoionization. The volumetric heating rate from photoionization,

$\Gamma_{\rm ion}$, is thus given by the photoionization rate weighted by the energy of the freed electron:

$$\Gamma_{\rm ion} = n_{\rm H} \int_{\nu_0}^{\infty} \frac{4\pi J_\nu}{h\nu}(h\nu - h\nu_0)\sigma_\nu({\rm H})d\nu\,, \tag{2.3}$$

where $n_{\rm H}$ is the neutral hydrogen density, σ_ν(H) is the photoionization cross-section of neutral hydrogen, ν_0 the ionization energy, and J_ν is the mean specific intensity of the radiation field. This form is similar to integrating a monochromatic version of $Q_{\rm H}$ weighted by the energy of each photoelectron. Thus for a given $Q_{\rm H}$, if there are relatively more high-energy photons (i.e., if the ionizing spectrum is harder), each photoionization will inject more kinetic energy, increasing the heating rate.

Cloud cooling is radiative, through a combination of line and continuum emission. We represent the total cooling rate, $\Lambda_{\rm rad}$, as a sum of each of the major cooling processes:

$$\Lambda_{\rm rad} = \Lambda_{\rm ce} + \Lambda_{\rm fb} + \Lambda_{\rm ff}\,, \tag{2.4}$$

where $\Lambda_{\rm ce}$ is the cooling from collisionally-excited metal ions, $\Lambda_{\rm fb}$ is the cooling from free-bound emission, and $\Lambda_{\rm ff}$ is the cooling from free-free emission[6]. In 2.4 the cooling rates are ordered by their contribution to the total cooling rate; for H II regions, the dominant cooling process is emission from collisionally-excited metal-ions.

In 2.5 we show the fractional contribution of collisionally excited metal ions to the total cloud cooling as a function of model age and metallicity. At near-solar and super-solar metallicities, the cooling is dominated by forbidden and fine-structure transitions from collisionally-excited metal-ions, which can provide up to 95% of the total cooling. However, for metal-poor nebulae, the contribution from collisionally-excited metal-ions is less than 1% of the total cooling rate. In this regime, hydrogen provides the bulk of the cooling emission via free-bound line and continuum emission.

The model H II regions are in thermal equilibrium, so the net energy gained and lost by the nebula is equal at every age and metallicity. While the net heating and cooling

[6] Γ and Λ are traditionally used to represent the net energy gained (and lost) per unit volume, with units erg·s^{-1}·cm^{-3}. In this work we use Γ and Λ to represent the total energy gained (and lost) in the nebula, with units erg·s^{-1}.

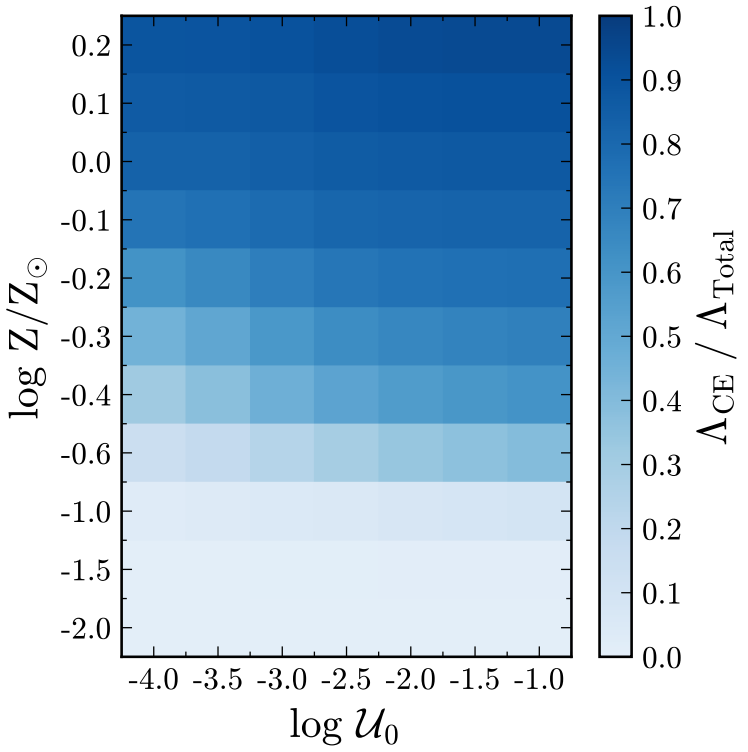

Figure 2.5 The fractional contribution of collisionally-excited metal lines to the total cooling in a 1 Myr population as a function of metallicity and ionization parameter. Metal lines are the dominant coolant for models with metallicities above $\log_{10} \mathrm{Z/Z_\odot} = -1.0$, and can provide as much as 95% of the cooling emission at the highest model metallicities. For models below $\log_{10} \mathrm{Z/Z_\odot} = -1.0$, the bulk of the cooling emission is through Lyα, recombination lines, and the bound-free continuum.

rates in each cloud are always equal, the efficiency of the various cooling processes is highly variable, resulting in different model equilibrium temperatures. Metal line cooling is a particularly efficient coolant and produces much lower equilibrium temperatures than cooling from recombination emission.

In the left panel of 2.6 we show the volume-averaged equilibrium temperatures of model H II regions as a function of metallicity and ionization parameter for a 2 Myr model. T_e varies from $\sim 4000 - 20,000$ K, with the lowest cloud temperatures found in the most metal-rich models. Metal line cooling is the dominant cooling process for nebulae with metallicities $-1.0 < \log \mathrm{Z/Z_\odot} < 0.1$, and the cooling efficiency is a strong function of the gas cloud metallicity. Scaling up the gas phase abundances increases the cooling efficiency, producing lower equilibrium temperatures, as expected from 2.5.

Below $\log_{10} \mathrm{Z/Z_\odot} = -1.0$, the shift in the dominant coolant produces a secondary dependence on ionization parameter. In these metal-poor gas clouds, hydrogen is the only available coolant, with most of the cloud cooling emission produced in recombination lines and continuum emission. The strength of the recombination emission is strongly dependent on the number of incident ionizing photons, thus below $\log_{10} \mathrm{Z/Z_\odot} = -1.0$, T_e depends on both metallicity and ionization parameter.

The right panel of 2.6 shows the time evolution of the model H II region temperatures at several different metallicities and ionization parameters. As the ionizing spectra soften with age, the equilibrium temperatures decrease. However, variations in metallicity and ionization parameter drive much larger variations in equilibrium temperature.

Ionization Structure and Line Emissivity of the Model HII Regions

The ionization state of the cloud is critical for determining a number of processes within the nebula: the rate of radiative cooling, the rate at which the cloud absorbs photons from stars, and the chemical processes that can proceed within the cloud. The ionization structure sets the accessibility of critical emission lines; for example, [O III] emission can only be produced if oxygen is doubly ionized. It is therefore necessary to understand what drives the ionization

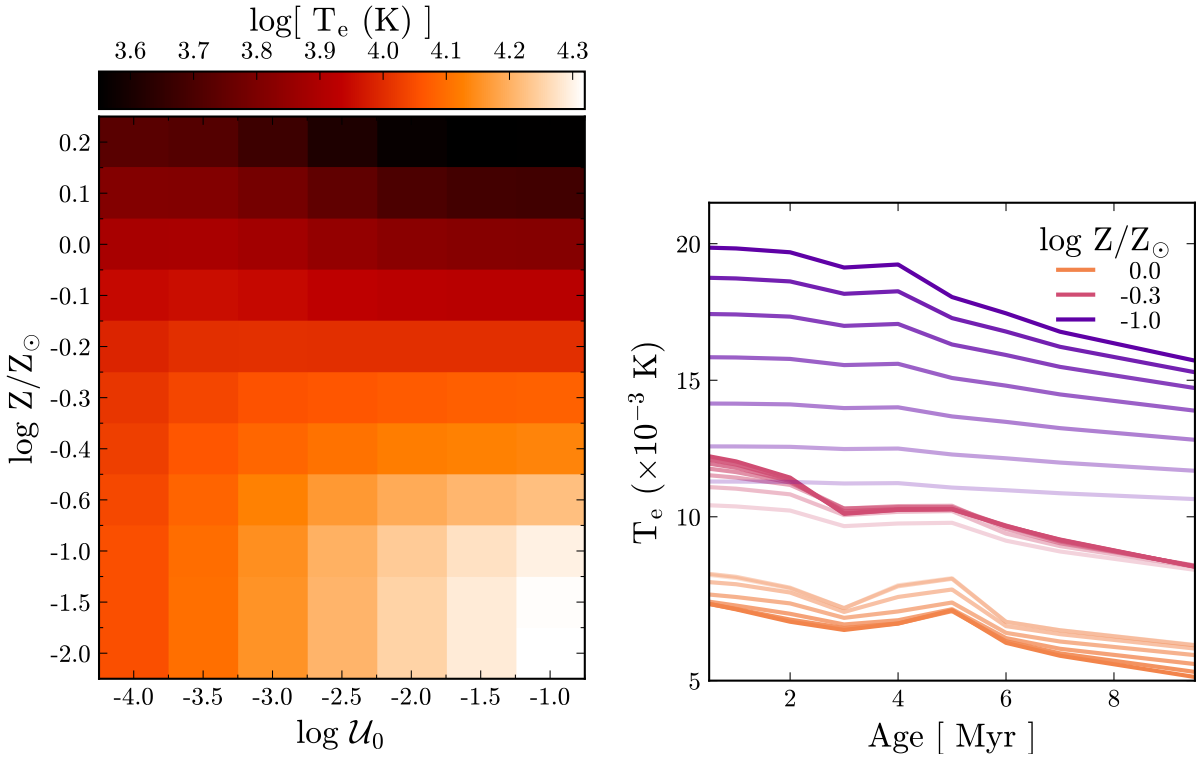

Figure 2.6 Volume-averaged electron temperatures (T_e) of model H II regions. **Left:** T_e as a function of $\mathcal{U}_0$ and $\log_{10} \mathrm{Z/Z_\odot}$ at fixed age, 2 Myr. Above $\log_{10} \mathrm{Z/Z_\odot} = -1$, metal line cooling dominates and T_e is primarily a function of metallicity. Below $\log_{10} \mathrm{Z/Z_\odot} = -1$, Ly-$\alpha$, free-bound, and free-free continuum emission provide most of the cooling radiation and T_e depends primarily on $\mathcal{U}_0$. **Right:** The time evolution of T_e at $\log_{10} \mathrm{Z/Z_\odot} = -0.3, -0.6, -1.0$. For each metallicity, the transparency of the line indicates the ionization parameter, from $\log_{10} \mathcal{U}_0$=-1 (opaque) to $\log_{10} \mathcal{U}_0$=-4 (transparent). At a fixed abundance, this demonstrates the sensitivity of T_e to the hardness of the ionizing spectrum, since the ionizing spectra soften with age.

structure of H II regions to understand the global emission line spectrum. Photoionization is by far the most important ionization process, and the frequency dependence of the ionization cross section means that the spectral shape will thus play an important role in determining the ionization structure within the model H II region.

In 2.7 we show the ionization structure and line emissivity of oxygen in a model H II region at 1, 2, and 3 Myr at fixed ionization parameter. At all ages, the high ionization species are found in the inner region of the nebula, while lower ionization species are found in the outer region of the nebula. Spectral shape regulates the spatial extent of high-ionization species and the prevalence of partial-ionization zones, which in turn controls where emission from collisionally-excited transitions is produced.

While oxygen emission is strong at all ages, the age-dependent softening of the ionizing spectrum changes the location within the cloud where each emission line is produced. In the 1 Myr model, O++ is appreciably present in $\sim 60\%$ of the cloud, with [O III] emission produced at nearly all radii. In the 3 Myr model, however, O++ is only present in the innermost 25% of the cloud, and the emission from [O III] is entirely contained within the doubly ionized oxygen zone. While the [O I], [O II], and [O III] lines are produced in overlapping physical regions in the 1 Myr model, the lines are produced in physically distinct regions of the cloud in the 3 Myr model.

Ideally, we would like temperature and density diagnostics for the same ionic state, which would probe the same physical region within the nebula. [O III] is a commonly-used temperature diagnostic, but probes the temperature in the O++ zone, near the inner edge of the nebula. [O II] is the only optically accessible oxygen density diagnostic, which measures the density in the the O+ zone, in the outer region of the nebula. The region probed in either case may not be representative of the nebula as a whole. This has implications for the interpretation of line ratios, as lines produced at different radii probe physically distinct regions of the nebula.

The strength of emission lines is not set solely by the total abundance of an ionic species in the nebula (i.e. the ionization structure shown in 2.7), but is modulated by the energetic

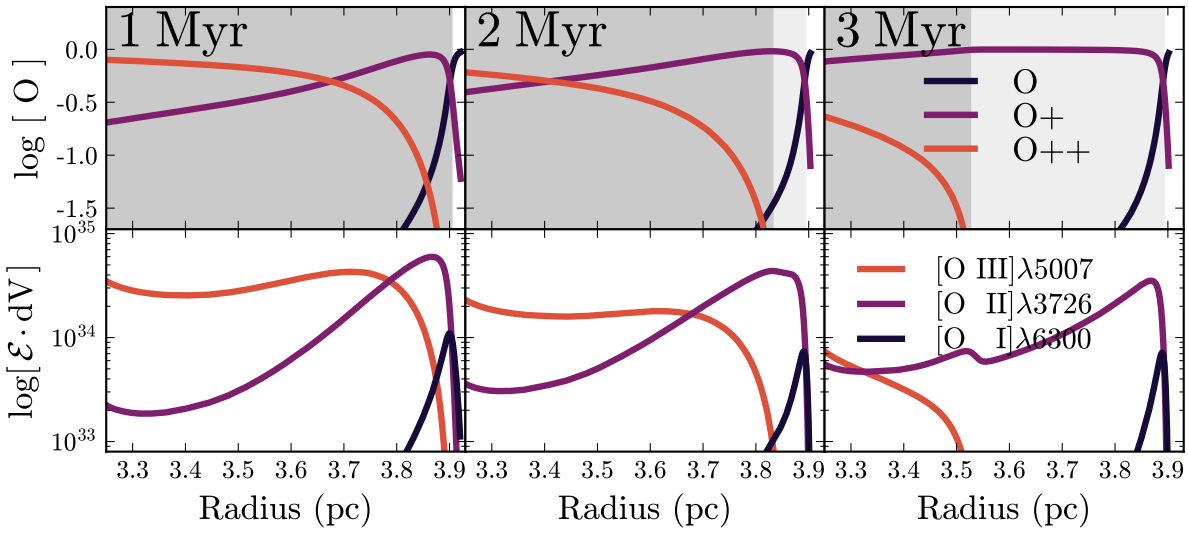

Figure 2.7 A detailed look at the structure of oxygen for a solar metallicity model with $\log_{10}\mathcal{U}_0 = -2.5$ at three different ages: 1, 2, and 3 Myr. **Top:** The ionization structure of the H II region. The dark- and light-grey shaded regions show location of the helium and hydrogen ionization zones, respectively. Oxygen is doubly ionized throughout the H II region at 1 Myr, but only in the innermost region at 3 Myr, reflecting the softening of the ionizing spectrum with age. **Bottom:** The location where important oxygen lines are produced, calculated by integrating the line emissivity over each volumetric shell in the cloud. The emission from various transitions generally follows the ionization structure of the cloud. This implies that different lines can probe physically distinct parts of the H II region: in the 3 Myr model, [O III] emission is produced in the innermost parts of the cloud while [O I] emission is produced in the outermost parts.

accessibility of energy levels as well. Collisional excitation involves an interaction between an ion and a free electron, and the rate of collisions will thus depend on the kinetic energy of the free electrons in the nebula[7].

This is especially important in the context of our nebular model, which links the gas phase abundances to the metallicity of the ionizing population. In §2.4.1, we demonstrated that T_e is a strong function of metallicity through the efficiency of metal line cooling. Both the hardness of the ionizing spectrum and the timescales associated with stellar evolution are metallicity-dependent, which has important effects on the thermodynamic properties of the model H II regions.

In 2.8 we show the oxygen ionization structure and line emissivity of a 3 Myr model at constant ionization parameter and different metallicities. In 2.7, the age-induced softening of the ionizing spectrum changed the spatial extent of different ionization zones. Here, we see a similar effect from the metallicity-induced changes in the ionizing spectrum, where the harder ionizing spectra in the low-metallicity model extends the O++ ionization zone.

Hydrogen Recombination Lines

Hydrogen recombination lines are typically the strongest lines in H II region spectra, and are widely used diagnostics of H II region conditions when combined with metal lines. However, the hydrogen lines have a fundamentally distinct emission mechanism than the collisionally-excited metal lines discussed in §2.4.1. Recombination lines are produced by the radiative recombination of a free electron with a proton into an excited state, followed by a radiative cascade to lower levels. They therefore have a different dependence on the properties of the nebula.

Analytic prescriptions for nebular emission generally assume that the number of ionizing photons and the number of recombination photons are equal, which yields a simple equation that converts $Q_{\rm H}$ to an Hα luminosity. It is thus unsurprising that the total power in the

[7]We implement a constant density model, but collisional excitation will also depend on the number of colliders and thus the density of the nebula.

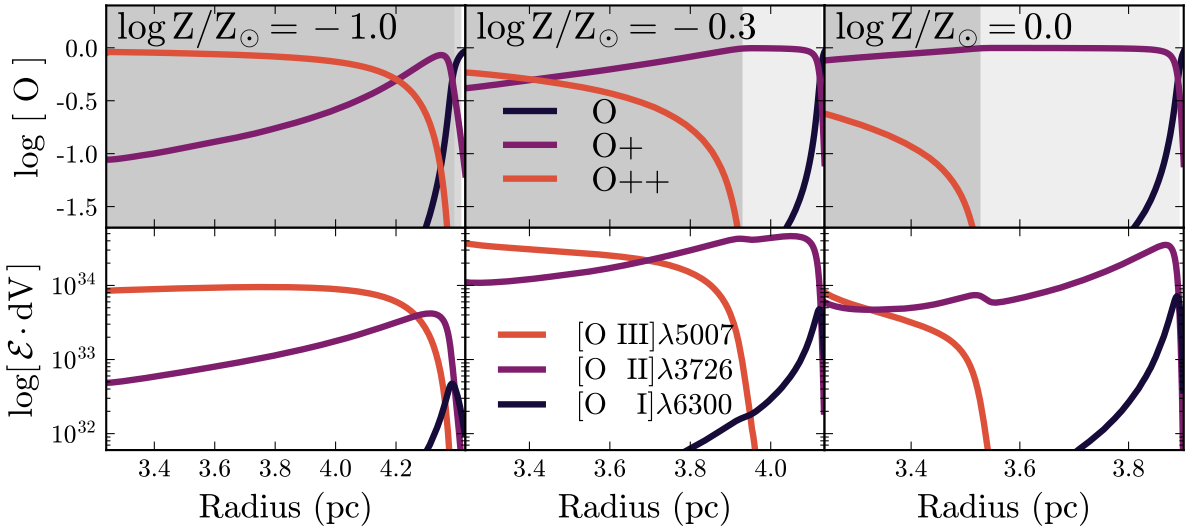

Figure 2.8 A detailed look at the structure of oxygen for a 3 Myr, $\log_{10}\mathcal{U}_0 = -2.5$ model at three different metallicities: -1.0, -0.3, 0.0. Just as in 2.7, the top panel shows the ionization structure and the bottom panel shows the integrated emissivity of various oxygen transitions. Here, the change in metallicity changes the temperature of the H II region, which ultimately alters the ionization structure of the cloud. Lower metallicities produce higher temperatures, increasing the fraction of doubly-ionized oxygen.

recombination lines closely tracks $Q_{\rm H}$ as measured from the ionizing spectrum.

However, the conversion between $Q_{\rm H}$ and $L_{\rm H\alpha}$ is not one-to-one, because the recombination coefficient, $\alpha_{\rm B}$, is a function of temperature. To get the correct luminosity of Hα and Hβ, it is essential to factor in both the number of ionizing photons and the temperature of the nebula. This is explicitly self-consistent in our nebular model, which adds the nebular emission to the same SSP (t, Z) as the one input to CLOUDY, preserving the temperature sensitivity of the recombination lines as a function of age and metallicity. We note that the POPSTAR models do include a metallicity-dependent T_e in their recombination coefficient, but not an age-dependent T_e.

In 2.9, we show the Hα luminosity of the model H II regions as a function of age, metallicity, and ionization parameter. We have normalized the Hα luminosities by $Q_{\rm H}$ to demonstrate the magnitude of the variations in Hα luminosity driven by changes in temperature. At young ages, metallicity changes produces $10-20\%$ variations in Hα line strength. The softening of the ionizing spectrum with age can change the recombination line strengths by $40-50\%$. Both of these will impact Hα-based SFR indicators that do not account for the temperature dependence of recombination lines.

Nebular Continuum

The nebular emission model has two components: line emission and continuum emission from ionized gas. The implementation within FSPS allows the user to choose whether to include one or both in the output spectrum. For young, metal-poor populations, the continuum can contribute a significant portion of the total flux at optical and IR wavelengths, with a relative contribution that can be comparable to the stellar flux (e.g., Reines et al., 2010).

For H II regions, the most important continuum emission processes are free-bound and free-free transitions: free-bound emission is responsible for most of the nebular continuum emission at optical and NIR wavelengths, while the free-free emission is more important at longer wavelengths.

The free-bound continuum is produced when a free electron recombines into an excited

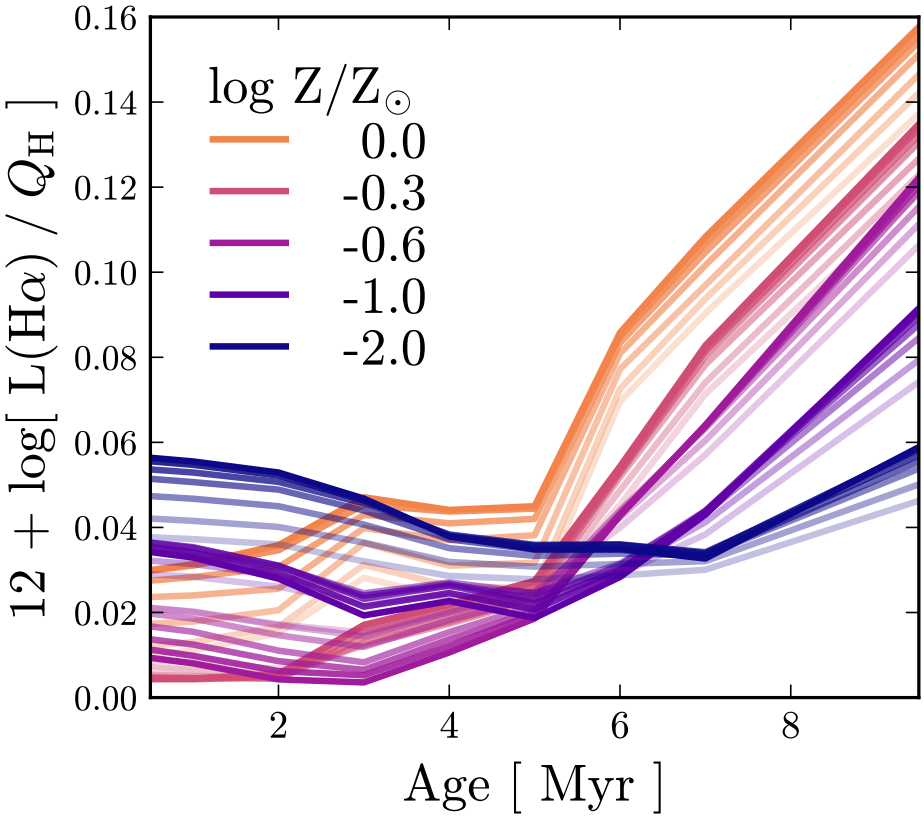

Figure 2.9 The time evolution of the Hα luminosity normalized by the ionizing photon rate, $Q_{\rm H}$. The different colors show different model metallicities and the transparency of the line indicates the model ionization parameter, from $\log_{10}\mathcal{U}_0 = -1$ (opaque) to $\log_{10}\mathcal{U}_0 = -4$ (transparent). Predictions of L(Hα) are often based solely on the ionizing photon rate, $Q_{\rm H}$. Deviations are driven by the temperature dependence of the hydrogen recombination coefficient, and will thus vary with the age and metallicity of the model.

level of hydrogen, followed by the radiative cascade that produces recombination lines. The resultant continuum spectrum has a sharp "edge" at the ionization energy followed by continuous emission to higher energies. As a hydrogen recombination process, the free-bound continuum is sensitive to model ionization parameter, which will set the overall intensity of the continuum emission. However, the general shape of the continuum is determined by the distribution of electron velocities and the recombination cross section, and will thus be sensitive to the temperature of the H II region as well.

The free-free continuum, which is the result of a free electron scattering off of an ion or proton, produces a roughly power-law ($\propto \nu^{-2}$) distribution of photon energies and is also sensitive to the temperature of the H II region. The two-photon continuum, while smaller in magnitude, can be important in the UV. The two-photon continuum is the result of a bound-bound process, where the excited 2s state of hydrogen decays to the 1s state by the simultaneous emission of two photons. The energy of the two photons totals to $h\nu_{\mathrm{Ly}\alpha}$, producing a bump in the UV portion of the spectrum.

In the top panel of 2.10 we show the nebular continuum spectrum for a 1 and 3 Myr solar metallicity model. The overall intensity of the nebular continuum spectrum is set by the model ionization parameter, since recombination emission depends on the number of incident ionizing photons. At fixed metallicity and age, the continuum spectrum is nearly identical modulo a scaling factor, $\hat{Q}_{\mathrm{H}}/Q_{\mathrm{H}}$, which scales the intensity of the model, described in §2.2.1. Several spectral features are easily discernible: bound-free transitions produce the characteristic sawtooth edges across the spectrum; the two-photon continuum is responsible for the bump at $\sim$1500Å.

While $\mathcal{U}_0$ sets the continuum normalization, the relative height and steepness of the recombination edges are sensitive to the nebular temperature and thus the metallicity of the model. The temperature-sensitivity of the recombination continuum is well-known, and the strength of the edge features have long been used as temperature diagnostics (e.g., Peimbert, 1967).

In the bottom panel of 2.10 we show the nebular continuum for models with different

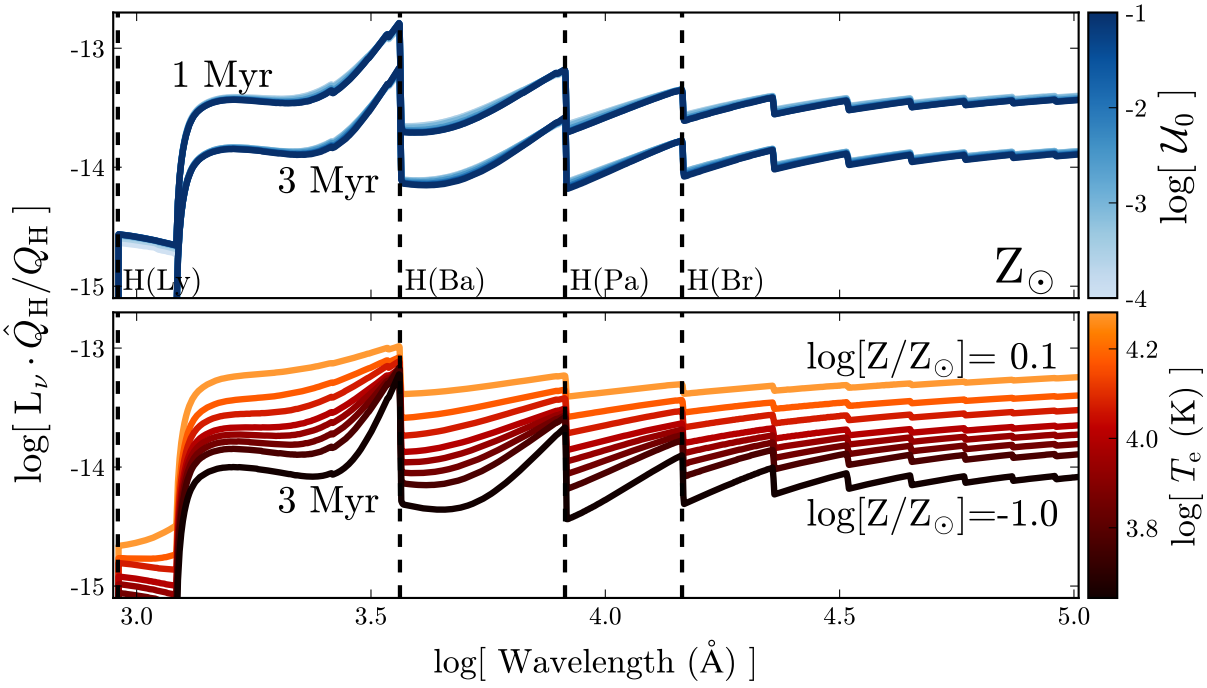

Figure 2.10 The nebular continuum emission spectrum. The dashed lines indicate the wavelength of various hydrogen series limits ($n = \infty \rightarrow \{1, 2, 3, \ldots\}$). **Top:** Continuum emission spectrum for 1 and 3 Myr models at solar metallicity and varying $\mathcal{U}_0$. Continuum emission is a combination of free-bound, free-free and two-photon emission processes. The intensity of continuum emission scales with model ionization parameter, since the free-bound continuum is a recombination process. To remove the $\mathcal{U}_0$ dependence we normalize the continuum by $\hat{Q}_{\rm H}/Q_{\rm H}$. **Bottom:** Normalized continuum emission for a 3 Myr SSP at $\log_{10}\mathcal{U}_0 = -1.0$ for different metallicities between $\log_{10}{\rm Z/Z_\odot} = -1.0$ and solar. To emphasize the relationship between gas temperature and gas metallicity, each metallicity is color-coded by T_e, the volume-averaged electron temperature of the gas. The changes in temperature alter the slope and sharpness of the recombination edges.

metallicities, again normalized by $\hat{Q}_{\rm H}/Q_{\rm H}$. Low metallicity models have relatively more continuum emission. The emission edges are much broader, and there is less difference in amplitude between recombination edges. This behavior is primarily due to temperature changes driven by the changing cooling efficiencies.

Nebular continuum emission is clearly strongest at high ionization parameters and low-metallicity. The harder ionizing spectra associated with young stellar populations further enhances this. In 2.11, we show the total SED for 1 and 5 Myr SSPs at high and low metallicities and $\log_{10}\mathcal{U}_0 = -1.0$. The 1 Myr model has much stronger line and continuum emission, which is strongest in the low-metallicity model.

Reines et al. (2010) found that the nebular continuum contributed significantly ($\sim 40\%$) to the NUV-NIR broadband flux of young (< 3 Myr) clusters, especially near the Balmer break. In 2.12, we show the fractional contribution to the total flux as a function of model age for several wavelength ranges from the EUV to the NIR at fixed ionization parameter ($\log_{10}\mathcal{U}_0 = -1.0$) and at two metallicities (solar and $\log_{10}\mathrm{Z}/\mathrm{Z}_\odot = -1$). Our emission models agree with Reines et al. (2010), with continuum and line emission contributing at least 30% of the total flux at young ages in every wavelength range considered.

The largest contribution from line and continuum emission relative to the stellar emission is seen in the optical and NIR. Nebular line and continuum emission contributes 95% of the total flux from $1.0 - 5.3\mu$m for several million years, with continuum emission producing 70% of the total flux.

We show the fractional contribution to the broadband flux for a $\log_{10}\mathrm{Z}/\mathrm{Z}_\odot = -1$ model in the bottom panel of 2.12. The broad behavior in the low metallicity model is nearly identical to the solar metallicity model. We might expect line emission to contribute a larger fraction of the total flux in the low-metallicity model, since oxygen emission is generally stronger at sub-solar metallicities; this effect is only a few percent. The most noticeable difference between the high and low metallicity models is the time dependence of the nebular emission. In the low metallicity model, nebular emission contributes a significant portion of the total flux for longer, by a few Myr. Lower metallicity stellar populations have extended main

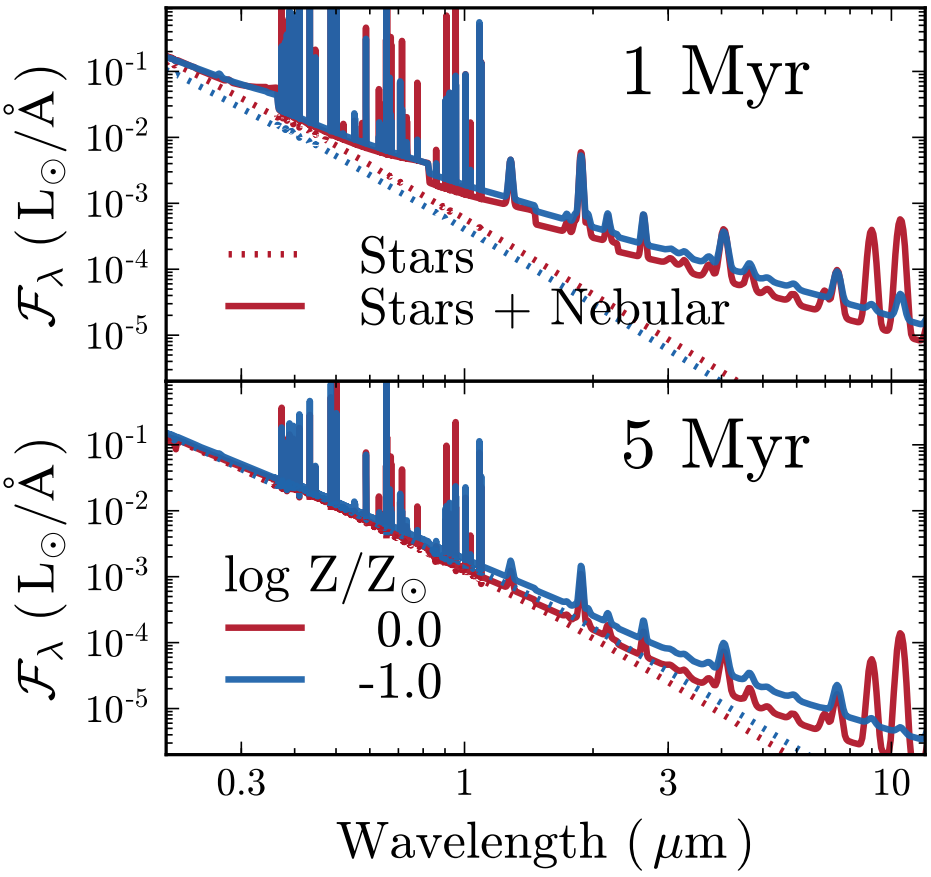

Figure 2.11 NUV to NIR spectra for instantaneous bursts with and without nebular emission. For models at 1 Myr (top) and 5 Myr (bottom) at solar metallicity (red) and $\log_{10} \mathrm{Z}/\mathrm{Z}_\odot = -1.0$ (blue) at $\log_{10} \mathcal{U}_0 = -1$. The 1 Myr model produces more nebular line and continuum emission than the 5 Myr model.

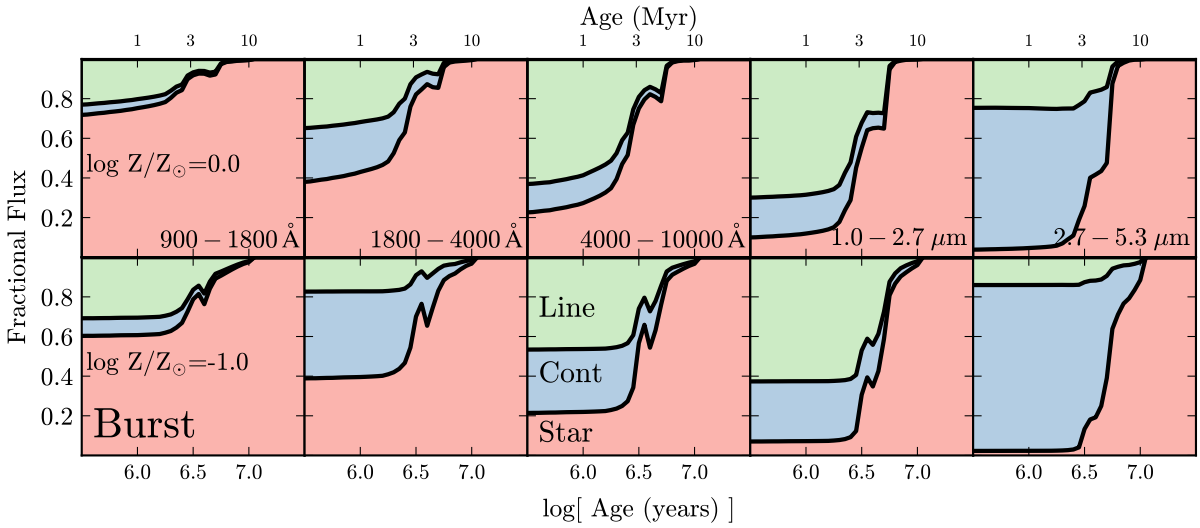

Figure 2.12 The fractional contribution of starlight (red), nebular continuum (blue) and nebular line emission (green) to the total flux, as a function of SSP age at $\log_{10} \mathrm{Z/Z_\odot} = 0$ (top) and $\log_{10} \mathrm{Z/Z_\odot} = -1$ (bottom) and $\log_{10} \mathcal{U}_0 = -1$. Each panel shows a different wavelength range from the UV to the IR. From left to right: FUV ($900 - 1800$Å), NUV ($1800 - 4000$Å), Optical ($4000 - 10,000$Å), NIR ($1 - 2.7\mu$m), NIR ($2.7 - 5.3\mu$m). For models below 5 Myr, nebular emission contributes $> 20\%$ of the flux in all panels.

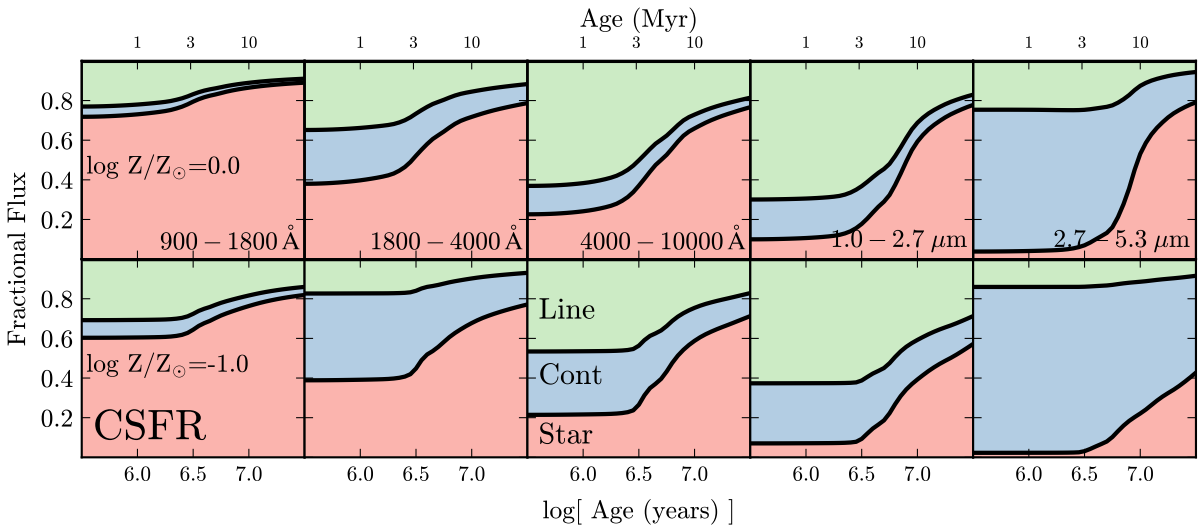

Figure 2.13 The fractional contribution of starlight (red), nebular continuum (blue) and nebular line emission (green) to the total flux, as a function of time for constant SFR models at $\log_{10} \mathrm{Z/Z_\odot} = 0$ (top) and $\log_{10} \mathrm{Z/Z_\odot} = -1$ (bottom) and $\log_{10} \mathcal{U}_0 = -1$. As described in 2.12, each panel shows a different wavelength range from the UV to the IR. In the optical and NIR, nebular emission can contribute $30 - 50\%$ of the total flux at 10 Myr.

sequence lifetimes, which in turn extends the timescale for nebular emission. This is an important feature of our nebular model, which links the stellar and nebular abundances, and ultimately allows for a more accurate accounting of the total flux from galaxies.

2.13 shows the same fractional contributions but for models assuming a constant SFR. As the young stars evolve off of the main sequence and a substantial population of older stars is built up, the stellar contribution increases. Nebular emission remains a significant fraction of the total light at 10 Myr and beyond, and is especially important at low metallicity. Thus, for galaxies with a burst of recent star formation or star formation extended over several million years, it is essential to include the contribution from nebular line and continuum emission to accurately predict the underlying properties of the stellar population from broadband photometry.

2.4.2 Line Emission from the Model HII Regions

With an understanding of the physical properties of the model H II regions, we can better understand the processes driving variations in nebular emission. In this section, we characterize the emission line properties of the model H II regions and their dependence on the model parameters.

Broad Trends in Emission Line Strength

2.14 shows global trends in line strength for the strongest optical emission lines: H$\beta\lambda$4861, [O III]λ5007, H$\alpha\lambda$6563, [N II]λ6584, and [S II]λ6713. To showcase the results of the implementation within FSPS, the emission lines plotted in 2.14 were generated directly from `python-fsps` by generating SSPs with and without emission lines and subtracting the stellar-only spectrum[8].

As discussed in §2.2.2, when FSPS adds in nebular emission, the emission lines are scaled by the number of ionizing photons in the incident SSP. To first order, the model

[8]Users can turn on nebular emission in the `StellarPopulation` class by setting the `add_neb_emission` parameter to `True`. See the documentation for more information.

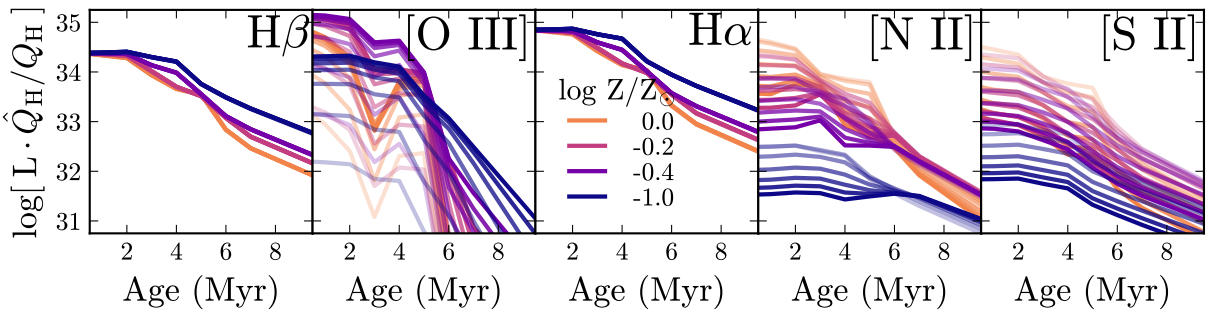

Figure 2.14 Emission line strength for Hβ λ4861Å, [O III] λ5007Å, Hα λ6563Å, [N II] λ6584Å, and [S II] λ6731Å as a function of model age. The lines are color-coded by model metallicity, and the transparency of the line indicates the ionization parameter, which varies from $\log_{10}\mathcal{U}_0 = -1$ (opaque) to $\log_{10}\mathcal{U}_0 = -4$ (transparent).

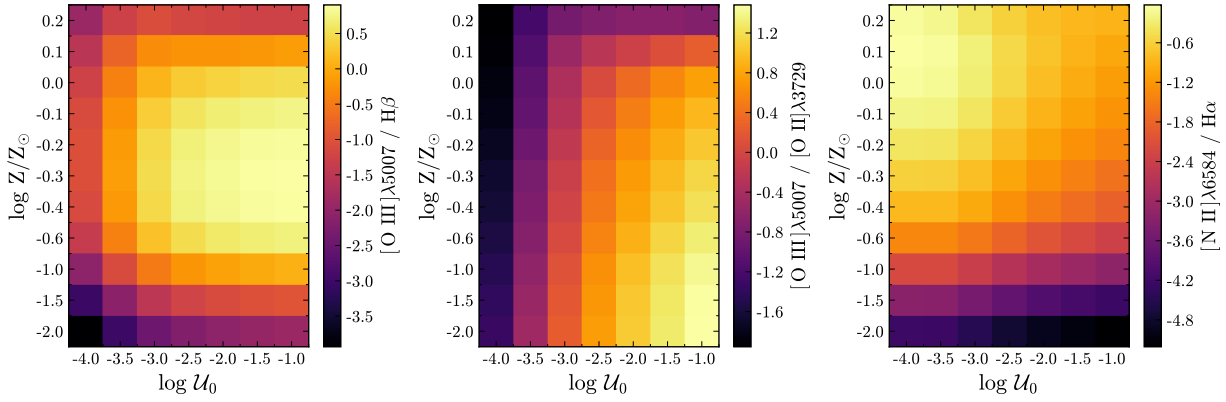

Figure 2.15 Emission line ratios as a function of metallicity and ionization parameter for a 1 Myr model: [O III]λ5007/Hβ (left); [O III]/[O II] (middle); [N II]λ6584/Hα (right).

age sets the overall intensity of the emission lines through this $Q_{\rm H}$ normalization. The 1 Myr SSP is much brighter and produces many more ionizing photons than the 4 Myr SSP and has stronger emission lines. Despite the normalization by $Q_{\rm H}$, emission lines sensitive to the overall ionization parameter still vary with $\mathcal{U}_0$. For example, [S II] is a well-known ionization-sensitive line, and is strongest at low $\mathcal{U}_0$.

For models at constant age and ionization parameter, changing the model metallicity has two effects: it changes (1) the shape of the ionizing spectrum and (2) the gas phase abundances. The first of these effects is reflected in the metallicity-dependent variability in Hα and Hβ line strengths. The metal poor models produce hotter H II regions, which in turn produces stronger recombination line emission. The second of these effects is demonstrated in the [N II] and [S II] line strengths, which are strongest in the highest metallicity models, which reflects the decreasing metal abundance.

The [O III] emission is less straightforward to describe due to the well-known double-valued and non-linear relationship between oxygen line strength and metallicity (Pilyugin & Thuan, 2005; Kewley & Ellison, 2008). For the selection of metallicities plotted in 2.14, [O III] emission is strongest at $\log_{10} {\rm Z}/{\rm Z}_{\odot} = -0.3$. At the lowest metallicities, oxygen is not abundant enough to produce significant emission; at the highest metallicities, the temperature is too low to collisionally excite a substantial population of O++ ions to make the [O III]λ5007 transition.

Emission Line Ratios

In the previous sections, we have tried to build intuition for the broad trends seen in metal and recombination line strengths. In this section we will build upon that intuition to better understand the behavior of various line ratios used to probe the physical state of the nebula.

Most line ratios involve the comparison of a metal line to a Balmer line. The total power emitted in collisionally-excited metal lines is proportional to the total cooling in metal lines, and thus sensitive to metallicity and ionization parameter (§2.4.1). As discussed in §2.4.1, the total power emitted in the hydrogen recombination lines is primarily driven by $Q_{\rm H}$ and

should thus trace the total luminosity of the ionizing source.

In practice, however, we never have access to reliable measurements of the total power in metal line emission and instead measure the fluxes of a small number of individual lines from a particular species. For example, in the left panel of 2.15 we show the the ratio of [O III]λ5007/Hβ as a function of metallicity and ionization parameter. The [O III] line strengths do not scale directly from the total metal line emission, and the resultant ratio between [O III] and Hβ does not monotonically scale with metallicity. Instead, the line ratio is double-valued with metallicity.

Some of this behavior is due to changes in the ionization state of oxygen from O+ to O++. At high metallicity temperatures are too low to collisionally excite an appreciable population of O++, decreasing the [O III] emission. The middle panel of 2.15 compares the line strengths of oxygen from two different ionization states, [O III]λ5007 and [O II]λ3727. While the [O III]λ5007 emission decreases, the [O II] emission stays relatively strong. The ratio of just these two lines proves to be an excellent probe of the overall excitation of the H II region.

In the right panel of 2.15 we show the [N II]λ6584/Hα line ratio as a function of model metallicity and ionization parameter. The [N II] line strength is not double-valued with metallicity at the temperatures found in our model H II regions.

2.5 Observational Comparisons and Nebular Diagnostic Diagrams

To first order, the spectrum of an ionized gas cloud depends on the ionization state and the temperature of the gas. These quantities are largely set by the strength of the ionizing radiation field and the gas phase metallicity. Observationally, astronomers probe the metallicity and strength of the ionizing radiation field by identifying sets of line ratios that uniquely map to these quantities. One of the most well-known examples is the classic BPT diagram (Baldwin et al., 1981), which compares the [N II]λ6584/Hα and [O III]λ5007/Hβ line ratios to separate objects by excitation mechanism.

The BPT diagram and diagnostic diagrams using other combinations of line ratios are

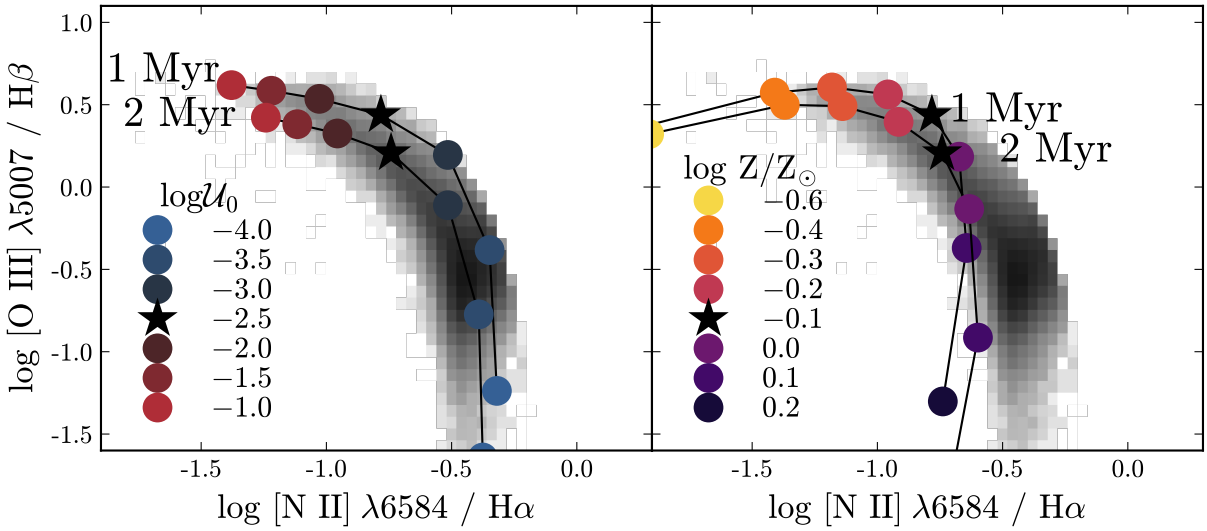

Figure 2.16 The effect of varying different model parameters on BPT diagram location. We show a fiducial model (shown as a star marker) with $\log_{10} \mathrm{Z}/\mathrm{Z}_\odot = -0.1$ and $\log_{10} \mathcal{U}_0 = -2.5$ at 1 and 2 Myr. The greyscale 2D histogram shows the number density of SDSS star-forming galaxies. **Left:** Varying the ionization parameter of the model while holding metallicity constant at $\log_{10} \mathrm{Z}/\mathrm{Z}_\odot = -0.1$ and ionizing spectrum constant at 1 Myr (top curve) and 2 Myr (bottom curve) instantaneous bursts. **Right:** Varying the metallicity of the model while holding $\mathcal{U}_0$ constant at $\log_{10} \mathcal{U}_0 = -2.5$ and ionizing spectrum constant.

often employed to test the agreement of theoretical emission line ratios from photoionization models with emission line ratios from observations. In this section we will discuss the location of the FSPS nebular model in various commonly-used diagnostic diagrams.

2.5.1 The Observational Comparison Sample

We test our predicted emission line luminosities against those measured from spectroscopic observations of both H II regions and star-forming galaxies to show that the FSPS nebular model can reproduce observed emission from both single H II regions and complex populations of multiple H II regions. Even though we do not know the $\mathcal{U}_0$, Z, t values of the observed objects independently, theoretical grids should at least be able to span the range of observed line ratios using reasonable physical parameters. The H II region comparison spectra from van Zee et al. (1998b), consist of observations of massive H II regions in nearby galaxies and are a standard comparison set for nebular emission models (Dopita et al., 2000; Kewley et al., 2006; Levesque et al., 2010; Dopita et al., 2013). For star-forming galaxies, SDSS galaxy spectra are another common comparison set used in optical line ratio diagnostic diagrams (Dopita et al., 2000; Kewley et al., 2006; Levesque et al., 2010). The SDSS spectra typically cover large areas of a galaxy and are likely to contain emission from multiple H II regions.

The van Zee et al. (1998b) catalog reports emission line intensities with contributions from both doublet lines for [N II] (6548, 6584) and [O III] (4959, 5007). Standard diagnostic diagrams only use the stronger of the two, [N II]λ6584 and [O III]λ5007; we remove the contribution from the weaker line using the theoretical intensity ratio between the two lines (e.g., $I_{5007} = 2.88\ I_{4959}$). This results in a decrease in the [N II]λ6584/Hα and [O III]λ5007/Hβ ratio of $\sim \log_{10}(3/4)$ or ~ 0.1 dex.

The star-forming galaxy sample is derived from galaxy spectra from the Sloan Digital Sky Survey Data Release 7 (SDSS DR7; York et al., 2000; Abazajian et al., 2009) and emission line fluxes measured from the publicly available SDSS DR7 MPA/JHU catalog4 (Kauffmann et al., 2003a; Brinchmann et al., 2004; Salim et al., 2007). We use the emission line sample presented in Telford et al. (2016), briefly summarized here. The sample includes $\sim 135,000$

galaxies with redshifts between 0.07 and 0.30. Galaxies are required to have S/N of 25 in the Hα line, 5 in the Hβ line, and 3 in the [S II] lines. Emission line fluxes are corrected for dust extinction using the Balmer decrement and the Cardelli et al. (1989) extinction law, assuming $R_V = 3.1$ and an intrinsic Balmer decrement of 2.86. AGNs are removed from the sample according to the empirical BPT diagram classification of Kauffmann et al. (2003b).

2.5.2 BPT line ratios

In Figs. 2.16 and 2.17, we show how each of the model parameters affects the location of a model H II region in the BPT diagram. In 2.16 we vary $\mathcal{U}_0$ and $\log_{10} Z/Z_\odot$ for 1 and 2 Myr model.

$\mathcal{U}_0$ *variations:* Increasing model $\mathcal{U}_0$ moves the model along the star-forming sequence to higher values of [O III]λ5007/Hβ and lower values of [N II]λ6584/Hα. Nitrogen and oxygen have similar ionization potentials, so comparing a doubly-ionized population, [O III], with a singly-ionized population, [N II], probes the ionization state of the gas cloud. Thus, increasing $\mathcal{U}_0$ will enhance the doubly-ionized population at the expense of the singly ionized population.

Abundance variations: Decreasing the gas phase abundances moves the model away from the star-forming sequence, to lower values of [N II]λ6584/Hα and [O III]λ5007/Hβ. However, decreasing the gas phase metallicity also results in a higher equilibrium temperature. Initially, the changing line ratios reflect the change in ionization state, with enhanced [O III] emission and decreased [N II] emission. Decreasing the gas phase abundances below $\log_{10} Z/Z_\odot = -0.6$, results in a decrease in both [O III]λ5007/Hβ and [N II]λ6584/Hα. For high metallicity models, the temperature is too low to collisionally excite O++ ions to make the [O III]λ5007 transition, and so [O III]λ5007/Hβ decreases at roughly constant [N II]λ6584/Hα.

Age variations: We show the age evolution of the $\log_{10} Z/Z_\odot$-$\log_{10} \mathcal{U}_0$ grid for instantaneous bursts in the top panel of 2.17. The grid is well-matched to the star forming sequence for the 1 Myr models. By 3 Myr, however, very few models can produce line ratios consistent with the star-forming locus or H II regions. Those that do have very high ionization parameters ($\log_{10} \mathcal{U}_0 > 2$) and a very narrow range of metallicities ($\log_{10} Z/Z_\odot \sim -0.6$). The

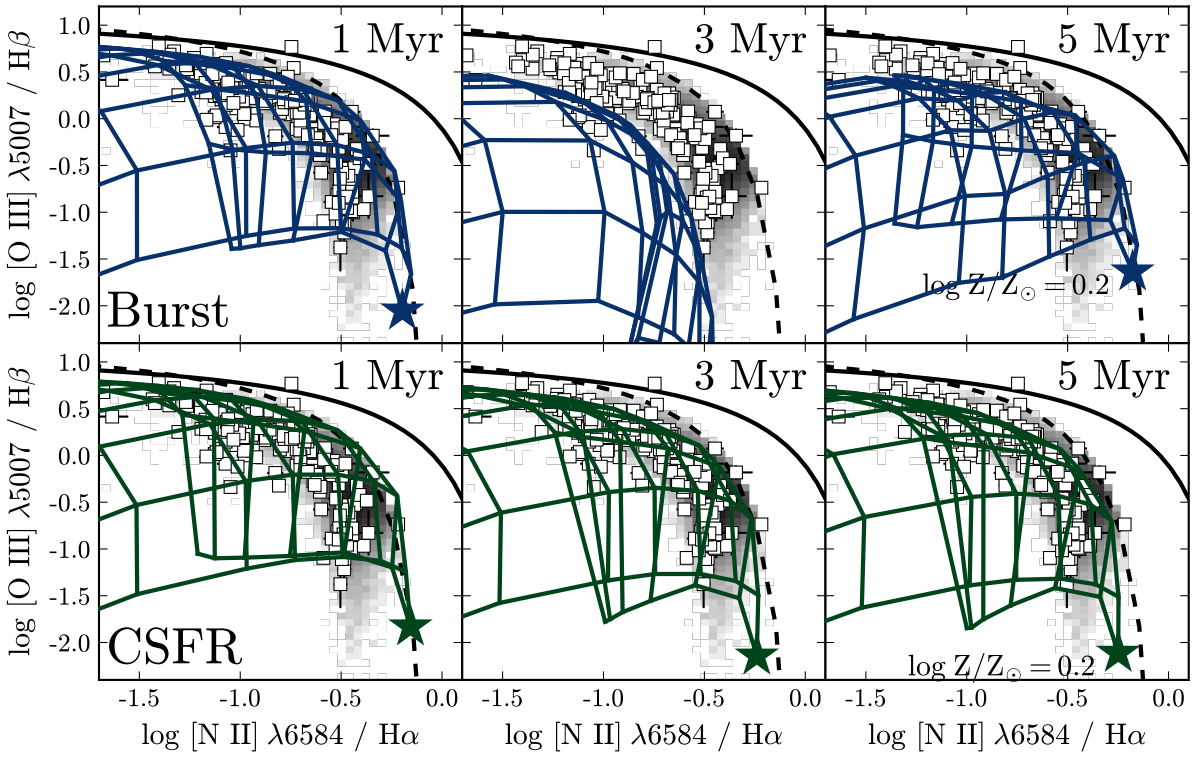

Figure 2.17 BPT diagram for instantaneous bursts (top) and constant SFR models (bottom) at 1, 3, and 5 Myr. The greyscale 2D histogram shows SDSS star-forming galaxies and the white squares are massive extragalactic H II regions. The solid black line is the extreme starburst classification line from Kewley et al. (2001) and the dashed line is the pure star formation classification line from Kauffmann et al. (2003a). In all panels, the star marker shows the location of a model with $\log_{10} \mathrm{Z}/\mathrm{Z}_{\odot} = 0.2$ and $\log_{10} \mathcal{U}_0 = -4$. After ~ 3 Myr the instantaneous burst spectra are no longer hard enough to produce line ratios consistent with the star-forming sequence.

WR phase at ~ 5 Myr significantly hardens the ionizing spectrum.

The bottom panel of 2.17 shows the time evolution of the $\log_{10} Z/Z_{\odot}$-$\log_{10} \mathcal{U}_0$ grid for constant SFR models. At the youngest ages, the ionizing spectra produced by the instantaneous burst models and the constant star formation models are very similar, and produce very similar line ratios. As discussed in §2.3.5, the CSFH models reach an equilibrium around ~ 4 Myr. Thus, the CSFH models continue to produce line ratios that match the observed star-forming locus to later ages.

We compare the constant SFR model grid to the model grid presented in Dopita et al. (2013) (hereto after D13), which uses Starburst-99 ionizing spectra and the Mappings-III photoionization code. We do not run the photoionization models ourselves, rather we use the line ratios from the D13 paper directly. To make a cleaner comparison, we run our constant SFR model through Cloudy at the same ionization parameters and metallicities used in the D13 model, and match the gas phase abundances to those used in D13 (see 2.1). We attempt to match the density of the D13 models, at $n_{\rm H} = 300$. However, as discussed previously, Mappings-III is pressure-based photoionization code, and $n_{\rm H} = 300$ is just the initial average density in the Dopita et al. (2013) model. The D13 paper tested several different electron velocity distributions; we compare our model to their model with $\kappa = \infty$, which corresponds to the standard Maxwell-Boltzmann distribution assumed in Cloudy.

We show the BPT diagram for the two constant SFR model grids in 2.18. Despite the different approaches, both models show substantial overlap and are able to reproduce most of the observed SF-sequence. While the two grids show similar trends with ionization parameter and metallicity, the overall model coverage is different. The FSPS model shows a wider spread in the [N II]λ6584/Hα and [O III]λ5007/Hβ line ratios, while the D13 grid extends to more extreme values in [O III]λ5007/Hβ. This difference is likely due to the fact that the D13 grids extend to higher metallicities than the FSPS grid, up to $\log_{10} Z/Z_{\odot} = 0.7$, or $5 Z_{\odot}$. Our model ties the gas phase abundances with the metallicity of the stellar population, and the maximum metallicity in the Pavoda+Geneva isochrones is $\log_{10} Z/Z_{\odot} = 0.2$.

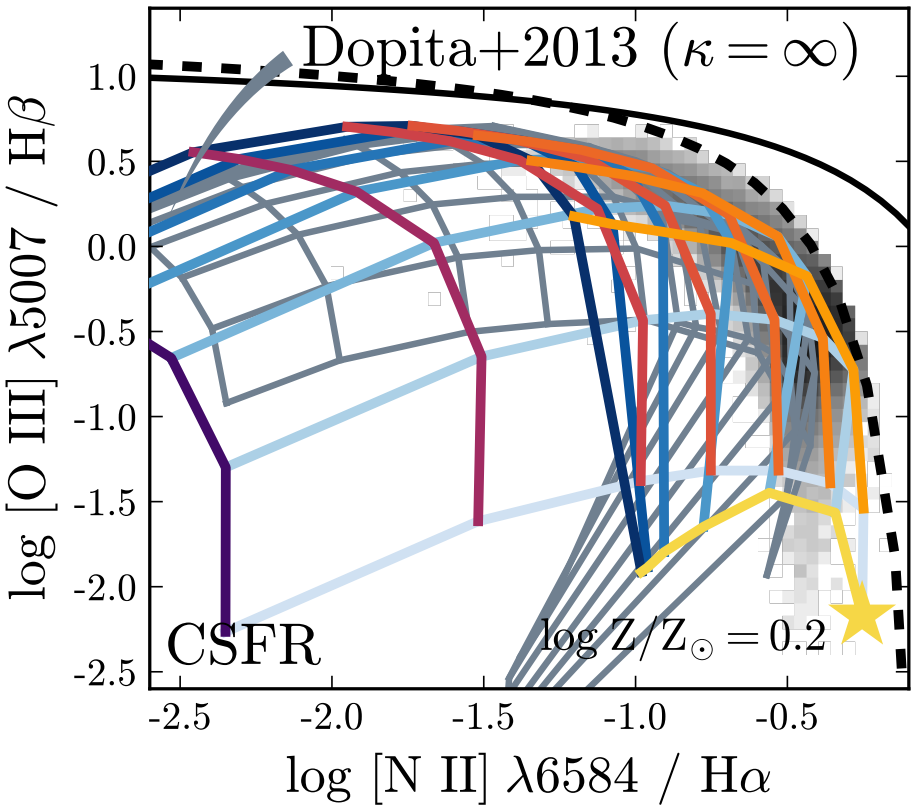

Figure 2.18 BPT diagram comparing the constant SFR grid with the grid from Dopita et al. (2013) (gray), which uses the MAPPINGS-III photoionization code.The ionization parameter varies from $\log_{10} \mathcal{U}_0 = -1.5$ (dark blue) to $\log_{10} \mathcal{U}_0 = -3.5$ (light blue) and metallicity varies from $\log_{10} Z/Z_\odot = -1$ (purple) to $\log_{10} Z/Z_\odot = 0.2$ (yellow). The solid black line shows the extreme starburst classification line from Kewley et al. (2001) and the dashed line is the pure star formation classification line from Kauffmann et al. (2003a). There is good overall agreement between the two grids, and both show similar trends with ionization parameter and metallicity.

2.5.3 Alternative Diagnostic Line Ratios

While the BPT diagram is the most widely used diagnostic diagram, there are many combinations of line ratios used to probe physical properties of H II regions and star forming galaxies. Theoretical grids of photoionization models are able to reproduce observed BPT diagram line ratios quite easily, but these same models can fail to reproduce observed line ratios in other diagnostic diagrams (e.g., Telford et al., 2016). In this section we assess several diagnostic diagrams and showcase our model's ability to reproduce observed line ratios.

N2O2: The [N II] λ6548 / [O II] λ3727 (N2O2) line ratio correlates with metallicity and is widely used as an abundance indicator (Levesque et al., 2010; Dopita et al., 2000; Veilleux & Osterbrock, 1987). The line ratio is especially useful as a diagnostic when paired with an ionization-sensitive line ratio like log[O III] λ5007 / [O II] λ3727 (O3O2), discussed in §2.4.2. In 2.19 we show the N2O2 and O3O2 line ratios for a 1 Myr instantaneous burst and a 4 Myr constant SFR model. The model grids show good overall agreement with the data, and can reproduce most of the observed H II region line ratios. The more extreme N2O2 line ratio values may produced by gas phase metallicities not reached by our model grid. The turn-over in ionization parameter at the highest metallicity in our model, $\log_{10} \mathrm{Z}/\mathrm{Z}_{\odot} = 0.2$, suggests that the ionizing spectra at high-metallicity are not hard enough.

Ne3O2: Levesque & Richardson (2014) presented the utility of the [Ne III] λ3869 / [O II] λ3727 (Ne3O2) line ratio as an ionization parameter diagnostic. The O3O2 line ratio is a well-known probe of excitation, but the wavelength separation of the lines make the diagnostic quite sensitive to reddening and requires observations that cover a wide wavelength range. The Ne3O2 remedies both of these issues, and shows a tight correlation with O3O2. However, Levesque & Richardson (2014) found considerable offset ($\sim$0.6 dex) between the models and the observations of Ne3O2 and O3O2 line ratios, suggesting an underlying deficiency in the predicted emission line fluxes, which they attributed to an insufficiently hard ionizing spectrum.

In 2.20, we show the Ne3O2 and O3O2 line ratios produced by our $\mathcal{U}_0 - Z$ model grid

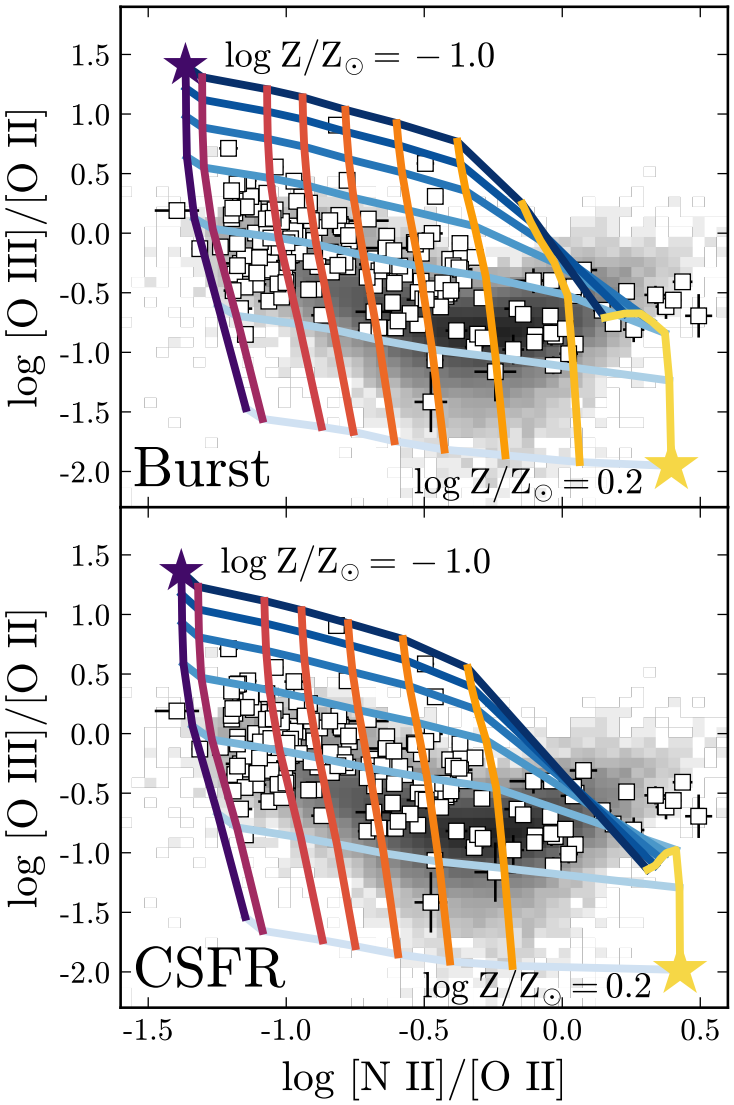

Figure 2.19 N2O2 versus O3O2 for instantaneous burst models (top) and constant SFR (bottom). Ionization parameter varies from $\mathcal{U}_0 = -1$ (dark blue) to $\mathcal{U}_0 = -4$ (light blue), and metallicity varies from $\log_{10} \mathrm{Z/Z_\odot} = -1$ (purple) to $\log_{10} \mathrm{Z/Z_\odot} = 0.2$ (yellow). The grids are compared to massive H II regions (white squares) and star-forming galaxies (grayscale 2D histogram).

for a 1 Myr instantaneous burst and a 4 Myr constant SFR model compared to the massive extragalactic H II regions from van Zee et al. (1998b). Our grids show considerable improvement from the models used in Levesque & Richardson (2014), reducing the offset between model and data to ~ 0.2 dex. Both the instantaneous burst and constant SFR models are able to reproduce 75% of the observed H II region line ratios.

For completeness, in Figs. 2.21 & 2.22 we show model grids for two additional common diagnostic diagrams, R23 versus O3O2 and [S II]/Hα versus [O III]/Hβ.

2.6 Model sensitivity to secondary parameters

In the default model presented in §2.4, we assumed Padova+Geneva isochrones, dust-free gas, and negligible contributions from old hot stars to the ionizing spectrum. Here we relax each of these assumptions in turn and show how the resultant models vary.

We present nebular model grids using MIST evolutionary tracks, computed with the Modules for Experiments in Stellar Astrophysics (MESA, Paxton et al., 2011). The MIST models sample the full range of stellar masses and ages (0.08 to 300 $M_\odot$, $\log t$ from 5.5 to 10.5) and include stellar rotation. For further details regarding the MIST models, see Choi et al. (2016). The model grids presented for the MIST and Padova+Geneva models are both computed self consistently: MIST ionizing spectra were input to Cloudy, and the resultant nebular emission were added to the same spectra used to produce the emission; likewise for the Padova+Geneva models. The nebular model in the current version of FSPS includes tables for both isochrone sets.

The MIST isochrones define solar metallicity at $Z = 0.0142$, compared to $Z = 0.019$ used in the Padova+Geneva isochrones. For the nebular model based on MIST ionizing spectra, we apply the gas phase abundances used in Dopita et al. (2013), which are based on the Grevesse et al. (2010b) solar abundance set. This is done for consistency, since the Grevesse et al. (2010a) abundance set has a similar solar metallicity to the MIST models. The detailed abundances for each element and depletion factors are given in 2.3.

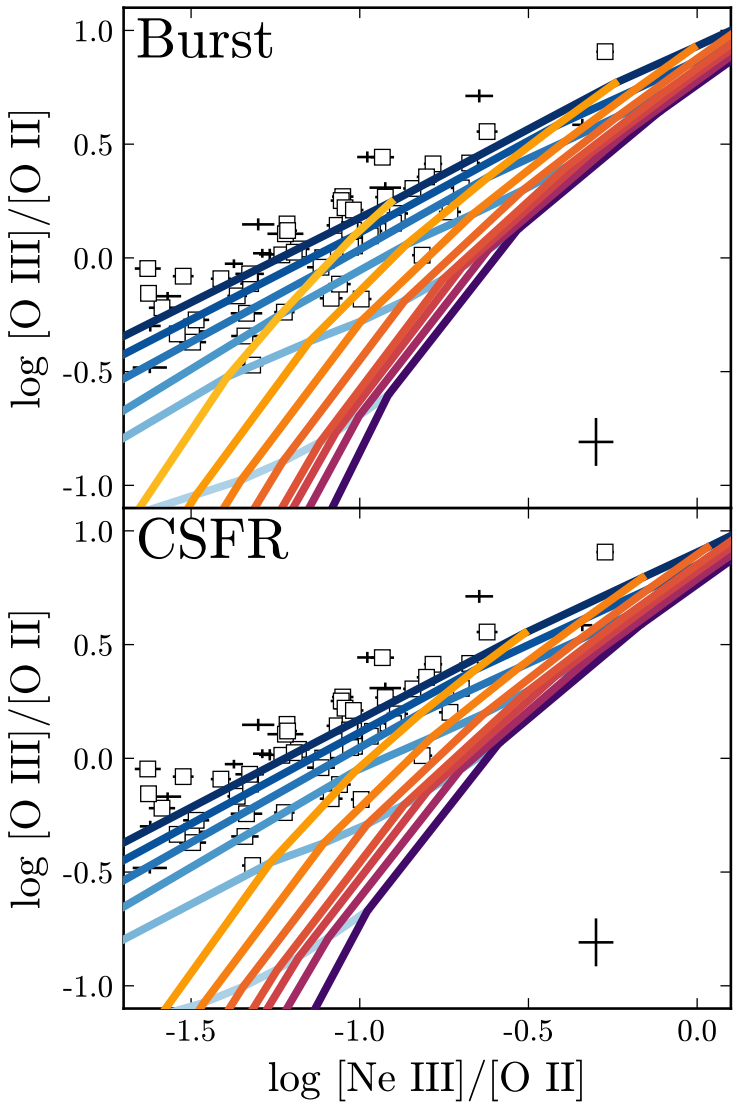

Figure 2.20 Ne3O2 versus O3O2 for instantaneous burst (top) and constant SFR (bottom) models. Ionization parameter varies from $\mathcal{U}_0 = -1$ (dark blue) to $\mathcal{U}_0 = -4$ (light blue), and metallicity varies from $\log_{10} \mathrm{Z}/\mathrm{Z}_\odot = -1$ (purple) to $\log_{10} \mathrm{Z}/\mathrm{Z}_\odot = 0.2$ (yellow). The white squares are massive extragalactic H II regions. Previous models were offset from the data by ~ 0.6 dex, our model shows considerable improvement and reduces the offset to ~ 0.2 dex.

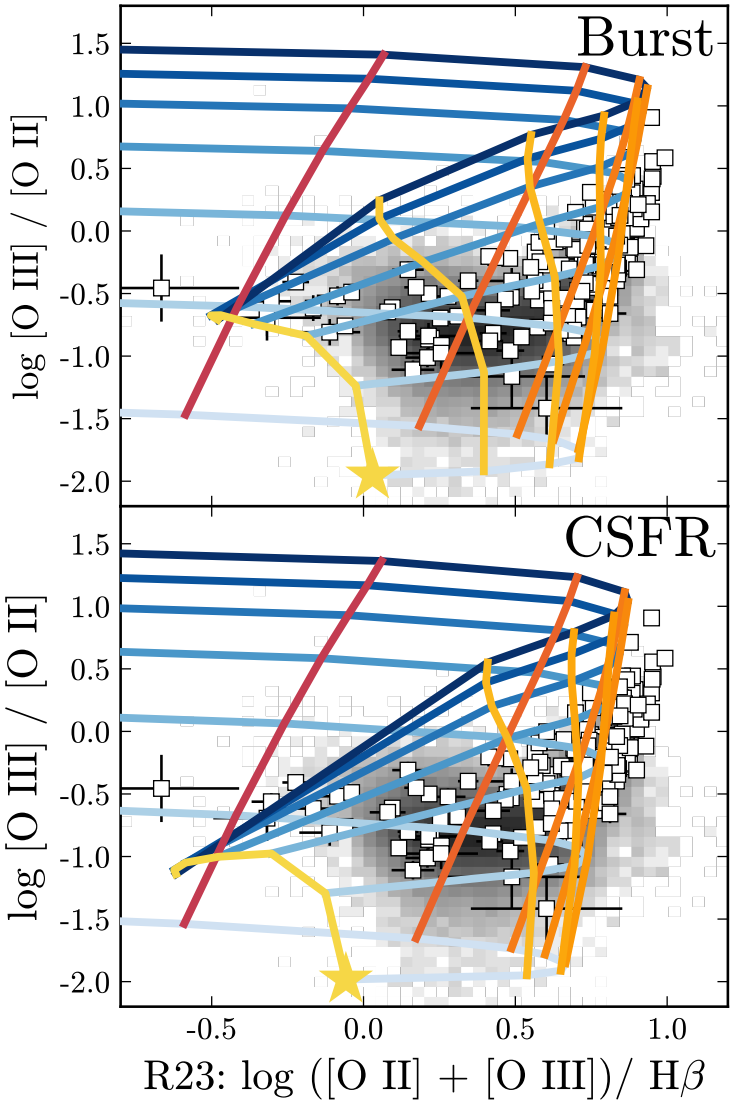

Figure 2.21 R23 versus O3O2 for instantaneous burst models (top) and constant SFR (bottom). Ionization parameter varies from $\mathcal{U}_0 = -1$ (dark blue) to $\mathcal{U}_0 = -4$ (light blue), and metallicity varies from $\log_{10} \mathrm{Z/Z_\odot} = -1$ (purple) to $\log_{10} \mathrm{Z/Z_\odot} = 0.2$ (yellow). The grids are compared to massive H II regions (white squares) and star-forming galaxies (grayscale 2D histogram). Large values of R23 observed are notoriously difficult to reproduce with photoionization models.

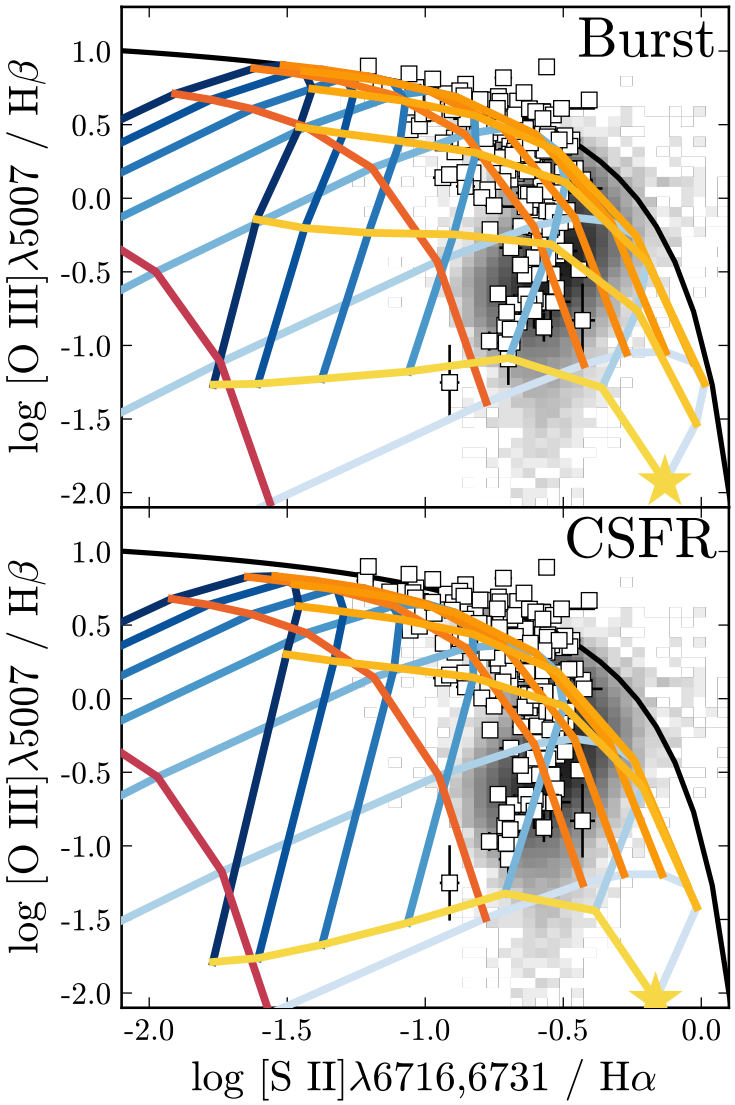

Figure 2.22 [S II]/Hα versus [O III]λ5007/Hβ for instantaneous burst models (top) and constant SFR (bottom). Ionization parameter varies from $\mathcal{U}_0 = -1$ (dark blue) to $\mathcal{U}_0 = -4$ (light blue), and metallicity varies from $\log_{10} \mathrm{Z}/\mathrm{Z}_\odot = -1$ (purple) to $\log_{10} \mathrm{Z}/\mathrm{Z}_\odot = 0.2$ (yellow). The grids are compared to massive H II regions (white squares) and star-forming galaxies (grayscale 2D histogram). The black line shows the pure star formation classification line from Kauffmann et al. (2003a).

Table 2.3. Solar Metallicity ($Z_\odot$) and Depletion Factors (D) adopted for each element for the MIST nebular model, which has $Z = 0.0142$.

Element	$\log_{10} Z/Z_\odot$	$\log(D)$
H	0	0
He	-1.01	0
C	-3.57	-0.30
N	-4.60	-0.05
O	-3.31	-0.07
Ne	-4.07	0
Na	-5.75	-1.00
Mg	-4.40	-1.08
Al	-5.55	-1.39
Si	-4.49	-0.81
S	-4.86	0
Cl	-6.63	-1.00
Ar	-5.60	0
Ca	-5.66	-2.52
Fe	-4.50	-1.31
Ni	-5.78	-2.00

Note. — Solar abundances are from Grevesse et al. (2010b) and depletion factors are from Dopita et al. (2013).

2.6.1 Isochrones and Stellar Atmospheres

Recent work has suggested that the redshift evolution in the location of the star-forming sequence in the standard BPT diagram can be attributed to harder ionizing spectra (e.g., Steidel et al., 2014). The intensity and hardness of the EUV portion of the spectrum dictate the overall ionization structure and temperature of the nebula, which in turn affects the overall location of the model grid in various diagnostic diagrams presented in §2.5.3. SPS models have a number of knobs to turn that can alter the amount of EUV flux significantly, through stellar atmospheres (winds, opacities) and stellar evolution (mass loss, rotation, binarity).

We do not compare different stellar atmospheric models since this is not currently an easily flexible aspect of FSPS. We do, however, consider different treatments of stellar evolution, by varying the evolutionary tracks used to produce the ionizing spectra input to CLOUDY. We first analyze bulk differences in the ionizing spectra generated with different isochrones and then discuss the effect on the resultant photoionization models. Within FSPS, there are four isochrone sets to choose from: Padova (Bertelli et al., 1994; Girardi et al., 2000; Marigo et al., 2008) + Geneva (Schaller et al., 1992; Meynet & Maeder, 2000), BaSTI (Pietrinferni et al., 2004; Cordier et al., 2007); PARSEC (Bressan et al., 2012); and MESA Isochrones & Stellar Tracks (MIST, Dotter, 2016; Choi et al., 2016). Here we focus on the comparison between the Padova+Geneva isochrones used in §2.4, which reflect the "industry standard" in this context, and the MIST isochrones (MIST, Dotter, 2016; Choi et al., 2016), the newest stellar evolution calculations included in FSPS.

The Padova+Geneva model uses 2007 Padova isochrones with high-mass-loss-rate Geneva isochrones adopted for $M > 70 M_{\odot}$. For the comparisons made in this work, both the Padova+Geneva models and the MIST models use a Kroupa IMF and identical stellar atmospheres. O-star spectra are from WM-BASIC (Pauldrach et al., 2001, updates from Eldridge et al., *in prep*); Wolf-Rayet stellar spectra are from CMFGEN (Hillier & Lanz, 2001); post-AGB stellar isochrones are from (Vassiliadis & Wood, 1994) with spectra from

(Rauch, 2003).

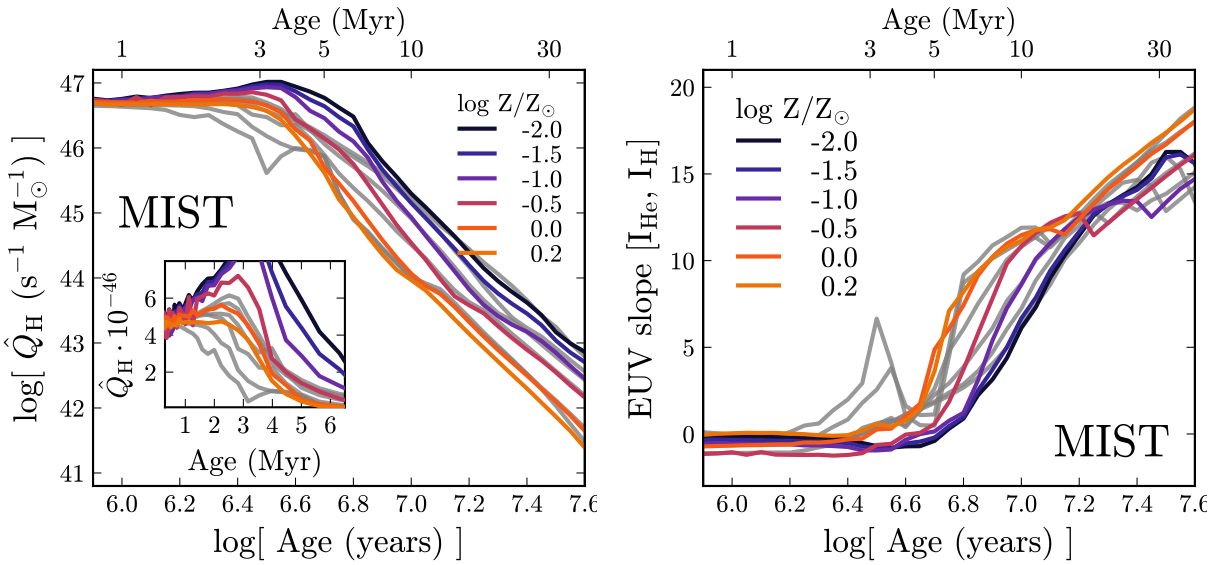

Figure 2.23 The time evolution of $\hat{Q}_{\rm H}$ and the EUV slope for ionizing spectra generated with the MIST models. The MIST models include rotation and produce larger $Q_{\rm H}$ and harder ionizing spectra compared to the Padova+Geneva models (shown in grey).

The MIST models include stellar rotation, which affects stellar lifetimes, luminosities, and effective temperatures through rotational mixing and mass loss (Choi et al., 2016, for further details). Rotating stars tend to have harder ionizing spectra and higher luminosities. In 2.23 we show the time and metallicity evolution of $\hat{Q}_{\rm H}$ and the EUV slope for the MIST evolutionary tracks, identical to the ones shown for the Padova+Geneva models in 2.3. The left panel of 2.23 shows the evolution of $\hat{Q}_{\rm H}$, the ionizing photon rate, which shows the same qualitative behavior as the Padova+Geneva models: $\hat{Q}_{\rm H}$ gradually decreases with time and the lower metallicity models produce higher values of $\hat{Q}_{\rm H}$. Quantitatively, however, the MIST values of $\hat{Q}_{\rm H}$ are larger by a factor of 2-3 and maintain larger values for longer. For MIST, the lowest metallicity spectra produce elevated values of $\hat{Q}_{\rm H}$ until nearly 10 Myr.

The right panel of 2.23 shows the time evolution of the EUV slope. At the earliest ages, the MIST and Padova+Geneva ionizing spectra have similar slopes, but the evolution with

time is significantly different. The Padova+Geneva spectra begin to soften around 3 Myr, while the MIST models stay relatively hard until 5 Myr. This is likely due to the extended main sequence lifetimes afforded by rotational mixing.

The prolonged high values of $Q_{\rm H}$ seen in the MIST models imply that the MIST SSPs could sustain ionizing radiation for a longer period of time compared to the Padova+Geneva models. We show the time evolution of the BPT diagram in 2.24. While the two models are qualitatively similar at the youngest ages, they produce very different line ratios at later ages. The Padova+Geneva grid begins to fall away from the star-forming locus on the BPT diagram at 2 Myr; at 3 Myr the Padova+Geneva models fail to reproduce H II region line ratios consistent with observed star forming regions. Conversely, the MIST models can match the star-forming locus until at least 4 Myr, due to the increased number of ionizing photons and harder ionizing spectra.

The effect of WR stars at 5 Myr for the Padova+Geneva models in 2.24 is striking. WR stars produce an extremely hard ionizing spectrum, which rejuvenates an ionizing spectrum that would otherwise be too soft to produce emission line ratios consistent with observed star forming galaxies. However, the short timescales associated with the WR phase imply that this effect would be minimal on galaxy scales.

Alternative Line Ratios

He2: [He II] emission is produced in H II regions but can also be produced in the atmospheres of WR stars. Steidel et al. (2016) discussed the discrepancy between predicted [He II] $\lambda1640$ / Hβ (He2) line ratios and those observed for a sample of massive star forming galaxies near $z \sim 2$. Predictions for the nebular [He II] emission from STARBURST-99 models were too weak to match observed [He II] line ratios. Only the BPASS models (Eldridge, 2012), which include stellar and nebular [He II] emission, could match the observed [He II] flux, thus Steidel et al. (2016) deduced that photospheric emission must also contribute to the [He II] flux.

In 2.25 we show the He2 line ratios predicted by our model grids. The Padova+Geneva

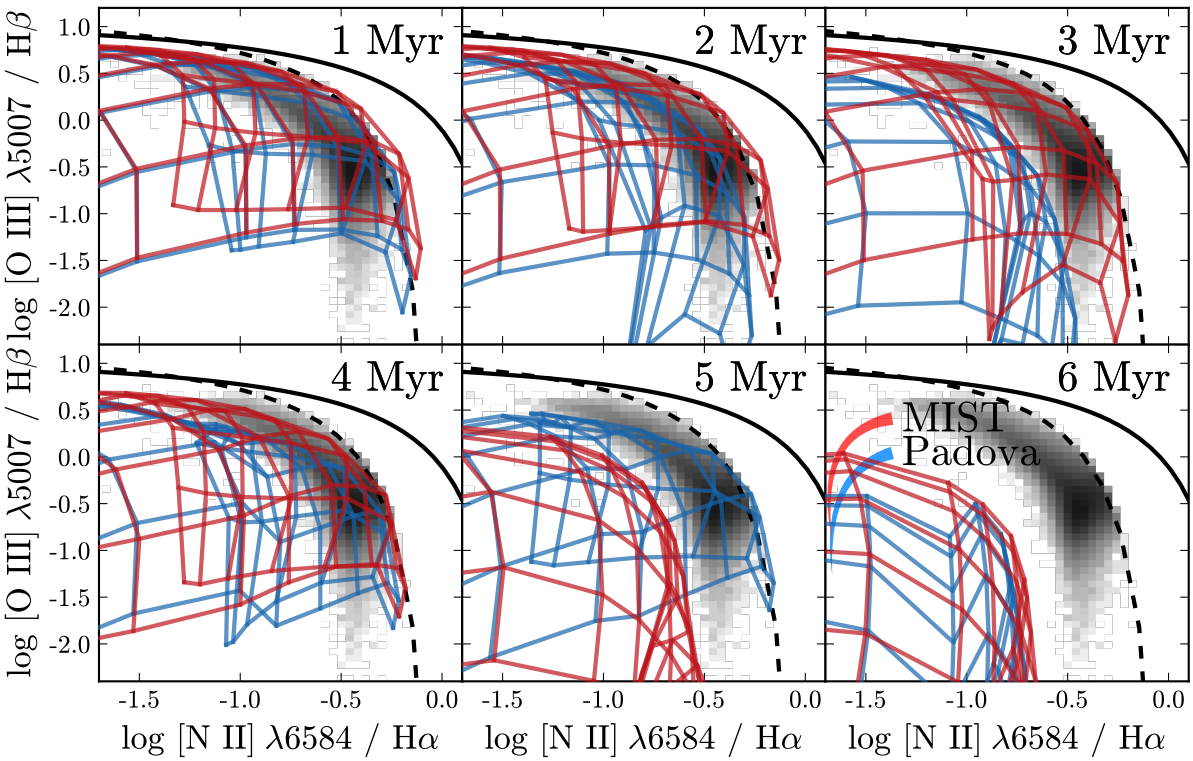

Figure 2.24 The time evolution of the model grids in a BPT diagram for models using ionizing spectra generated with MIST models (red) and Padova+Geneva models (blue). The solid black line shows the extreme starburst classification line from Kewley et al. (2001) and the dashed line is the pure star formation classification line from Kauffmann et al. (2003a). The grayscale 2D histogram shows the number density of SDSS star-forming galaxies. The models agree well at young ages but evolve differently with time. The MIST models, which account for stellar rotation, produce more ionizing photons and harder ionizing spectra (seen in 2.23). While the Padova+Geneva models begin to fall away from the star-forming locus around 2 Myr, the MIST models continue to reproduce the star-forming sequence until ∼4 Myr. The sudden increase in the Padova+Geneva grid at 5 Myr is due entirely to the presence of WR stars.

models are shown in gray, and are unable to produce enough [He II] emission to explain the observed He2 line ratios from Steidel et al. (2016). However, the MIST models produce significant nebular [He II] emission from 3-5 Myr, which can fully account for the observed He2 line ratio without the need to include stellar emission as well. The harder ionizing spectra produced by the MIST models show clear improvement from the Padova+Geneva models for emission lines associated with high excitation species.

For completeness, in 2.26 we show MIST model grids for several additional common diagnostic diagrams, including R23 and [S II]/Hα.

2.6.2 Old Stellar Contribution

The region of the BPT diagram between the star-forming sequence and the AGN sequence is occupied by objects classified as "low ionization emission regions" (LIERs, Belfiore et al., 2016)[9]. LIER-like emission is characterized by strong low-ionization forbidden lines (e.g., [N II], [S II], [O II], [O I]) relative to recombination lines, and was originally discovered in the nuclear regions of galaxies and attributed to AGN-related activity (Kauffmann et al., 2003b; Kewley et al., 2006; Ho, 2008). While some cases are certainly still driven by the presence of a weak AGN, the discovery of spatially extended ($\sim$kpc scales) LIER-like emission has led to work suggesting that hot, evolved stars could be responsible for the ionizing radiation in other cases (Singh et al., 2013; Belfiore et al., 2016). The leading candidate for the ionizing source is the population of post-AGB stars (Binette et al., 1994; Sarzi et al., 2010; Yan & Blanton, 2012). Extreme horizontal branch stars have also been suggested candidates, but considering their effect is beyond the scope of this paper.

Post-AGB stars are stars that have left the AGB, evolving horizontally across the HR diagram towards very hot temperatures ($\sim 10^5$ K) before cooling down to form white dwarfs, with a fraction of the post-AGB population forming planetary nebulae. The exposed cores of post-AGB stars are hot enough to ionize hydrogen and thus could produce a radiation field

[9]Low ionization nuclear emission regions (LINERs, Heckman, 1980) refers to centrally concentrated low ionization emission, which are likely attributed to weak AGN-related activity.

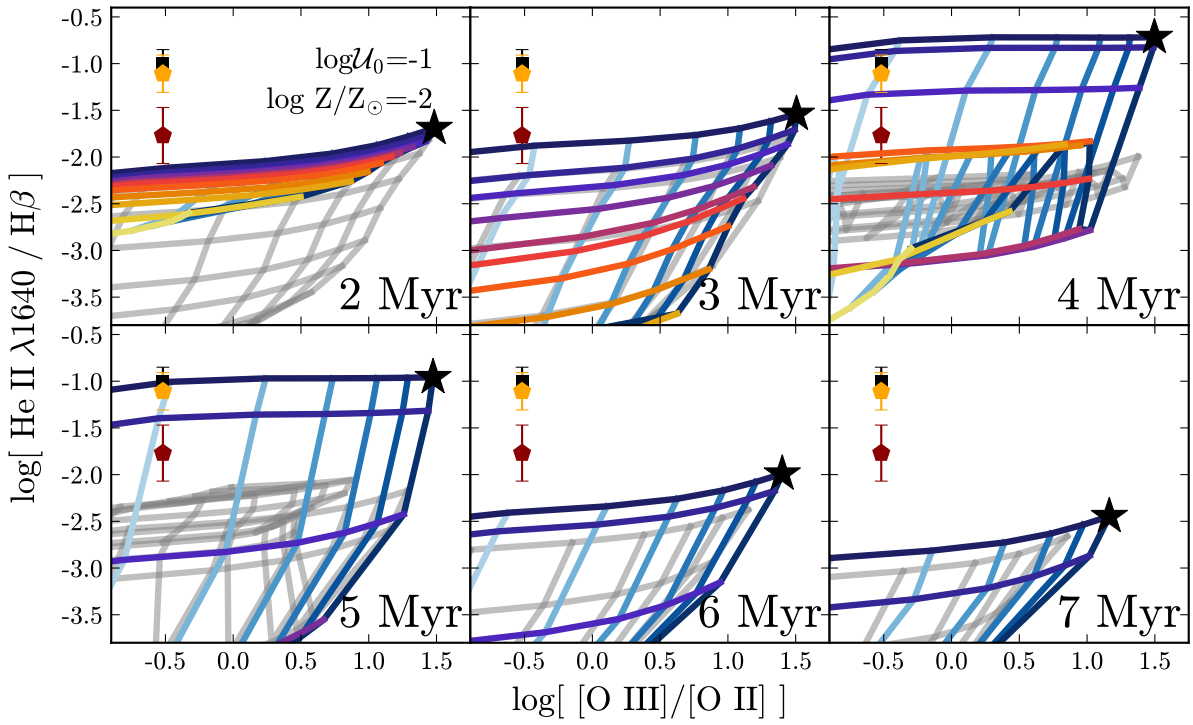

Figure 2.25 O3O2 versus [He II] λ1640 / Hβ (He2) for the Padova+Geneva (gray) and MIST (colored) model grids as a function of age. The ionization parameter varies from $\log_{10}\mathcal{U}_0 = -1$ (dark blue) to $\log_{10}\mathcal{U}_0 = -4$ (light blue), and metallicity varies from $\log_{10}\mathrm{Z/Z}_\odot = -2$ (purple) to $\log_{10}\mathrm{Z/Z}_\odot = 0.5$ (yellow). The data points are from Steidel et al. (2016) for a $z = 2$ star forming galaxy. The black square shows the measured line ratios; the orange and red points show the assumed residual nebular [He II] emission after accounting for stellar [He II] emission. While the Padova+Geneva models cannot account for the observed He2 strengths, the MIST models can fully account for high observed He2 line ratios between 3 and 5 Myr.

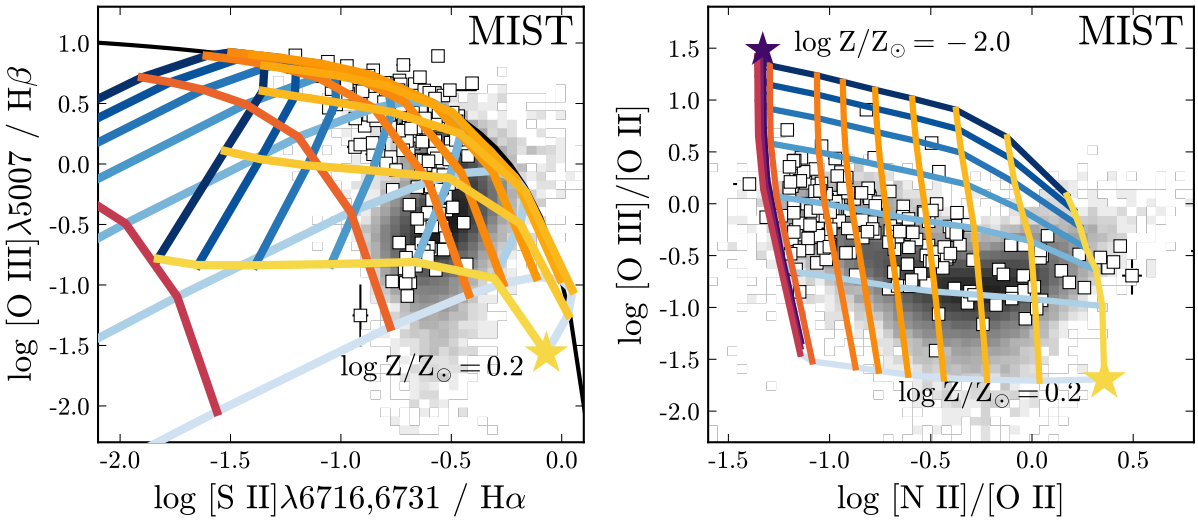

Figure 2.26 Diagnostic diagrams for the $\mathcal{U}_0 - Z$ model grids for 1 Myr instantaneous bursts with ionizing spectra generated using the MIST models. Ionization parameter varies from $\mathcal{U}_0 = -1$ (dark blue) to $\mathcal{U}_0 = -4$ (light blue), and metallicity varies from $\log_{10} \mathrm{Z/Z_\odot} = -2$ (purple) to $\log_{10} \mathrm{Z/Z_\odot} = 0.2$ (yellow). The grids are compared to massive H II regions (white squares) and star-forming galaxies (grayscale 2D histogram).

capable of ionizing the surrounding ISM, provided that there are enough post-AGB stars.

Post-AGB stars are not capable of matching the ionizing flux produced by a single O-star; their strength lies in numbers. The progenitors of these stars have initial masses from 1-5 $M_\odot$, and are much more common than O-type stars. For early-type galaxies where the bulk of the stellar population is old, AGB and post-AGB stars can contribute a significant portion of the total galaxy luminosity. Yan & Blanton (2012) measured the ionization parameter and gas density for galaxies with LIER-like emission and compared it to the typical numbers of ionizing photons produced by post-AGB stars. They deduced that the ionization parameter for post-AGB stars falls short of the required value by a factor of 10, implying that the gas geometry must be quite close to the stars themselves.

The geometry between the stars and gas is one of the major uncertainties associated with interpreting LIER-like emission. We first determine if populations including post-AGB stars are capable of producing line ratios consistent with LIER-like emission. The geometry previously assumed in this work ($\log_{10} R_{\rm inner} = 19$; $n_{\rm H} = 100$) is appropriate for massive H II regions found in star forming galaxies, where the gas is associated with the natal gas cloud, butmay not accurately describe the gas geometry in a scenario where old stars provide the ionizing radiation.

To test the sensitivity to geometry, we generate ionizing spectra for older SSPs (> 1 Gyr) that include post-AGB stars to use as input to Cloudy, and run photoionization models at different values of $R_{\rm inner}$ and $n_{\rm H}$. In 2.27 we show the BPT diagram line ratios for the post-AGB star ionizing spectra at several different ionization parameters, with $n_{\rm H}$ varied from 10-1000 and the inner radius varied from $10^{18} - 10^{20}$ cm (0.3-30 pc).

The post-AGB models produce line ratios consistent with LIER-like emission, well outside of the "pure star forming" region of the BPT diagram, as identified by Kauffmann et al. (2003a). The ionization parameters required to produce observable line ratios are $\log_{10} \mathcal{U}_0 \sim -5$ to $\log_{10} \mathcal{U}_0 \sim -3$. At $R_{\rm inner} = 10^{19}$ and $n_{\rm H} = 100$ cm^{-3}, this implies a total initial stellar mass of 10^6-10^8 $M_\odot$. The required stellar mass would be higher for models where the inner radius is further from the ionizing source. We note that the ionizing spectrum was based

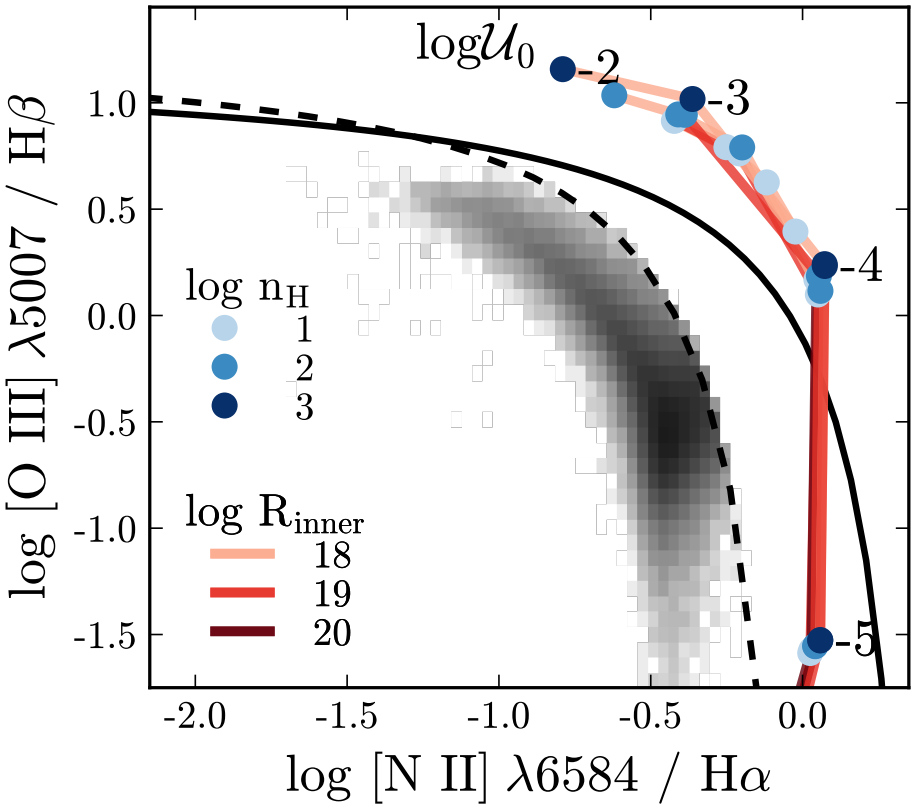

Figure 2.27 BPT diagram for an ionizing spectrum produced by a 3 Gyr solar metallicity SSP that includes post-AGB stars. The grayscale 2D histogram is star forming galaxies from SDSS. The solid black line shows the extreme starburst classification line from Kewley et al. (2001) and the dashed line is the pure star formation classification line from Kauffmann et al. (2003a). Our old-star models with post-AGB stars do produce line ratios consistent with LIER-like emission, but large numbers of post-AGB stars (at least $M_{initial} \sim 10^6\,M_\odot$) would be required to produce enough ionizing photons.

on a stellar population at solar metallicity; low-metallicity post-AGB stars are hotter and would likely enhance the ionizing radiation.

The line ratios in 2.27 show little sensitivity to the star-gas geometry, a result of our simplified model in which the gas exists in a plane-parallel shell surrounding a central point source of ionizing radiation. If the gas is produced by the AGB stars themselves or has a spatial distribution that differs from the distribution of stars, the geometry will differ substantially from the simplified shell used in this work. In future work we plan to test the effects of model geometry in more detail.

Another major uncertainty associated with the interpretation of LIER-like emission lies in our incomplete understanding of the late stages of stellar evolution. In addition to the poor constraints on the age distribution and lifetimes of post-AGB stars, it is uncertain what fraction of post-AGB stars contribute to the large-scale photoionizing radiation field. A recent census of the old, UV-bright stellar population in M31 was unable to reproduce predicted numbers of post-AGB stars (Brown et al., 2008).

To understand the sensitivity of LIER-like emission to the underlying stellar model, we generate ionizing spectra with varying contribution from post-AGB stars using the `pagb` parameter in FSPS. This parameter specifies the weight given to the post-AGB star phase, where `pagb=0.0` turns off post-AGB stars and `pagb=1.0` implies that the Vassiliadis & Wood (1994) tracks are implemented as-is, the default behavior in FSPS. In the top panel of 2.28 we show the ionizing spectrum produced by a 3 Gyr SSP with `pagb` set to 1, 10^{-1}, 10^{-2}, and 10^{-3}. Scaling down the implemented post-AGB stars scales down the emergent EUV radiation in the spectrum.

We show the resultant BPT diagram for the photoionization models that vary in both $\mathcal{U}_0$ and `pagb` in the bottom panel of 2.28. We find that the luminosity of the post-AGB stars could be reduced by a factor of two and still produce LIER-like emission, provided there are enough stars.

Belfiore et al. (2016) found that the [S II]/Hα line ratio provided a clean separation between LIER-like emission and Seyfert-like emission. In 2.29, we show the [S II] emission

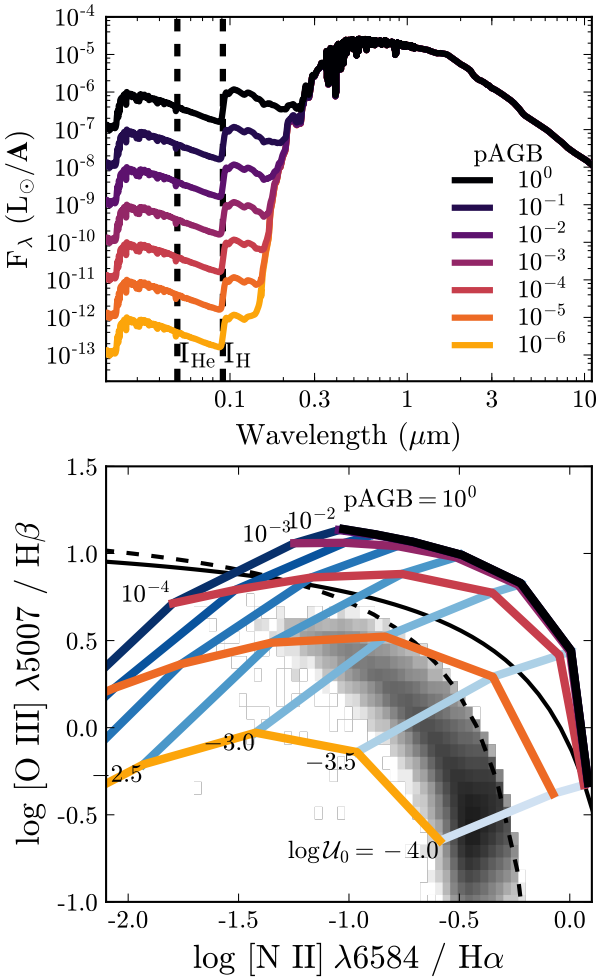

Figure 2.28 **Top:** The effect of hot, evolved stars on the ionizing spectrum. The default default spectrum for a 3 Gyr SSP at solar metallicity is shown shown in black. The weight of the post-AGB phase is modulated from 1 (full inclusion of post-AGB stars) to 10^{-4}, which decreases the amount of EUV flux relative to the rest of the population. **Bottom:** BPT diagram for photoionization models where $\mathcal{U}_0$ and the weight of the post-AGB phase are varied. The solid black line shows the extreme starburst classification line from Kewley et al. (2001) and the dashed line is the pure star formation classification line from Kauffmann et al. (2003a). The grayscale 2D histogram shows the number density of SDSS star-forming galaxies. The Vassiliadis & Wood (1994) tracks used for post-AGB stars must be correct within a factor of two if post-AGB stars are responsible for LIER-like emission.

produced by our post-AGB models. The line ratios produced by our post-AGB star models show the elevated [S II]/Hα ratios observed in LIER galaxies, and confirms the utility of [S II] as a means of identifying low-ionization emission.

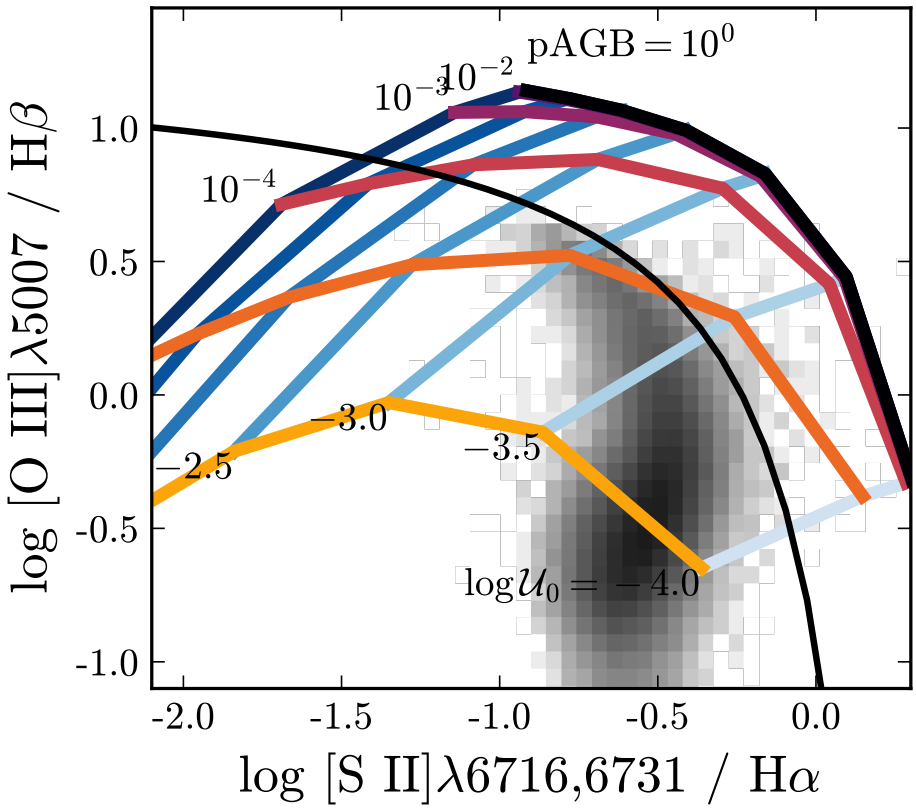

Figure 2.29 [S II]/Hα versus [O III]λ5007/Hβ diagnostic diagram. Ionization parameter varies from $\mathcal{U}_0 = -1$ (dark blue) to $\mathcal{U}_0 = -4$ (light blue), and the weight of the post-AGB stars is varied (purple to yellow). The grayscale 2D histogram shows the density of star-forming galaxies and the black line shows the pure star formation classification line from Kauffmann et al. (2003a). The old star models that include post-AGB stars are able to reproduce the elevated [S II]/Hα emission observed in LIERs.

2.6.3 Nebular Dust

FSPS includes two separate nebular emission models: one that is dust-free and one that includes the effects of dust within the gas cloud itself. We note that neither the dusty nor the dust-free models include the effect of reddening or extinction. The effect of including grains is primarily on the thermodynamic properties of the cloud, and extinction and reddening should be applied to the emergent spectrum.

Users should pair the dusty nebular grids with the dust model used in Conroy et al. (2009) from Charlot & Fall (2000), already included within FSPS. This dust model has two separate dust attenuation prescriptions: a component that affects the entire stellar population and a component that applies additional extinction to the young stellar populations to mimic the effect of young clusters embedded in a birth cloud. The wavelength dependent extinction, $\hat{\tau}_\lambda$ is given by:

$$\hat{\tau}_\lambda(t) \equiv \begin{cases} \hat{\tau}_1(\lambda/5500)^{-0.7} & t \leq t_{\rm esc} \\ \hat{\tau}_2(\lambda/5500)^{-0.7} & t > t_{\rm esc} \end{cases}$$

with $\hat{\tau}_1 = 1.0$ for the galaxy-wide attenuation and $\hat{\tau}_2 = 0.3$ for the young populations. $t_{\rm esc} = 10^7$ years, roughly matched to the timescale of birth cloud disruption (Conroy et al., 2009).

The combination of the dusty nebular model with the Charlot & Fall (2000) dust model assumes a very simple gas-dust geometry for the H II regions, where the ionizing source is embedded within a gas cloud, with a layer of "natal" dust exterior to the ionized region. We do not include the effects of dust attenuation or extinction on the ionizing spectrum input to CLOUDY, and the nebula experiences the full, unattenuated ionizing photon flux. The emergent spectrum is subsequently attenuated and reddened before leaving the galaxy. This is an unrealistic take on the dust geometry, since the dust and gas is likely to be clumpy and unevenly distributed around the stellar population.

The main difference between the dusty and dust-free models is in their thermodynamic properties. Dust changes the temperature structure of the cloud, since it provides alternative

mechanisms for heating and cooling the gas. If cloud temperatures are low enough to allow the survival of dust grains, grain photoionization and thermionic emission can be an efficient heating mechanism ($\lesssim 10\%$ of the total heating).

In 2.30 we show the change in temperature produced by model H II regions that include dust grains when compared to the grain-free model as a function of metallicity and ionization parameter for instantaneous burst models at 1 Myr. The models that include grains produce slightly hotter H II regions; at solar metallicity and $\log_{10}\mathcal{U}_0 = -1$, the grain model produces a volume-averaged electron temperature that is 25% hotter than the grain-free model. This effect is only important at high metallicity, where the nebula is cool enough such that dust grains survive and contribute additional heating. In the high temperatures associated with the low-metallicity models, dust grains are destroyed and the inclusion of grains has little effect on the thermal properties of the H II region.

The inclusion of dust grains is most important for highly-ionized gaseous regions at high metallicity, where they have a non-negligible effect on emission line strengths. In 2.31 we show the BPT diagram for the model H II regions with and without dust grains. Both grids do a reasonable job at covering the range of observed emission line strengths. However, for models at high metallicity and ionization parameter, the higher equilibrium temperatures produced in the dusty models produce enhanced [O III]λ5007/Hβ at the same [N II]λ6584/Hα. The line ratios differ by less than 10% at their most extreme values and still fail to reproduce the star-forming locus beyond $\sim$ 3 Myr. A more careful analysis is required to determine which model provides the best fit to the data, we leave this for future studies.

2.7 Conclusions

We have presented a model for nebular emission based on photoionization models from Cloudy and ionizing spectra from FSPS. The FSPS nebular model's self-consistent coupling of the nebular emission to the matched ionizing spectrum produces emission line intensities that correctly scale with the stellar population as a function of age and metallicity. The model includes nebular emission for both Padova+Geneva and MIST evolutionary tracks,

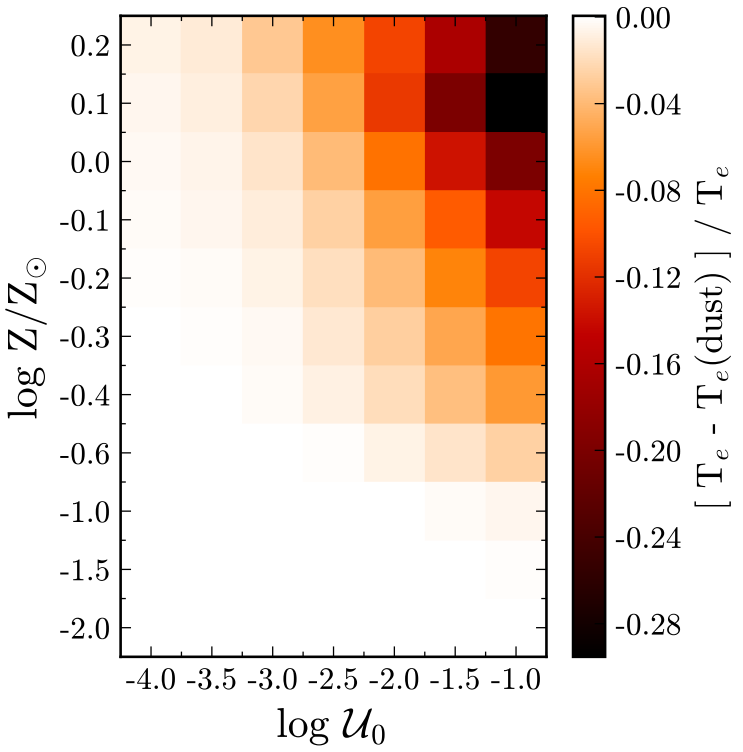

Figure 2.30 Effect of including grains within the nebular cloud on the resultant gas equilibrium temperature, T_e. For most models, heating from dust has a negligible effect on the equilibrium temperature of the model H II region. However, for models with near-solar and super-solar abundances, heating from dust grains can change the temperature by as much as $\sim$30%.

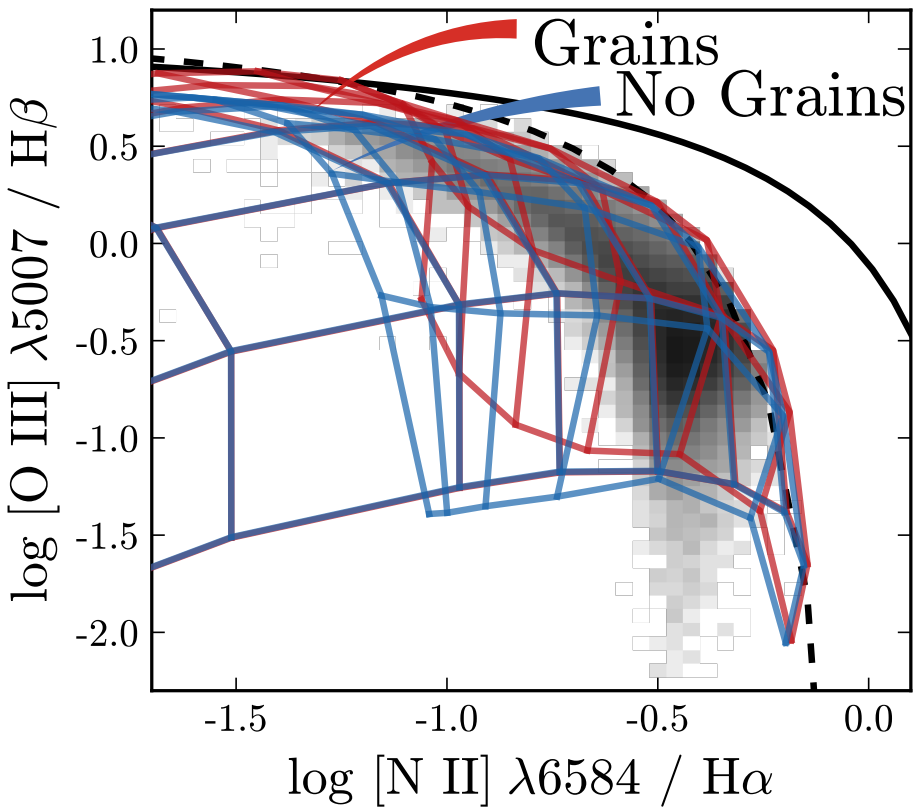

Figure 2.31 Effect of including grains within the nebular cloud on line ratios in the BPT diagram. The solid black line shows the extreme starburst classification line from Kewley et al. (2001) and the dashed line is the pure star formation classification line from Kauffmann et al. (2003a). The grayscale 2D histogram shows the number density of SDSS star-forming galaxies. The dusty models have slightly higher temperatures at high metallicity, which results in slightly elevated [O III]λ5007/Hβ ratios.

retaining the flexibility of FSPS. Our conclusions are as follows:

- Our model links the stellar and nebular abundances, coupling the metallicity-dependent changes in the ionizing spectrum and stellar evolution to changes in the gas phase coolants. The low-metallicity models have harder ionizing spectra, produce hotter nebulae, and sustain nebular emission for several Myr over the solar metallicity models. At very low metallicities, however, the models cannot produce observed line ratios simply due to the paucity of gas phase metals like N and O.

- Nebular emission is primarily produced by the youngest populations, 5 Myr and younger. Single burst models cannot match the star forming sequence in the BPT diagram at ages greater than 3 Myr, unless the stellar tracks include rotation. Models that assume constant star formation rates do produce acceptable fits.

- Hydrogen emission line strengths depend primarily on the number of ionizing photons, but have an important secondary dependence on the nebular temperature, which can change Hα line strengths by $\sim$ 15%. This produces age and metallicity-dependent variations in Balmer line strength which is important to consider when estimating SFRs.

- For instantaneous burst populations 3 Myr and younger, nebular line and continuum emission is responsible for at least 30% of the total flux in the UV and optical, and at least 60% of the total flux in the optical and NIR regimes. For models that assume a constant SFR, nebular emission remains a significant fraction of the total flux even at 10 Myr. When interpreting the broadband fluxes for stellar populations with any recent star formation, it is essential to include the contribution from nebular emission, especially for populations at low metallicity.

- The FSPS nebular model can reproduce observed line ratios of massive H II regions and star-forming galaxies, and shows good agreement with the photoionization models from

D13 in standard BPT diagrams. The FSPS nebular model shows improved coverage of observed line ratios for N2O2, O3O2, Ne3O2.

- Stellar rotation extends the ionizing lifetime of the stellar population and produces harder ionizing spectra. The FSPS nebular models using MIST models can produce BPT line ratios consistent with observed H II regions until $\sim$5 Myr. The MIST models produced [He II] emission strong enough to fully account for high He2 line ratios observed in star-forming galaxies at $z\sim2$.

- Post-AGB stars have ionizing spectra that are hard enough to ionize the surrounding gas and produce line ratios consistent with LIER-like emission in the BPT diagram and in the [S II] diagnostic diagram. To achieve the luminosities necessary to produce significant nebular emission, stellar masses of $10^6 - 10^8\,M_\odot$ are required. Future work will study the effect of geometry in more detail.

Chapter 3

SELF-CONSISTENT UV EMISSION AND ABSORPTION LINE DIAGNOSTICS

In this work we assess the diagnostic potential of both absorption and emission features in the UV and evaluate the diagnostics against observations of local galaxies and galaxies at high redshift. We use the `Cloudy+FSPS` nebular emission model, extended to include emission predictions in the UV, to identify which of the established UV stellar absorption indices include a significant contribution from nebular emission and evaluate their sensitivity to metallicity. We also present model UV emission line fluxes as a function of metallicity and ionization parameter for stellar populations, assuming both instantaneous bursts and constant SFRs. We identify combinations of strong emission lines that correlate with metallicity and ionization parameter, including [CIII]λ1907, CIII]λ1909, OIII]λ1661, 1666, SiIII]λ1883, 1892, CIVλ1548,1551, NII]λ1750, 1752, and MgIIλ2796, and generate diagnostic UV "BPT" diagrams. We discuss the uncertainties associated with the choice of a fixed relationship between [N/H] and [C/H] with [O/H] in photoionization models, and argue for an improved relationship for N and C enrichment. We also consider the implications of decoupling the stellar metallicity from the gas phase metallicity, as it pertains to high redshift galaxies where high SFRs may rapidly enrich the gas in α-elements. We summarize the best diagnostic choices and the associated redshift range for low-, mid-, and high-resolution rest-UV spectroscopy in preparation for the launch of JWST.

3.1 Introduction

In star-forming galaxies, emission from gas can be a factor of ten times brighter than the emission from stars. These emission lines can also reveal key physical properties of the gas

and its ionizing source. For gas that is ionized by stars, various combinations of emission lines are frequently used to estimate the gas-phase metallicity of a galaxy. Popular combinations of emission lines include the "R23" (Pagel et al., 1979) and "N2"(Pettini & Pagel, 2004) diagnostics, which use ratios of strong emission lines from Oxygen, Nitrogen, and Hydrogen that have been calibrated by theoretical models (e.g., McGaugh, 1991; Kewley & Dopita, 2002).

Paired with the historical accessibility of optical observations, it is a natural development that the most well-used nebular diagnostics are based in the optical portion of the spectrum. Unfortunately, however, by $z \sim 3$, the emission lines required for traditional optical diagnostics have been redshifted out of the wavelength window accessible to ground-based near-IR observatories. Luckily, strong nebular emission lines exist across the spectrum, from the UV through the IR, which can potentially be used as equally useful gas diagnostics. Diagnostics based on UV emission lines are of particular interest, since they are applicable to galaxies at high redshift.

The UV also offers a number of informative absorption features as well. A galaxy's spectrum is typically dominated by light from young, massive stars in addition to the emission from the ionized gas surrounding them. While there are fewer emission lines in the UV than in the optical, we gain additional diagnostic features from the numerous stellar UV absorption lines. Many of these line are produced in the atmospheres of young massive stars that should share the same metallicity as the gas producing the emission lines. Because these same O- and B-type stars are responsible for producing the ionizing radiation incident to the gas cloud, it is possible to jointly analyze absorption and emission features when inferring the metallicity and ionization state of a galaxy. However, doing so requires that one self-consistently links the temporal and metallicity-dependent changes in the stellar absorption features to the nebular emission lines.

In this paper, we take advantage of the work of Byler et al. (2016), who paired the population synthesis models from the Flexible Stellar Population Synthesis code (FSPS; Conroy et al., 2009) with photoionization models from CLOUDY to self-consistently model

the flux from star-forming galaxies. We build on the UV absorption indices identified in Leitherer et al. (2011), focusing on the wind-driven and photospheric absorption lines, and the UV emission features identified in Erb et al. (2010). We present the most promising combinations of nebular emission line ratios and stellar absorption features in the UV that can be used to estimate stellar and nebular metallicities for galaxies at high and low redshift.

We describe the stellar and nebular model in §3.2. In §3.3 we identify combinations of emission and absorption features in the UV that track the gas-phase metallicity. In §3.4 we compare the most promising diagnostics to galaxies locally and at redshift $z \sim 3$ and in §3.6 discuss the utility of the various diagnostics in the context of current and future observatories.

3.2 Description of the stellar and nebular model

We use the CLOUDY nebular model implemented within the stellar population synthesis code FSPS to generate spectra for composite stellar populations that include nebular line and continuum emission. We describe the process of generating observed spectral energy distributions (SEDs) for model stellar populations in this section. We describe the stellar models in §3.2.1 and summarize the nebular model in §3.2.2.

3.2.1 The stellar model

For stellar population synthesis, we use the Flexible Stellar Population Synthesis (FSPS) package[1] (Conroy et al., 2009) via the Python interface, `python-fsps`[2]. We adopt a Kroupa initial mass function (IMF) (Kroupa, 2001). We discuss our choice for evolutionary tracks and spectral library in detail below; for all other SPS parameters, we use the default parameters in FSPS[3].

---

[1] `https://github.com/cconroy20/fsps`

[2] `https://github.com/dfm/python-fsps`

[3] GitHub commit hash `4e1b3f5`

Evolutionary Tracks

We use the MESA Isochrones & Stellar Tracks (MIST; Dotter, 2016; Choi et al., 2016), single-star stellar evolutionary models which include the effect of stellar rotation. The evolutionary tracks are computed using the publicly available stellar evolution package Modules for Experiments in Stellar Astrophysics (MESA v7503; Paxton et al., 2011, 2013, 2015) and the isochrones are generated using Aaron Dotter's publicly available `iso` package on github[4]. A complete description of the models can be found in Choi et al. (2016), however, we describe some relevant model properties below.

The MIST models cover ages from 10^5 to $10^{10.3}$ years, initial masses from 0.1 to 300 $M_\odot$, and metallicities in the range of $-2.0 \leq [Z/H] \leq 0.5$. Abundances are solar-scaled, assuming the Asplund et al. (2009) protosolar birth cloud bulk metallicity, for a reference solar value of $Z_\odot = 0.0142$.

The MIST models include the effect of rotation, discussed at length in Choi et al. (2017). 1D rotation is implemented assuming the so-called "shellular approximation," which modifies the stellar structure equations with a centrifugal acceleration term in the presence of rotation. The models assume an initial rotation rate of $\nu_{\rm ZAMS}/\nu_{\rm crit} = 0.4$, meaning that the the surface velocity is set to 40% of the critical, or break-up, velocity. This rotation rate is also adopted in the Geneva models (Ekström et al., 2012)[5], and is motivated by observations of young B stars (Huang et al., 2010) and theoretical work on rotation rates in massive stars (Rosen et al., 2012).

As explained in Choi et al. (2017), the effects of rotation appear in the MESA stellar evolution calculations in three main ways. First, rotation decreases the gravitational acceleration via the centrifugal force, which in turn affects the stellar structure. Second, rotation can promote extra mixing in the interior, boosting the transport of chemicals and angular

[4]https://github.com/dotbot2000/iso

[5]Note that $\nu_{\rm crit}$ and $\Omega_{\rm crit}$ are defined differently in MESA and in the Geneva models. In the Geneva models, the equatorial radius is 1.5 times larger than the polar radius when $\Omega = \Omega_{\rm crit}$ but this distinction is not made in MESA. See Section 2.1 in Georgy et al. (2013) for more details.

momentum. MESA adopts the common approach of treating the chemical and angular momentum transport in a diffusion approximation. Third, rotation enhances mass loss. MESA adopts the formulation from Langer (1998), where the mass loss rate $\dot{M}$ is multiplied by a factor that increases dramatically as the surface angular velocity Ω approaches critical, or break-up, angular velocity.

For hot luminous stars, line-driven winds can cause significant mass loss. For stars with $T_{\rm eff} > 1.1 \times 10^4\,{\rm K}$ and surface hydrogen mass fraction $X_{\rm surf} > 0.4$, the mass loss prescription from Vink et al. (2000, 2001) are adopted. If the star loses a considerable amount of its outer hydrogen layer ($X_{\rm surf} < 0.4$) and becomes a Wolf-Rayet (WR) star, the Nugis & Lamers (2000) wind prescription is used instead. For cooler stars with effective temperatures below $10^4\,{\rm K}$, the wind prescription from de Jager et al. (1988) is used. As noted in a recent review, these prescriptions fail to account for clumpiness and inhomogeneities in outflows, and may overestimate mass loss rates by a factor of 2 to 3 (Smith, 2014).

Choi et al. (2016) compared the rotating MIST and Geneva evolutionary tracks and found that at fixed stellar mass, the Geneva models are hotter and more luminous at the end of their main sequence lifetimes, implying that rotational mixing is more efficient in the Geneva models. In general, the Geneva rotating models have enhanced main sequence lifetimes compared to the default MIST model; however, main sequence lifetimes in Geneva and MIST agree to within 10-15% at solar metallicity. For higher mass stars the MIST models have MS lifetimes that fall between those of the non-rotating and rotating Geneva models.

Spectral Library

We combine the MIST tracks with a new, high resolution theoretical spectral library (C3K; Conroy, Kurucz, Cargile, Castelli, in prep) based on Kurucz stellar atmosphere and spectral synthesis routines (ATLAS12 and SYNTHE). The spectra use the latest set of atomic and molecular line lists and include both lab and predicted lines. The grid was computed assuming the Asplund et al. (2009) solar abundance scale and a constant microturbulent velocity

of 2 km s^{-1}.

We require high resolution model spectra, since stellar photospheric lines have equivalent widths ∼1-3Å. Typical stellar wind lines have equivalent widths (EWs) of ∼5-15Å. We use a version of the C3K spectral library that has $R = 1000$ from $\lambda = 100$-1500Å and $R = 10,000$ from $\lambda = 1500$Å-1μm.

For very hot stars and stars in rapidly evolving evolutionary phases, we use alternative spectral libraries. We focus on the libraries used for very hot stars in this work, since these will be responsible for providing the radiation necessary to ionize hydrogen. For main sequence stars with temperatures above 25,000 K (O- and B-type stars) we use spectra from M. Ng, G. Taylor & J.J. Eldridge (priv. comm), as described in Eldridge et al. (2017), using WM-Basic (Pauldrach et al., 2001). For WR stars, we use the spectral library from Smith et al. (2002) using CMFGEN (Hillier & Lanz, 2001).

3.2.2 The nebular model

We use the CLOUDY nebular model implemented within FSPS to generate spectra that include nebular line and continuum emission. The model is described in detail in Byler et al. (2016), and summarized briefly here. The nebular model is a grid in (1) simple stellar population (SSP) age, (2) SSP and gas-phase metallicity, and (3) ionization parameter, $\mathcal{U}_0$, a dimensionless quantity that gives the ratio of ionizing photons to the total hydrogen density.

The model uses FSPS to generate spectra from coeval clusters of stars, each with a single age and metallicity (SSPs). Using the photoionization code CLOUDY, the SSP is used as the ionization source for the gas cloud and the gas-phase metallicity is scaled to the metallicity of the SSP. For each SSP of age t and metallicity Z, photoionization models are run at different ionization parameters, $\mathcal{U}_0$, from $\log_{10}\mathcal{U}_0 = -4$ to $\log_{10}\mathcal{U}_0 = -1$ in steps of 0.5. The resultant line and continuum emission is normalized by the number of ionizing photons calculated from the input ionizing spectrum. The normalized line and continuum emission are recorded in separate look-up tables.

For a given SSP (t, Z) and specified $\mathcal{U}_0$, FSPS returns the associated line and continuum

emission associated with that grid-point from the look-up table. This approach maintains the model self-consistency, such that the nebular emission is added to the same spectrum that was used to ionize the gas cloud. FSPS removes the ionizing photons from the SED to enforce energy balance; in this work we assume an ionizing photon escape fraction of zero.

Gas Phase Abundances

We assume that the gas phase metallicity scales with the metallicity of the stellar population, given that the metallicity of the most massive stars should be identical to the metallicity of the gas cloud from which the stars formed.

For most elements we use the solar abundances from Grevesse et al. (2010a), based on the results from Asplund et al. (2009), and adopt the depletion factors specified by Dopita et al. (2013). We treat nitrogen and carbon differently, however, as both these elements likely contain a primary nucleosynthetic contribution, as well as a secondary (pseudo-secondary in the case of C) nucleosynthetic source that becomes important at higher abundances (e.g., Henry et al., 2000; Berg et al., 2016)

To set the relationship between N/H and O/H we use the following equation:

$$\begin{aligned} \log_{10}(\mathrm{N/O}) = \\ -1.5 + \log\left(1 + e^{\frac{12+\log_{10}(\mathrm{O/H})-8.3}{0.1}}\right), \end{aligned} \tag{3.1}$$

and for C/H and O/H we assume:

$$\begin{aligned} \log_{10}(\mathrm{C/O}) = \\ -0.8 + 0.14 \cdot (12 + \log_{10}(\mathrm{O/H}) - 8.0) \\ + \log\left(1 + e^{\frac{12+\log_{10}(\mathrm{O/H})-8.0}{0.2}}\right), \end{aligned} \tag{3.2}$$

These choices are largely modeled after the empirical fits used by Dopita et al. (2013). However, we have found that the N/H and C/H relationship used in Dopita et al. (2013) is far too steep at the lowest metallicities. We discuss this issue at length in §3.5.1, given that the predicted emission lines are extremely sensitive to the abundance prescription applied, especially for important coolants like C, N, and O.

The abundance for each element and applied depletion factors at solar metallicity are given in Table 3.1.

[b!]

3.3 Model Spectra

In this section we discuss the general behavior of UV emission and absorption features in the model spectra and their utility as probes of stellar and gas physical properties. We first show example spectra and describe our methodology for calculating absorption and emission line strengths in §3.3.1. We then analyze the metallicity dependence of stellar absorption (§3.3.3) and nebular emission (§3.3.4) features and identify useful combinations of emission and absorption lines that track well with the properties of the ionizing SSP and gas-phase metallicity in §3.3.5. We connect the identified UV diagnostics with commonly used diagnostics in the optical in §3.3.6.

3.3.1 Emission and absorption features in the UV

The UV portion of a galaxy spectrum is rich in absorption features, including stellar absorption features and absorption from the interstellar gas and circumgalactic medium (Leitherer et al., 2011). While there has been work highlighting the utility of UV interstellar absorption features (e.g., Rix et al., 2004) as metallicity diagnostics, in this work we focus primarily on the stellar absorption features produced by wind-driven and photospheric absorption, since these will link the metallicity-dependent changes in the stellar population with the metallicity-dependent changes in the gas. For short-lived massive stars, the metallicity of the stars should be nearly identical to that of the surrounding natal gas cloud.

In Fig. 3.1 we show example spectra for a population with constant SFR over 4 Myr at $\log_{10} Z/Z_{\odot} = -1.5, -1.0, -0.5$, and 0.0 over the wavelength range 1275-3100Å to highlight various emission and absorption features. The models in Fig. 3.1 are plotted for a constant SFH, but the reader should note that in the presence of bursts of variable SFRs, the emission and absorption features will be highly dependent on age, as the massive star population

Table 3.1. Elemental abundances at solar metallicity and depletion factors (D) adopted for each element in the MIST nebular model, which has $Z = 0.0142$ ($\log_{10}$(O/H) = -3.31 or $12 + \log_{10}$(O/H) = 8.69).

Element	$\log_{10}$(E/H)	$\log_{10}(D)$
H	0	0
He	-1.01	0
C	-3.57	-0.30
N	-4.60	-0.05
O	-3.31	-0.07
Ne	-4.07	0
Na	-5.75	-1.00
Mg	-4.40	-1.08
Al	-5.55	-1.39
Si	-4.49	-0.81
S	-4.86	0
Cl	-6.63	-1.00
Ar	-5.60	0
Ca	-5.66	-2.52
Fe	-4.50	-1.31
Ni	-5.78	-2.00

Note. — Solar abundances are from Grevesse et al. (2010a) and depletion factors are from Dopita et al. (2013).

evolves.

We show a model with $\log_{10} Z/Z_{\odot} = -0.5$ at several different ages in Fig. 3.2 to demonstrate the evolution of the UV spectrum with time. We emphasize that the stellar and nebular emission are computed self-consistently as a function of age and metallicity. Nebular line and continuum emission is strongest between 1 and 3 Myr, and significant line emission is sustained to 7 Myr. The time dependence of some stellar wind features is visible, with the CIV wind feature near 1550Å increasing with age until 7 Myr. Broad [He II] λ1640 emission can be seen briefly at 3 Myr due to the presence of WR stars.

In Figs. 3.1 & 3.2 we have highlighted the set of 12 UV line indices defined by Leitherer et al. (2011) in grey. Most of these indices are dominated by lines from interstellar gas, which are not included in this model. Exceptions include the `SiIV_1400` and `CIV_1550` indices, which are typically dominated by stellar-wind lines, and `AlIII_1670`, which is a blend of wind and interstellar lines. The depth of these features changes with metallicity, since the efficiency of hot star winds is metallicity-dependent.

We also highlight important emission lines, noted by their species name below the continuum. The strength of the various emission lines will depend on the gas phase metallicity, the ionization parameter, and the hardness of the ionizing spectra, which will change with the age and metallicity of the stellar population responsible for ionizing the surrounding gas.

3.3.2 Measuring emission and absorption line features

One of the challenges associated with measuring the strength of absorption lines is defining the continuum. In the UV this choice is especially difficult, since metals in the stellar atmosphere absorb heavily, masking the true continuum level. Without knowledge of the true continuum level, equivalent width measurements will only place lower limits on the absolute line strength.

The high density of metal lines in the UV presents another difficulty for absorption line equivalent width measurements, as absorption line indices often cover multiple blended absorption features. While blended features may still track the overall metallicity, many promi-

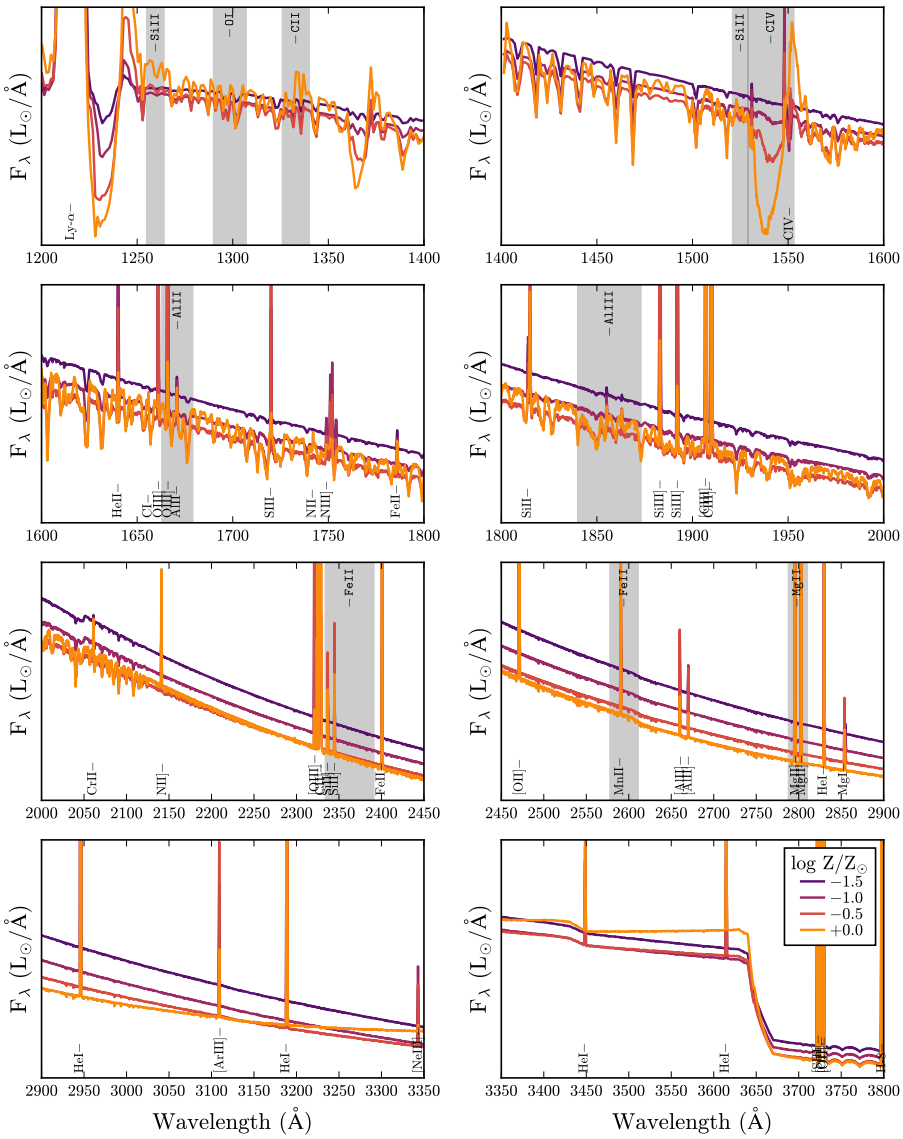

Figure 3.1 The spectrum for a stellar population with constant SFR at 4 Myr with $\log_{10}\mathcal{U}_0 = -2.5$ at $\log_{10} \mathrm{Z}/\mathrm{Z}_\odot = -1.5, -1.0, -0.5$, and 0.0. The shaded regions highlight the Leitherer et al. (2011) absorption indices, labeled at the top of the axes. The labels at the bottom of the axes identify strong emission lines included in the FSPS nebular model. The shape of the nebular continuum and the strength of the emission lines vary with age and metallicity as the thermodynamic properties of the gas cloud change.

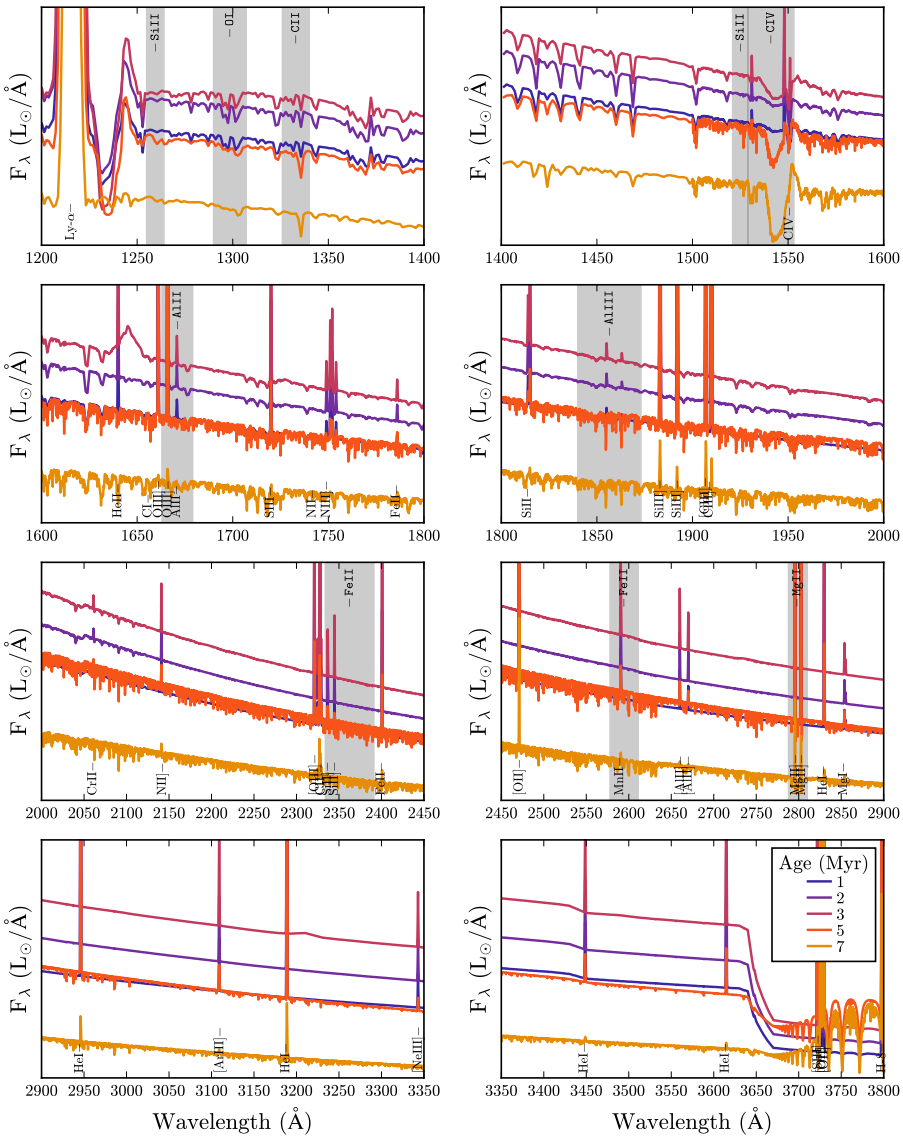

Figure 3.2 The spectrum for $\log_{10} Z/Z_{\odot} = -0.5$ instantaneous burst populations with $\log_{10} \mathcal{U}_0 = -2.5$ at 1, 2, 3, 5 and 7 Myr. The shaded regions highlight the Leitherer et al. (2011) absorption indices, labeled at the top of the axes. The labels at the bottom of the axes identify strong emission lines included in the FSPS nebular model. The shape of the nebular continuum and the strength of the emission lines vary with age and metallicity as the thermodynamic properties of the gas cloud change.

nent absorption lines have complicated dependencies on stellar spectral type or individual abundance patterns (Maraston et al., 2009).

To measure absorption feature equivalent widths, we adopt the set of 12 UV line indices defined by Leitherer et al. (2011). For each index, Leitherer et al. (2011) defined a central bandpass and two flanking continuum bandpasses, given in Table 3.2, and shown in Fig. 3.3.

Following Leitherer et al. (2011), the continuum flux in a region is defined as the median value of the flux within the bandpass, and is assigned to the midpoint wavelength. The continuum, $\mathcal{F}_{\rm cont}(\lambda)$, is then taken to be the straight line connecting the midpoints of the continuum bands on either side of a line. We then calculate the equivalent width with:

$$\text{EW (Å)} = \int_{\lambda_i}^{\lambda_f} \frac{\mathcal{F}_{\lambda,\,\rm cont}(\lambda) - \mathcal{F}_{\lambda,\,\rm line}(\lambda)}{\mathcal{F}_{\lambda,\,\rm cont}(\lambda)}\, d\lambda, \tag{3.3}$$

where $\mathcal{F}_{\rm line}(\lambda)$ is the flux in the central bandpass spanning $\lambda_i < \lambda < \lambda_f$.

Much of the pioneering work analyzing the UV absorption line behavior of massive stars and stellar populations only considered the effects of stellar absorption and interstellar absorption (e.g., Rix et al., 2004; Maraston et al., 2009; Leitherer et al., 2011; Zetterlund et al., 2015). This assumption is reasonable for comparisons against observations of globular clusters and some young massive star clusters. However, the UV spectrum of star forming galaxies contains significant contributions from nebular lines and continuum emission from ionized gas.

The nebular continuum emits significantly in the UV redward of the Balmer break[6], which acts to increase the continuum level for the entire spectrum, reducing the equivalent width compared to a pure stellar prediction. In addition, prominent emission lines from the gas surrounding star-forming regions fall within many of the defined line and continuum bandpasses (as seen in Fig. 3.4), which also affects the calculated equivalent widths.

We show the effect of adding in nebular line and continuum emission to a solar-metallicity single-burst stellar population in Fig. 3.4, where we plot the UV spectrum near the absorption

[6]Byler et al. (2016) the nebular continuum can account for $\sim 5-10\%$ of the total flux between 900 and 1800Å, and as much as $\sim 20\%$ of the total flux between 1800 and 4000Å.

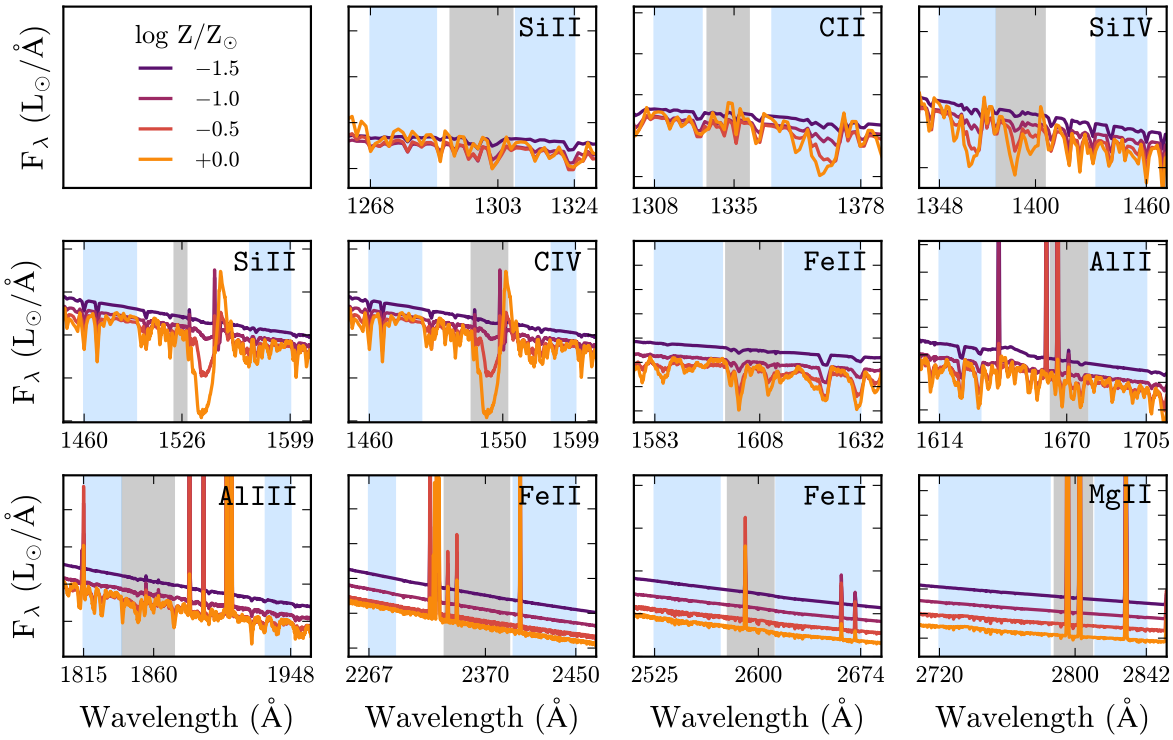

Figure 3.3 We show the absorption indices defined by Leitherer et al. (2011) for a stellar population with constant SFR at 4 Myr with $\log_{10}\mathcal{U}_0 = -2.5$ at $\log_{10} \mathrm{Z/Z_\odot} = -1.5$, -1.0, -0.5, and $+0.0$. Each panel shows a different index, noted in the top right corner. The shaded regions show the wavelength ranges of the red and blue continuum and the central bandpass used to measure the equivalent width of the feature. The line indices are a combination of stellar photospheric absorption lines, stellar wind lines, and blends of lines. We note that many of the defined bandpasses include nebular emission, which changes their utility as metallicity diagnostics.

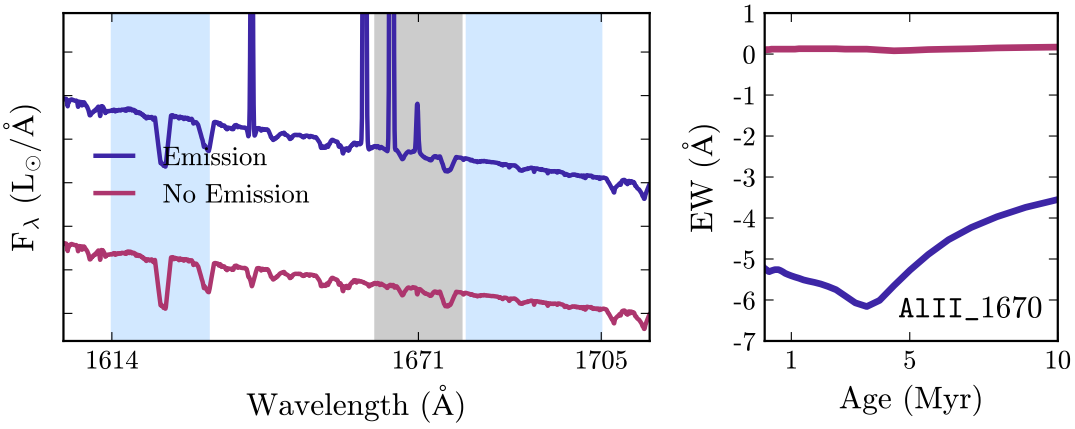

Figure 3.4 Including nebular line and continuum emission changes equivalent widths measured in standard UV absorption indices. *Left:* The UV spectrum surrounding the Al III index for models with and without nebular emission. *Right:* The `AlIII_1860` index equivalent width as a function of time for single burst models with and without nebular emission at solar metallicity. Nebular continuum emission increases the overall continuum level. Nebular line emission occurs throughout the spectrum, and in the case of `AlIII_1860`, there are emission lines included in the feature bandpass.

line and continuum bandpasses for the `AlIII_1670` Leitherer et al. (2011) absorption index. When nebular emission is included, the spectrum becomes brighter and contains line emission throughout the plotted wavelength range, including in the continuum and feature bandpasses. Nebular emission changes the expected EWs by 10-50% in most cases, but by as much as an order of magnitude for cases like `MgII_2800` where the central bandpass covers three emission lines. The effect of including nebular emission is most important for young populations; for bursts older than 10 Myr, the difference in the absorption index EW when compared to the stellar only EW is less than 5%.

In what follows, we include the effects of both emission and absorption when computing absorption line equivalent widths. We do not fit detailed line profiles to model the superpo-

Table 3.2. UV Line Indices from Leitherer et al. (2011)

Index Name	Index Bandpass	Blue Continuum	Red Continuum	Features Included
SiII_1260	1255 – 1264	1268 – 1286	1268 – 1286	SiIIλ 1260; SIIλ 1259
OI_SiII_1303	1290 – 1307	1268 – 1286	1308 – 1324	OIλ 1302; SiIIλ 1304; SiIIIλ 1295
CII_1335	1326 – 1340	1308 – 1324	1348 – 1378	CIIλ 1334; CII*λ 1335
SiIV_1400	1379 – 1405	1348 – 1378	1433 – 1460	SiIVλ 1393, 1402
SiII_1526	1521 – 1529	1460 – 1495	1572 – 1599	SiIIλ 1526
CIV_1550[e]	1529 – 1553	1460 – 1495	1583 – 1599	CIVλ 1548[e],1550[e]; SiII*λ 1533
FeII_1608	1600 – 1613	1583 – 1599	1614 – 1632	FeIIλ 1608
AlII_1670[e]	1663 – 1679	1614 – 1632	1680 – 1705	AlIIλ 1670[e]; ([O III] λ 1666, AlIIλ 1670)
AlIII_1860[e]	1840 – 1873	1815 – 1839	1932 – 1948	AlIIIλ 1854,1862
FeII_2370[e]	2334 – 2391	2267 – 2290	2395 – 2450	FeIIλ 2344,2374,2382
FeII_2600[e]	2578 – 2611	2525 – 2572	2613 – 2674	MnIIλ 2576,2594,2606; FeIIλ 2586,2600
MgII_2800[e]	2788 – 2810	2720 – 2785	2812 – 2842	MgIIλ 2796[e],2803

[e]One or more emission lines falls within a defined bandpass for this index

Note. — The last column includes only stellar absorption features. If present, nebular emission lines are indicated in parentheses. Lines that can appear in emission or absorption are flagged with *e*.

sition of emission and absorption, however. Instead, we take the emission line luminosities to be those reported directly by CLOUDY.

3.3.3 Absorption line trends with model age and metallicity

In Fig. 3.5 we show the absorption indices defined by Leitherer et al. (2011) for our model spectra as a function of age for a single burst (top) and a constant SFR (bottom). The time and metallicity evolution of these absorption indices is frequently complex, due to their dependence on a combination of stellar photospheres, nebular emission, and stellar winds.

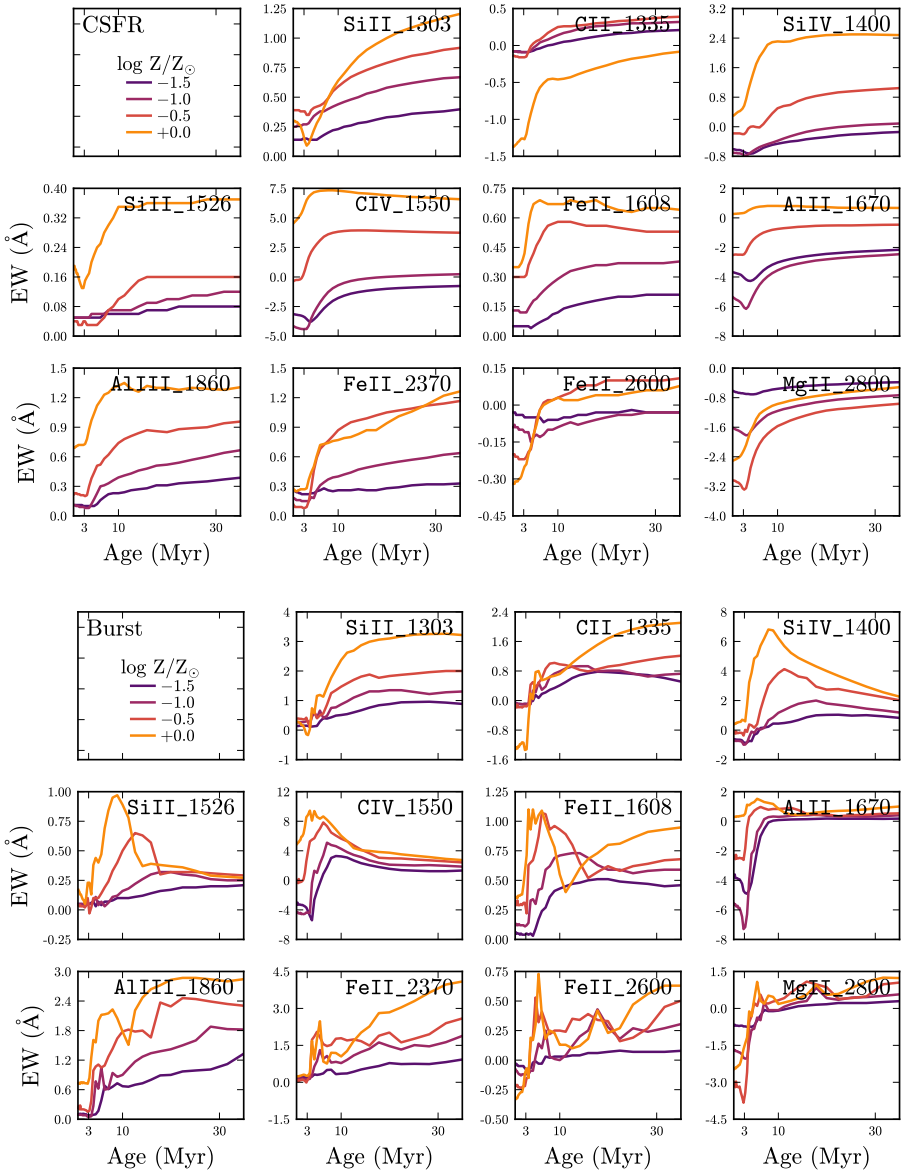

Figure 3.5 The time evolution of absorption index equivalent widths at $\log_{10} Z/Z_{\odot} = -1.5$, -1.0, -0.5, and $+0.0$, for single-aged populations (top) and a constant SFR (bottom). The most promising absorption features show a large dispersion in equivalent width with metallicity. The C IV 1335Å feature (middle row, second column) correlates strongly with metallicity at young ages.

The indices that probe stellar wind features (SiIV_1400, CIV_1550) are strongest at young ages and gradually decrease with time, as the massive stars evolve off the main sequence. In particular, the CIV index at 1550Å shows equivalent widths as high as 12Å in the first few million years, making it both easy to detect and highly age-sensitive.

Fig. 3.5 also shows how each absorption index changes with metallicity. In general, the high metallicity models have larger equivalent widths, as line blanketing in the upper atmosphere of O- and B-type stars drastically reduces the amount of emergent flux at high metallicities. This effect is clearest in the Fe_2370 index, which shows dense photospheric absorption in the highest metallicity models, clearly distinguishing low-metallicity stellar populations from the high metallicity stellar populations.

For young, massive stars, radiatively-driven winds produce significant mass loss on the main sequence (Kudritzki & Puls, 2000). These winds are metallicity dependent; Vink et al. (2001) estimate that mass loss rates scale as $\dot{M} \sim Z^{0.69,0.64}$ for O- and B-type stars (Vink et al., 2001). Thus, absorption indices that include stellar winds like CIV_1550 and SiIV_1400 will be strongly dependent on metallicity. For populations 10 Myr and younger, these indices have equivalent widths that vary by factors of 2-6 between different metallicity models.

The AlIII_1670 index is one of the indices that inadvertently includes emission lines in the feature bandpass ([O III] λ 1666, Aliiλ 1670). However, this actually makes it a stronger metallicity diagnostic, since the emission line features are metallicity dependent as well.

3.3.4 Nebular Emission features in the UV

The same O- and B-type stars that produce the absorption lines in Fig. 3.6 are also responsible for providing the ionizing radiation incident to the surrounding natal gas cloud, linking the metallicity-dependent changes in the timescales of stellar evolution to the nebular emission features. These stars are short-lived, thus nebular line and continuum emission is strong function of the stellar population age.

We show the time evolution of several prominent emission lines in Fig. 3.6. As expected, the emission lines are strongest at young ages, and eventually disappear entirely as the

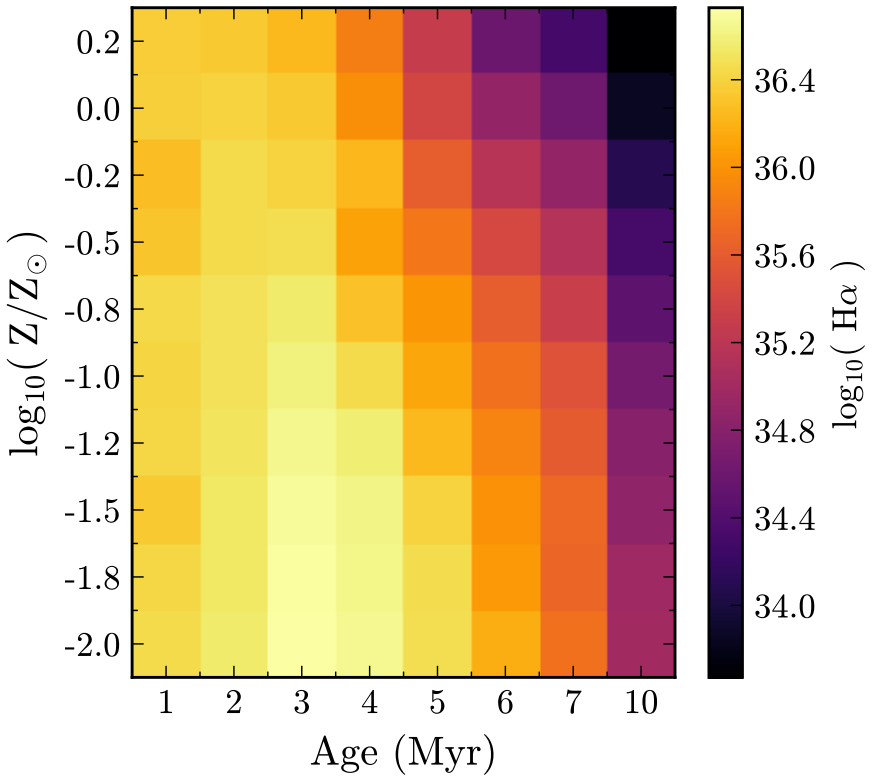

Figure 3.6 The time evolution of Hα emission as a function of metallicity for models with $\log_{10}\mathcal{U}_0 = -2.5$. H$\alpha$ fluxes are normalized to $1\,M_\odot$. Nebular emission is strongest at young ages, with the bulk of the emission from populations 3-5 Myr and younger.

Table 3.3. UV line fluxes given by the `CloudyFSPS` models, assuming a 4 Myr CSFR at solar metallicity. The lines are given as $\log_{10}[\,\mathrm{F_{line}}/\mathrm{F_{H\beta}}\,]$.

$\log_{10}\mathcal{U}_0$	CII	SiIV	CIV	CIV	HeII	OIII	AlII	SIII	NIII	SiIII	CIII
	1335Å	1394Å	1548Å	1551Å	1640Å	1666Å	1671Å	1720Å	1752Å	1883Å	1907Å
-4.0	-1.3804	-5.6837	-5.3685	-5.6693	-2.5986	-4.0755	-2.7892	-3.2152	-4.7364	-2.9110	-1.5986
-3.5	-1.1597	-4.1242	-3.8339	-4.1284	-2.4043	-3.2482	-2.7037	-2.9654	-3.9361	-2.5309	-1.2809
-3.0	-1.0009	-2.9794	-2.7862	-2.9548	-2.3324	-2.8136	-2.6589	-2.9105	-3.5459	-2.3823	-1.1719
-2.5	-0.9153	-2.6391	-2.5328	-2.5903	-2.2930	-2.6281	-2.6377	-2.9451	-3.4055	-2.3526	-1.1719
-2.0	-0.8786	-2.4956	-2.4178	-2.4682	-2.2557	-2.5136	-2.6262	-2.9821	-3.3233	-2.3426	-1.1793
-1.5	-0.8664	-2.3376	-2.2980	-2.3705	-2.2184	-2.4379	-2.6251	-3.0010	-3.2685	-2.3348	-1.1752
-1.0	-0.8641	-2.1745	-2.1487	-2.2430	-2.1831	-2.3742	-2.6178	-3.0043	-3.2203	-2.3239	-1.1583

Note. — Only a portion of this table is shown here to demonstrate its form and content. A machine-readable version of the full table is available.

massive star population required to ionize the surrounding gas evolves off of the main sequence (MS). The exact timescales associated with strong nebular emission will depend on the underlying stellar evolutionary models. For models that do not include stellar rotation or multiplicity, nebular emission persists for at most 3-4 Myr. Models that include stellar rotation can extend the lifetime of nebular emission up to 5-7 Myr (e.g., MIST; Byler et al., 2016; Choi et al., 2017). For evolutionary tracks that include the effects of stellar multiplicity, the lifetime of nebular emission can extend to greater than 10 Myr (e.g., BPASS; Eldridge, 2012).

We distinguish which emission lines are the most promising diagnostics by identifying bright lines that also show significant variation in strength with metallicity and ionization parameter. We first calculate $f_{\rm line}$, the median line strength relative to Hβ to identify emission lines that are relatively bright. We then characterize the sensitivity of the lines to the ionization parameter or metallicity by calculating $\sigma_{\mathcal{U}}$ and σ_Z, the variance in $f_{\rm line}$ over the full parameter range for $\mathcal{U}_0$ and $\log_{10}{\rm Z/Z_\odot}$, respectively.

We show $\sigma_{\mathcal{U}}$ and σ_Z as a function of $f_{\rm line}$ in Figs. 3.7 & 3.8 for a number of UV emission lines, for a model with constant SFR over 4 Myr. Emission lines that lie in the upper right hand of the plot are the most promising, since these lines are relatively bright and show significant variation with gas-phase metallicity (Fig. 3.7) or ionization parameter (Fig. 3.8). This also means that for some of the parameter space, these lines will be difficult to detect. The well-known C III] λ1909 and [O III] λ1666 lines fall into the promising regime of Fig. 3.7. Strong C III] emission appears in spectra of low-metallicity galaxies at low and high redshift (e.g., Shapley et al., 2003; Erb et al., 2010; Leitherer et al., 2011; Bayliss et al., 2014; Stark et al., 2014, 2015; Berg et al., 2016; Senchyna et al., 2017; Stroe et al., 2017b).

The [Ne III] λ3869 and [O II] λ3727 lines are also found in the promising region of Fig. 3.8; the Ne3O2 ratio was previously highlighted by Levesque & Richardson (2014) as an excellent probe of gas cloud ionization state. Other promising emission lines in Figs. 3.7 & 3.8 include [Al II] λ2661, [Mg II] λ2796, C IV λ1548, C IV λ1551, [S III] λ1720, and [Si III] λ1883, which we will discuss at length in the following sections. [Mg II] λ2796 emission was detected in a

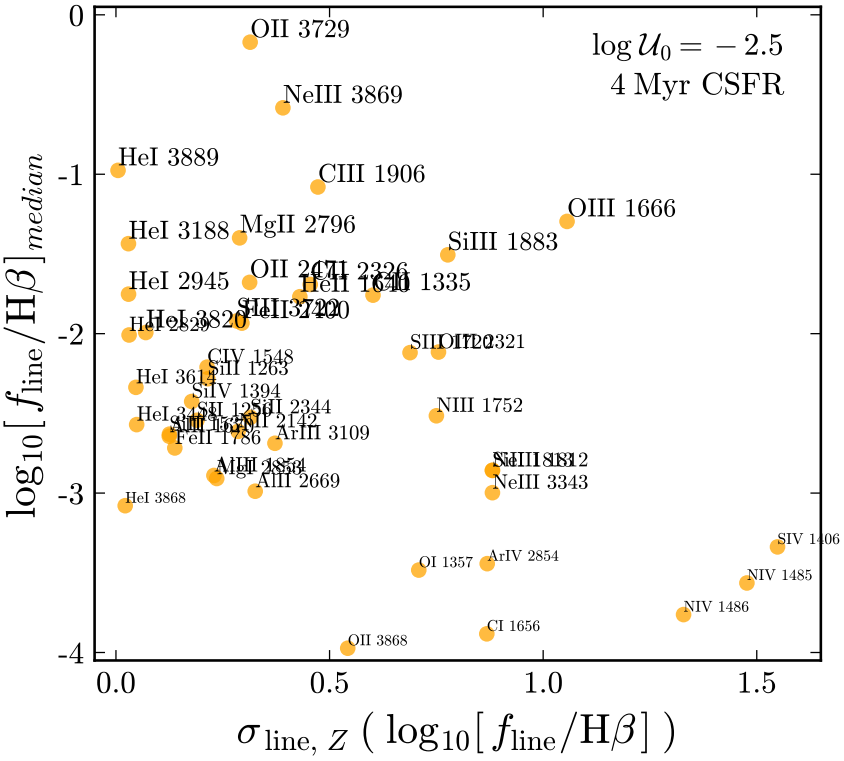

Figure 3.7 The variance in emission line strength, $\sigma_{\rm line}$, from changes in metallicity as a function of $f_{\rm line}$, the median emission line strength relative to Hβ. Emission lines with high $\sigma_{\rm line}$ and $f_{\rm line}$ are both relatively bright and show significant variation with model metallicity or ionization parameter. These emission lines are potentially useful diagnostics for the gas phase metallicity and ionization state of galaxies.

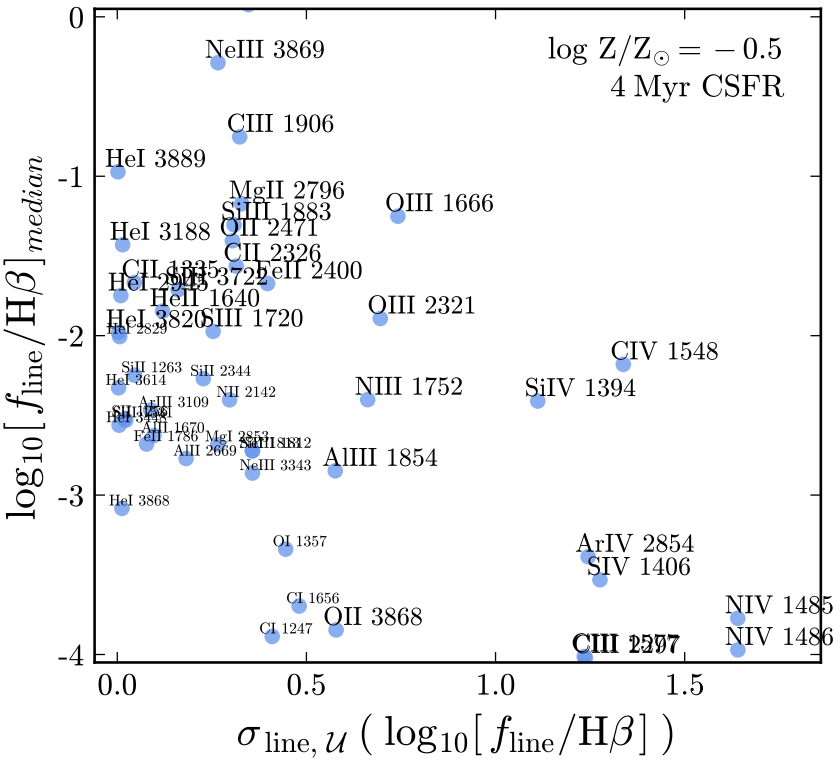

Figure 3.8 The variance in emission line strength, $\sigma_{\rm line}$, from changes in ionization parameter as a function of $f_{\rm line}$, the median emission line strength relative to Hβ. Emission lines with high $\sigma_{\rm line}$ and $f_{\rm line}$ are both relatively bright and show significant variation with model metallicity or ionization parameter. These emission lines are potentially useful diagnostics for the gas phase metallicity and ionization state of galaxies.

stacked spectrum of a $z\sim2$ galaxies by Du et al. (2016). While C IV λ1548 has been used to identify AGN sources (Stroe et al., 2017a; Feltre et al., 2016), sources with moderate C IV equivalent widths have been detected at high redshift that may be attributable to nebular emission and emission from massive star winds (Stark et al., 2014; Mainali et al., 2017; Schmidt et al., 2017).

A full list of predicted UV emission line fluxes as a function of metallicity and ionization parameter is given in Table 3.3[7].

Emission line ratios

Emission line ratios are widely used to infer the properties of the ionizing radiation and the surrounding gas cloud. The most useful emission line ratios should be easy to measure, relatively insensitive to reddening, and strongly correlated with bulk properties like the gas phase metallicity or the hardness of the ionizing spectrum. In this section we determine which combination of emission lines in the UV are best able to fulfill these requirements.

We first make a number of observationally motivated cuts to the emission lines considered for candidate line ratios. There are a total of 382 emission lines included in the FSPS nebular model, 159 of which are in the UV. We remove 21 Hydrogen Lyman series lines, because they are notoriously difficult to interpret due to resonant scattering effects. We also do not consider emission lines blueward of Lyα, which will be observationally difficult to access. We further restrict the line list to the brightest lines in multiplet series and elemental species with abundance by number relative to hydrogen of $\log[\mathrm{n/H}] > -6$, which leaves 60 remaining emission lines. Finally, we restrict ourselves to lines with $\log[f_{\mathrm{line}}/\mathrm{H}\beta] > -4$, which is sufficient to catch the weak but temperature-sensitive auroral lines, leaving 42 candidate emission lines to consider for possible line ratio diagnostics.

We determine all possible non-repeating combinations of the 42 emission lines, choosing the brighter of the two emission lines (using the median value over the range of models

[7]The table is available online in a machine readable format.

considered) as the denominator in each line ratio. For each of these line ratios, we calculate the variance in the line ratio, $\sigma_{\rm ratio}$, by taking the standard deviation of the line ratio across a range of model parameters. To find ratios that are sensitive to changes in metallicity, we calculate $\sigma_{{\rm ratio},\,Z}$ at fixed age and ionization parameter. Similarly, we calculate $\sigma_{{\rm ratio},\mathcal{U}}$ at fixed age and metallicity to find ratios that are sensitive to changes in the ionization parameter.

In Figs. 3.9 & 3.10 we plot the variance in the brightest of the candidate emission line ratios. Fig. 3.9 shows the line ratio variance, $\sigma_{\rm ratio}$, versus the median luminosity of the less luminous emission line in the pair, which would be the observationally limiting factor. Fig. 3.9 shows variance in emission line ratios driven by metallicity changes ($\sigma_{{\rm ratio},\,Z}$) while Fig. 3.10 shows variance in emission line ratios driven by ionization parameter changes ($\sigma_{{\rm ratio},\mathcal{U}}$). As in Figs. 3.7 & 3.8, emission line ratios in the upper right corner of these figures will be the easiest to detect and should have the most sensitivity to changes in metallicity or ionization parameter. We limit our study to emission line ratios with $\log[f_{\rm line\,1}] > 33$ and with $\sigma_{\rm ratio} > 0.3$. The latter choice corresponds to line ratios that experience factor of four difference in line ratio flux over the parameters of interest.

As discussed in §3.3.4, the Ne3O2 emission line ratio was identified by Levesque & Richardson (2014) as an excellent probe of gas ionization state. The Ne3O2 ratio appears high in the bottom panel of Fig. 3.10, confirming that our technique can identify emission line ratios that are sensitive to metallicity and ionization parameter. Similarly, the metallicity-sensitive O3C3 ratio (e.g., Stark et al., 2015; Du et al., 2016; Ding et al., 2016; Gutkin et al., 2016; Feltre et al., 2016) is strong in the top panel of Fig. 3.9.

Other promising line ratios include [O III] λ2322 / [C II] λ2326 (O3C2), [Si II] λ1263 / [C II] λ1335 (Si2C2), [N III] λ1752 / [O III] λ1666 (N3O3), and [Si III] λ1883 / C III] λ1907 (Si3C3); a full list is included in Table 3.4.

In Fig. 3.11 we show each of these line ratios as a function of metallicity to highlight their utility as metallicity indicators. These ratios show several orders of magnitude variation with metallicity and ionization parameter. These emission line ratios can be used by themselves

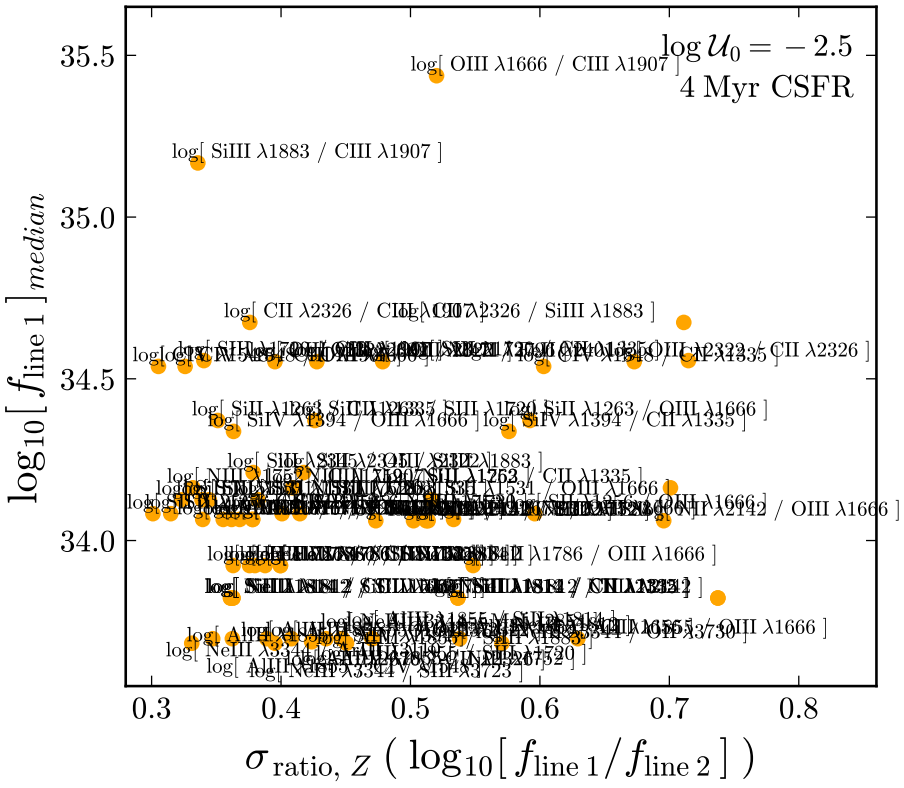

Figure 3.9 We show the variance in emission line ratio, σ_{ratio}, as a function of the median luminosity of the less luminous emission line used in the ratio, by definition the numerator. Here we show the variance in the line ratio due to changes in metallicity, for a 4 Myr CSFR model at $\log_{10}\mathcal{U}_0 = -2.5$. Emission line ratios in the upper right corner of this plot will be the easiest to observe and should provide the most leverage in determining gas phase metallicities.

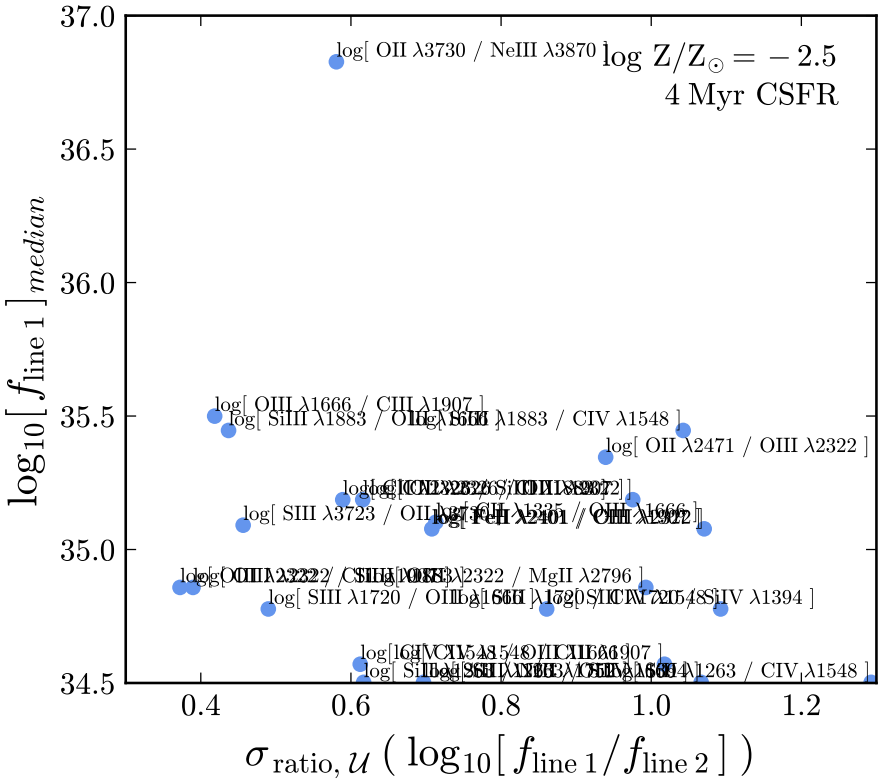

Figure 3.10 We show the variance in emission line ratio, $\sigma_{\rm ratio}$, as a function of the median luminosity of the less luminous emission line used in the ratio, by definition the numerator. Here we show the variance in the line ratio due to changes in ionization parameter, for a 4 Myr CSFR model at $\log_{10} {\rm Z/Z_\odot} = -0.5$. Emission line ratios in the upper right corner of this plot will be the easiest to observe and should provide the most leverage in determining ionization parameters.

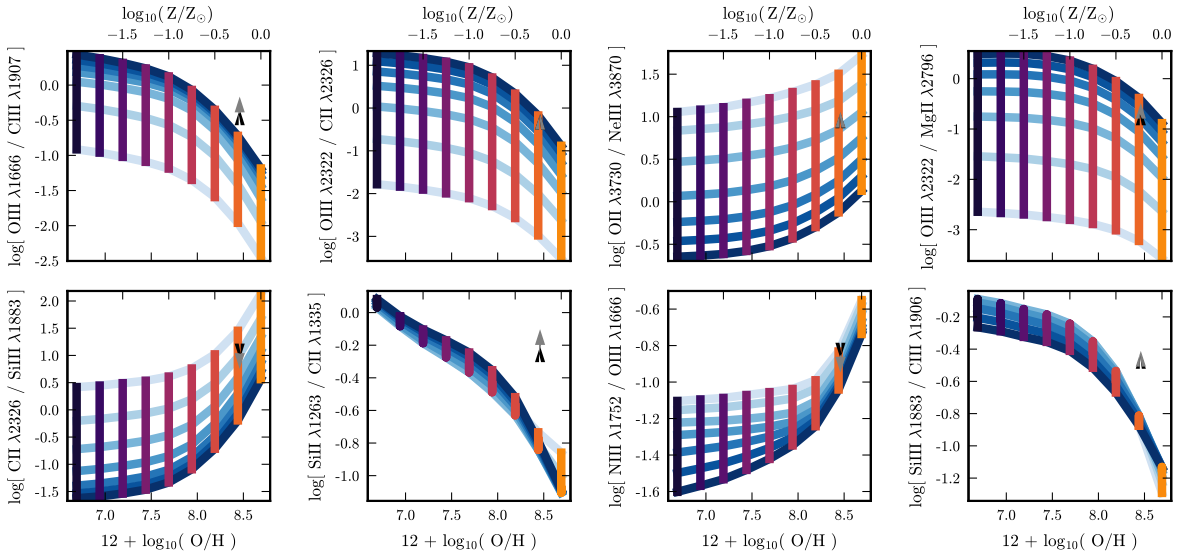

Figure 3.11 Several emission line ratios as a function of model metallicity (purple to yellow) and ionization parameter (blue) for 4 Myr constant SFR populations. The blue lines connect models of constant ionization parameter, with $\log_{10}\mathcal{U}_0 = -1$ in dark blue and $\log_{10}\mathcal{U}_0 = -4$ in light blue. Models of constant metallicity span from $\log_{10} \mathrm{Z/Z_\odot} = -2$ in purple to $\log_{10} \mathrm{Z/Z_\odot} = 0.0$ in yellow. The grey and black arrows show one magnitude of extinction assuming SMC and Calzetti reddening laws, respectively.

to estimate the gas phase metallicity of a galaxy, but with uncertainty due to the unknown ionization parameter. Alternatively, they can be combined with other emission line ratios to create "diagnostic diagrams" in the UV, like the well-used Baldwin Phillips Terlevich (BPT) diagram in the optical (Baldwin et al., 1981). These combinations of emission line ratios may better distinguish the metallicity and ionization parameter of the observed population than the use of a single line.

We show several promising emission line ratio combinations in Fig. 3.12. The [Si II] λ1263 / [C II] λ1335 (Si2C2) vs. [O III] λ1666 / C III] λ1907 (O3C3) diagnostic diagram (*left*) is very sensitive to the gas phase metallicity while remaining relatively insensitive to ionization

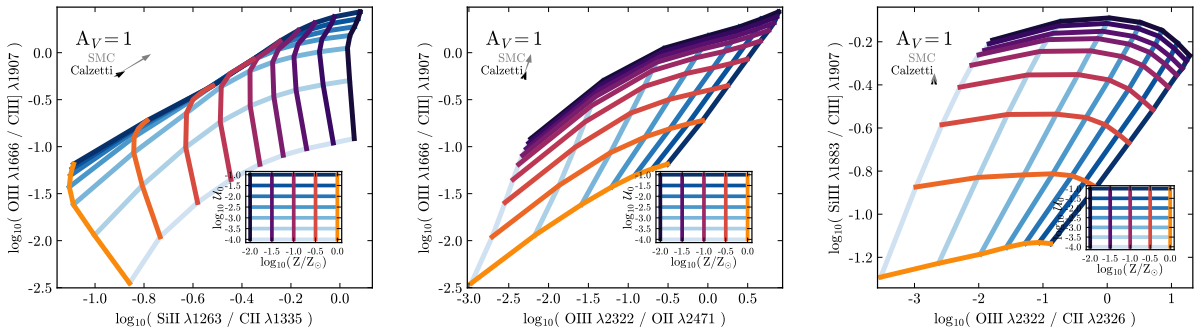

Figure 3.12 UV diagnostic diagrams using combinations of emission line ratios for 4 Myr constant SFR populations. The blue lines connect models of constant ionization parameter, from $\log_{10}\mathcal{U}_0 = -1$ in dark blue to $\log_{10}\mathcal{U}_0 = -4$ in light blue. Models of constant metallicity span from $\log_{10} \mathrm{Z}/\mathrm{Z}_\odot = -2$ in purple to $\log_{10} \mathrm{Z}/\mathrm{Z}_\odot = 0.0$ in yellow. The grey and black arrows show one magnitude of extinction assuming SMC and Calzetti reddening laws, respectively.

parameter, due to combining species from several ionization states. The O3C3 ratio also pairs well with the [O III] λ2322 / [O II] λ2471 ratio for a diagnostic diagram (*middle*) that has the potential to distinguish metallicity and ionization parameter. The [Si III] λ1883 / C III] λ1907 (Si3C3) vs. [O III] λ2322 / [C II] λ2326 diagnostic diagram (*right*) is sensitive to both ionization parameter and metallicity, though the sensitivity to metallicity seems to saturate below $\log_{10} \mathrm{Z}/\mathrm{Z}_\odot = -1.5$.

All of these diagnostic diagrams make use of emission lines that are relatively close in wavelength space, making them less sensitive to the effects of reddening. We show the direction that 1 magnitude of reddening ($A_V = 1$) would change the emission line ratios, assuming two different extinction laws, the canonical Calzetti extinction curve and the steeper SMC extinction curve, which may be more appropriate for low-metallicity galaxies.

Table 3.4. UV Emission line ratios

Ratio	Definition
Si2C2	$\log_{10}$([Si II] λ1263 / [C II] λ1335)
Si4C2	$\log_{10}$(SiIVλ1394 / [C II] λ1335)
C4O3^{w,s}	$\log_{10}$(C IV λ1551 / [O III] λ1666)
He2Hb^{w,s}	$\log_{10}$([He II] λ1640 / Hβ)
O3C3	$\log_{10}$([O III] λ1666 / C III] λ1907)
N3O3	$\log_{10}$([N III] λ1752 / [O III] λ1666)
Fe2N3	$\log_{10}$(FeIIλ1786 / [N III] λ1752)
Si3C3	$\log_{10}$([Si III] λ1883 / C III] λ1907)
Si3N3	$\log_{10}$([Si III] λ1883 / [N III] λ1752)
O3C2	$\log_{10}$([O III] λ2322 / [C II] λ2326)
O3C2	$\log_{10}$([O III] λ2322 / [O II] λ2471)
O3Mg2	$\log_{10}$([O III] λ2322 / [Mg II] λ2796)
C2Si3	$\log_{10}$([C II] λ2326 / [Si III] λ1883)
Al2Mg2	$\log_{10}$([Al II] λ2661 / [Mg II] λ2796)
Ne3O2	$\log_{10}$([Ne III] λ3870 / [O II] λ3727)

[w]Ratio may include contribution from stellar wind emission

[s]Ratio may be sensitive to shock contribution

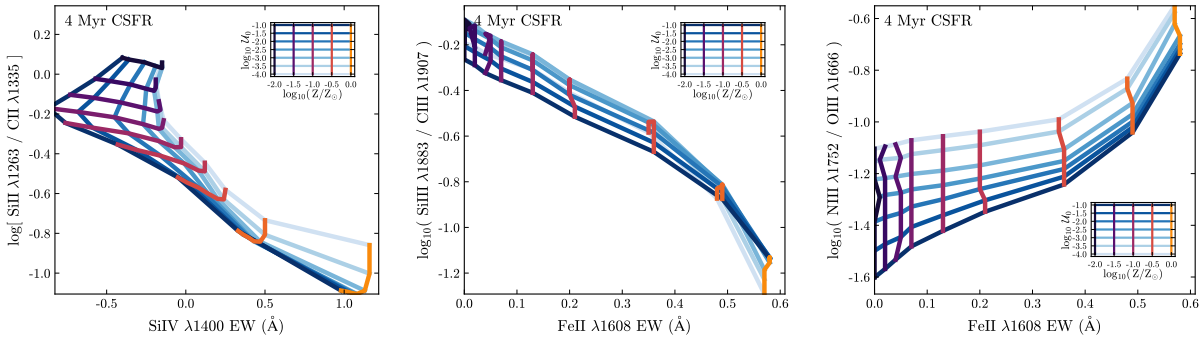

Figure 3.13 Combining the diagnostic capabilities of emission and absorption features. The y-axis shows an emission line ratio while the x-axis shows the equivalent width of an absorption feature. The blue lines connect models of constant ionization parameter. $\log_{10}\mathcal{U}_0 = -1$ is shown in dark blue and $\log_{10}\mathcal{U}_0 = -4$ is shown in light blue. Models of constant metallicity are connected by the colored lines, from $\log_{10}\mathrm{Z}/\mathrm{Z}_\odot = -1$ in purple and $\log_{10}\mathrm{Z}/\mathrm{Z}_\odot = 0.0$ in yellow.

3.3.5 UV diagnostics combining emission and absorption features

For short-lived massive stars, the metallicity of the stars should be nearly identical to that of the surrounding natal gas cloud, but also see Steidel et al. (2016) for a discussion of α-enhanced systems. There are notably fewer nebular emission lines in the UV compared to the optical, but we can gain additional metallicity leverage by considering combinations of stellar absorption features and nebular emission features.

In this section we identify useful combinations of emission and absorption lines that track well with the properties of the ionizing SSP and gas-phase metallicity. We use the strongest absorption features identified in §3.3.3 and combine them with the most promising diagnostic ratios determined in §3.3.4.

Fig. 3.13 shows metallicity diagnostics using the combination of an emission line ratio and an absorption feature. Both of the absorption features strongly track the metallicity of the young stellar population and provide complimentary metallicity information where

the emission line ratios are be less sensitive. The Si4C2 emission line ratio excels at low metallicities where the `SiV_1400` absorption feature is weakest (left panel). The `FeII_1608` index has a better sensitivity to changes in abundance at low-metallicity, pairing nicely with the Si3C3 and N3O3 emission line ratios (middle and right panels of Fig. 3.13, respectively), which are most sensitive at moderate metallicities.

3.3.6 Comparisons with optical line ratios

In this section, we compare several of the ratios presented in §3.3.4, listed in Table 3.4, to well-known emission line ratios in the optical. In Fig. 3.14, we show four UV-optical emission line ratio comparisons, where the optical ratio is on the x-axis and the UV ratio is on the y-axis. We have highlighted two UV ratios that show sensitivity to ionization parameter and two UV ratios that show sensitivity to metallicity.

The top panel of Fig. 3.14 shows the emission line ratios that are sensitive to ionization parameters. The UV ratios are compared to the optical $\log_{10}$([O III] λ 5007 / [O II] λ 3727,9) ratio, also referred to as O3O2 or O_{32}, which is known to be sensitive to ionization parameter. Both the $\log_{10}$([O III] λ1666 / C III] λ1907) (O3C3; *top left*) and $\log_{10}$([O III] λ2322 / C III] λ2326) (O3C2; *top right*) UV ratios show similar sensitivity to ionization parameter and correlate positively with the optical O3O2 ratio. The UV ratio is more metal-dependent at fixed ionization parameter, but at low metallicity (below $\log_{10} Z/Z_{\odot} = -1$) the sensitivities are comparable.

The bottom panel of Fig. 3.14 shows UV emission line ratios that are sensitive to metallicity. We compare UV metallicity-sensitive emission line ratios to the optical $\log_{10}$([N II] λ 6584 / [O II] λ 3727,9) emission line ratio, which correlates strongly with metallicity and has little dependence on ionization parameter (Kewley & Dopita, 2002). The UV $\log_{10}$([N III] λ1752 / [O III] λ1666) ratio (N3O3; *bottom left*) shows a strong correlation with the optical N2O2 ratio, where larger values of both indicate higher metallicities. Neither ratio does particularly well at low metallicity, though. The UV $\log_{10}$([Si III] λ1883 / C III] λ1907) (Si3C3; *bottom right*) is anti-correlated with the optical N2O2 ratio. The Si3C3 ratio is

strongest at low-metallicity and will thus have slightly different optimal applications.

3.4 Observational Comparison

In this section we evaluate the diagnostics discussed in §3.3.5 by comparing them with observed galaxies. We verify that these diagnostics hold across redshift by comparing them to observations of both local galaxies with UV spectra and high redshift galaxies with rest frame UV spectra.

3.4.1 UV spectra of local galaxies

Blue Compact Dwarfs (BCDs[8]), originally defined by Sargent & Searle (1970), are characterized by blue optical colors, small sizes (< 1 kpc), and low luminosities ($M_B >$-18). These galaxies have strongly enhanced star formation in extremely metal-poor environments, and have thus been proposed as nearby analogs of star formation in young galaxies observed at high redshift (Thuan, 2008). The young ages associated with recent star formation make these objects very UV-bright, and their optical spectra are indistinguishable from H II regions.

Emission lines

In this section we compare our models with data from Berg et al. (2016), who presented both UV and optical spectra for a sample of 7 nearby, low-metallicity, high-ionization BCDs. In this pioneering analysis to connect UV and optical emission line properties, Berg et al. (2016) obtained UV spectra with the Cosmic Origins Spectrograph (COS) on the Hubble Space Telescope (HST) for galaxies with existing optical SDSS spectra. The UV spectra have $\sim$0.6Å resolution at 1600Å, which is sufficient for the emission line ratios considered in this paper. We include 13 additional galaxies from the upcoming Berg et al., 2017 (*in prep*, priv. comm.) paper.

[8]Blue Compact Dwarf is used here instead of Blue Compact Galaxy to avoid acronym confusion with Brightest Cluster Galaxies

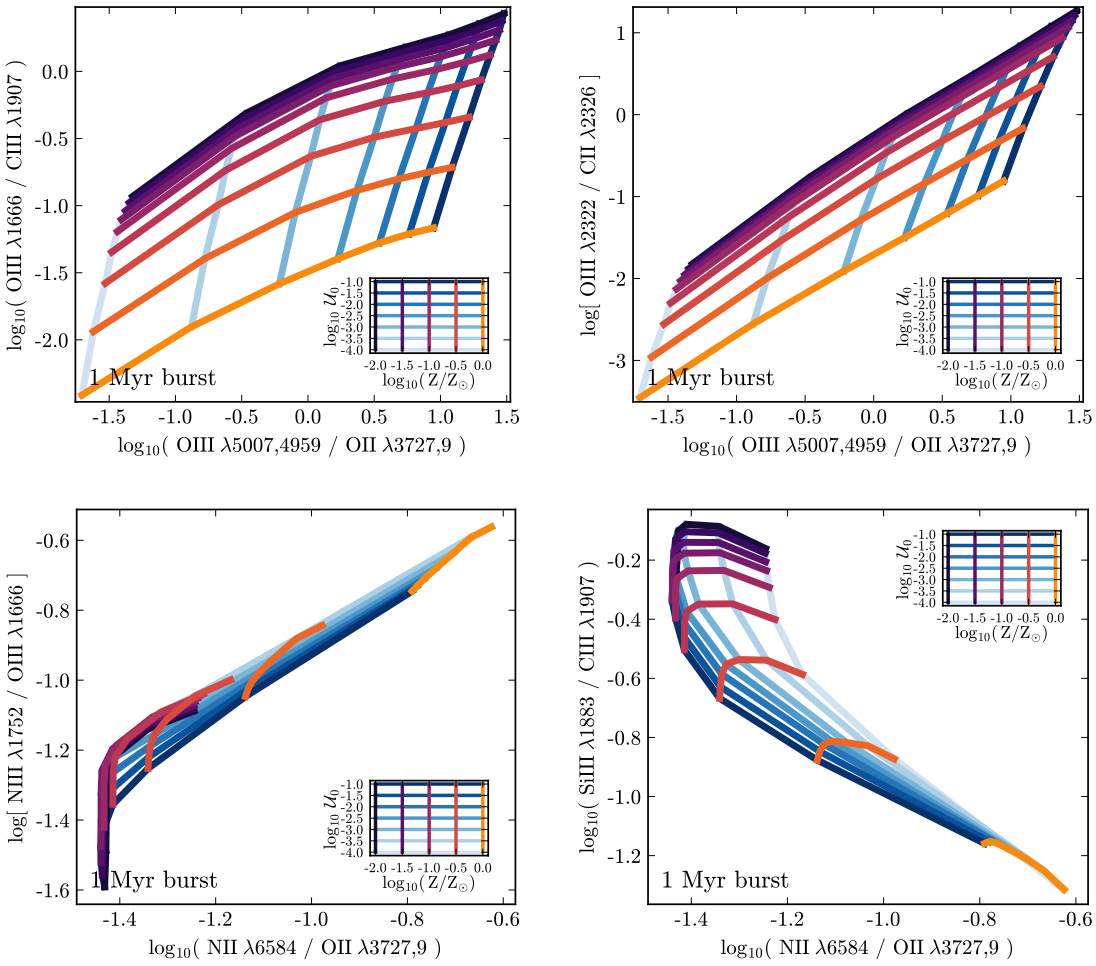

Figure 3.14 Comparisons of UV and optical emission line ratios. The model colors are the same as indicated in Fig. 3.12. *Top row:* Emission line ratios sensitive to ionization parameter: the UV O3C3 emission line ratio (*top left*) and the UV O3C2 emission line ratio (*top right*) compared to the O3O2 optical emission line ratio. *Bottom row:* Emission line ratios sensitive to metallicity: the UV N3O3 emission line ratio (*bottom left*) and the UV Si3C3 emission line ratio (*bottom right*) compared to the optical N2O2 emission line ratio.

The galaxies in Berg et al. (2016) are nearby ($0.003 < z < 0.040$), UV-bright ($m_{FUV} \leq$ 19.5 AB), compact (D < 5"), low-metallicity ($7.2 \leq 12 + \log(O/H) \leq 8.0$) dwarf galaxies. These galaxies have relatively low masses ($\sim 10^7\,M_\odot$) and high sSFRs ($\sim 10^{-8}$ yr^{-1}). All of the galaxies in the sample have auroral line detections in the optical for direct-method calculations of the nebular temperature, density, and metallicity.

Emission lines of C III] 1907,1909Å and [O III] 1666Å emission lines are detected in all 20 galaxies, while the SiIII]λ1883,1893Å emission doublet is only detected in 13/20 galaxies. The non-detection is not unusual since these galaxies are reasonably metal-poor and the SiIII]λ1893Å emission feature is strongest around $12 + \log(O/H) \sim 8.3$ and gets weaker with decreasing metallicity.

In Figs. 3.15, 3.16, & 3.17, we show measured emission line ratios from the Berg et al. (2016) sample on various UV diagnostic diagrams. The diagnostic diagrams shown here are only a subset of those from §3.3.5, since we are limited to those diagrams where all four emission lines were measurable in the observed galaxies.

Fig. 3.15 shows [O III] λ1666/C III] λ1906 (O3C3) vs. [Si III] λ1883/C III] λ1906 (Si3C3) for both a 1 Myr burst and a 4 Myr constant SFR model. The model grid is able to reproduce the full range of observed line ratios. The data points cover a region of the model grid with low metallicities ($\log_{10} Z/Z_\odot \sim -1.25$ to -0.5, or $\log(O/H) + 12 \sim -7.5$ to -8.0) and high ionization parameters (between $\log_{10}\mathcal{U}_0 \sim -2$ and -1), both of which are consistent with estimates from the optical spectroscopy.

Fig. 3.16 shows O3C3 vs. [Ne III] λ3869/[O II] λ3727 (Ne3O2) for stellar populations assuming a 1 Myr burst and a 4 Myr constant SFR. The young burst and the constant SFR models are very similar, and both grids are able to reproduce the observed line ratios. The O3C3 and Ne3O2 line ratios are sensitive to ionization parameter, and the combination of them provides the most leverage for discriminating among models of constant ionization parameter. The BCDs in the O3C3 vs. Ne3O2 diagram have line ratios consistent with ionization parameters around $\log_{10}\mathcal{U}_0 = -2.0$. For the galaxies that appear in both Fig. 3.15 and Fig. 3.16, the UV model grids predict ionization parameters that are consistent with

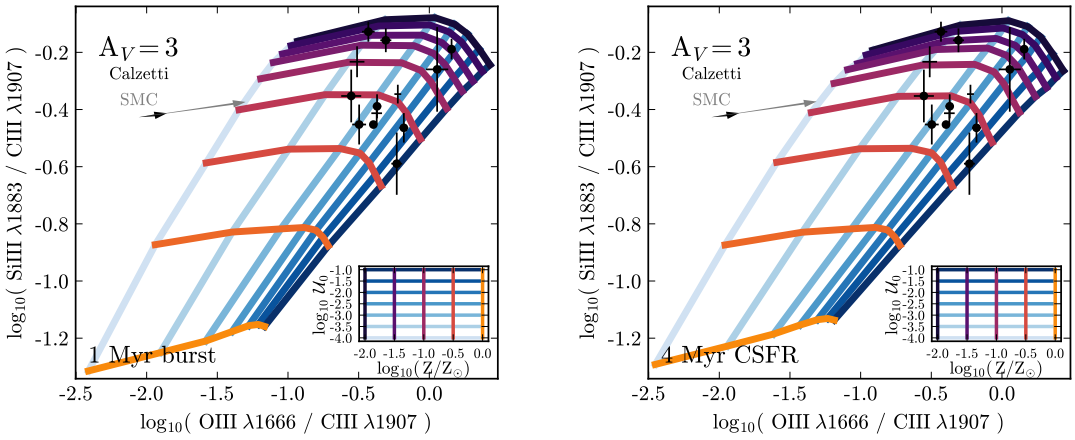

Figure 3.15 The Berg et al. (2016) BCD sample compared to UV diagnostic diagrams for a 1 Myr burst (left) and a 4 Myr constant SFR (right). The blue lines connect models of constant ionization parameter. $\log_{10}\mathcal{U}_0 = -1$ is shown in dark blue and $\log_{10}\mathcal{U}_0 = -4$ is shown in light blue. Models of constant metallicity are connected by the colored lines, from $\log_{10} \mathrm{Z}/\mathrm{Z}_\odot = -1$ in purple and $\log_{10} \mathrm{Z}/\mathrm{Z}_\odot = 0.0$ in yellow. The grey and black arrows show three magnitudes of extinction assuming SMC and Calzetti reddening laws, respectively.

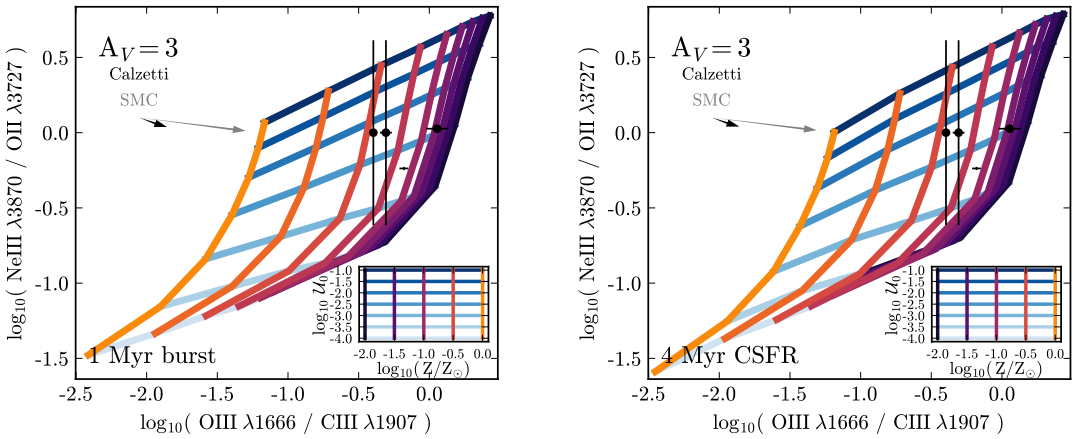

Figure 3.16 The Berg et al. (2016) BCD sample compared to UV diagnostic diagrams for a 1 Myr burst (left) and a 4 Myr constant SFR (right). The blue lines connect models of constant ionization parameter. $\log_{10}\mathcal{U}_0 = -1$ is shown in dark blue and $\log_{10}\mathcal{U}_0 = -4$ is shown in light blue. Models of constant metallicity are connected by the colored lines, from $\log_{10} Z/Z_\odot = -1$ in purple and $\log_{10} Z/Z_\odot = 0.0$ in yellow. The grey and black arrows show three magnitudes of extinction assuming SMC and Calzetti reddening laws, respectively. The models are able to reproduce observed line ratios.

one another and with the optically-derived ionization parameters.

Fig. 3.17 shows O3C3 vs. C IV λ1548/[O III] λ1666 (C4O3; bottom row) and C4O3 vs. Si3C3 (top row) for a 1 Myr burst and 4 Myr constant SFR. In the bottom row of Fig. 3.17 we include the sample of nearby dwarf galaxies presented in Senchyna et al. (2017), which agree well with the Berg et al. (2016) sample. This comparison is only possible for Fig. 3.17, since the Senchyna et al. (2017) sample only includes emission line measurements for C III] λ1906, [O III] λ1666, and C IV λ1548.

In contrast to Figs. 3.15 & 3.16, these diagnostics are not able to fully reproduce the range of observed line ratios. In particular, the majority of the C4O3 ratios lie beyond the

highest ionization parameters in the model grid, which could indicate that the models do not reach high enough ionization states. However, the consistency of the other grids with $\log_{10}\mathcal{U}_0 = -2$ suggest that instead this behavior is primarily driven by larger-than-predicted contributions from stellar wind emission to the C IV λ1548 flux. This emission is not included in our models of the nebular contribution, and thus the C4O3 ratio should thus be considered a lower limit when compared to the observed C4O3 ratios. We note that the C IV λ1548 lines in the Berg et al. (2016) spectra are in fact broader than the other nebular emission lines, which is consistent with wind contamination.

Contribution from both nebular emission and stellar wind emission is a known issue for other UV emission lines as well (e.g., [He II] λ1640). In theory, with sufficient resolution and signal-to-noise, one could distinguish the two components by their different line profiles, as the nebular emission component should be narrow while the stellar wind emission component should be fairly broad. However, this measurement is difficult in the more common low-to-mid-resolution spectra. For this reason, we recommend limiting diagnostic diagrams to line ratios that include no more than one emission line with a well-known stellar emission contribution. For example, the commonly used [He II] λ1640 / C IV λ1548 line ratio (e.g., Feltre et al., 2016; Nakajima et al., 2017) may be difficult to interpret due to the unknown contribution from stellar and nebular emission in both the numerator and denominator.

Emission line equivalent widths

Emission line equivalent widths (EWs) are frequently reported instead of fluxes. However, EWs are sensitive to the luminosity of the underlying continuum relative to the strength of the emission line.

To measure emission line equivalent widths from our models, we follow the methodology applied to observed data. In broad terms, the process involves subtracting the best-fit stellar continuum, and then fitting the residual emission line with a Gaussian. We generate two spectra with FSPS, one that includes nebular emission lines and one that does not. We use the "non-emission" spectrum as the best-fit stellar continuum. FSPS returns

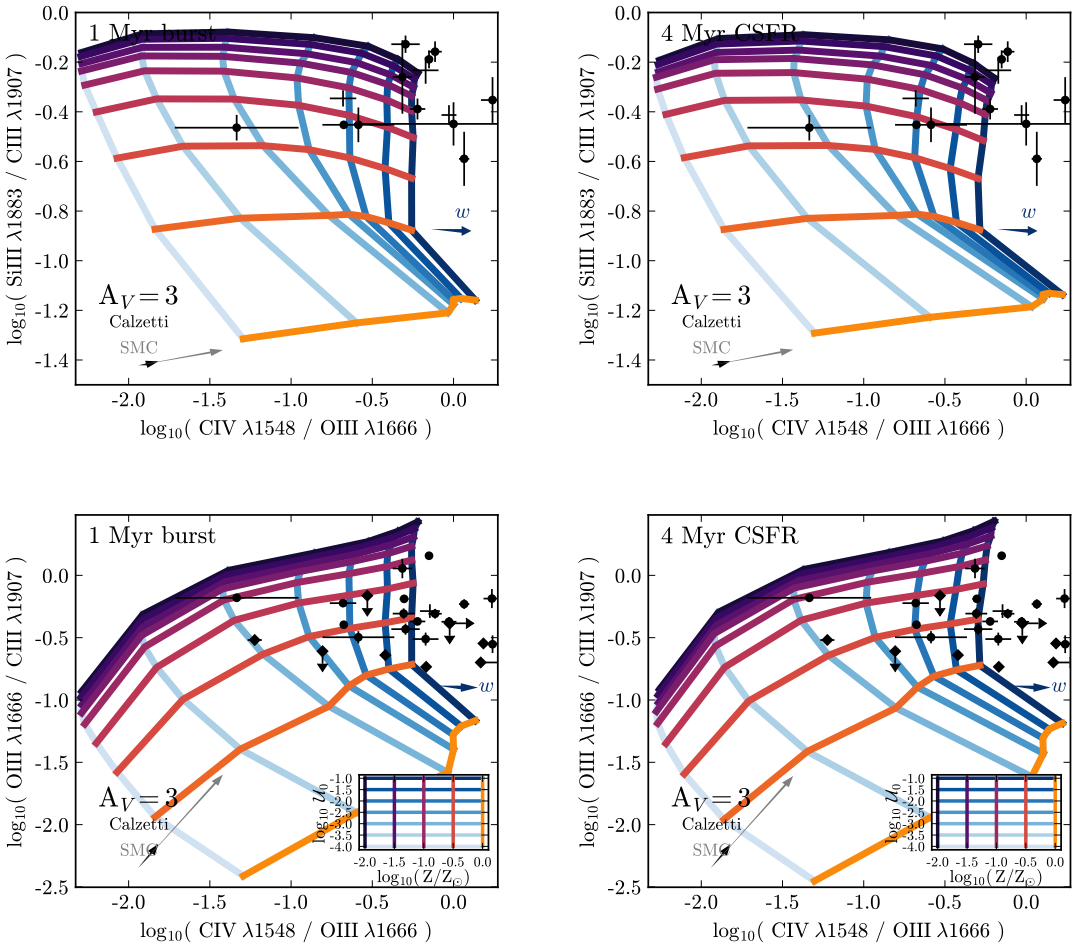

Figure 3.17 The Berg et al. (2016) BCD sample compared to UV diagnostic diagrams for a 1 Myr burst (left) and a 4 Myr constant SFR (right). Observations from Senchyna et al. (2017) are shown with grey diamonds on the bottom two plots. The blue lines connect models of constant ionization parameter. $\log_{10}\mathcal{U}_0 = -1$ is shown in dark blue and $\log_{10}\mathcal{U}_0 = -4$ is shown in light blue. Models of constant metallicity are connected by the colored lines, from $\log_{10} Z/Z_\odot = -1$ in purple and $\log_{10} Z/Z_\odot = 0.0$ in yellow. Stellar wind emission can inflate the measured CIV1548 flux, we indicate the direction of this with the blue arrow. The grey and black arrows show three magnitudes of extinction assuming SMC and Calzetti reddening laws, respectively.

$\mathcal{F}_\lambda$ in $L_\odot/\text{Å}$, which we convert to cgs units ($\text{erg/s/cm}^{-2}/\text{Å}$) by assuming a total stellar mass of $M = 10^7\,M_\odot$[9] and a distance of 10 Mpc. We subtract the continuum spectrum from the emission spectrum and fit the resultant scaled emission-line-only spectrum with `scipy.optimize.curvefit` (Jones et al., 2001–) using a 3-parameter Gaussian function of the form:

$$f(x) = a \cdot \exp\left(\frac{-(x-b)^2}{2c}\right), \tag{3.4}$$

such that the integrated flux in the Gaussian is simply $\sqrt{2\pi} \cdot ac$ and an equivalent width with units of Å.

In Fig. 3.18 we plot the model equivalent width of C III] $\lambda\lambda 1907, 1909$ as a function of metallicity for a 1 Myr instantaneous burst, where we have added the equivalent widths of the C III] $\lambda 1907$ and C III] $\lambda 1909$.

The equivalent width of C III] depends strongly on ionization parameter, where models with high ionization parameters produce larger C III] equivalent widths. The equivalent widths are also strongly dependent on metallicity. The largest C III] equivalent width (nearly 40Å) is seen at $\log_{10}(\text{O/H}) \sim 8$, and declines toward both higher and lower metallicities. C III] equivalent widths decrease much more rapidly towards high metallicities, and are essentially non-existent at solar and super-solar metallicities. C III] equivalent widths decline to ~ 10Å at $\log_{10} Z/Z_\odot = -2$ due to the increasing deficit of carbon.

We compare the models in Fig. 3.18 to measured equivalent widths and metallicities from the Berg et al. (2016) and Senchyna et al. (2017) samples, both of which also measure equivalent widths using single gaussian fits to the emission line. Fig. 3.18 also includes the literature measurements compiled by Senchyna et al. (2017), which include nearby galaxies from Giavalisco et al. (1996) ("G96") and Leitherer et al. (2011) ("L11").

The models in Fig. 3.18 are able to reproduce the range of observed C III] equivalent widths and their distribution with metallicity. In particular, our models show weak C III]

[9] We chose this mass to match the observed properties of the Berg et al. (2016) sample. However, we note that the C III] equivalent widths presented here are not sensitive to that choice, since both the underlying UV stellar continuum and the C III] luminosity scale directly with the flux of the same massive star population.

equivalent widths at high metallicity ($\log_{10}(O/H \gtrsim 8.4$) and show the strongest C III] equivalent widths at low metallicity ($\log_{10}(O/H) \sim 8$). This behavior is in agreement with Senchyna et al. (2017), who suggested that there seemed to be a metallicity threshold in the observations, where large C III] equivalent widths were only observed in galaxies with metallicities below $\log_{10}(O/H) \sim 8.4$. Our model envelope naturally suppresses the C III] EW at high metallicity, though perhaps not as strongly as is seen in the data.

Higher ionization parameters produce larger C III] equivalent widths at all metallicities. Thus, observations with large C III] equivalent widths should be also biased toward high ionization parameters, and should have emission line ratios that similarly reflect that bias. We test this hypothesis in Fig. 3.19, where we show our models on optical diagnostic diagrams color-coded by their UV C III] equivalent width. The left and middle panels show the BPT diagram and the O_{32}-R_{23} diagram respectively. Models with large C III] equivalent widths (redder colors) occupy the region of the BPT diagram with large values of [O III]/Hβ and large ionization parameters. Similarly, the models with large C III] equivalent widths have large O_{32} ratios, also indicating high ionization parameters.

Finally, the right panel of Fig. 3.19 shows the C III] equivalent width as a function of the optical [O III] λ 5007 equivalent width. Objects with large [O III] equivalent widths have been suggested as a means of optically selecting galaxies with strong UV C III] emission (Berg et al., 2016; Senchyna et al., 2017). Our models confirm this correlation, although with an offset, due to the different metallicity dependence of carbon and oxygen line strength. The largest C III] equivalent widths in the models do not coincide with the largest [O III] equivalent widths, since oxygen emission lines are strongest at a slightly higher metallicity ($\log_{10}(O/H) \sim 8.4$) than the metallicity with peak C III] emission ($\log_{10}(O/H) \sim 8$).

Absorption Indices

To evaluate the absorption line indices identified in §3.3.3, we compare our models to measurements of 14 nearby ($0.003 < z < 0.03$) BCDs presented in Zetterlund et al. (2015), observed using the HST COS spectrograph. This sample has metallicities derived from

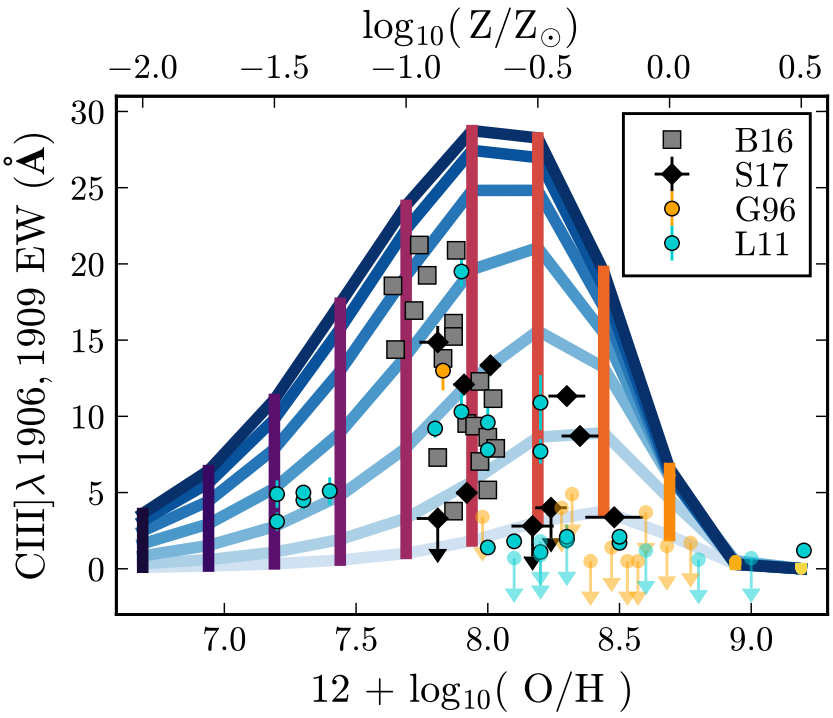

Figure 3.18 The equivalent width of C III] $\lambda\,1907, 1907$ as a function of metallicity for a 1 Myr instantaneous burst with $M = 10^7\,\mathrm{M}_\odot$. The blue lines connect models of constant ionization parameter. $\log_{10}\mathcal{U}_0 = -1$ is shown in dark blue and $\log_{10}\mathcal{U}_0 = -4$ is shown in light blue. Models of constant metallicity are connected by the colored lines, from $\log_{10}\mathrm{Z}/\mathrm{Z}_\odot = -1$ in purple and $\log_{10}\mathrm{Z}/\mathrm{Z}_\odot = 0.0$ in yellow. As noted in Senchyna et al. (2017), there seems to be a metallicity ceiling around $\log_{10}(\mathrm{O/H}) \sim 8$, above which C III] emission is very weak.

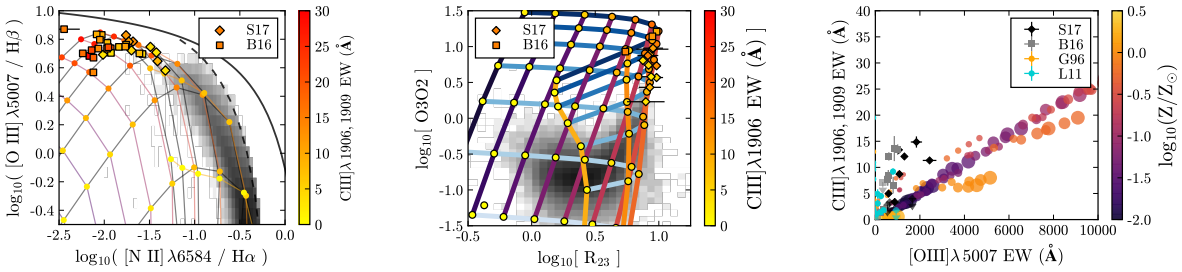

Figure 3.19 *Left and Center:* Optical diagnostic diagrams color-coded by the equivalent width of C III] $\lambda\,1907, 1907$. Large C III] equivalent widths occur in models with high ionization parameter, and thus coincide with observations that have large values of [O III]/Hβ (*left*) and large values of O3O2 (*center*). *Right:* C III] $\lambda\,1907, 1907$ equivalent width as a function of [O III] $\lambda\,5007$ equivalent width. Large C III] equivalent widths correlate with large [O III] equivalent widths.

optical emission line ratios from KK04 based on the R_{23} diagnostic, giving an estimated accuracy of $\sim$0.15 dex (Zetterlund et al., 2015). The accuracy of the R_{23} metallicity diagnostic is worse near $12 + \log(O/H) \sim 8.4$, where the value of R_{23} rolls over, and may be biased high compared to stellar metallicities (e.g., Kudritzki et al., 2012).

There were no nebular emission features detected in this sample, due to sample selection effects and low signal-to-noise (S/N$\sim$1-5). However, Zetterlund et al. (2015) did provide measurements of `AlII_1670` and `CIV_1550`, two of the Leitherer et al. (2011) absorption indices.

In Fig. 3.20 we show equivalent widths of `AlII_1670` and `CIV_1550` as a function of galaxy metallicity. In general, the `CIV_1550` EWs are large, as expected for this strong, stellar-wind dominated line. The weaker `AlII_1670` index takes both positive and negative values, potentially reflecting the influence of filling from emission lines (negative EWs), which is particularly problematic for this index, as discussed in 3.3.3.

Although some `AlII_1670` measurements lie systematically above our model predictions,

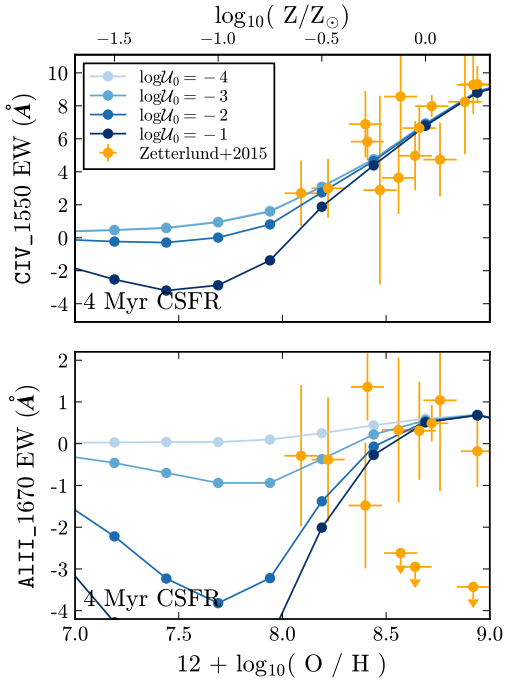

Figure 3.20 The equivalent widths of the `AlII_1670` and `CIV_1550` Leitherer et al. (2011) absorption indices as a function of metallicity. The orange markers are measured from local BCD spectra, with metallicity estimates derived from optical emission line ratios. The blue lines show our emission model at several different ionization parameters for a 4 Myr CSFR.

we note that our models only include the contribution from stellar and nebular emission, and do not include the effects of interstellar absorption. This was considered in detail in Vidal-García et al. (2017), who found that interstellar line absorption near Al II λ1670 can be significant, especially at high metallicity. Interstellar absorption can also affect the `CIV_1550` index, for which Leitherer et al. (2011) noted could account for as much as 1/3 of the absorption in the index.

In addition to the effects from interstellar absorption, the central bandpass of the `AlII_1670` index also includes the [Al II] λ1670 emission line. We briefly estimate the total possible con-

tribution from nebular emission to the absorption indices shown in Fig. 3.20. Models that include nebular emission predict equivalent widths $0.1 - 0.5$ Å smaller than the stellar-only predictions; this contribution can be significant, however, since typical `AlII_1670` EWs are of order 0.5Å.

Similarly, the central bandpass of the `CIV_1550` absorption index includes the C IV λ1548 emission line. However, `CIV_1550` is less susceptible to nebular influence since the stellar wind absorption feature that dominates the central bandpass has equivalent widths of order 5-10Å, whereas the nebular emission contributes 0.01Å at most to the total equivalent width, which is entirely negligible compared to the measured errors.

3.4.2 UV spectra of high redshift galaxies

Rest-frame UV spectra of distant galaxies are a powerful tool to study the star formation environment of young galaxies, and will become higher quality and increasingly commonplace with future optical and IR instruments on the next generation of telescopes. In this section we compare the UV diagnostic diagrams presented in §3.3.5 to the rest-frame UV spectra of galaxies at intermediate- and high-redshift obtained with ground-based optical and IR instruments.

Before proceeding, we note that that estimates of metallicity for these distant galaxies, when used, are determined from rest-frame optical emission line diagnostics observed in the IR. These diagnostics are calibrated against local galaxies, where the star forming environment could be drastically different from the star forming environment typical of distant galaxies, and for which the application of local metallicity diagnostics may not be appropriate. It is still interesting, however, to understand where and why the emission line models succeed or fail; to that end, we compare our model to as many observations of galaxies between redshifts 1 and 3 as possible.

In Fig. 3.21, we show several diagnostic diagrams with a sample of intermediate and high redshift galaxies compiled from Stark et al. (2014) (black circles) and Christensen et al. (2012) (white diamond). The C IV λ1548, [Si III] λ1883, [O III] λ1666, C III] λ1906 emission

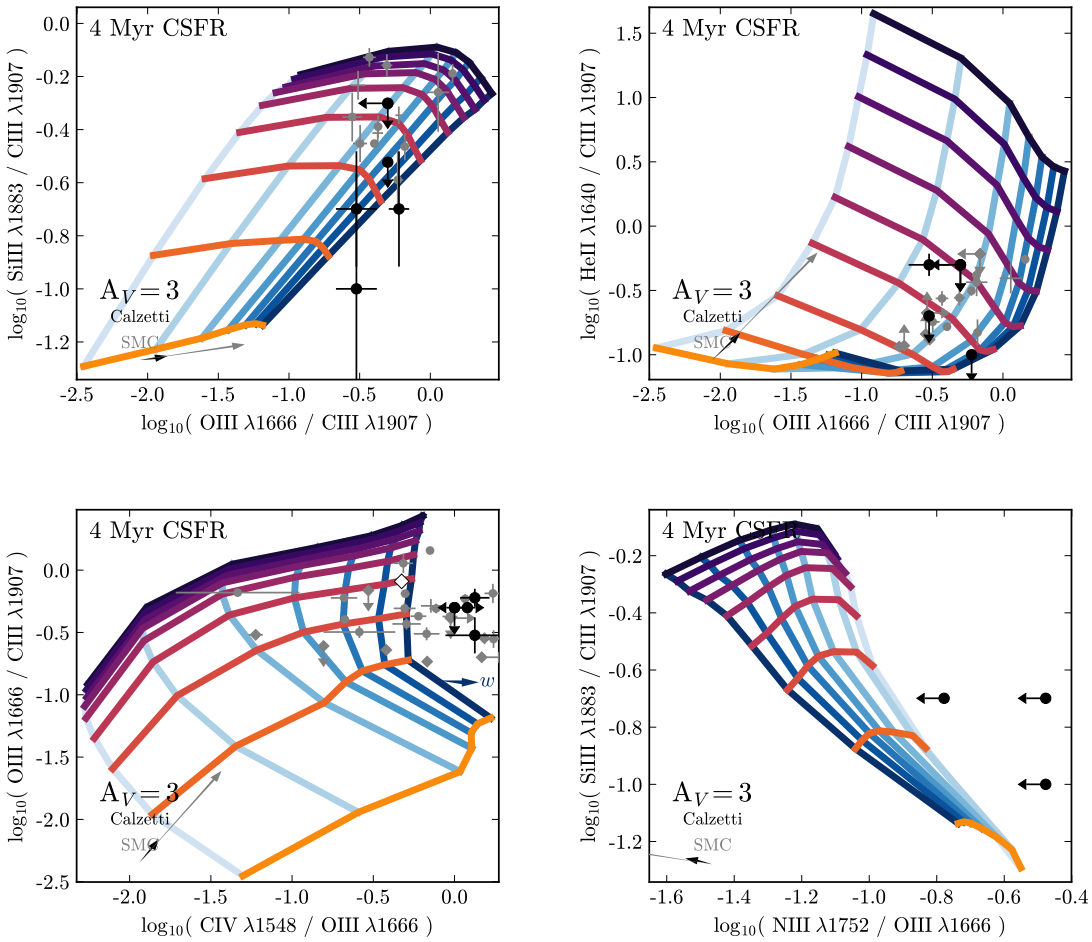

Figure 3.21 The Stark et al. (2014) galaxies at $z\sim2$ (solid black circles) compared to UV diagnostic diagrams assuming a 4 Myr stellar population with constant SFR. The Berg et al. (2016) local BCD sample (grey circles) is included in the upper left, upper right, and lower left diagrams; the Senchyna et al. (2017) local BCD sample (grey diamonds) is included in the lower left diagram. Stellar wind emission can inflate the measured CIV1548 flux, we indicate the direction of this with the blue arrow. The grey and black arrows show three magnitudes of extinction assuming SMC and Calzetti reddening laws, respectively.

lines are measured in both the local galaxy sample from Berg et al. (2016) and the lensed $z\sim3$ galaxy sample from Stark et al. (2014). We include the local galaxy observations in Fig. 3.21 as grey circles. Stark et al. (2015) provides lower limits on the [Si III] λ1883 emission line in cases where it was not detected based on observational limits.

In the Si3C3 vs. O3C3 diagram in Fig. 3.21 (*upper left*), all of the high redshift galaxies have emission line ratios consistent with the model predictions. Overall, the line ratios for the high redshift galaxies tend toward higher ionization parameters and slightly higher metallicities than the local sample. This trend is likely driven entirely by the strength of the C III] line, which is notably large in many of the high redshift galaxies (Stark et al., 2014), but variations in [Si III] λ1883 (an α-element) could also play a role. Again, the shift towards higher ionization parameters and higher metallicities in the high redshift sample compared to local BCDs is not unexpected, given the bias toward more massive, high SFR galaxies in the former.

We show [He II] λ1640/C III] λ1907 ratio (He2C3) vs. the [O III] $lambda$1666/C III] λ1907 ratio (O3C3) in the upper right panel of Fig. 3.21. All of the high redshift galaxies have emission line ratios consistent with the model predictions. The high redshift galaxies and the local galaxies occupy similar regions of the diagram, with no clear offset in metallicity or ionization parameter. However, all of the observations lie near models with higher metallicities than in previous diagnostic diagrams. The He2C3 ratio uses emission lines more widely spaced in wavelength than the other ratios in Fig. 3.21, which could indicate that reddening corrections are responsible for the shift.

In the C4O3 vs. O3C3 diagram in Fig. 3.21 (*lower left*), the high redshift galaxies occupy a region entirely beyond the model grid with large values of C4O3. The range of observed C4O3 and O3C3 values in the high redshift galaxies are consistent with values observed in the local galaxy sample from Berg et al. (2016) and Senchyna et al. (2017), though the local sample extends to lower values of C4O3 and has a wider range in O3C3. These differences are not entirely unexpected, since the high redshift sample is smaller and necessarily probes the brightest observable targets. The high C4O3 ratios observed in the high redshift sample

may support the idea that high redshift galaxies have on average "harder" ionizing spectra. Though we again note the important contribution stellar winds make to the C4O3 ratio, as noted by the blue arrow and discussed in §3.4.1 (Fig. 3.17).

The NII]λ1750, 1752 emission doublet was not detected in any of the Stark et al. (2014) sample, but lower limits were provided based on observational constraints. Despite the current non-detection, with more sensitive facilities the NII]λ1750 / OIII]λ1666 line ratio (N2O3) could become a promising diagnostic when paired with Si3C3, which we show in the bottom right panel of Fig. 3.21.

3.5 Metallicity and abundance complications

In the previous sections, we used the abundances specified in §3.2.2 and assumed that the gas phase abundances track the stellar metallicity closely. In the early universe, however, these assumptions may not be appropriate in all cases. To explore this possibility, in this section, we modify the gas phase abundances from our original prescription and explore the resultant changes in emission line properties. We begin with a discussion of important gas coolants, carbon and nitrogen, before discussing more general implications of elemental abundance patterns.

3.5.1 Sensitivity to C/O prescription

Photoionization models must make various assumptions about the relative gas phase abundances of different elements. In general, nebular models assume that the abundances of all elements increase linearly with increasing metallicity. Specific choices are usually motivated by the desire to match the observed properties of samples of H II regions. Most emission line strengths will depend linearly on their elemental abundances, to first order, but variations in important gas coolants like C, N, and O have additional effects on the H II region structure and temperature, which in turn complicates the response of emission lines to changes in their abundances.

The treatment of relative elemental abundances is further complicated by the likelihood

that both C and N scale non-linearly with metallicity. Nitrogen has known secondary nucleosynthetic production at high metallicity, wherein nitrogen is dredged up during the bottleneck step of the CNO cycle, which is directly dependent on metallicity. In the case of carbon, the triple-α process is the only known production process, but it does not depend on metallicity. Instead, additional carbon is produced through metallicity-dependent processes such as stellar winds, rather than a nucleosynthetic process. Thus, carbon is said to have a "pseudo-secondary" production process.

Nitrogen abundances are relatively easy to determine for local galaxies with optical spectra, and the relationship between N/O with metallicity has been well-studied (e.g., Garnett, 1990; van Zee et al., 1998a; Berg et al., 2012). Based on existing data, most photoionization models adopt a functional form for the relationship between the oxygen abundance and the N/O ratio that matches observations of local dwarf galaxies, massive extragalactic H II regions, and starburst nucleus galaxies.

The C/O relationship is particularly relevant to this work, since C III] is one of the strongest emission lines in the UV and is included in many of the emission line diagnostics presented in this work. Historically, carbon has been a difficult element to derive absolute abundances for, since few strong transitions exist in the optical or IR, and the optical recombination lines (RLs) become too faint to detect below $12 + \log(O/H) = 8$ (Esteban et al., 2014).

Recently, Berg et al. (2016) analyzed the relationship of C/O with metallicity in low-metallicity galaxies using collisionally-excited lines (CELs) for C and O in the UV. Berg et al. (2016) found that the C/O ratio was roughly constant across the metallicity range of their sample ($7 < 12 + \log(O/H) < 8$). However, when combined with C/O measurements based on optical recombination lines from galaxies at higher metallicities, C/O appears to increase with metallicity above $12 + \log(O/H) = 8$. These data are shown in the right panel of Fig. 3.22.

In Fig. 3.22, we show the existing N/O (*left*) and C/O (*right*) measurements along with the relationships between N/O and C/O used here and in various other nebular models.

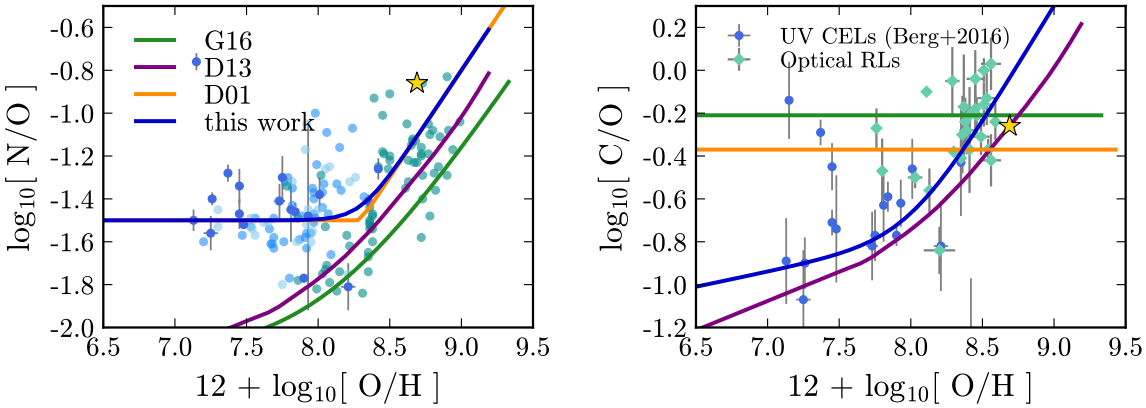

Figure 3.22 *Left:* N/O relationships used by different nebular models. The dark and light blue points are from Berg et al. (2016) and Berg et al. (2012). The grey points are massive extragalactic H II regions from van Zee et al. (1998a), used to calibrate the Dopita et al. (2013) and Dopita et al. (2000) models. The teal points are from Contini et al. (2002), part of the calibration sample used by Gutkin et al. (2016). *Right:* C/O relationships used by different nebular models. The blue points are from Berg et al. (2016), with C/O abundances derived from UV collisionally excited lines. The teal points are extragalactic recombination line estimates from Esteban et al. (2014). The gold star in both plots represents where the sun would be located according to the Asplund et al. (2009) solar abundance set.

For both N/O and C/O, we have modified the Dopita et al. (2013) prescription such that it plateaus for $12 + \log[O/H] \lesssim 8$ to better match observations. The exact functional form is given in Eqs. 3.1 & 3.2 in §3.2.2, and shown as the blue line in Fig. 3.22. As noted in Steidel et al. (2014), the precise behavior of the N/O ratio with metallicity depends on the calibration sample and the details of the methods used to measure the abundances, and unsurprisingly there is a substantial range in the N/O versus O/H relationships applied in recent literature.

The behavior of both the N/O and C/O ratio are important for the UV emission line

diagnostics presented in this work. In Fig. 3.23 we show how the C III] λ1907 emission line changes while varying C/O at constant oxygen abundance. The left panel of Fig. 3.23 demonstrates that at constant 12+log(O/H), while C III] λ1907 emission depends strongly on ionization parameter (varying from 10^{32} to 10^{36}ergs·s^{-1}), the strength of the line is essentially independent of the actual carbon abundance.

While C III] λ1907 is not a direct measure of the carbon abundance on its own, when C III] λ1907 is paired with [O III] λ1666 it becomes much more sensitive to the relative abundance of carbon. Fig.3.24 shows the [O III]/C III] emission line ratio as a function of ionization parameter and carbon abundance at constant $12 + \log_{10}(\mathrm{O/H})$. The decreasing abundance of carbon ultimately inhibits cloud cooling, which raises the temperature of the nebula slightly and produces variations in oxygen line strength at constant $12 + \log_{10}(\mathrm{O/H})$. The O3C3 line ratio is very sensitive to ionization parameter and the C/O ratio while being relatively insensitive to gas density.

Despite our modifications to previous abundance prescriptions, our nebular model still produces BPT diagram line ratios that are consistent with observations. In Fig. 3.25 we show model grids on BPT diagrams assuming the four different abundance prescriptions considered in Fig. 3.22: the abundance prescription used in this work, the Dopita et al. (2013) prescription ("D13"), the Dopita et al. (2000) prescription ("D00"), and the Gutkin et al. (2016) abundance prescription ("G16"). The models are run for identical input parameters and the only modification is the mixture of gas-phase abundances specified in Cloudy. However, the resultant model grids vary by 0.4 dex in [N II]/Hα.

The model presented here is able to reproduce the star-forming sequence quite well, while simultaneously producing UV emission line ratios consistent with observed galaxies. The other abundance prescriptions struggle with this: the Dopita et al. (2013) nitrogen abundances are too low to correctly reproduce the optical star-forming sequence, though they do well at predicting the UV C III] behavior. The Dopita et al. (2000) model is able to reproduce the optical star-forming sequence, but does not include the additional pseudo-secondary contribution for carbon needed to explain the UV observations.

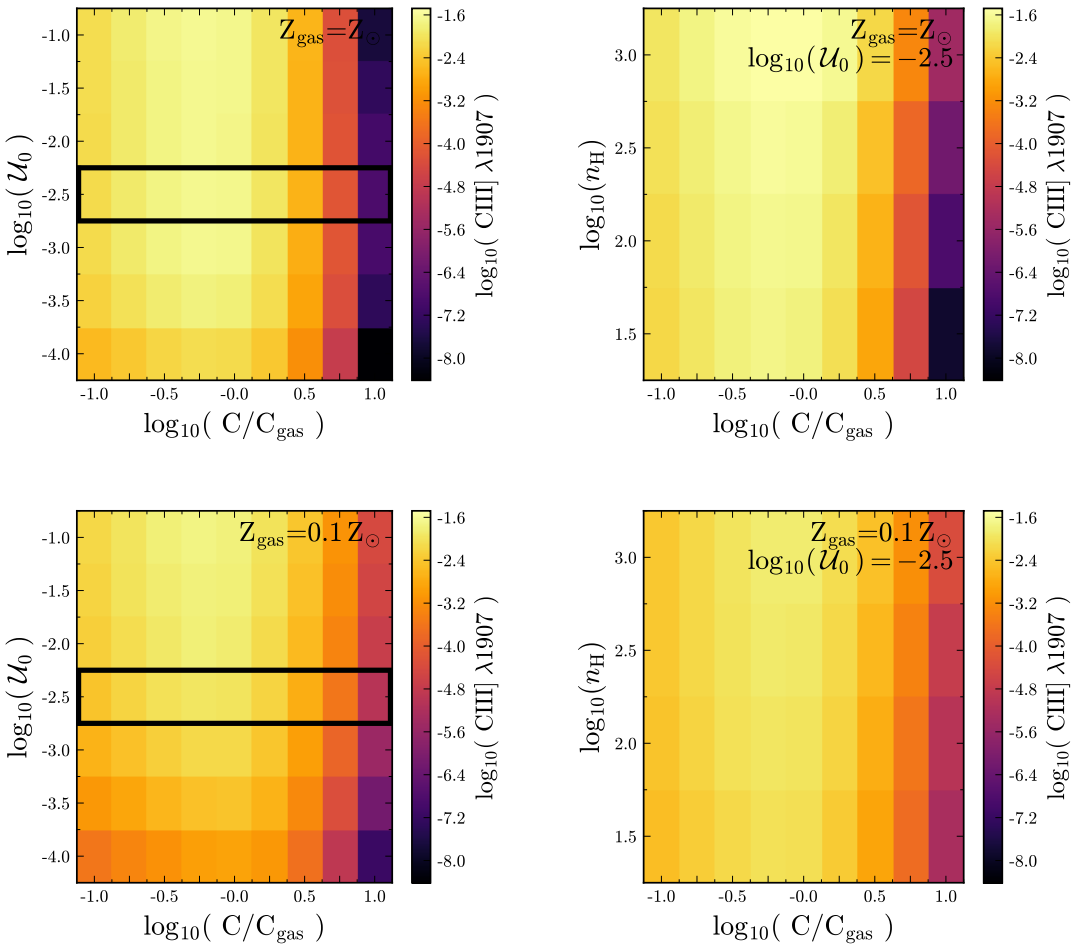

Figure 3.23 The variation in C III] λ1907 line strength as the abundance of C is changed at constant $12+\log[O/H]$ abundance. *Left:* The variation in C III] λ1907 strength as a function of ionization parameter and C abundance for a 4 Myr CSFR model with gas at solar (*top*) and 10% solar (*bottom*) metallicity. *Right:* The C III] emission strength for the same 4 Myr model at $\log_{10}\mathcal{U}_0 = -2.5$ as a function of gas density: $n_{\rm H} = 30$, 100, 300, 1000 cm^{-3}. C III] is sensitive to ionization parameter and moderately sensitive to gas density. C III] is sensitive to the overall gas phase metallicity; at fixed oxygen abundance, a two order of magnitude change in carbon abundance produces relatively little variation in line strength.

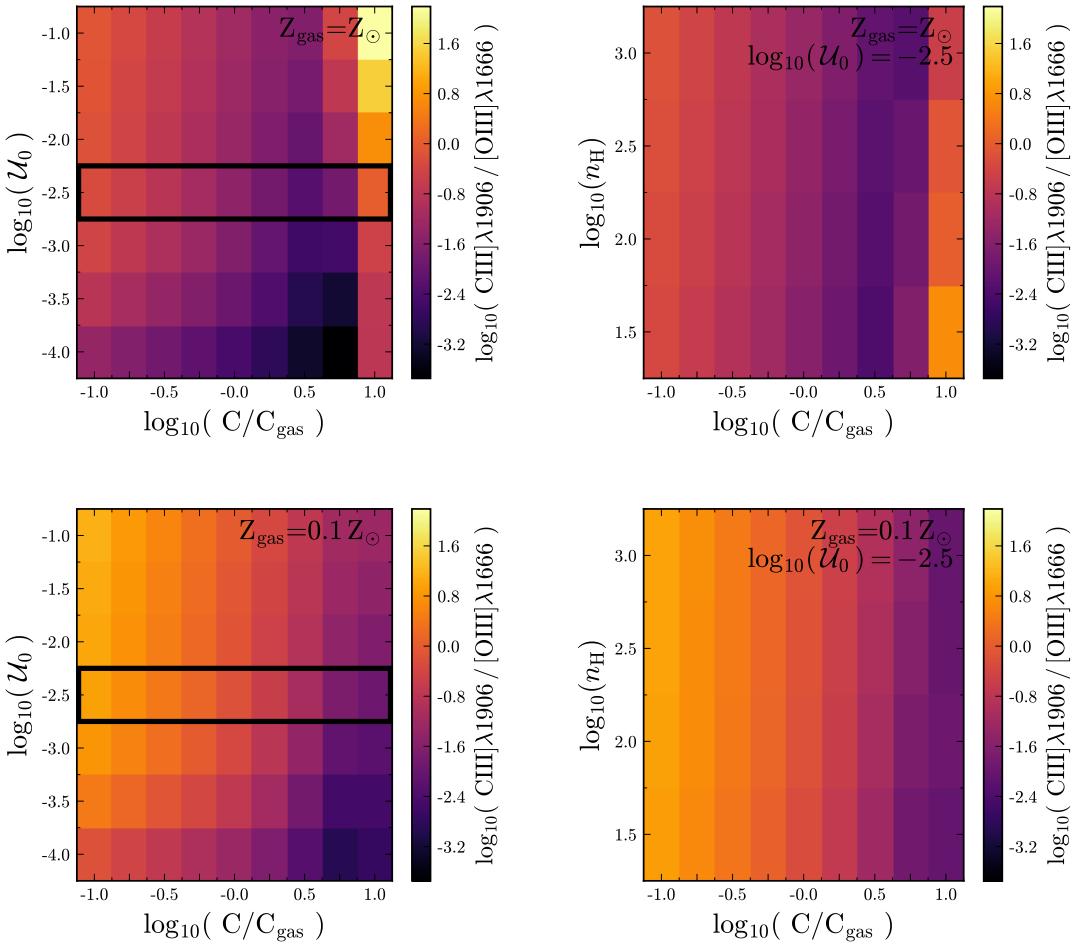

Figure 3.24 The variation in the [O III] λ1666/C III] λ1907 (O3C3) emission line ratio as the abundance of C is decreased at constant $12 + \log[O/H]$ abundance. *Left:* The variation in O3C3 as a function of ionization parameter and C abundance for a 4 Myr CSFR model with gas at solar (*top*) and 10% solar (*bottom*) metallicity. *Right:* The variation in O3C3 for the same 4 Myr model at $\log_{10}\mathcal{U}_0 = -2.5$ as a function of gas density: $n_{\rm H}$ = 30, 100, 300, 1000 cm^{-3}. The decrease in C abundance inhibits cloud cooling, raising the temperature of the nebula slightly, producing variations in oxygen line strength at constant $12 + \log[O/H]$. The O3C3 line ratio is very sensitive to ionization parameter, metallicity, and the C/O ratio while being relatively insensitive to gas density.

We note that Fig. 3.25 is only intended to highlight how changes in the adopted relative elemental abundances can change emission line ratio predictions. The behavior displayed in Fig. 3.25 is not representative of the other models' ability to reproduce observed line ratios, as each of these models can and does adequately reproduce the locus of star-forming galaxies through adopting different physical parameters than that used in `CloudyFSPS`. The grids shown in Fig. 3.25 use the elemental abundance prescriptions from the above models, but are all run using the specific combination of input parameters chosen for the `CloudyFSPS` nebular model.

This reflects the particular strengths of the different nebular models. The Dopita et al. (2013) models allow users to make use of different, non-Maxwellian electron velocity distributions in the nebula. The Gutkin et al. (2016) model is unique in that by design it does *not* fix the C and N abundances to solar-scaled values and allows them to be varied to produce arbitrary C/O and N/O ratios. This makes their model uniquely qualified to understand the behavior of C/O and N/O "outliers".

We show the model grids with different abundances on alternative emission line diagnostic diagrams in Fig. 3.26 and Fig. 3.27 to highlight how the different abundance prescriptions change the model grid. The abundance prescription used in this work produces optical line ratios that are well-matched with observed galaxies. To show where observed galaxies lie in each of these diagnostic diagrams, we include a 2D histogram showing the number density of star forming galaxies, as done in Byler et al. (2016). The star-forming galaxy sample is derived from galaxy spectra from the Sloan Digital Sky Survey Data Release 7 (SDSS DR7; York et al., 2000; Abazajian et al., 2009) and emission line fluxes measured from the publicly available SDSS DR7 MPA/JHU catalog (Kauffmann et al., 2003a; Brinchmann et al., 2004; Salim et al., 2007). We use the emission line sample presented in Telford et al. (2016), briefly summarized here. The sample includes $\sim 135,000$ galaxies with redshifts between 0.07 and 0.30. Galaxies are required to have S/N of 25 in the Hα line, 5 in the Hβ line, and 3 in the [S II] lines. Emission line fluxes are corrected for dust extinction using the Balmer decrement and the Cardelli et al. (1989) extinction law, assuming $R_V = 3.1$ and an intrinsic Balmer

decrement of 2.86. AGNs are removed from the sample according to the empirical BPT diagram classification of Kauffmann et al. (2003b).

3.5.2 Decoupled gas and stellar metallicities

Our models assume that the massive stars that dominate the UV stellar continuum have the same metallicity and abundance pattern as the gas that they ionize. However, there are scenarios in which it is possible that the gas phase abundances differ from the stellar abundances. These include the injection of metal-enriched gas from stellar outflows or the rapid accretion of metal-poor gas during fueling of a star formation event. The latter of these would likely be most important during early epochs of star formation, with high gas inflow rates, which would be required for accretion to dilute the gas on $< 10\,\mathrm{Myr}$ timescales. Early star formation could also take place in gas enriched in α-elements, due to the reduced fraction of Type Ia supernovae (SNe).

Recently, Steidel et al. (2016) have suggested that the stellar and gas phase abundances should be decoupled due to the α enhancement of the gas relative to the stellar population. In their scenario, to first order, the stellar metallicity will follow the iron abundances while the gas metallicity should follow the measured oxygen abundances. From Salpeter IMF-averaged yields for O/Fe based on core collapse supernovae, Steidel et al. (2016) estimates that this could produce nebular oxygen abundances that are 4-5 times larger than the stellar Fe-based metallicity.

We have generated models where both the gas and stellar abundances are allowed to vary to explore the observable consequences of this choice.

We cannot self-consistently model $\alpha-$enhanced gas, since the MIST models used in this work for the stellar ionizing spectrum rely on solar-scaled abundances. To mimick the effects of $\alpha-$enhancement, we thus decouple the stellar metallicity from the gas phase metallicity and allow the relative gas phase abundances to increase above the stellar abundances. This will "enhance" the gas in α-elements like O, Mg, Al, Ti, and Si, but will also enhance Fe-peak elements in the gas. We do not expect this to change the results qualitatively, since Fe does

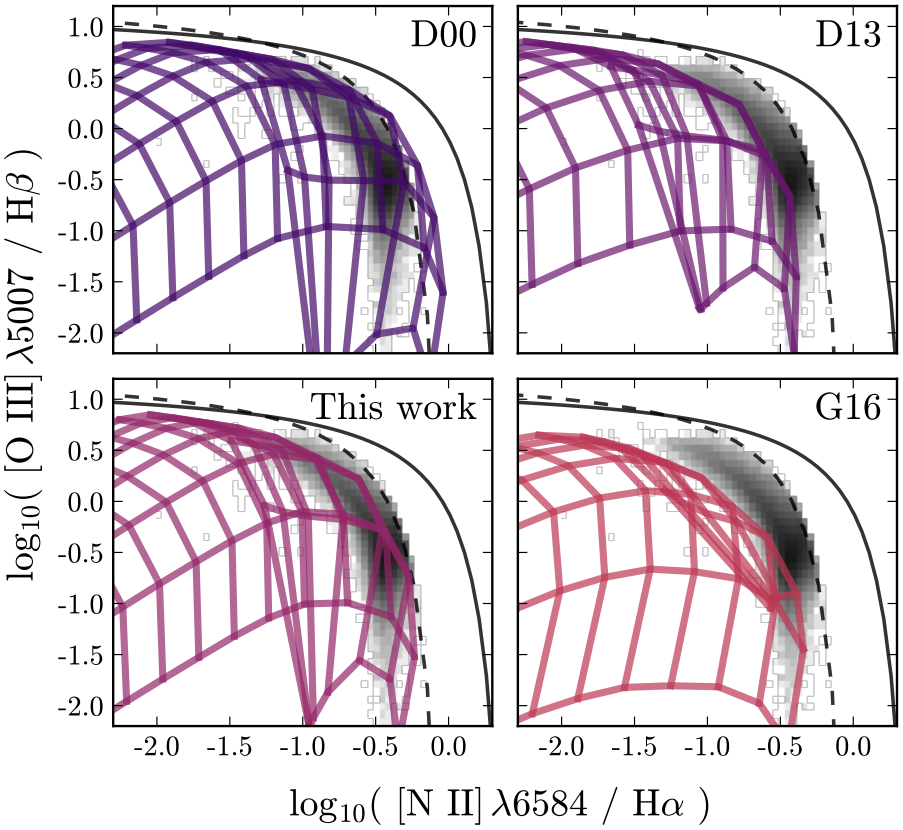

Figure 3.25 Model grids on the standard BPT diagram. The greyscale 2D histogram shows the number density of SDSS star-forming galaxies from the Telford et al. (2016) sample. All models assume a 1 Myr instantaneous burst and otherwise identical input parameters. Each panel represents a model run with a different abundance prescription, as noted in the upper right corner of each plot, and shown in Fig. 3.22. Changing the behavior of the N/O ratio relative to solar at a given [O/H] shifts the [N II]/Hα emission line ratio and the location of the models in a BPT diagram.

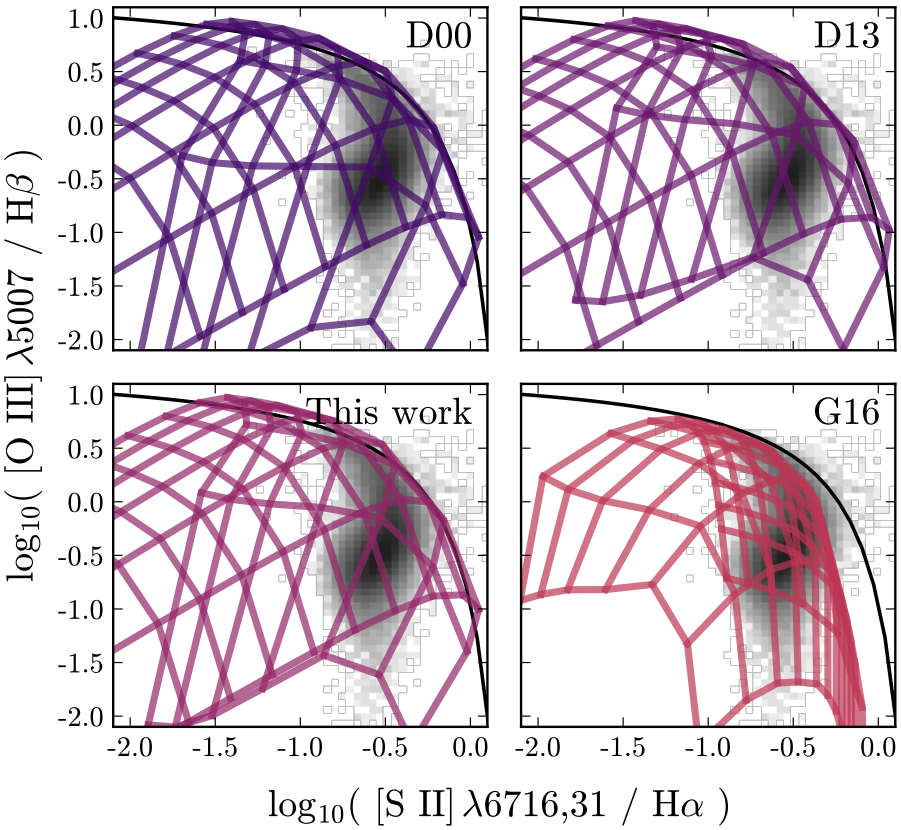

Figure 3.26 Model grids on a diagnostic diagram. The greyscale 2D histogram shows the number density of SDSS star-forming galaxies from the Telford et al. (2016) sample. All models assume a 1 Myr instantaneous burst and otherwise identical input parameters. Each panel represents a model run with a different abundance prescription, as noted in the upper right corner of each plot, and shown in Fig. 3.22.

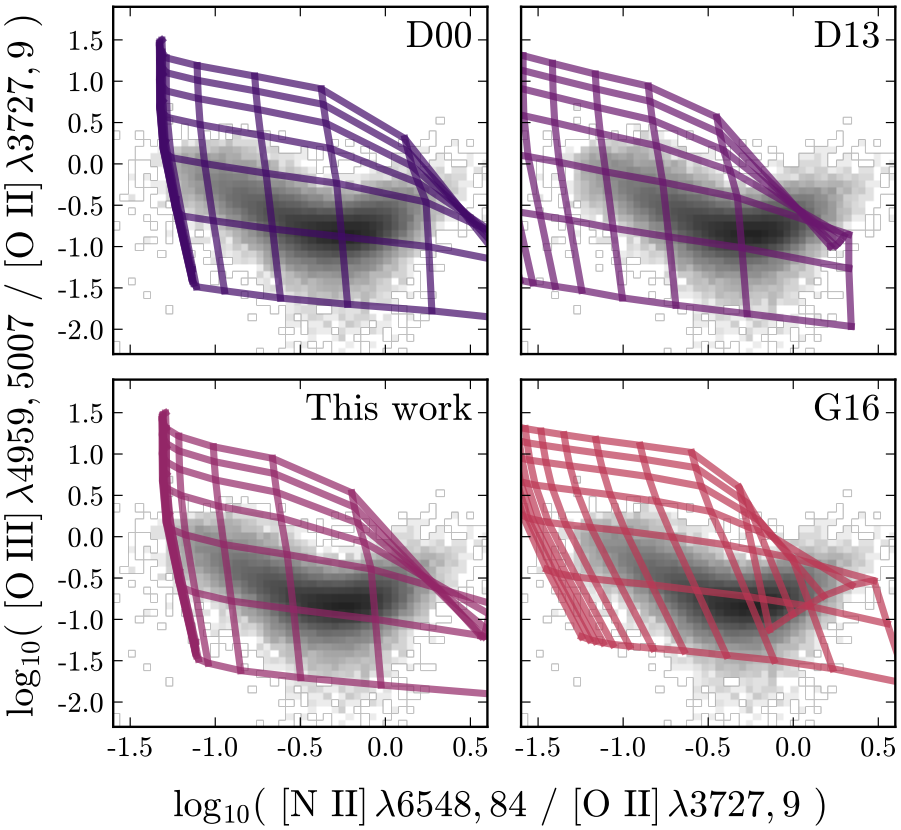

Figure 3.27 Model grids on a diagnostic diagram. The greyscale 2D histogram shows the number density of SDSS star-forming galaxies from the Telford et al. (2016) sample. All models assume a 1 Myr instantaneous burst and otherwise identical input parameters. Each panel represents a model run with a different abundance prescription, as noted in the upper right corner of each plot, and shown in Fig. 3.22.

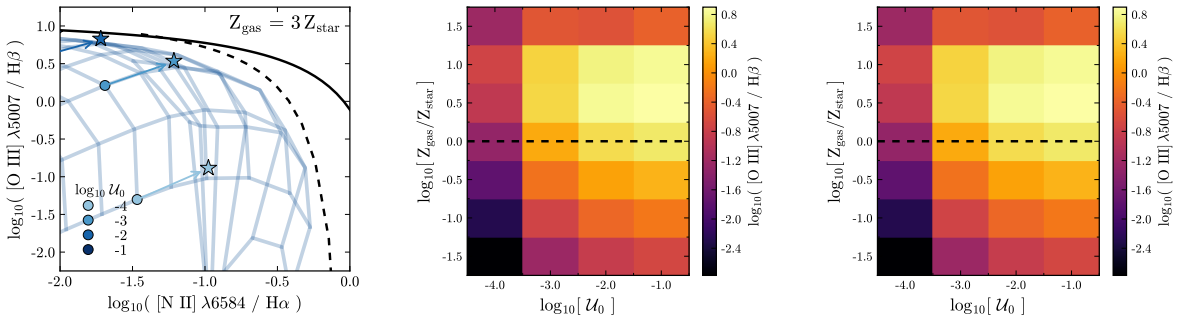

Figure 3.28 Impact of varying the gas phase metallicity (Z_{gas}) for a fixed stellar metallicity (Z_{star}; $\log_{10} Z/Z_\odot = -1$). *Left:* The standard BPT diagram. The blue lines show a standard model grid varying in ionization parameter and metallicity, where $Z_{gas} = Z_{star}$. The markers show the models where Z_{gas} is decoupled from Z_{star}. All model points assume the same ionizing spectrum: a stellar population with constant SFR over 4 Myr and $\log_{10} Z_{star}/Z_\odot = -1$. The color of the markers represent models with different ionization parameters. The circular marker shows the location where the gas phase metallicity equals the stellar metallicity, Z_{gas} =Z_{star}. The star-shaped marker shows the "enriched model" ($\log_{10} Z/Z_\odot = -0.5$; $Z_{gas} = 3\,Z_{star}$). *Center & Right:* The [N II]/Hα (*center*) and [O III]/Hβ (*right*) line ratios as a function of Z_{gas} and ionization parameter. The dashed line indicates where $Z_{gas} = Z_{star}$. Both line ratios increase as the gas metallicity is enhanced.

not play a large role in determining the thermodynamics of the gas.

We first model the "enriched gas" scenario by pairing a low-metallicity SSP ($\log_{10} Z/Z_\odot = -1$) with moderate metallicity gas ($\log_{10} Z/Z_\odot = -0.5$). These values are motivated by Steidel et al. (2016), who found that abundance determinations sensitive to stellar photospheric line blanketing features gave a metallicity of $\log_{10} Z/Z_\odot = -1$ while nebular emission lines, primarily optical oxygen and nitrogen lines, gave a metallicity of $\log_{10} Z/Z_\odot = -0.4$, or $Z_{gas} = 4\,Z_{star}$.

We show the models with decoupled gas and stellar metallicities in Fig. 3.28. These decou-

pled models reflect responses to gas inflow or localized enrichment with the same abundance pattern, or alternatively, can reflect abundance differences between the gas and stars in part due to the different elements that dominate the ISM cooling and emission lines and the stellar atmosphere.

For a fixed ionizing spectrum, an enhanced gas phase metallicity shifts line ratios to larger [N II]/Hα and [O III]/Hβ ratios by $\sim$1 dex at all ionization parameters. This shift occurs because the metal-poor ionizing spectrum is harder and provides more ionizing photons, while the gas enriched in N and O produces larger BPT line ratios. This shift would be consistent with observations of galaxies at high redshift, which show extreme BPT line ratios, particularly at high [O III]/Hα. Decoupling the gas and stellar metallicities is thus an enticing explanation for the optical emission lines.

Unlike the optical, where [O III] is one of the strongest optical emission lines, the C III] $\lambda\lambda$1907,9 doublet is the strongest UV emission line after Lyα. In Fig. 3.29 we show how C III] λ1907 emission responds to a change in gas phase metallicity for a fixed stellar metallicity of $\log_{10} Z/Z_{\odot} = -1$. C III] λ1907 is very sensitive to ionization parameter and weak at high metallicities. In an enriched gas model ($Z_{gas} > Z_{star}$) we would expect C III] λ1907 to be weaker and the ratio of [O III] λ1666/C III] λ1907 to be weaker. This is in conflict with observations, which show strong C III] λ1907 emission and strong [O III] λ1666/C III] λ1907 ratios, implying gas phase oxygen abundances at or below $12 + \log_{10}(O/H) \sim 8$. Explaining the extreme [O III]/Hα ratios and C III] emission in objects at high redshift may require a combination of α-enhancement and elevated N/O abundances.

3.6 Feasibility Estimates

In this section we discuss the feasibility of measuring important UV lines with existing and planned observatories. We quantify the utility of the diagnostics from §3.4 with the launch of JWST, which will provide rest-frame UV spectra of galaxies at $z \geq 4$, and we identify potential diagnostics for the redshift ranges probed by the JWST spectrograph.

In Fig. 3.30, we show observable UV emission lines as a function of the desired redshift

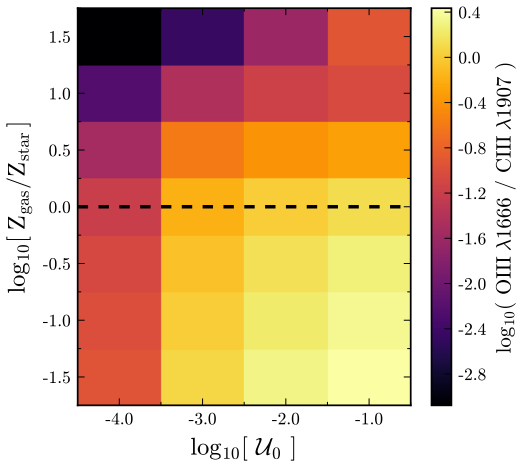

Figure 3.29 Changes in the [O III]/C III] ratio from varying the gas phase abundances (Z_{gas}) at fixed stellar metallicity (Z_{star}; $\log_{10} Z/Z_{\odot} = -1$). The dashed line indicates where the stellar and gas phase metallicities are equal. Unlike the BPT line ratios shown in Fig. 3.28, which increase as Z_{gas} gets larger than Z_{star}, the [O III]/C III] ratio is largest when $Z_{gas} \lesssim Z_{star}$.

range to be probed with JWST. Each emission line is color-coded by its strength relative to Hβ for a fiducial model assuming a 4 Myr constant SFR, $\log_{10}\mathcal{U}_0 = -2.5$ and $\log_{10}\mathrm{Z}/\mathrm{Z}_\odot = -0.5$, so users can determine the brightest emission lines in their desired redshift range. We also highlight the range of redshifts where each of the emission line ratios presented in Table 3.4 are observable.

For the highest redshift galaxies expected to be discovered with JWST, $7 < z < 10$, low-resolution spectroscopy ($R \sim 10 - 100$) can be obtained with NIRSpec (Levesque, 2015), allowing for the detection of the brightest emission lines like C III] $\lambda\,1906, 1909$ and [O III] $\lambda\,1661, 1666$. In this regime, the O3C3 emission line ratio and the slope of the UV continuum are likely to be the most useful probes of the ISM properties.

For galaxies between $5 < z < 7$, NIRSpec will provide mid-resolution ($R \sim 1000$) spectroscopy for reasonable exposure times. This is high enough resolution to employ most of the diagnostic diagrams presented in this work, including O3C3, Si3C3, S3C3, Si3N3, S3O3, and N3O3. These diagnostics are sensitive to ionization, metallicity, and the underlying stellar population, which we can use to understand and distinguish the ISM properties of galaxies during the epoch of their formation.

For a smaller subset of galaxies, high-resolution ($R \sim 2700$) spectra can be obtained. These spectra will be able to resolve stellar absorption features, enabling the simultaneous study of the nebular emission and stellar population. In this regime, the diagnostics combining emission and absorption features will provide insight into the conversion of gas into stars, stellar feedback and chemical enrichment.

3.7 Conclusions

We build upon the nebular model framework established in Byler et al. (2016), extending the self-consistent predictions for nebular line and continuum emission from stellar populations into the UV regime. Our conclusions are as follows:

- We have identified UV emission lines that are bright and correlate strongly with bulk

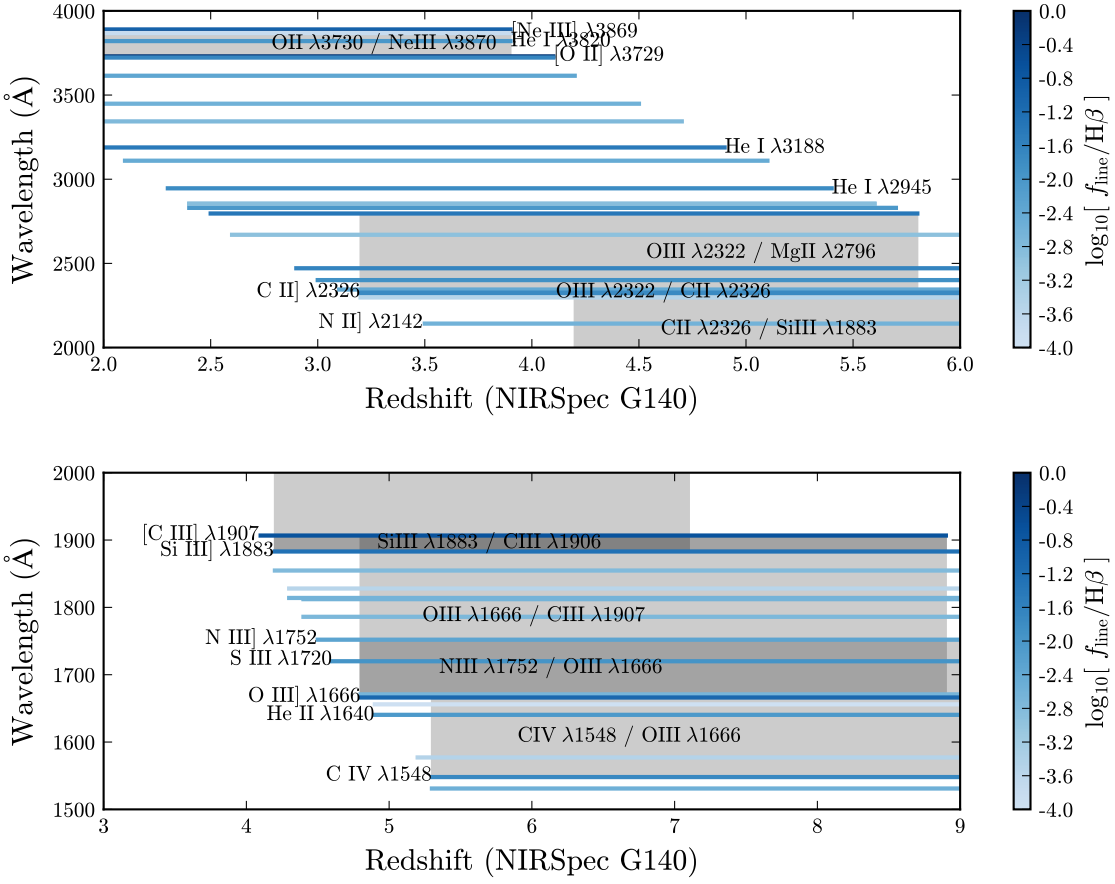

Figure 3.30 We show the relevant redshift ranges observable with JWST's NIRSpec instrument with the G140 grating. Each line is color-coded by its luminosity compared to the luminosity of Hβ, assuming a 4 Myr constant SFR population with $\log_{10} \mathrm{Z}/\mathrm{Z}_{\odot} = -0.5$ and $\log_{10} \mathcal{U}_0 = -2.5$.

physical properties of the nebula like the gas phase metallicity and the hardness and intensity of the ionizing spectrum. We provide predicted UV emission line fluxes as a function of metallicity and ionization parameter in a machine-readable format.

- We distinguish combinations of emission lines that will be useful diagnostics for bulk properties like metallicity and ionization parameter. These emission line ratios are bright, relatively insensitive to reddening, and correlate with metallicity and ionization parameter.

- Unlike the optical portion of the spectrum, the stellar continuum in the UV is dominated by the same stars that are responsible for producing the ionizing radiation that drives nebular emission. We gain additional metallicity leverage by considering stellar absorption features as diagnostics. We determine which of the absorption line indices presented by Leitherer et al. (2011) are the most useful metallicity diagnostics and quantify the contribution from nebular emission to each absorption index.

- The metallicity of the short-lived massive stars that produce the UV continuum should be nearly identical to that of the surrounding nebula. The joint analysis of stellar and nebular features leverages our model's ability to self-consistently link the temporal and metallicity dependent changes in the stellar absorption features to the nebular emission lines. We identify combinations of stellar absorption features and nebular emission lines that can be used as metallicity and ionization parameter diagnostics.

- We evaluate the emission and absorption diagnostics by comparing them with observed galaxies. We confirm that the diagnostics can reproduce observed emission and absorption from a sample of local BCDs. For line ratios where the contribution from stellar wind emission plays a role in one of the emission lines (e.g., C IV or [He II]), the model predictions are unable to fully reproduce observations. We advise caution when interpreting line ratios where both emission lines could include a significant contribution

from stellar winds, like C IV/[He II].

- We verify that the diagnostics hold across redshift by comparing them with observations of high redshift galaxies. In general, the model grids are consistent within errors of high redshift observations.

- We explore the repercussions of decoupling the stellar metallicity from the gas phase metallicity. Pairing an ionizing spectrum for a metal-poor stellar population with gas enriched in N and O produces BPT line ratios that are 3 dex larger than if the metal-poor population was paired with similarly metal-poor gas. This may help explain the observations of objects at high redshift with "extreme" [O III]/Hα ratios. However, this explanation does not hold for extreme C III] emission, which is strongest when the stars and gas are similarly metal-poor.

- We discuss the importance of the relative elemental abundance prescriptions used in photoionization models. In particular, the applied relationship between nitrogen and carbon with metallicity ultimately dictates the model's ability to reproduce observed emission line ratios in various diagnostic diagrams. We apply relationships that specify the behavior of [N/H] and [C/H] with [O/H] that are designed to better match observed galaxies. Our model is able to simultaneously reproduce observed UV *and* optical emission line ratios, including the standard BPT diagram and its most common variants.

- We recommend diagnostics for the redshift ranges probed by the JWST spectrograph. The mid-resolution ($R \sim 1000$) spectroscopy that NIRSpec will provide for galaxies between $5 < z < 7$ is ideal for the use of the emission line diagnostics presented here, including O3C3, Si3C3, S3C3, Si3N3, S3O3, and N3O3.

It is a pleasure to thank Grace Telford and Claus Leitherer for helpful discussions informing the ideas presented here. Special thanks to JJ Eldridge, Mason Ng, and Georgie

Taylor for sharing with us unpublished WMBasic models (Eldridge et al., in prep); to Erika Zetterlund and Charles Danforth for sharing with us the reduced spectra from Zetterlund et al. (2015); and to Danielle Berg, for sharing with us unpublished emission line measurements (Berg et al., in prep). C.C. acknowledges support from NASA grant NNX13AI46G, NSF grant AST- 1313280, and the Packard Foundation. N.B. acknowledges support from the University of Washington's Royalty Research Fund Grant 65-8055.

Chapter 4

SELF-CONSISTENT PREDICTIONS FOR LIER-LIKE EMISSION LINES FROM POST-AGB STARS

In early type galaxies (ETGs), emission from warm ionized gas, characterized by Low Ionization Emission Regions (LIERs), was originally attributed to a central, low-luminosity active galactic nuclei. However, the recent discovery of spatially-extended LIER emission suggests ionization by something with a stellar-like radial distribution. For passively-evolving galaxies with old stellar populations, hot post-Asymptotic Giant Branch (AGB) stars are the only viable source of ionizing photons. In this work, we present the first prediction of LIER-like emission from post-AGB stars that is based on fully self-consistent photoionization modelling, as implemented in `CloudyFSPS`. We show that models where post-AGB stars are the dominant source of ionizing photons are able to reproduce the nebular emission signatures observed in ETGs. Our models produce LIER-like emission line ratios in standard optical diagnostic diagrams and produce Hα equivalent widths (EWs) of order 0.1-10Å, in agreement with observations. Models with with delayed-τ star formation histories with τ between 0 and 0.5 Gyr, ages between 2 and 13 Gyr and metallicities between $\log_{10} \mathrm{Z}/\mathrm{Z}_{\odot} = -1$ and 0.25 are able to reproduce LIER-like emission line ratios and EWs without any tuning. These same models accurately reproduce the UV and optical colors typical of the ETG population, and we discuss the implication for the stellar populations responsible for the UV-excess observed in some ETGs. Finally, we test the sensitivity of the post-AGB phase and the resultant LIER-like emission to the mass loss efficiency, convective mixing efficiency, and rotation rate used in the MIST isochrones. We find that increasing the mass loss efficiency factor can increase observed Hα EWs from post-AGB stars.

4.1 Introduction

Early type galaxies (ETGs) are usually assumed to be gas-poor, passively-evolving systems. However, we now know that ETGs can harbor reservoirs of diffuse ionized gas (Sarzi et al., 2006; Singh et al., 2013; Kehrig et al., 2012; Papaderos et al., 2013). The source of ionization in these systems has been under recent debate, with explanations that include the heat transfer from hot to cold gas (Heckman, 1981), shock waves (Koski & Osterbrock, 1976; Dopita & Sutherland, 1995; Allen et al., 2008), central active galactic nuclei (AGN; Ferland & Netzer, 1983; Halpern & Steiner, 1983; Heckman et al., 1998; Ho, 1999; Kauffmann et al., 2003b; Kewley et al., 2006; Ho, 2009), or evolved stellar sources (Binette et al., 1994; Taniguchi et al., 2000). However, current research supports the view that for most galaxies, the gas excitation is driven by photoionization from evolved stars and fast shocks on extended kpc scales, with additional contributions from low-luminosity AGN on nuclear scales (e.g., Pandya et al., 2017).

The low-ionization emission was originally discovered in the nuclear regions of galaxies, and then attributed to AGN-related activity. However, recent spatially resolved spectroscopy has revealed that low-ionization emission regions (LIERs) are not always centrally concentrated and instead can be spatially extended over ∼kpc scales (Belfiore et al., 2016; James & Percival, 2015; Gomes et al., 2016). While central LIER emission is likely still attributable to low-luminosity AGN activity (Sarzi et al., 2010; Belfiore et al., 2016; Kormendy & Ho, 2013; Pandya et al., 2017), it has been suggested that hot evolving stars, which are the primary source of ionizing photons when main sequence stars are absent, are responsible for the spatially-extended LIER emission (Binette et al., 1994; Stasińska et al., 2008; Sarzi et al., 2010; Yan & Blanton, 2012; Woods & Gilfanov, 2014; Johansson et al., 2016).

In the quiescent stellar populations that dominate ETGs and spiral bulges, the source of ionizing photons cannot be young massive stars. Instead, the ionization is likely due to evolving low- and intermediate-mass stars. There are two main candidates for stars that are hot enough and either luminous or numerous enough to power significant ionization. The

first is extreme horizontal branch (EHB) stars, a sub-group of HB stars, the evolutionary stage immediately following the Red Giant Branch (RGB) phase. Stars with initial masses between 0.8 and 2 $M_\odot$ undergo a helium flash and begin core-helium fusion on the HB. Stars that have experienced more mass loss during their RGB evolution begin their HB phase with less massive hydrogen shells, producing hot or "extreme" HB stars. These stars are relatively faint when compared to other possible ionizing sources (50-100 $L_\odot$) but are very numerous and relatively long-lived, with lifetimes $\sim 10^8$ years.

The second stellar candidate is post-Asymptotic Giant Branch (AGB) stars, which are stars with initial masses between 0.8 and 8 $M_\odot$ that have left the AGB and are evolving horizontally across the HR diagram towards very hot temperatures ($\sim 10^5$ K) before cooling down to form white dwarfs. Although they are not as long-lived as EHB stars ($\sim 10^3 - 10^7$ years), post-AGB stars are much more luminous ($L_{bol} = 10^{2-4}\, L_\odot$) and possibly hotter (see reviews in O'Connell, 1999; Grevesse et al., 2010a; also Bressan et al., 2012).

As an ionizing source, the term "post-AGB" sometimes encompasses a broader category of hot evolving stars that includes early-AGB stars, AGB-Manque stars, pre-planetary nebulae and white dwarfs (Stasińska et al., 2008). Broader terms for this larger category include "hot old low mass evolved stars" (HOLMES; Cid Fernandes et al., 2011a) and "hot post-horizontal branch stars," (HPHB; Rosenfield et al., 2012).

These different subclasses include stars with a range of temperatures, luminosities, and lifetimes, not all of which are equally effective at driving ionization. They can however, produce significant UV flux longwards of 912Å, even for old stellar populations. This flux has been detected with facilities like GALEX, SWIFT, or IUE at low redshift, or with optical or NIR facilities for highly redshifted galaxies. In some cases the UV flux is seen to rise towards short wavelengths, in a phenomenon referred to as the "UV upturn".

The source of the UV-upturn phenomenon in ETGs is still debated, with suggestions that include a population of helium-rich stars or stars who have had their atmospheres stripped away through binary interactions. The manifestation of the UV upturn phenomenon is highly variable, occuring in roughly 3-10% of local ETGs (depending on selection criteria, see for

example Smith, 2014), independent of whether the ETG hosts LIER-like emission. Likewise, recent work has found that ETGs with similar morphologies and optical colors can display a wide range of NUV-optical colors (Yi et al., 2005; Kaviraj et al., 2007; Schawinski et al., 2007).

All of these UV-emission phenomena in old stellar populations (photoionization to produce LIER-like emission, UV upturn, diverse UV-optical colors) are likely to be driven by stars of similar masses ($\sim$3, 2, and 1 $M_\odot$ for 2, 6, and 12 Gyr old populations) given the rapidity of post-RGB evolution. As such, a self-consistent model of the stellar and nebular spectral energy distribution (SED) should be able to simultaneously reproduce the UV and optical colors and emission line ratios of LIER-like galaxies, if HPHB models are correct.

Calculating the needed self-consistent models of UV emission requires making predictions for the nebular emission produced by ionization from the hottest HPHB phases. Estimates of LIER-like emission based on the numbers of ionizing photons produced by post-AGB stars in stellar evolution models indicate Hα equivalent widths of order a few angstroms for ETGs (Maraston, 2005; Cid Fernandes et al., 2011b; Belfiore et al., 2016; Gomes et al., 2016). However, these current estimates are first-order calculations assuming case-B recombination for fixed-temperature gas. In Byler et al. (2016), we showed that accounting for temperature variations is essential when predicting emission line strengths. Accurate predictions of emission line luminosities and equivalent widths require the consideration of metallicity- and age-driven changes to the ionizing spectrum and metallicity-driven changes in the gas phase abundances.

There have been a few attempts to use photoionization modelling to explore the origin of LIER-like emission. In Byler et al. (2016), we demonstrated that our nebular model was able to reproduce LIER-like emission line ratios using older populations where hot evolved stars are the dominant ionization source. This work confirmed that current stellar evolution models and stellar atmospheres are capable of producing appropriately hard ionizing spectra. Similarly, Hirschmann et al. (2017) used old stellar populations to predict emission line ratios from evolved stars to explore the relative contribution from star formation, AGN, and post-

AGB stars to the cosmic evolution of the BPT emission line ratios. While the work in Byler et al. (2016) and Hirschmann et al. (2017) provides useful insight into the physical origin of observed optical line ratios, they do not reveal anything about the nature of LIER-like emission or post-AGB stars as ionizing sources, nor do they show simultaneous consistency with the broader UV emission from the larger HPHB population.

In this work, we present the first prediction of LIER-like emission from post-AGB stars that is based on fully self-consistent photoionization modelling. We build on the work from Byler et al. (2016), who paired the population synthesis models from the Flexible Stellar Population Synthesis code (FSPS; Conroy et al., 2009) with photoionization models from Cloudy (Ferland et al., 2013) to self-consistently model the flux from star-forming galaxies. As we show here, this model can simultaneously reproduce the nebular emission signatures of star forming galaxies and LIER-like emission signature observed in ETGs. We also show that this model accurately reproduces the UV and optical colors observed in the ETG population.

We describe the stellar and nebular model in §4.2. In §4.3, we introduce the ionizing radiation produced by hot evolved stars (§4.3.1) and the range emission line luminosities they produce (§4.3.2). To measure emission line equivalent widths we must correctly model the underlying stellar continuum, so we take a brief detour in §4.3.3 to demonstrate that our models reproduce observed ETG optical colors and absorption line properties. Then, in §4.3.4, we present equivalent width predictions and demonstrate that our models reproduce observed LIER-like equivalent widths. In §4.3.5, we show that our models produce LIER-like emission line ratios in various diagnostic diagrams. Finally, in §4.4, we discuss various UV emitting populations and their potential implication for the UV-excess observed in some ETGs. Our conclusions are summarized in §4.6.

4.2 Description of Model

We use the publicly available `CloudyFSPS`[1] from Byler et al. (2016) to compute the line and continuum emission for stellar populations from FSPS using the photoionization code Cloudy. The nebular model is described in detail in Byler et al. (2016), but we briefly summarize the process of generating model spectra in this section. We describe the stellar models in §4.2.1 and the nebular model in §4.2.2.

4.2.1 The stellar model

We generate the underlying stellar spectra using the Flexible Stellar Population Synthesis (FSPS) package[2] (Conroy et al., 2009) via the Python interface, `python-fsps`[3]. We assume a Kroupa initial mass function (IMF) (Kroupa, 2001) and use the default parameters in FSPS[4] unless otherwise noted.

We use evolutionary tracks from the MESA Isochrones & Stellar Tracks (MIST[5]; Dotter, 2016; Choi et al., 2016), single-star stellar evolutionary models which include the effect of stellar rotation. The evolutionary tracks are computed using the publicly available stellar evolution package Modules for Experiments in Stellar Astrophysics (MESA v7503; Paxton et al., 2011, 2013, 2015) and the isochrones are generated using Aaron Dotter's publicly available `iso` package on github[6]. A complete description of the models can be found in Choi et al. (2016), however, we describe some relevant model properties below, particularly those relevant to the HPHB phases.

The MIST models cover ages from 10^5 to $10^{10.3}$ years, initial masses from 0.1 to 300 $M_\odot$,

[1] Available on GitHub; a project description and instructions for use can be found at `http://nell-byler.github.io/cloudyfsps/`

[2] `https://github.com/cconroy20/fsps`

[3] `https://github.com/dfm/python-fsps`

[4] FSPS GitHub commit hash `3656df5`; `python-fsps` GitHub commit hash `57e59f7`

[5] Documentation, packaged model grids, and a web interpolator are available at `http://waps.cfa.harvard.edu/MIST/`

[6] available at `https://github.com/dotbot2000/iso`

and metallicities in the range of $-2.0 \leq [\mathrm{Z/H}] \leq 0.5$. The evolution is continuously computed from the pre-main sequence phase to the end of white dwarf (WD) cooling phase or the end of carbon burning, depending on the initial stellar mass and metallicity. Abundances are solar-scaled, assuming the Asplund et al. (2009) protosolar birth cloud bulk metallicity, for a reference solar value of $\mathrm{Z}_{\odot} = 0.0142$.

We are primarily concerned with the evolution of low- and intermediate-mass stars in this work, especially at late times; we briefly summarize key model parameters that affect the evolution of these stars. Mass loss for stars with initial masses below $10\,\mathrm{M}_{\odot}$ is treated with a combination of the Reimers (1975) prescription for the red giant branch (RGB) and the Bloecker (1995) prescription for the AGB. The MIST models adopt $\eta_{\mathrm{R}} = 0.1$ and $\eta_{\mathrm{B}} = 0.2$ to match the initial-final mass relation (Kalirai et al., 2009) and the AGB luminosity function (Rosenfield et al., 2014).

The post-AGB timescales in the MIST models are consistent with those calculated by Miller Bertolami (2016) and Weiss & Ferguson (2009), which are a factor of 310 times faster than older post-AGB stellar evolution models (Vassiliadis & Wood, 1994; Bloecker, 1995). Choi et al. (2016) noted that at late times (1 Gyr and beyond) the MIST predictions for FUV - V colors turn over toward bluer colors while the PARSEC/COLIBRI (Bressan et al., 2012; Marigo et al., 2013; Rosenfield et al., 2014) and BaSTI (Pietrinferni et al., 2004) predictions continue to get redder. The authors attributed this qualitative difference to the inclusion of post-AGB and WD phases in the MIST models, which are currently absent in the PARSEC and BaSTI models.

We combine the MIST tracks with a new, high resolution theoretical spectral library (C3K; Conroy, Kurucz, Cargile, Castelli, in prep) based on Kurucz stellar atmosphere and spectral synthesis routines (ATLAS12 and SYNTHE). The spectra use the latest set of atomic and molecular line lists and include both lab and predicted lines. The grid was computed assuming the Asplund et al. (2009) solar abundance scale and a constant microturbulent velocity of 2 km s^{-1}.

For very hot stars and stars in rapidly evolving evolutionary phases, we use alternative

spectral libraries. We focus on the libraries used for very hot stars in this work, since these will be responsible for providing the radiation necessary to ionize hydrogen. For main sequence stars with temperatures above 25,000 K (O- and B-type stars) we use spectra from M. Ng, G. Taylor & J.J. Eldridge (priv. comm), as described in Eldridge et al. (2017), using WM-Basic (Pauldrach et al., 2001). For Wolf-Rayet (WR) stars, we use the spectral library from Smith et al. (2002) using CMFGEN (Hillier & Lanz, 2001).

In this work, we are primarily interested in the hot, evolved stars that are capable of producing hydrogen-ionizing radiation. The post-AGB stars use non-LTE model spectra from Rauch (2003). We use the H-Ni composition library, which has two metallicities: solar and 10% solar. The 10% solar metallicity spectra are applied to populations with metallicities $\log_{10} \mathrm{Z}/\mathrm{Z}_{\odot} = -0.5$ and lower.

4.2.2 The nebular model

We use the Cloudy nebular model implemented within FSPS to generate spectra that include nebular line and continuum emission, described in detail in Byler et al. (2016). The nebular model is a grid in (1) simple stellar population (SSP) age, (2) SSP and gas-phase metallicity, and (3) ionization parameter, $\mathcal{U}_0$, a dimensionless quantity that gives the ratio of ionizing photons to the total hydrogen density.

The model uses FSPS to generate spectra from coeval clusters of stars, each with a single age and metallicity (SSPs). Using the photoionization code Cloudy, the SSP is used as the ionization source for the gas cloud and by default the gas-phase metallicity is scaled to the metallicity of the SSP. For each SSP of age t and metallicity Z, photoionization models are run at different ionization parameters, $\mathcal{U}_0$, from $\log_{10}\mathcal{U}_0 = -4$ to $\log_{10}\mathcal{U}_0 = -1$ in steps of 0.5. The resultant line and continuum emission is normalized by the number of ionizing photons calculated from the input ionizing spectrum. The normalized line and continuum emission are recorded in separate look-up tables.

For a given SSP (t, Z) and specified $\mathcal{U}_0$, FSPS returns the associated line and continuum emission associated with that grid-point from the look-up table. This approach maintains

the model self-consistency, such that the nebular emission is added to the same spectrum that was used to ionize the gas cloud. FSPS removes the ionizing photons from the SED to enforce energy balance; in this work we assume an ionizing photon escape fraction of zero.

4.2.3 Modifications for modelling LIER emission

The default settings of the `CloudyFSPS` model are most appropriate for modeling Strömgren sphere emission in H II regions powered by young massive stars. Extended LIER emission, however, has two significant differences we must account for. First, unlike young massive stars, we can no longer assume that the gas and ionizing stars have the same metallicity, given that the stars are much older than the surrounding gas. Second, the gas geometry is quite different. We discuss the modifications we have made to deal with these to issues.

Gas and star geometry

In Byler et al. (2016) we tested the sensitivity of emission line ratios to the assumed geometry by running models at several different ionization parameters, varying n_H from $10-1000\,\mathrm{cm}^{-3}$, and varying the inner radius of the gas cloud from $10^{18}-10^{20}\,\mathrm{cm}$ $(0.3-30\,\mathrm{pc})$. We found that the BPT line ratios produced by the post-AGB star models showed little sensitivity to the star-gas geometry, a result of our simplified model in which the gas exists in a plane-parallel shell surrounding a central point source of ionizing radiation. If the gas is produced by the AGB stars themselves or has a spatial distribution that differs from the distribution of stars, the geometry will differ substantially from the simplified shell used in this work.

The gas in early-type galaxies is much more diffuse and extended than that found in star-forming galaxies. Ionization parameters estimated from emission lines indicate much lower ionization parameters, $\log_{10}\mathcal{U}_0 = -5$ to $\log_{10}\mathcal{U}_0 = -3.5$, indicating that the gas has lower densities and is physically further from the ionizing sources than in star-forming galaxies (Yan & Blanton, 2012). Density estimates show typical gas densities of $10-100\,\mathrm{cm}^{-3}$ in elliptical galaxies, compared to the $10-1000\,\mathrm{cm}^{-3}$ more typical of star-forming galaxies.

Table 4.1. Solar Metallicity ($Z_\odot$) and Depletion Factors (D) adopted for each element for the MIST nebular model, which has $Z = 0.0142$ ($\log O/H = -3.31$ or $12 + \log O/H = 8.69$).

Element	$\log_{10}$[E/H]	$\log_{10}(D)$
H	0	0
He	-1.01	0
C	-3.57	-0.30
N	-4.60	-0.05
O	-3.31	-0.07
Ne	-4.07	0
Na	-5.75	-1.00
Mg	-4.40	-1.08
Al	-5.55	-1.39
Si	-4.49	-0.81
S	-4.86	0
Cl	-6.63	-1.00
Ar	-5.60	0
Ca	-5.66	-2.52
Fe	-4.50	-1.31
Ni	-5.78	-2.00

Note. — Solar abundances are from Grevesse et al. (2010a) and depletion factors are from Dopita et al. (2013).

To describe the star-gas geometry for H II regions, Byler et al. (2016) used $n_H = 100\,\mathrm{cm}^{-3}$ and $\mathrm{R_{inner}} = 10^{19}\,\mathrm{cm}$ ($\sim$3 pc). In this work we probe geometric extremes by running models with radii of R_{inner} = 3, 30, 300 pc (10^{19}, 10^{20}, 10^{21} cm) and n_H = 10,100 cm^{-3}. Achieving ionization parameters between 10^{-5} and 10^{-3} with the ionizing photon rates measured from the stellar population models, requires an initial stellar masses of $10^{6-8}\,\mathrm{M}_{\odot}$.

Stellar and gas phase abundances

For young stellar populations, the stars and the surrounding nebular gas should have nearly identical chemical compositions. In early type galaxies, it is much more likely that the interstellar gas has experienced significant processing over the several billion years since the formation of post-AGB star progenitors. The interstellar gas has been mixed with material lost through winds from low- and intermediate-mass stars, and enriched in carbon, nitrogen and dust. In this work, we assume that the gas in these systems is metal-rich, with a solar-like abundance pattern, given in Table 4.1. The same enriched gas phase abundances are used regardless of the stellar metallicity.

4.3 Ionization and emission associated with hot evolved stars

In this section we discuss the properties of the ionizing spectra and the emission lines they produce.

4.3.1 Ionizing properties of evolved stellar populations

In Fig. 4.1, we show the UV-optical spectrum produced by a 0.1 Gyr and 8 Gyr instantaneous burst populations. We note the ionization energy of Hydrogen and Helium, and the location of GALEX FUV and NUV and SDSS r-band filters. The top panel shows the total SED as a function of metallicity, from $\log_{10}\mathrm{Z/Z}_{\odot} = -2$ to $\log_{10}\mathrm{Z/Z}_{\odot} = 0.5$. The 0.1 Gyr population is more luminous and has bluer GALEX colors than the 8 Gyr population at all metallicities. At both ages, the metal-poor populations are hotter and have bluer GALEX colors than the

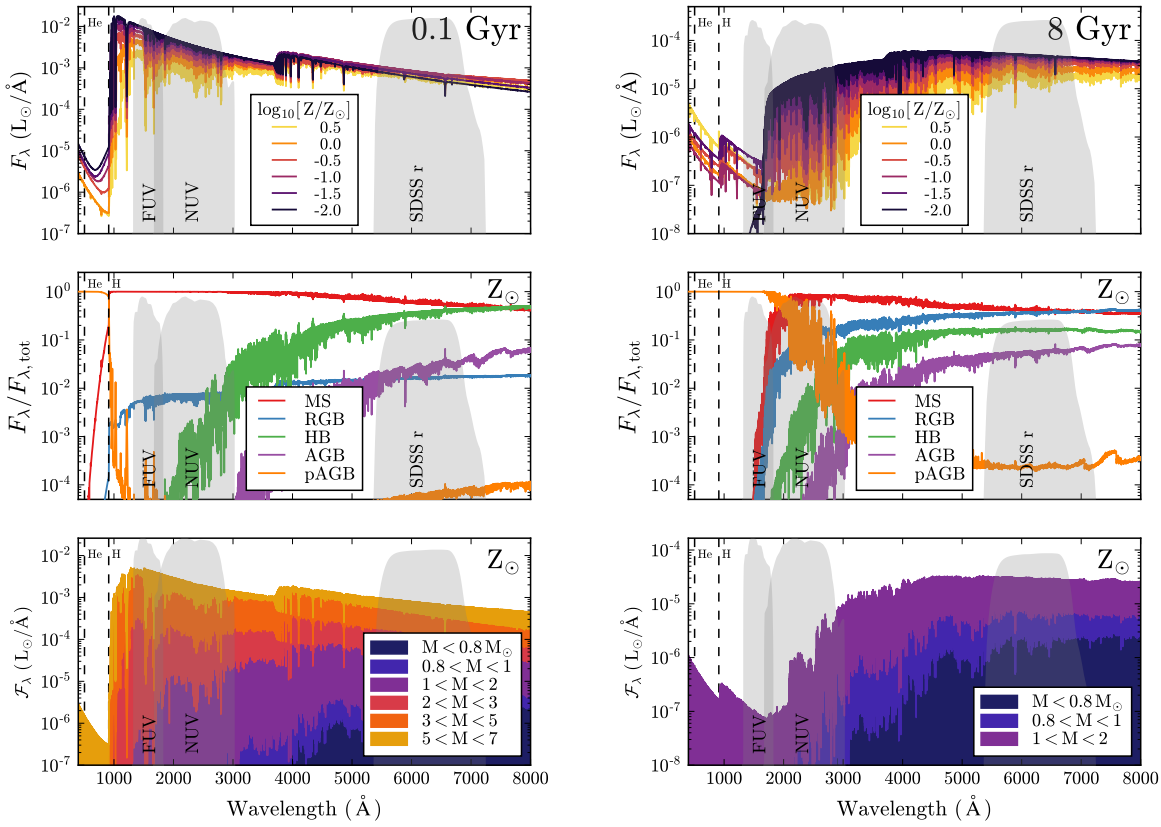

Figure 4.1 The UV-optical spectrum for an instantaneous burst at 0.1 Gyr (*left*) and 8 Gyr (*right*). In all panels, we overlay the transmission of the GALEX FUV, NUV and SDSS r-band filters, and the dashed lines indicate the ionization energy of helium ($E \geq 24.6\,\mathrm{eV}$ or $\lambda \geq 504\,\text{Å}$) and hydrogen ($E \geq 13.6\,\mathrm{eV}$ or $\lambda \geq 912\,\text{Å}$). *Top:* The total SED at several metallicities, from $\log_{10} \mathrm{Z/Z_\odot} = -2$ to 0.5. *Middle:* The fractional contribution of various evolutionary phases to the total SED for a solar metallicity population, including main sequence (MS), red giant branch (RGB), horizontal branch (HB), post-AGB (pAGB), and Wolf-Rayet (WR) stars. *Bottom:* For a solar metallicity SSP, the SED is now broken down by stellar mass.

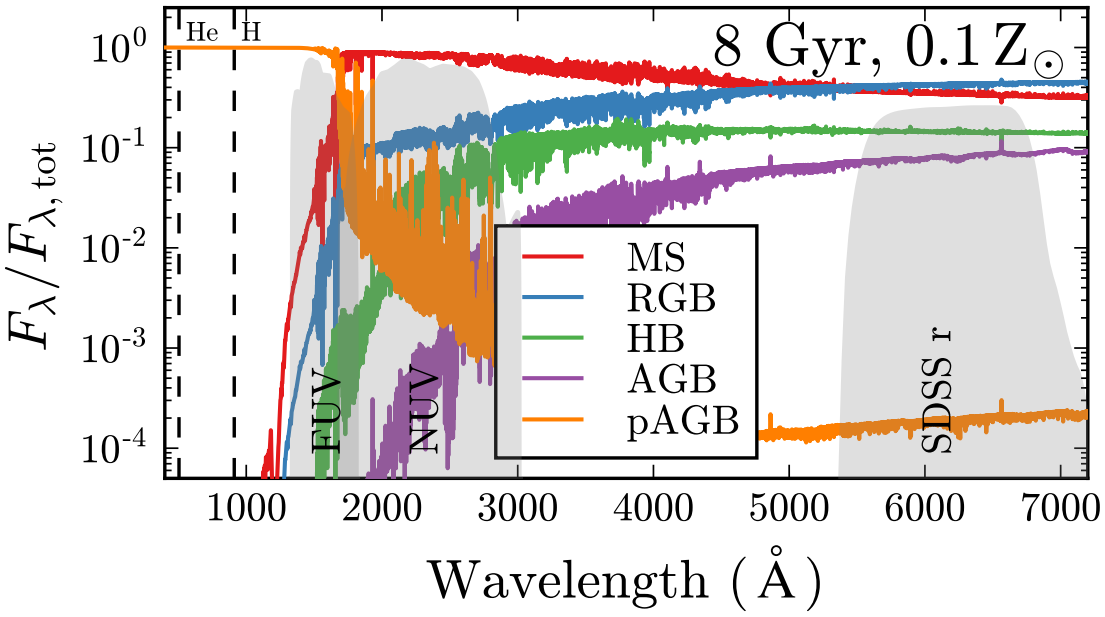

Figure 4.2 The ionizing spectrum from an 8 Gyr old burst ($\log t = 9.9$) at $\log_{10} \mathrm{Z}/\mathrm{Z}_\odot = -1$, showing the fractional contribution of different evolutionary types to the total flux. The vertical dashed lines show the ionization energy of helium ($E \geq 24.6\,\mathrm{eV}$ or $\lambda \geq 504\,\text{Å}$) and hydrogen ($E \geq 13.6\,\mathrm{eV}$ or $\lambda \geq 912\,\text{Å}$). The grey shaded region shows the transmission of the GALEX FUV, NUV and the SDSS r-band filters.

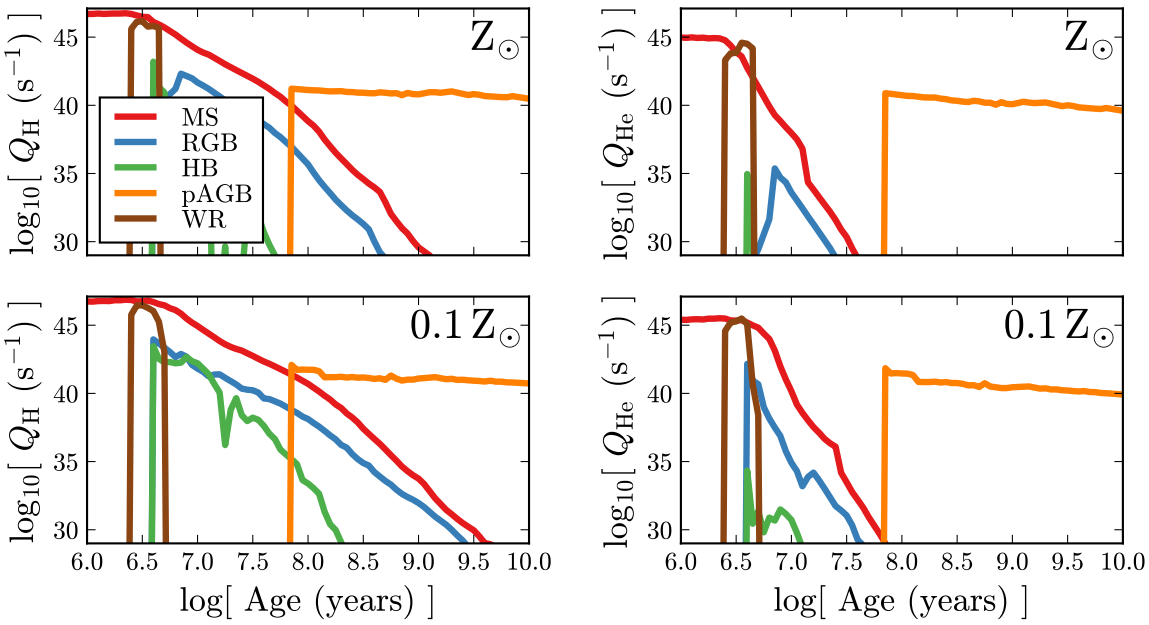

Figure 4.3 *Left column*: The ionizing photon flux per unit stellar mass for Hydrogen, $Q_{\rm H}$, as a function of time for different stellar types at solar metallicity (*top*) 1/10 solar (*bottom*) for instantaneous burst populations. *Right column*: The ionizing photon flux per unit stellar mass for Helium, $Q_{\rm He}$, as a function of time for different stellar types at solar metallicity (*top*) 1/10 solar (*bottom*) for instantaneous burst populations. The evolutionary phases shown include the Main Sequence (MS), Red Giant Branch (RGB), Horizontal Branch (HB), post-AGB (pAGB), and Wolf-Rayet (WR) stars. After the massive main sequence and WR stars have died, post-AGB stars provide the bulk of the ionizing radiation. These stars are hot enough to ionize both hydrogen and helium, but produce ionizing photon rates that are 10^5 times lower than MS stars, requiring large numbers of stars to produce substantial Hα flux. Binary evolution can potentially extend the initial ionizing phase to $\sim 10 - 15\,$Myr.

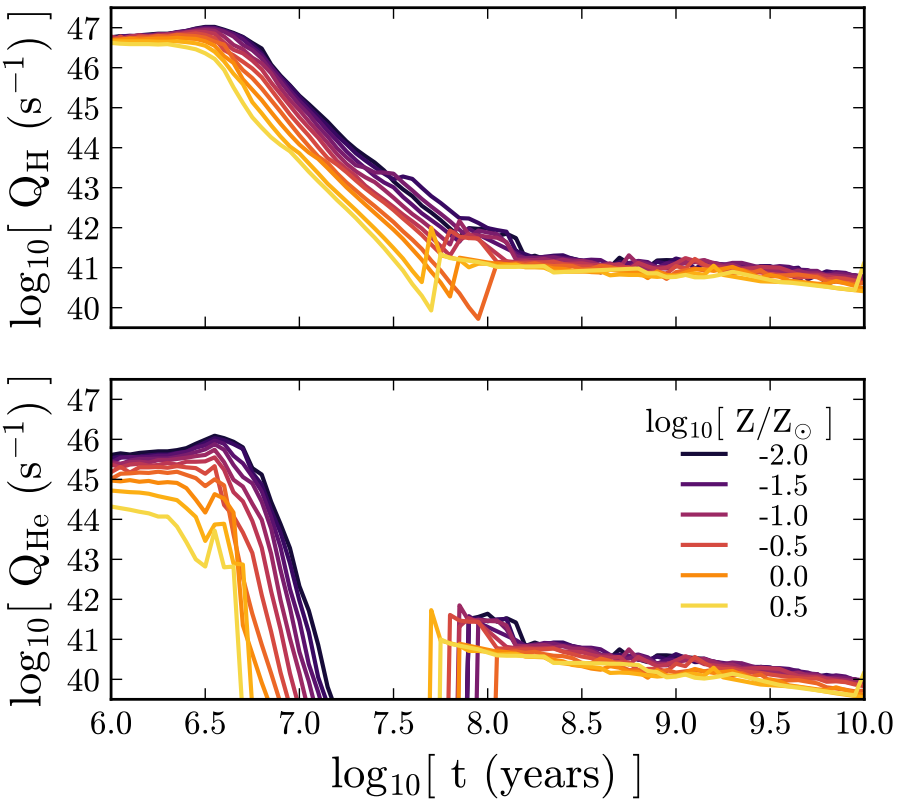

Figure 4.4 *Top*: The ionizing photon flux per unit stellar mass, $Q_{\rm H}$, as a function of time for stellar populations with metallicities varying from $\log_{10} {\rm Z/Z}_\odot = -2$ to $\log_{10} {\rm Z/Z}_\odot = 0.25$. *Bottom*: The ionizing photon flux per unit stellar mass for Helium, $Q_{\rm He}$, as a function of time. For young stars, the metal-poor populations have higher ionizing photon rates and extended main-sequence lifetimes. The bump in $Q_{\rm H}$at $\log t = 7.8$ seen in populations with metallicities below $\log_{10} {\rm Z/Z}_\odot = -0.5$ is due to hot horizontal branch stars, which are not hot enough to produce a similar bump in $Q_{\rm He}$. The large increase in $Q_{\rm He}$ after $\log t = 8$ is due to the first onset of post-AGB stars.

metal-rich populations. However, blueward of the hydrogen ionization energy, the spectrum behaves similarly at all metallicities.

To understand the origin of this UV emission, the middle panel in Fig. 4.1 shows the break down of the spectrum by evolutionary type at solar metallicity for the 0.1 Gyr and 8 Gyr populations. We plot the fractional contribution to the total flux from main sequence, red giant branch, horizontal branch, AGB, and post-AGB stars, as designated by the phases tagged in the MIST isochrone tables. The AGB label includes the contribution from both early-AGB and thermally pulsing-AGB (TP-AGB) phases. We omit the WR phase from the plot, as these stars are present for $\lesssim 5$ Myr in instantaneous burst populations.

At 0.1 Gyr main sequence stars produce more than 99% of the flux probed by the GALEX FUV and NUV filters. Main sequence stars are also responsible for most of the hydrogen-ionizing photons, but their contribution rapidly decreases towards shorter wavelengths. By 0.1 Gyr MS stars are not hot enough to produce significant amounts of He-ionizing photons. Post-AGB stars have a negligible contribution to the GALEX filters but produce ∼10% of the hydrogen-ionizing photons and all of the helium-ionizing photons. MS and HB (core-He burning) stars dominate the SDSS r-band.

At 8 Gyr, main sequence stars still dominate the GALEX NUV band, though post-AGB stars contribute significantly, nearly 10% of the total flux. Post-AGB stars produce 98% of the flux in the GALEX FUV band, and all of the photons capable of ionizing hydrogen and helium. The optical light is dominated by main sequence and RGB stars.

The bottom panel of Fig. 4.1 shows break down of the total spectrum by stellar mass for the solar metallicity population at 0.1 Gyr and 8 Gyr. For the 0.1 Gyr population, stars with initial masses above 5 $M_\odot$ make up the post-AGB star population, while stars with initial masses between 1 and 3 $M_\odot$ occupy the main sequence, producing the bulk of the UV and optical light. At 8 Gyr, however, the post-AGB and MS phases are comprised of stars with very similar initial masses, between 1 and 2 $M_\odot$.

This behavior will change with metallicity, since metallicity can change the temperature and lifetime of various stellar phases. In Fig. 4.2, we show the fractional contribution by

evolutionary phase (i.e., the middle panel of Fig. 4.1) for an instantaneous burst at 8 Gyr with $\log_{10} \mathrm{Z}/\mathrm{Z}_{\odot} = -1$. At low metallicity, the hotter main sequence stars contribute a higher fraction of the total flux in the GALEX FUV and NUV filters. At solar metallicity, post-AGB stars are responsible for $\sim 98\%$ and $\sim 10\%$ of the FUV and NUV flux, respectively. At $\log_{10} \mathrm{Z}/\mathrm{Z}_{\odot} = -1$, the post-AGB contribution decreases to $\sim 90\%$ and $\sim 1\%$ of the FUV and NUV filters, respectively. In both cases, however, the post-AGB stars are responsible for all of the flux produced at energies sufficient to ionize hydrogen and helium. Though the ionizing photon contribution from these evolutionary types will change with time, in the standard MIST models, post-AGB stars make up more than 95% of the ionizing flux after ~ 100 Myr, while HB stars never contribute more than 10%.

In Fig. 4.3, we show the ionizing flux from different types of stars as a function of time for instantaneous burst populations. The top panel shows the time evolution of Q_{H}, the number of photons emitted per second that are capable of ionizing hydrogen ($E \geq 13.6$ eV or $\lambda \geq 912$ Å) for a solar (*left*) and 10% solar (*right*) population. The bottom panel shows the time evolution of Q_{He}, the number of photons emitted per second that are capable of ionizing helium ($E \geq 24.6$ eV or $\lambda \geq 504$ Å). For the single-star MIST models, main sequence stars dominate the ionizing photon budget for nearly 100 Myr, with the exception of the brief but intense contribution from Wolf-Rayet stars at 2-4 Myr ($\log t \sim 6.5$). The ionizing photon flux declines with time until the population is about 1 Gyr, when the first post-AGB stars appear. These stars are quite hot and dominate both the hydrogen- and helium-ionizing flux once they appear.

We show the resulting time evolution of $Q_{\mathrm{H}}$and Q_{He} for instantaneous bursts in Fig. 4.4. As explained, $Q_{\mathrm{H}}$and Q_{He} decline steadily and by orders of magnitude as young, massive stars evolve off of the main sequence. After 1 Gyr, Q_{H}plateaus as the first post-AGB stars appear, but at a level that is more than 10^5 times smaller than the initial burst. The evolution of helium ionization is somewhat different. Q_{He} also declines by orders of magnitude over the first Gyr, however, because post-AGB stars can have temperatures akin to late-O or early-B-type stars (15,000-50,000K), Q_{He} *rises* after 1 Gyr. The He ionizing photon flux is

still 10^5 times smaller than during the initial burst, however.

4.3.2 Emission lines from hot evolved stars

We have used the spectra presented in §4.3.1 as the ionizing source input to CLOUDY models. In this section we discuss models run at a range of ionization parameters, $-6 < \log_{10}\mathcal{U}_0 < -3$, and assume constant gas phase metallicity, using the solar-like abundances specified in Table 4.1.

To first order, the luminosity of Hα emission will correlate with $Q_{\rm H}$, the ionizing photon flux. In Fig. 4.5, we show the luminosity of Hα emission as a function of ionizing spectrum age and metallicity, at $\log_{10}\mathcal{U}_0 = -4$. Since $Q_{\rm H}$decreases with time, Hα emission similarly decreases with age since the initial burst. There is also a metallicity dependence in $Q_{\rm H}$(and thus Hα) at early times, since metal line blanketing in the atmospheres of stars reduces the amount of emergent flux in the UV. This metallicity dependence largely disappears at late times when post-AGB stars dominate the ionizing flux. The late time evolution of $Q_{\rm H}$and $Q_{\rm He}$ is therefore largely independent of metallicity, because the post-AGB models occupy a narrow range of luminosities and the temperature sequence is an aging process rather than a metallicity driven process.

Second-order variations in Hα luminosity are driven by the temperature dependence in α_B, the recombination coefficient. The temperature of the nebula will depend on the specific elemental abundances in the gas cloud, since metal lines are responsible for most of the cloud cooling. The temperature of the nebula will also depend on the hardness of the ionizing spectrum, since photons with energy in excess of the ionization potential of hydrogen will impart additional kinetic energy to photoelectrons, ultimately raising the temperature of the cloud.

4.3.3 The underlying stellar continuum

For young stellar populations in H II regions, it is typical to measure Hα fluxes, since these can be tied directly to the mass of recently formed stars. For old stellar populations it

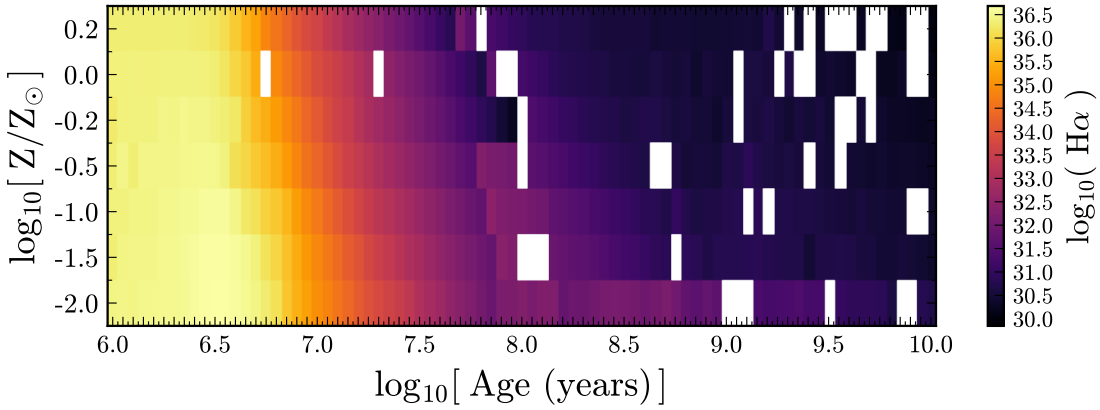

Figure 4.5 The time evolution of Hα emission for instantaneous bursts as a function of metallicity at fixed $\log_{10}\mathcal{U}_0 = -4$. H$\alpha$ luminosity depends primarily on the number of ionizing photons, following the behavior of $Q_{\rm H}$with time closely.

is more typical to measure the flux of Hα relative to the continuum using an equivalent width (EW), which partially removes the dependence on stellar mass. The equivalent width of Hα, however, will depend on the strength of Hα *and* the strength of the underlying stellar continuum at optical wavelengths. Making predictions of Hα EWs in old populations therefore requires the self-consistent stellar and nebular models we developed in Byler et al. (2016). In this section, we take a brief detour to demonstrate that our models have sensible optical colors and absorption lines before presenting the equivalent width results in §4.3.4.

Although it is an oversimplification to model early-type galaxies as a single age, single metallicity population, it is not always an inappropriate representation. In this section, we first demonstrate that instantaneous bursts adequately reproduce observed properties of the ETG population. We then extend the analysis to include more realistic SFHs, with a delayed-τ model of the form:

$$\mathrm{SFR}(t) = t\exp(-t/\tau), \tag{4.1}$$

for τ =0.1, 0.5, and 1.0 Gyr and total stellar mass between 10^{10} and 10^{11} $M_\odot$ (Thomas et al., 2005; Choi et al., 2014).

In the top row of Fig. 4.6 we show the SDSS $u-r$ vs. $r-z$ color-color diagram for our instantaneous burst models at a range of ages and metallicities, for stellar-only models (*left*) and stellar+nebular emission models (*right*, shown for models assuming $\log_{10}\mathcal{U}_0 = -4$). The $u-r$ vs. $r-z$ diagram has proven to be an efficient means of selecting quiescent, red-sequence ETGs. The Holden et al. (2012) boundary for selecting quiescent ETGs is indicated with the black dotted line; the McIntosh et al. (2014) extension for "recently quenched" ETGs is shown with the black solid line. For instantaneous bursts, models with metallicities richer than $\log_{10} Z/Z_\odot = -1$ and ages older than ~ 2 Gyr have optical colors that are appropriate for the ETG population.

Rows 2 through 4 of Fig. 4.6 show the same color-color diagrams for the delayed-τ models. Each row shows a different τ, from 0.1 Gyr to 1.0 Gyr. The models with $\tau = 0.1$ Gyr are essentially indistinguishable from the instantaneous bursts, and the $\tau = 0.5$ Gyr models show qualitatively similar behavior to the instantaneous bursts. The $\tau = 1$ Gyr models are much bluer than the instantaneous bursts, and only the most metal rich models produce colors consistent with the red, quiescent galaxy population. The models with nebular emission have qualitatively similar colors.

Lick indices

The Lick/IDS line strength system (Worthey et al., 1994; Trager et al., 2000) leverages specific spectral features in the optical spectrum that correlate with the age and metallicity of a stellar population. For elliptical galaxies with old stellar populations, stars with initial masses between 1 and 2 $M_\odot$ dominate both the optical spectrum and the ionizing radiation responsible for LIER-like emission. In this section, we show that our models with nebular emission still produce Lick indices consistent with the general ETG population.

We use Lick definitions from Vazdekis et al. (2010). We compare our models to the Hβ Lick index and the [MgFe] index, a combination of several Lick indices (`Mg_b`, `Fe5270`,

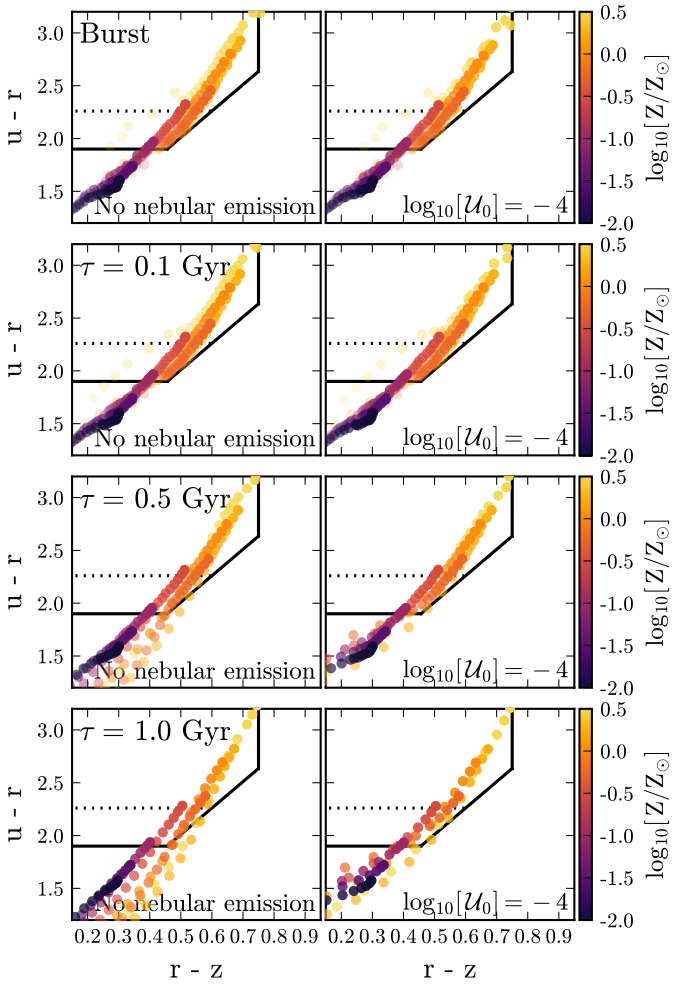

Figure 4.6 Optical color-color diagram for stellar populations using a delayed$-\tau$ model SFH, with $\tau = 0.0$ Gyr (instantaneous burst, *top row*), $\tau = 0.1$ Gyr (*second row*), $\tau = 0.5$ Gyr (*third row*), and $\tau = 1$ Gyr (*bottom row*). Models with ages between 1 and 13 Gyr are plotted, color-coded by metallicity. Age is indicated by the transparency of the points, with the 13 Gyr model points fully opaque. The SDSS $u-r$ vs. r-z colors efficiently separate blue, star-forming galaxies from quiescent, red galaxies. The black line selects ETGs from Holden et al. (2012), revised by McIntosh et al. (2014) to include recently quenched ETGs. The models used in this work have optical colors representative of the general ETG population.

and Fe5335) which is sensitive to metallicity, where higher metallicity populations produce larger values of [MgFe]. The [MgFe] index is also relatively insensitive to $\alpha-$abundance enhancements. To calculate [MgFe], we use the definition from Galleti et al. (2009):

$$[\mathrm{MgFe}] = \sqrt{\mathtt{Mg\_b} \times \frac{\mathtt{Fe5270} + \mathtt{Fe5335}}{2}}. \tag{4.2}$$

In Fig. 4.7 we show the [MgFe] index compared to the optical SDSS $g-r$ color for our ETG models at different metallicities. As in previous figures, the left column shows models without nebular emission, while the right column shows models that include both nebular line and continuum emission, assuming $\log_{10}\mathcal{U}_0 = -4$, typical for LIER-like galaxies. Each row shows a different delayed$-\tau$ model, from $\tau = 0\,\mathrm{Gyr}$ (instantaneous burst, *top row*) to $\tau = 1\,\mathrm{Gyr}$ (*bottom row*). The grey shaded region indicates the location of elliptical galaxies and ancient, massive, globular clusters (GCs) from Schombert (2016).

Our models produce reasonable [MgFe] values, consistent with the low-metallicity GCs and the more metal-rich ETGs. For the $\tau = 1\,\mathrm{Gyr}$ model, the extended SF changes the $g-r$ colors significantly until $\sim 5\,\mathrm{Gyr}$, after which the [MgFe] and $g-r$ colors are consistent with the observed ETGs. The [MgFe] indices do not cover spectral regions with any strong nebular emission lines, thus, the models with and without emission are very similar for models at late ages.

In Fig. 4.8 we show the age-sensitive Hβ Lick index compared to the optical SDSS $g-r$ color in the same style as Fig. 4.7. The Hβ index is a well-known age-indicator, decreasing as the stellar population ages. The ETGs and GCs from Schombert (2016) have Hβ between 0 and 4Å, with Hβ decreasing as the $g-r$ color gets redder. Our models with and without emission show similar behavior, with high values and blue colors for young models and low Hβ combined with redder colors for models over a few Gyr. Models with ages between $2-13\,\mathrm{Gyr}$ are best matched to the ETG and GC data, with lower metallicities for the GCs and higher metallicities for the ETGs. The models with nebular emission show slightly modified Hβ values and colors, though overall still consistent with the data. In the models that include emission, Hβ emission causes the Hβ index to decreases rapidly while the $g-r$

color stays the same.

In what follows, we will largely restrict our analysis of emission lines and UV emission to the subset of models that are also consistent with the observed properties of ETGs in Figures 4.6 - 4.8.

4.3.4 Emission line equivalent widths

To measure Hα equivalent widths from our models, we largely follow the methodology of Belfiore et al. (2016), who measured Hα equivalent widths in LIER galaxies with the Mapping Nearby Galaxies at APO survey (MaNGA; Bundy et al., 2015). In broad terms, the process involves subtracting the Balmer absorption due to the best-fit stellar continuum, and then fitting the residual emission with a Gaussian. In practice, our methodology differs from this slightly, since we are measuring model equivalent widths with a perfect knowledge of the underlying stellar continuum.

In detail, the process is as follows. We generate two spectra with FSPS, one that includes nebular emission lines and one that does not. We use the "non-emission" spectrum as the best-fit stellar continuum. FSPS returns $\mathcal{F}_\lambda$ in $L_\odot/$Å, which we convert to cgs units (erg/s/cm^{-2}/Å) by arbitrarily assuming a mass of $6\times10^{10}\,M_\odot$, typical of a massive early-type galaxy, and a distance of 10 Mpc. For both spectra, we scale the flux to the median flux in the continuum spectrum as measured in the 6000-6200Å range and subtract the continuum spectrum from the emission spectrum.

We fit the resultant scaled emission-line-only spectrum with `scipy.optimize.curvefit` (Jones et al., 2001–) using a 3-parameter Gaussian function of the form:

$$f(x) = a \cdot \exp\left(\frac{-(x-b)^2}{2c}\right), \tag{4.3}$$

such that the integrated flux in the Gaussian is simply $\sqrt{2\pi}\cdot ac$ and an equivalent width with units of Å.

In Fig. 4.9 we show the Hα EW as a function of time for single-aged populations at different metallicities after an initial burst. Hα EWs are strongest at young ages, when

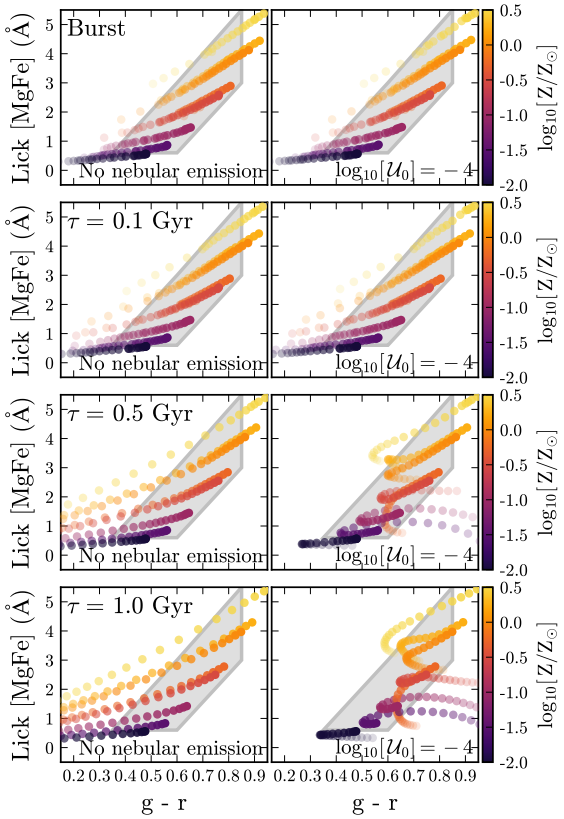

Figure 4.7 Optical $g - r$ color and the [MgFe] Lick index for our ETG models with stellar only (*left column*) and stellar+nebular emission (*right column*). Each row shows a different delayed$-\tau$ model SFH: $\tau = 0.0$ Gyr (instantaneous burst, *top row*), $\tau = 0.1$ Gyr (*second row*), $\tau = 0.5$ Gyr (*third row*), and $\tau = 1$ Gyr (*bottom row*). Models with ages between 1 and 13 Gyr are plotted, color-coded by metallicity. Age is indicated by the transparency of the points, with the 13 Gyr model points fully opaque. The grey shaded region shows the location of observed objects from Schombert (2016), which includes globular clusters and elliptical galaxies. For models with extended SF ($\tau = 1$ Gyr), the inclusion of nebular emission alters the $g-r$ color at young ages. After ~ 5 Gyr the models with nebular emission are consistent with the observed population of ETGs.

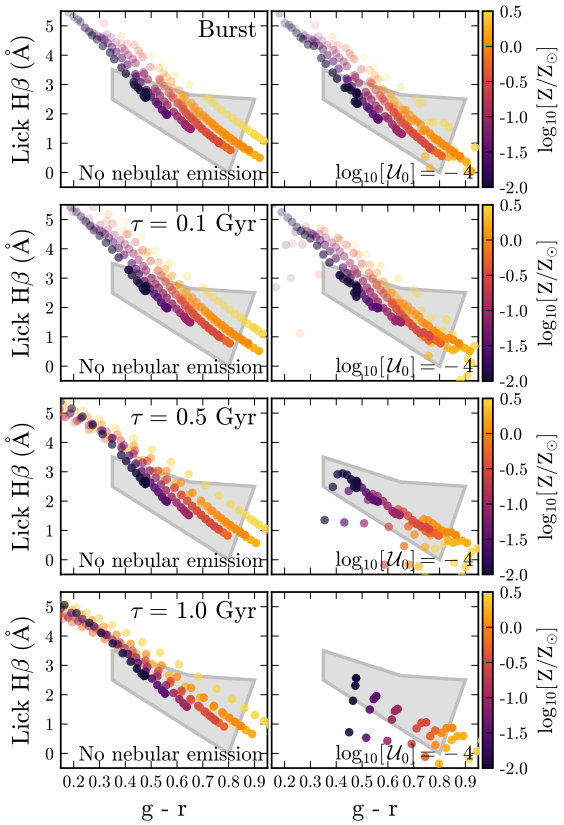

Figure 4.8 Optical $g - r$ color and the Hβ Lick index for our ETG models with stellar only (*left column*) and stellar+nebular emission (*right column*). Each row shows a different delayed$-\tau$ model SFH: $\tau = 0.0$ Gyr (instantaneous burst, *top row*), $\tau = 0.1$ Gyr (*second row*), $\tau = 0.5$ Gyr (*third row*), and $\tau = 1$ Gyr (*bottom row*). Models with ages between 1 and 13 Gyr are plotted, color-coded by metallicity. Age is indicated by the transparency of the points, with the 13 Gyr model points fully opaque. The grey shaded region shows the location of observed objects from Schombert (2016), which includes globular clusters and elliptical galaxies. Nebular emission has an significant impact on the Hβ index, since the emission fills in the Hβ absorption feature, lowering the index.

hot, young stars produce copious amounts of ionizing radiation and strong Hα emission is on top of a weaker optical stellar continuum. At the same age, Hα EWs for metal-poor populations are larger, due to the harder ionizing spectra of metal-poor stars. The metal-poor populations also have longer main-sequence lifetimes, producing larger Hα EWs for several Myr longer than the solar-metallicity population.

In general, the Hα equivalent widths in Fig. 4.9 decline with time until $\sim$1 Gyr, where EWs increase again due to the onset of the post-AGB phase. After $\log t \sim 9$, equivalent widths increase as the population of stars in the post-AGB phase grows. The elevated Hα EWs seen in populations with metallicities below $\log_{10} \mathrm{Z}/\mathrm{Z}_{\odot} = -0.5$ just before $\log t \sim 8$ reflect the rising contribution from hot horizontal branch stars. As seen in Fig. 4.3, these stars are important between 10 and 100 Myr. The effect is stronger with decreasing metallicity, and the lowest metallicity populations ($\log_{10} \mathrm{Z}/\mathrm{Z}_{\odot} = -2$) produce H$\alpha$ EWs an order of magnitude larger than the solar-metallicity populations at the same age.

The grey shaded region in Fig. 4.9 shows the range of EWs measured in typical LIER-like galaxies, of order 0.1-6Å. At late times ($\log t \gtrsim 9$), our models produce equivalent widths consistent with observed LIERs.

We compare the Hα equivalent widths for instantaneous bursts and delayed-τ models in Fig. 4.10. The top panel shows the variation of Hα equivalent widths with time for the different model SFHs, at solar metallicity and $\log_{10} \mathcal{U}_0 = -4$. Each "pixel" represents a different model, where each row shows a different τ and each column shows a different age. The pixels are only filled in if that model has optical colors consistent with the ETG region shown in Fig. 4.6 and Lick indices (Hβ and [MgFe]) consistent with observed ETGs as shown in Figs. 4.7 & 4.8. For those models that look like ETGs, the "pixel" is color-coded by the Hα equivalent width. Equivalent widths vary from 0.1 to 2.5Å. Larger values of τ extend the duration of SF in a model, and these models look like ETGs much later than the instantaneous bursts.

The bottom panel of Fig. 4.10 shows the variation of Hα equivalent widths with metallicity, for models at $\log t = 9.9$ (8 Gyr) and $\log_{10} \mathcal{U}_0 = -4$. The range of H$\alpha$ equivalent widths

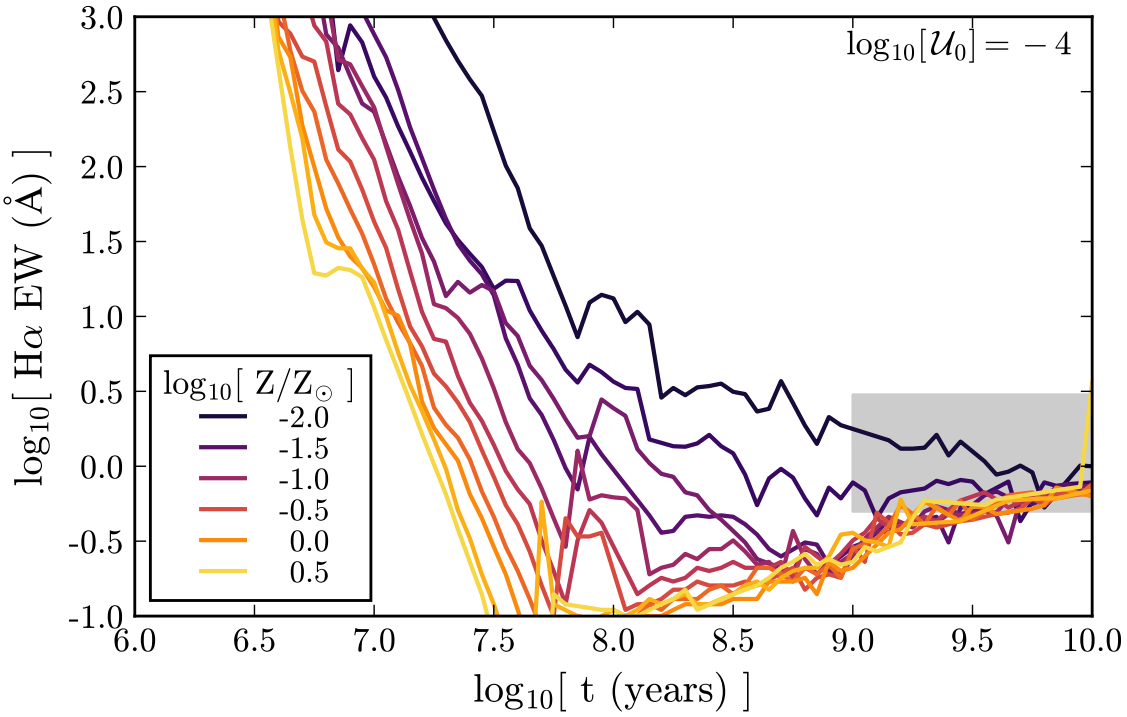

Figure 4.9 The time evolution of Hα equivalent widths for single-aged populations with $\log_{10}\mathcal{U}_0 = -4$, a reproduction of Figure 2 from Belfiore et al. (2016). Nebular emission is strongest at young ages, and Hα equivalent widths decline quickly after the first few Myr. The grey shaded region highlights Hα EWs observed in typical LIER-like galaxies, of order $0.1 - 3$ Å. The post-AGB stars are responsible for the increase in Hα EW seen at $\log t \gtrsim 9$.

is much smaller here, varying from 0.5 to 0.9Å.

LIER models with self-consistent colors and emission line properties

We have demonstrated that there are a broad range of model ages, SFHs, and metallicities that are able to reproduce the optical colors and absorption indices of ETGs. Here we assess the emission line properties of the subset of models with optical spectra that "look" like LIER galaxies. For the full grid of models that include nebular emission, we determine if the resultant broad-band colors and Lick indices fall within the observed range of ETGs, as shown by the grey shaded region of Figs. 4.6, 4.7, & 4.8.

We compare the Hα equivalent widths for instantaneous bursts and delayed-τ models in Fig. 4.10. The top panel shows the variation of Hα equivalent widths with time for the different model SFHs, at solar metallicity and assuming $\log_{10}\mathcal{U}_0 = -4$. Each "pixel" represents a different model, where each row shows a different τ and each column shows a different age. If the model associated with that particular pixel does not have "ETG-like" optical properties, the pixel is greyed out. For those model with "ETG-like" optical properties, the pixel is color-coded by the Hα equivalent width. For the models at solar metallicity and $\log_{10}\mathcal{U}_0 = -4$, equivalent widths vary from 0.1 to 2.5Å with age and SFH.

The main effect of SFH is to change the age at which a model looks like an ETG. Larger values of τ extend the duration of SF in a model, and these models do not look like ETGs until much later than the instantaneous bursts. The instantaneous bursts have "ETG-like" colors after ~ 3 Gyr, while the models with τ=1 Gyr only have "ETG-like" colors after 8 Gyr. The initial large EWs in the delayed-τ models may be associated with contamination from residual star formation.

The lower left panel of Fig. 4.10 shows the variation of Hα equivalent widths with metallicity, for models at $\log t = 9.9$ (8 Gyr) and $\log_{10}\mathcal{U}_0 = -4$. The range of H$\alpha$ equivalent widths is much smaller here, varying from 0.5 to 0.9Å. For stellar populations at all metallicities, the post-AGB population has very similar temperatures, producing ionizing spectra with similar hardness. We thus expect that the models have similar ionization states, producing similar

emission line ratios. However, metallicity does change the emission properties of the models in two subtle ways. First, metallicity does change the underlying stellar continuum, and thus the Hα equivalent width. As shown in Fig. 4.1, lower metallicity models are brighter and hotter in the optical, and will have a larger contribution from the continuum. For a fixed number of ionizing photons, a larger continuum contribution produces smaller equivalent widths. Second, the lower metallicity models have more ionizing photons per unit stellar mass, and will thus produce more Hα emission. Fig. 4.10 shows some evidence of larger EWs in lower metallicity models, but few of these lower-metallicity models produce optical colors that are consistent with the general ETG population.

Finally, the lower right panel of Fig. 4.10 shows the variation of the Hα equivalent width as a function of SFH and ionization parameter, for 8 Gyr models at solar metallicity. The behavior is as expected here, where models with higher ionization parameters produce larger Hα equivalent widths. However, the range of EW is quite modest in spite of the large variation in $\mathcal{U}_0$, with the Hα EWs varying by only 15% as the ionization parameter changes by 2 orders of magnitude. This suggests that although $\mathcal{U}_0$ is a significant uncertainty in our physical model, the predictions of Hα EWs are relatively insensitive to the exact value of $\mathcal{U}_0$.

To briefly summarize, our models that include nebular emission are able to reproduce the optical properties of the general ETG population over a range of ages, SFHs, and metallicities. We find that instantaneous bursts and delayed-τ models with τ=0.1, 0.5 Gyr, ages older than 3 Gyr, and metallicities between $\log_{10} \mathrm{Z/Z_\odot} = -1$ and $\log_{10} \mathrm{Z/Z_\odot} = 0.25$ produce the most consistent combination of optical colors and Lick indices when compared with ETGs. This same subset of models produces Hα equivalent widths of order 0.1-3Å, consistent with LIER-like galaxies. We find some evidence for higher Hα equivalent widths in lower metallicity models and models with higher ionization parameters, but in general the Hα EW is far more sensitive to age and SFH than either metallicity or $\mathcal{U}_0$.

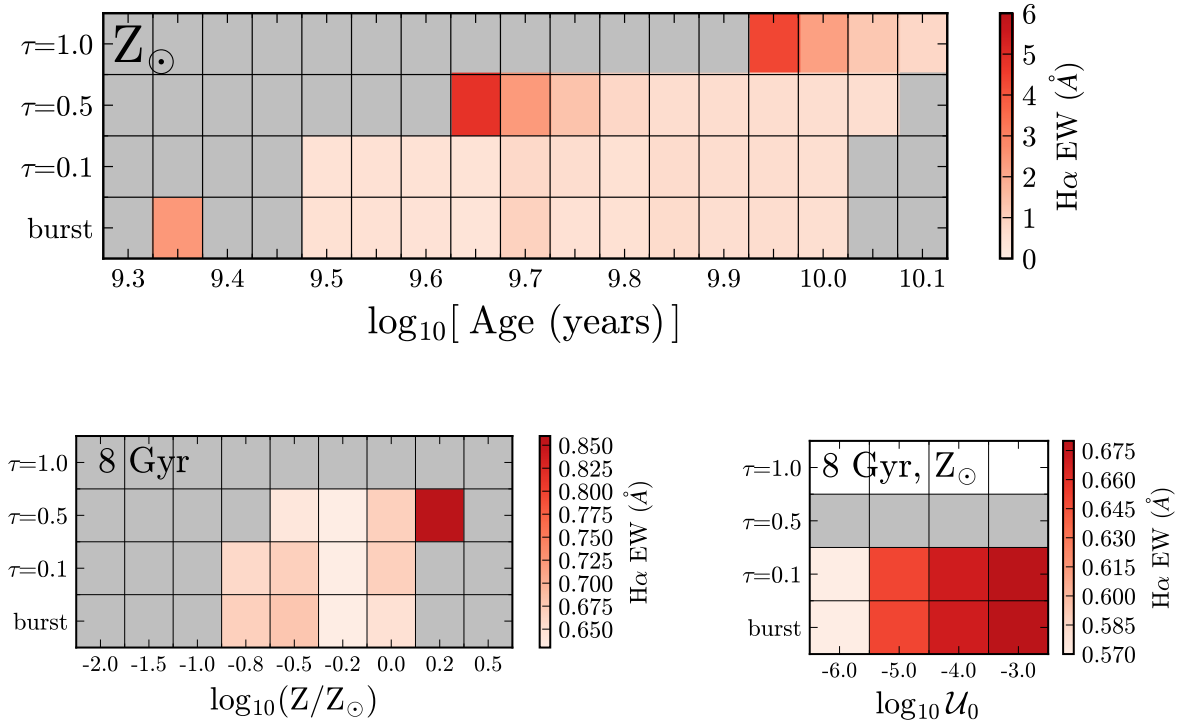

Figure 4.10 *Top:* The time evolution of Hα equivalent widths for models at solar metallicity with $\log_{10}\mathcal{U}_0 = -4$. Each row of the plot line shows a different delayed-τ model, and the color of each "pixel" shows the strength of the Hα equivalent width. The pixels without data represent models that did not have optical colors or Lick indices consistent with the general ETG population. *Bottom:* For models at 8 Gyr we show the Hα equivalent width as a function of SFH and metallicity. Again, the uncolored pixels represent models with optical colors and lick indices inconsistent with the ETG population.

4.3.5 Emission line ratios

In this section we confirm that our models produce emission line ratios consistent with LIER-like emission in several widely-used diagnostic diagrams.

In Fig. 4.11 we show three optical emission line diagnostic diagrams: the standard BPT (*left*), [S II]/Hα vs. [O III]/Hβ diagram (*middle*), and the [O I]/Hα versus [O III]/[O II] diagram (*right*). The BPT diagram is a widely-used diagnostic that generally separates objects with different ionization states, while the [S II]/Hα and [O I]/Hα diagrams have been highlighted as LIER diagnostics, since they make use of low-ionization lines. We show 8 Gyr instantaneous bursts for a range of stellar metallicities, with the gas phase metallicity fixed at solar metallicity.

In the standard BPT diagram (*left*), the post-AGB models produce emission line ratios in good agreement with the LIER/LINER region of the diagram. Models with ionization parameters between $\log_{10}\mathcal{U}_0 = -5$ and $\log_{10}\mathcal{U}_0 = -3$ easily match line ratios observed in LIER-like galaxies. In both the [S II]/Hα diagram (*middle*) and [O I]/Hα diagram (*right*), the models produce line ratios well above the Kewley et al. (2006) classification line for star-forming galaxies, such that they would be classified as classic LIER galaxies.

From Fig. 4.1 we should not be surprised that there is little difference between models with different stellar metallicities, since the post-AGB stars producing the ionizing radiation have very similar colors. The ionizing spectra have similar hardness, producing gas with similar ionization states and thus similar emission line ratios. While stellar metallicity has little effect on the emission line ratios, it does change the equivalent widths, as seen in Figs. 4.9 & 4.10, but largely through the properties of the continuum, rather than the emission lines.

In summary, Figures 4.9 - 4.11 indicate that our models produce emission line ratios that agree well with those observed in LIER-like galaxies, with no fine tuning needed to produce acceptable models. Their optical colors and line indices are consistent with ETGs and simultaneously produce emission line equivalent widths and emission line ratios observed in LIER-like galaxies. Moreover, consistent models are produced for a wide range of possible

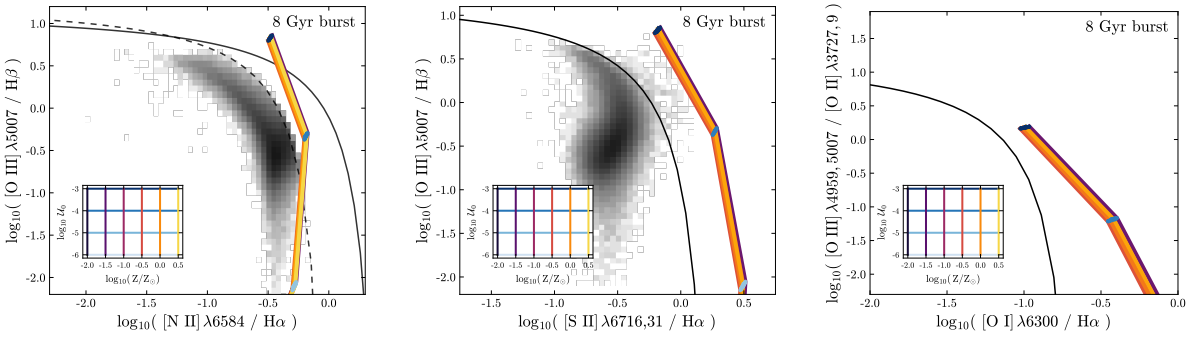

Figure 4.11 Emission line ratio diagnostic diagrams. The classic BPT diagram (*left*), the [S II]/Hα vs. [O III]/Hβ BPT diagram (*middle*), and the [O I]/Hα vs. O_{32} diagram (*right*).The models shown are for instantaneous bursts at 8 Gyr. The stellar metallicities vary from $\log_{10} Z/Z_{\odot} = -2$ to 0.5, but the gas phase metallicity is held constant with solar-like abundances. The ionization parameter is varied from $\log_{10} \mathcal{U}_0 = -6$ to $\log_{10} \mathcal{U}_0 = -3$, typical for LIER-like emission. In the left figure, the dashed line from Kauffmann et al. (2003b) separates pure star forming galaxies, while the solid line from Kewley et al. (2001) shows the limit for extreme starbursts. The solid black lines in the middle and left panels show the Kewley et al. (2006) classification for star-forming galaxies. In all diagnostic diagrams, the models occupy a region distinct from star forming galaxies and consistent with line ratios observed in LIER-like galaxies.

SFHs and ages, with only weak dependencies on metallicity and ionization parameter.

4.4 UV emission from hot evolved stars

As discussed in §4.3.3, there are broad classes of star formation histories that produce reasonable SDSS ETG colors. Thus, the emission line ratios and equivalent widths presented in §4 are relatively model independent, as the optical properties of ETGs are fairly well understood. The UV is much more uncertain, however, as galaxies with similar optical colors can have very different UV colors. In this section, we ask if the models from §4 are also able to correctly predict the properties of other UV populations, including post-AGB stars, hot horizontal branch stars, and blue straggler stars. We note that the evolutionary pathways and lifetimes of these populations are not well-understood and models of their SEDs are uncertain.

In this section we explore the contribution from three main stellar types. We first consider post-AGB stars, which we have shown dominate the ionizing photon budget at old ages and are able to reproduce the emission line properties of LIER-like galaxies. We can vary the contribution from post-AGB stars to the total SED using the `pagb` parameter in FSPS. This parameter specifies the weight given to the post-AGB star phase, where `pagb=0.0` turns off post-AGB stars and `pagb=1.0` implies that the MIST models are implemented as-is, the default behavior in FSPS. Models with `pagb` between 0 and 1 have the flux from the post-AGB stars scaled down by `pagb`.

Second, we explore the contribution from hot horizontal branch stars. These stars are not as luminous as post-AGB stars, but are longer-lived and thus more numerous. Blue horizontal branch (BHB) stars typically have temperatures between 7,000 and 20,000K (Schiavon et al., 2004), with the hottest BHB stars often referred to as Extreme Horizontal Branch (EHB) stars. A modest population of BHB stars can alter the UV colors of a stellar population. However, since temperatures in excess of 15,000K are required to ionize hydrogen, only in the most extreme cases will BHB stars contribute significantly to the ionizing photon budget. BHB stars are not included in the default FSPS parameters, but they can be included

using the `fbhb` parameter, which specifies the fraction of horizontal branch stars that are blue. FSPS redistributes the specified fraction of HB stars such that they are uniformly spread in $\log T_{\rm eff}$ to 10^4K (e.g., Sarajedini et al., 2007). However, BHB temperatures have been observed in excess of 10^4K, to include the most extreme cases we increase the BHB temperature limit to $10^{4.5}$K ($\sim$30,000 K, the limit of a B-type star) in the following tests.

Finally, we also explore the contribution from blue straggler stars. These are rejuvenated main sequence stars that appear blueward of the main sequence turn-off in globular clusters (GCs). We vary the contribution of these stars in FSPS using the $S_{\rm BS}$, or `sbss` parameter, which specifies the specific frequency of blue straggler stars relative to the number of horizontal branch stars ($S_{\rm BS} = N_{\rm BS}/N_{\rm HB}$). This number can be varied between 0 and 10, but is observed to be between 0.1 and 5 in GCs, and its value in ETGs is unknown.

In Fig. 4.12 we show an example spectrum from a 3 Gyr SSP at solar metallicity, shown in black. We indicate the ionization energies of hydrogen and helium with the black dashed lines, and show the GALEX FUV and NUV bandpasses in grey. We then systematically vary the `pagb`, `fbhb`, `sbss` parameters from the baseline models.

We show the effect of decreasing `pagb` from 1 to 10^{-1}, 10^{-2}, and 10^{-3} in orange. Scaling down the implemented post-AGB star contribution scales down the emergent EUV radiation in the spectrum. The MIST models do not include evolutionary pathways for early-AGB or AGB-Manque stars, so varying `pagb` could be interpreted as varying the number of stars evolving through the traditional post-AGB phase. If a substantial fraction of post-AGB stars have untraditional evolutionary pathways, the ionizing photon budget would change significantly.

We show the effect of adding BHB stars in purple, where `fbhb` is increased from 0 to 0.1, 0.5 and 1.0. Allowing hotter BHB stars does not change the ionizing photon budget but does change the UV colors dramatically.

The addition of blue straggler stars is shown in blue, where we have increased the specific frequency `sbss` from 0 to 0.1, 1, and 5. These stars are not as hot as the BHB stars, and primarily change the NUV flux. In older populations, as the main sequence turn-off evolves

to cooler temperatures, the NUV contribution from BS stars should decrease.

4.4.1 UV-upturn colors

Fig. 4.12 suggests that the FUV and NUV properties of early type galaxies will be sensitive to the details of the post-AGB, HB, and BS populations. Models of ETG UV emission will therefore depend on exactly how these models are implemented. We first compare our baseline ETG models to GALEX observations. We then consider variations in the default FSPS parameters that bring the models and observations into better alignment.

In Fig. 4.13 we show the $FUV - NUV$ vs. $NUV - r$ color evolution of our baseline ETG models as a function of SFH, age and metallicity. Just as in Fig. 4.6, each row shows a different SFH, from $\tau = 0$, an instantaneous burst, to τ=1 Gyr. The points are color-coded by their metallicity, and the model age is indicated by the opacity, where 13 Gyr models points are fully opaque. The left column shows models that do not include nebular emission, while the right column shows models that include the contribution from nebular line and continuum emission, assuming an ionization parameter of $\log_{10}\mathcal{U}_0 = -4$.

Fig. 4.13 is a reproduction of a figure presented in Hernández-Pérez & Bruzual (2014). To appropriately compare with the Hernández-Pérez & Bruzual (2014) results, we adopt the same observational cut of H$\beta \leq 2.1$Å used in their work on our models. The vertical dashed line at $NUV - r$=5.4 is their galaxy red sequence limit and the horizontal line at $FUV - NUV = 0.9$ shows the limit for selection of classical UV- upturn galaxies. Galaxies on the red sequence that fall below this line are said to have a "UV excess" (UVX) (Smith, 2014). Galaxies below this line but on the blue side of the red sequence division are thought to have blue colors originating from residual star-formation (RSF), rather than canonical UVX emission.

The grey region in Fig. 4.13 shows the range of UV colors observed for ETGs in the Hernández-Pérez & Bruzual (2014) sample. This region is most easily populated by models with high metallicity or somewhat extended SF. Though our models had very similar optical colors, they show a wide range of UV colors in Fig. 4.13, primarily driven any amount of

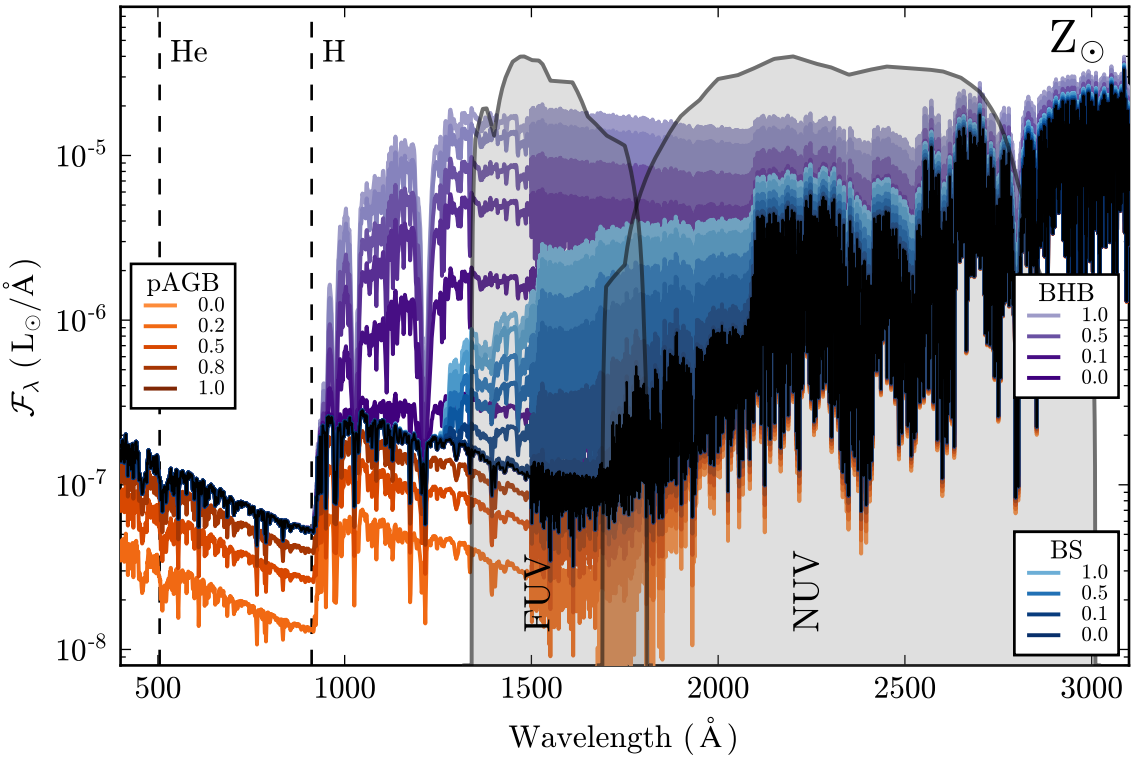

Figure 4.12 The UV spectrum of a solar-metallicity instantaneous burst where the contribution of post-AGB stars (orange), blue HB stars (purple), and blue straggler stars (blue) are varied. The unmodified spectrum is shown in black. The post-AGB stars are responsible for the ionizing radiation responsible for producing LIER-like emission, but have little influence over the galaxy's UV colors. In contrast, the blue HB stars and blue straggler stars significantly change the UV color of the population but have little effect on the ionizing radiation output.

recent star formation. The sustained star formation in the delayed-τ models with τ=1 Gyr limited the range of ages and metallicities that could produce ETG-like colors. In Fig. 4.13, most of these models fall in the "residual star formation" section of the diagram.

We note that most of our default models (*left column*) are slightly too red in $FUV-NUV$ to adequately match the Hernández-Pérez & Bruzual (2014) sample. This is slightly improved if we consider the models that include nebular emission (*right column*), which are able to reproduce a wider range of observed ETG colors. At low metallicity however, the models with nebular emission are too blue in $NUV-r$, masquerading as galaxies with residual star formation despite their low Hβ equivalent widths and old ages.

Hernández-Pérez & Bruzual (2014) found it difficult to generate models in the UVX portion of the UV color-color diagram without invoking binary star interactions, which can strip the outer envelope of a star, making it appear hotter. In contrast, our models are able to populate the UVX portion of Fig. 4.13, but only at high metallicity. It is easier to populate the UVX portion of the color-color diagram when including nebular emission, though none of our models reach the most extreme regions of the UVX region.

The default models in Fig. 4.13 do not include BHB or BS populations, (i.e., `fbhb`, `sbss` = 0). Including these populations will add flux to the FUV and NUV bands, making $NUV-r$ and $FUV-NUV$ colors bluer. It thus seems likely that post-AGB stars are not solely responsible for the observed UV-excess in ETGs. This points to a scenario where the post-AGB stars produce the ionizing radiation necessary for LIER-like emission, while a different population of HPHB stars drive the FUV and NUV behavior.

We show the same UV color-color diagram from Fig. 4.13 in Fig. 4.14V, except now for models where we vary the various HPHB populations. We show instantaneous bursts at 8 and 13 Gyr (left and right panels, respectively), and metallicities of $\log_{10} Z/Z_{\odot} = -0.5$, 0.0, and 0.25. The baseline model from Fig. 4.13 is shown in black, for comparison. Variations due to changes in `pagb` are shown in orange, changes in `fbhb` are shown in purple, and changes in `sbss` are shown in blue.

Variations in `sbss` produce negligible changes in the ionizing spectrum at 8 and 13 Gyr,

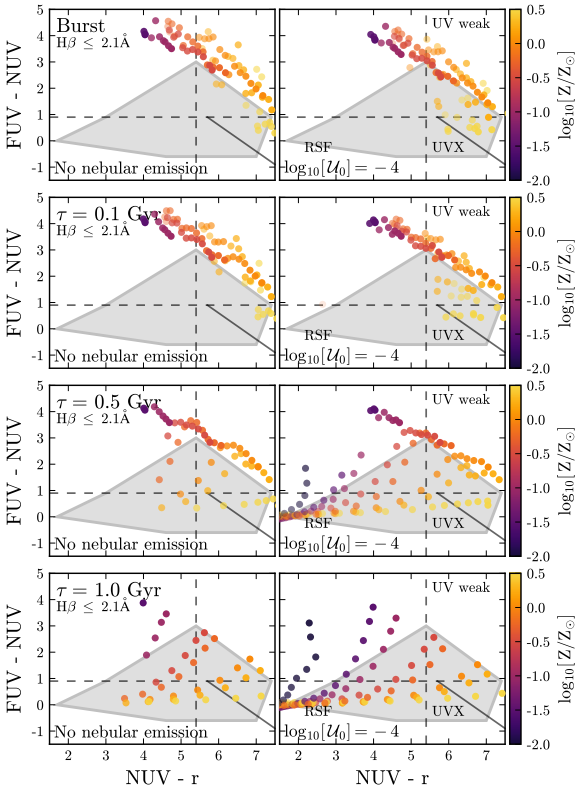

Figure 4.13 $FUV - NUV$ vs. NUV - r colors for our ETG models with stellar only (*left column*) and stellar+nebular emission (*right column*). Each row shows a different delayed$-\tau$ model: $\tau = 0.0$ Gyr (instantaneous burst, *top row*), $\tau = 0.1$ Gyr (*second row*), $\tau = 0.5$ Gyr (*third row*), and $\tau = 1$ Gyr (*bottom row*). Models with ages between 1 and 13 Gyr are plotted, color-coded by metallicity. Age is indicated by the transparency of the points, with the 13 Gyr model points fully opaque. The vertical dashed line at $NUV - r$=5.4 separates red-sequence galaxies, and the horizontal line at $FUV - NUV$=0.9 shows the boundary of classic UV-upturn galaxies from Smith (2014). Hernández-Pérez & Bruzual (2014) further separates strong UV emitters with a FUV-r cut, shown with the grey line. To compare our models with the sample of ETGs from Hernández-Pérez & Bruzual (2014), we have made the same cut in Hβ equivalent width (H$\beta < 2.0$Å) in our models.

because at these late ages, the rejuvenated main sequence stars are too cool to contribute significantly to the UV flux. Variations in `pagb` parameter move the models away from the observed locus of ETGs, while variations in `fbhb` move the models towards the center of the observed ETG locus. For some models, even a small fraction of BHB stars ($\sim$10%) can successfully move the model into the UVX portion of the diagram. However, for most models, increasing `fbhb` largely moves the models to bluer $NUV - r$ colors at similar $FUV - NUV$ colors, indicating that the BHB stars considered here are not hot enough to explain all ETGs with UVX emission. We note that in FSPS, the BHB stars are evenly distributed across the horizontal branch in temperature. Models with only BHB or EHB stars could still produce the necessary FUV flux needed to move the baseline models into the UVX region.

4.5 Isochrone variations

In §4 we demonstrated that the MIST models are able to simultaneously reproduce the optical colors and nebular emission properties of LIER-like galaxies for a range of ages, SFGs, and metallicities. Post-AGB stars are the sole provider of ionizing photons in these models. In the MIST models, the evolution of stars at all masses is continuously computed, from the pre-main sequence phase to the end of white dwarf (WD) cooling phase. This means that we can directly probe the sensitivity of post-AGB star evolution to the various default assumptions in the evolutionary tracks.

In this section we explore modifications to the MIST models that affect the duration and intensity of the post-AGB phase to test how this alters the resultant nebular emission. We test three variants: overshoot mixing efficiency, mass loss, and rotation rate. We briefly describe each of these variants in turn.

Overshoot mixing efficiency In the MIST models, the convective mixing of elements in the stellar interior is implemented using the mixing length theory (MLT) formalism, described at length in Choi et al. (2016). The mixing is a time-dependent diffusive process, which is modified by overshoot mixing across convection boundaries. The overshoot action

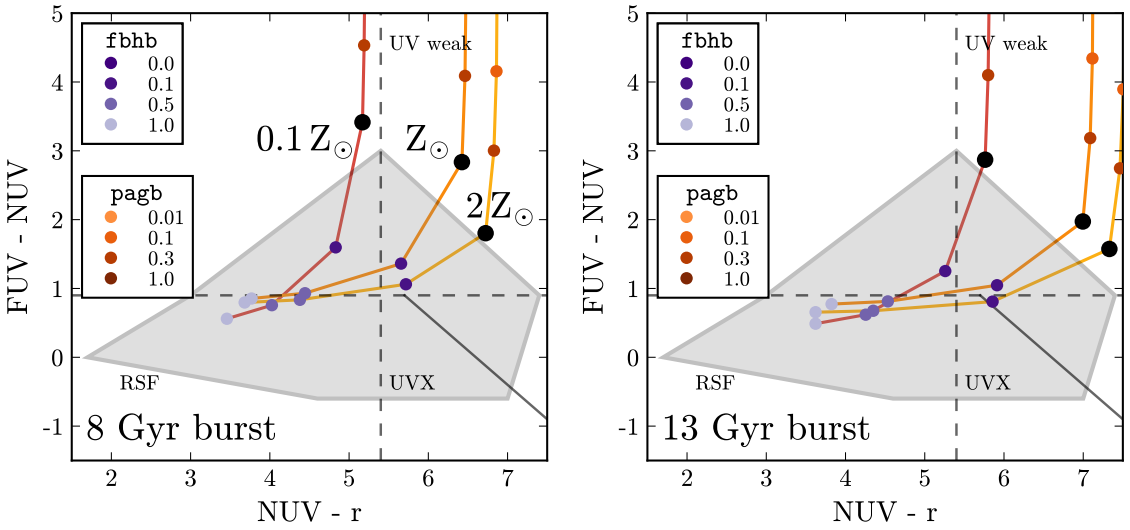

Figure 4.14 $FUV - NUV$ vs. NUV - r colors for our ETG models for an instantaneous burst at 8 Gyr (*left*) and 13 Gyr (*right*). Models are connected by lines that are color-coded by metallicity, for $\log_{10} Z/Z_{\odot} = -0.5$, 0.0, and 0.25. The black marker indicates the standard stellar population, where `pagb` = 1 and `fbhb` = 0. The varying blue markers show the change in color when `fbhb` is varied from the fiducial model, and the orange colored points show the change in color when `pagb` is varied from the fiducial model. The vertical dashed line at $NUV - r$=5.4 separates red-sequence galaxies, and the horizontal line at $FUV - NUV$=0.9 shows the boundary of classic UV-upturn galaxies from Smith (2014). Hernández-Pérez & Bruzual (2014) further separates strong UV emitters with a FUV-r cut, shown with the grey line.

leads to enhanced mixing, and is used to account for the observed properties of AGB and post-AGB stars (Herwig, 2000). The method adopted by MIST follows the parametrization of Herwig (2000), which modifies the diffusion coefficient in the overshoot region through an exponentially decaying diffusion process. The efficiency of that decay is set by f_{ov}, a free parameter that determines the efficiency of overshoot mixing. In this work we use MIST variants where the efficiency of overshoot mixing in the envelope of thermally pulsing (TP)-AGB stars has changed. The default MIST model has $f_{\rm ov,env}$ =0.0174. Our modified model has f_{ov} =0.0052, corresponding to a 30% decrease in mixing efficiency. We refer to this model as `MIST_DUPx0.3`.

Rotation The MIST models include the effect of rotation, discussed at length in Choi et al. (2017). The effects of rotation appear in the MESA stellar evolution calculations in three main ways. First, rotation decreases the gravitational acceleration via the centrifugal force, which in turn affects the stellar structure. Second, rotation can promote extra mixing in the interior, boosting the transport of chemicals and angular momentum. MESA adopts the common approach of treating the chemical and angular momentum transport in a diffusion approximation. Third, rotation enhances mass loss. MESA adopts the formulation from Langer (1998), where the mass loss rate $\dot{M}$ is multiplied by a factor that increases dramatically as the surface angular velocity Ω approaches critical, or break-up, angular velocity. The default MIST model assumes an initial rotation rate of $\nu_{\rm ZAMS}/\nu_{\rm crit} = 0.4$, meaning that the the surface velocity is set to 40% of the critical, or break-up, velocity. In this work we use MIST variants where the rotation rate is increased to $\nu_{\rm ZAMS}/\nu_{\rm crit} = 0.6, 0.8$ (`MIST_vvcrit0.6` and `MIST_vvcrit0.8`, respectively).

Mass Loss We use MIST variants related to mass loss. In the first, both η_M and η_B, the mass loss efficiency factors for the RGB and AGB, respectively, are decreased by half (`MIST_mdotx0.5`). In the second, both η_M and η_B are doubled (`MIST_mdotx2`).

We run each of the above MIST variants through CLOUDY at solar metallicity using identical input parameters. In Fig. 4.15, we show the resultant Hα equivalent widths produced by the MIST variants at 8 Gyr for a range of ionization parameters. The format of Fig. 4.15 is similar to that in Fig. 4.10, where each pixel represents a different model. The x-axis shows each of the MIST variants, where the fiducial column represents the standard MIST model. The y-axis shows ionization paramter, which varies from $\log_{10}\mathcal{U}_0 = -6$ to -3. The Hα equivalent widths vary from 0.42 to 0.66Å. Unsurprisingly, all the MIST variants show Hα equivalent widths that increase as $\log_{10}\mathcal{U}_0$is increased.

The MIST variants show a range of behaviors when compared to the fiducial model. The model where the overshoot mixing efficiency has been decreased by 30% (DUP$\times$0.3) shows smaller Hα equivalent widths than the fiducial model, though only by a few percent.

The models where the mass loss efficiency factors show different emission properties. The model with less efficient mass loss has smaller equivalent widths than the fiducial model at all ionization parameters. In contrast, the model with increased mass loss efficiency shows enhanced equivalent widths when compared to the fiducial model.

The models with increased rotation rates show very little change compared to the fiducial model. This is not unexpected, since rotation plays an important role for young, massive stars but has minimal effect on the TP-AGB to post-AGB transition.

Enhanced mass loss seems like a promising way enhance the ionizing properties of post-AGB stars. We note that doubling the mass loss efficiency factors is not an unreasonable, the default MIST model uses $\eta_{\rm R} = 0.1$ and $\eta_{\rm B} = 0.2$, which increases to $\eta_{\rm R} = 0.2$ and $\eta_{\rm B} = 0.4$, respectively, in the `MIST_mdotx2` model. Mass loss efficiency parameters as high as 0.8 have been suggested in some cases.

4.6 Conclusions

In this work, we present the first prediction of LIER-like emission from post-AGB stars that is based on fully self-consistent photoionization modelling. We use these models to characterize the physical origin of LIER-like emission and post-AGB stars as an ionizing source. We have

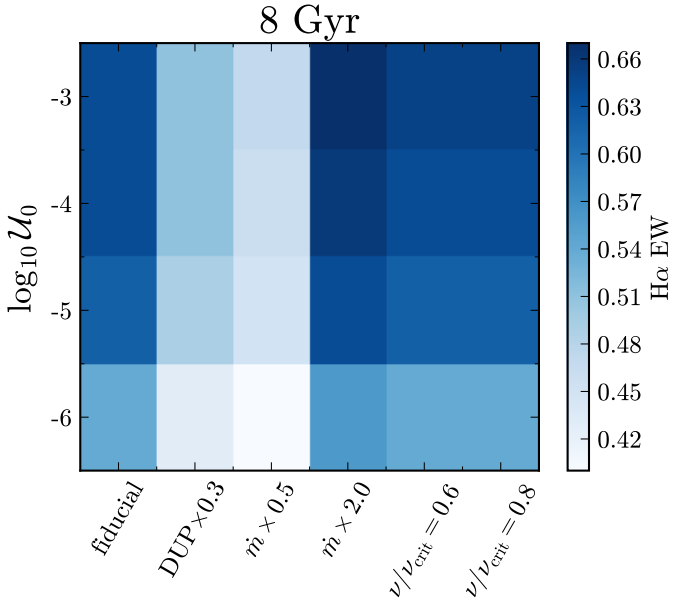

Figure 4.15 For solar metallicity models at 8 Gyr and $\log_{10}\mathcal{U}_0 = -4$, we show the H$\alpha$ equivalent width for the MIST variations.

shown that evolved stellar populations where post-AGB stars provide the ionizing radiation source successfully reproduce LIER-like emission line ratios and Hα equivalent widths. These same models simultaneously reproduce the optical colors and absorption features observed in the general ETG population. We summarize our conclusions below.

- For instantaneous bursts, post-AGB stars make up more than 95% of the ionizing flux after $\sim$100 Myr, while horizontal branch stars never contribute more than 10% of the total ionizing flux, assuming the default FSPS parameters.

- Post-AGB star models produce emission line ratios consistent with LIER-like emission in the standard BPT diagram, the [S II]/Hα diagram, and the [O I]/Hα diagram.

- Post-AGB star models produce Hα equivalent widths between 0.1 and 6Å, depending on the age, metallicity, and ionization parameter of the model.

- Post-AGB stars have very similar ionizing spectra at all metallicities. Metallicity mainly changes the age at which the first post-AGB stars appear, which occurs earlier in high-metallicity models, and later in low-metallicity models. For instantaneous bursts, the hardness of the ionizing spectrum produced by post-AGB stars is very similar after $\sim$2 Gyr at all metallicities. The similar hardness in the ionizing spectrum produces gas with similar ionization states, thus, emission line ratios from post-AGB stars do not vary much with stellar metallicity. The metallicity of the stellar population does, however, change the measured equivalent widths, since the underlying stellar continuum varies with metallicity as does the absolute number of ionizing photons produced per solar mass.

- Our models that include nebular emission are able to reproduce the optical properties of the general ETG population over a range of ages, SFHs, and metallicities. We find that instantaneous bursts and delayed-τ models with $\tau \lesssim 0.5$ Gyr, ages above 3 Gyr, and metallicities between $\log_{10} \mathrm{Z/Z_\odot} = -1$ and $\log_{10} \mathrm{Z/Z_\odot} = 0.25$ produce the

most consistent combination of optical colors and Lick indices when compared with ETGs. This same subset of models produces Hα equivalent widths of order 0.1-5Å for $\log_{10}\mathcal{U}_0 = -4$, consistent with LIER-like galaxies. Models with higher ionization parameters produce larger Hα equivalent widths, and we find some evidence for higher Hα equivalent widths in lower metallicity models.

- For the standard set of models presented here, we find that the UVX region of the $FUV - NUV$ versus $NUV - r$ diagram can only be populated by high metallicity models. Populating the UVX region is easier with models that include nebular emission. Models with high metallicity and somewhat extended SF are most easily able to reproduce the observed UV colors from Hernández-Pérez & Bruzual (2014).

- Post-AGB stars can drive LIER-like emission and contribute to the UV-excess observed in ETGs. It is more likely, however, that the UVX is driven by a small population of alternative HPHB stars, like blue horizontal branch stars. These stars do not contribute significantly to the ionizing photon budget of evolved stellar populations, but can change the UV colors by orders of magnitude.

- We have tested the sensitivity of the post-AGB phase to several of the default parameters used in the MIST models. We have found that rotation has a negligible affect on the ionizing properties of post-AGB stars. We have found that increasing the mass loss efficiency increased the resultant Hα equivalent widths and decreasing the mass loss efficiency decreased the resultant Hα equivalent widths from the fiducial model. This is a promising area to explore in future work.

Chapter 5

SUMMARY

Broadband photometry of galaxies measures an unresolved mix of complex stellar populations, gas, and dust. Accurate determinations of the nebular emission properties are thus a critical consideration when interpreting observations of distant galaxies. The goal of this thesis is to tackle this problem through the simultaneous and self-consistent modelling of the stars, gas, and dust.

In Chapter 2 we have presented a model for nebular emission based on photoionization models from CLOUDY and ionizing spectra from FSPS. The FSPS nebular model's self-consistent coupling of the nebular emission to the matched ionizing spectrum produces emission line intensities that correctly scale with the stellar population as a function of age and metallicity. The model includes nebular emission for both Padova+Geneva and MIST evolutionary tracks, retaining the flexibility of FSPS.

For instantaneous burst populations 3 Myr and younger, nebular line and continuum emission is responsible for at least 30% of the total flux in the UV and optical, and at least 60% of the total flux in the optical and NIR regimes. For models that assume a constant SFR, nebular emission remains a significant fraction of the total flux even at 10 Myr. When interpreting the broadband fluxes for stellar populations with any recent star formation, it is essential to include the contribution from nebular emission, especially for populations at low metallicity.

The strength of hydrogen emission lines depends primarily on the number of ionizing photons produced by the ionizing stellar population. Hydrogen emission lines have a secondary dependence on the nebular temperature, which can drive variations in line strength of order $\sim 15\%$. This means that the Hα line strength will change with metallicity and time,

which is important to consider when estimating SFRs.

My nebular model has already advanced our ability to decipher the signatures of star formation from nebular emission. For a sample of nearby galaxies with both broadband photometry *and* low-resolution aperture matched-spectroscopy, Leja et al. (2017) found that the Hα luminosities predicted by my nebular model based *purely* on fits to the broadband photometry agreed well with observed Hα strengths, with a scatter of ~ 0.16 dex and an offset of 0.08 dex across a wide range of morphological types and stellar masses. This agreement is remarkable, as the predicted Hα luminosity is dependent on accurate star formation rates, dust attenuation, and stellar metallicities.

In Chapter 3, we presented the effort to extend the self-consistent predictions for nebular line and continuum emission into the UV wavelength regime. We have identified UV emission lines that are bright and correlate strongly with bulk physical properties of the nebula like the gas phase metallicity and the hardness and intensity of the ionizing spectrum. We identify combinations of stellar absorption features and nebular emission lines that can be used as metallicity and ionization parameter diagnostics. We evaluate the emission and absorption diagnostics by comparing them with observed galaxies. We confirm that the diagnostics can reproduce observed emission and absorption from a sample of local BCDs and verify that the diagnostics hold across redshift by comparing them with observations of high redshift galaxies.

In the JWST era, UV diagnostics will be instrumental in characterizing high-redshift galaxies. With the self-consistent diagnostics developed as a part of this thesis, we can simultaneously decipher the contribution of stars, gas, and dust from the galaxy SED. We recommend diagnostics for the redshift ranges probed by the JWST spectrograph. The mid-resolution ($R \sim 1000$) spectroscopy that NIRSpec will provide for galaxies between $5 < z < 7$ is ideal for the use of the emission line diagnostics presented here, including O3C3, Si3C3, S3C3, Si3N3, S3O3, and N3O3.

In Chapter 4, we presented a self-consistent analysis of the stellar populations and nebular emission properties of early type galaxies with LIER-like emission. We demonstrate that

models where post-AGB stars are the dominant source of ionizing photons can produce nebular emission consistent with observed LIER-like galaxies. The same models have optical properties consistent with the ETG population. We have demonstrated that hot evolved stars are responsible for LIER-like emission and the UV-excess observed in early-type galaxies, though with varying contribution. Post-AGB stars provide the ionizing radiation that drives LIER-like emission, but contribute a small fraction of the total flux attributed to the UV-upturn. Blue horizontal branch stars provide a much more likely explanation for the UV-excess. The number of blue horizontal branch stars and their temperature distribution depends on metallicity, which explains the spread of UV-colors observed in ETGs.

Appendix A

COMPARISON WITH Starburst-99

We compare the Padova+Geneva models with the STARBURST-99 instantaneous bursts recommended by Levesque et al. (2010) by running both sets of ionizing spectra through CLOUDY with identical parameters. The STARBURST-99 models adopt similar ingredients, including the same high mass-loss rate evolutionary tracks from the Geneva group, described in Meynet & Maeder (2000), the BaSeL spectral library (STARBURST-99 uses an earlier compilation, presented in Lejeune et al. (1997)) and the same spectral libraries for hot stars (WM-BASIC for O-type stars and and CMFGEN for WR stars, earlier versions).

We compare the resultant line ratios in A.1, which show excellent agreement, as expected, since both models use the same isochrones and an almost identical combination of stellar libraries. The emission line ratios differ quantitatively by $\sim 5-10\%$, but show the same qualitative behavior and overlap in much of parameter space. Emission line tables for the STARBURST-99 models are available upon request.

The set of STARBURST-99 models from Levesque & Richardson (2014) apply new Geneva tracks that include the effect of stellar rotation. Shown in §2.6.1, this has important implications on the time evolution of the BPT line ratios, and ultimately the lifetimes associated with ionization regions. A detailed study on the effects of stellar rotation on ionizing radiation and a full comparison between the STARBURST-99 models with rotation and the MIST models (which include rotation) will be discussed in a future paper, Choi et al. (in prep).

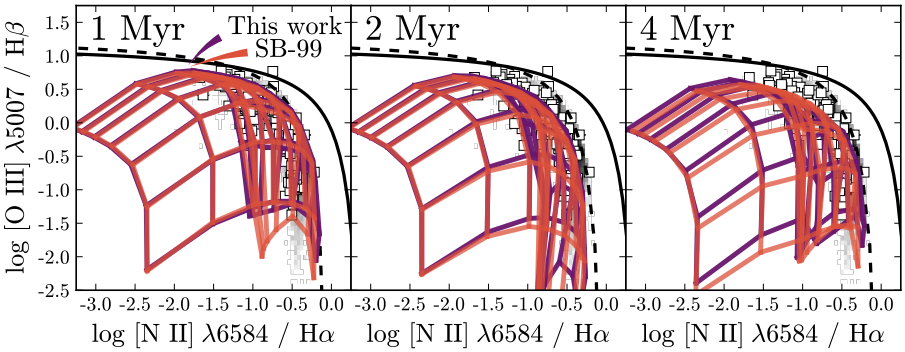

Figure A.1 BPT diagram comparing line ratios from CLOUDY models run with ionizing spectra generated by two different SPS codes: FSPS and STARBURST-99. The models agree within $\sim 5-10\%$ and show similar qualitative behavior.

Appendix B

EMISSION LINE LIST

The list of emission lines in the FSPS nebular model is included here.

Table B.1. Emission lines included in the FSPS nebular model

Vacuum Wavelength (Å)	Line ID	CLOUDY ID
1215.6701	H I (Ly-α)	`H 1 1215.68A`
1025.728	H I (Ly-β)	`H 1 1025.73A`
972.517	H I (Ly-γ)	`H 1 972.543A`
949.742	H I (Ly-δ)	`H 1 949.749A`
937.814	H I (Ly-5)	`H 1 937.809A`
930.751	H I (Ly-6)	`H 1 930.754A`
926.249	H I (Ly-7)	`H 1 926.231A`
923.148	H I (Ly-8)	`H 1 923.156A`
6564.6	H-α 6563	`H 1 6562.85A`
4862.71	H-β 4861	`H 1 4861.36A`
4341.692	H-γ 4340	`H 1 4340.49A`
4102.892	H-δ 4102	`H 1 4101.76A`
3971.198	H-5 3970	`H 1 3970.09A`
3890.166	H-6 3889	`H 1 3889.07A`
3836.485	H-7 3835	`H 1 3835.40A`
3798.987	H-8 3798	`H 1 3797.92A`
18756.4	H I (Pa-α)	`H 1 1.87511m`
12821.578	H I (Pa-β)	`H 1 1.28181m`
10941.17	H I (Pa-γ)	`H 1 1.09381m`
10052.6	H I (Pa-δ)	`H 1 1.00494m`
9548.8	H I (Pa-5)	`H 1 9545.99A`
9232.2	H I (Pa-6)	`H 1 9229.03A`
9017.8	H I (Pa-7)	`H 1 9014.92A`
40522.79	H I (Br-α)	`H 1 4.05116m`
26258.71	H I (Br-β)	`H 1 2.62515m`
21661.178	H I (Br-γ)	`H 1 2.16553m`

Table B.1 (cont'd)

Vacuum Wavelength (Å)	Line ID	CLOUDY ID
19450.89	H I (Br-δ)	`H 1 1.94456m`
18179.2	H I (Br-5)	`H 1 1.81741m`
17366.885	H I (Br-6)	`H 1 1.73621m`
74599.0	H I (Pf-α)	`H 1 7.45781m`
46537.8	H I (Pf-β)	`H 1 4.65250m`
37405.76	H I (Pf-γ)	`H 1 3.73953m`
32969.8	H I (Pf-δ)	`H 1 3.29609m`
30392.02	H I (Pf-5)	`H 1 3.03837m`
123719.12	H I (Hu-α)	`H 1 12.3685m`
75024.4	H I (Hu-β)	`H 1 7.50043m`
59082.2	H I (Hu-γ)	`H 1 5.90659m`
51286.5	H I (Hu-δ)	`H 1 5.12725m`
4472.735	He I 4472	`He 1 4471.47A`
5877.249	He I 5877	`He 1 5875.61A`
6679.995	He I 6680	`He 1 6678.15A`
10832.057	He I 10829	`He 1 1.08299m`
10833.306	He I 10833	`He 1 1.08303m`
3889.75	He I 3889	`He 1 3888.63A`
7067.138	He I 7065	`He 1 7065.18A`
1640.42	He II 1640	`He 2 1640.00A`
9852.96	[C I] 9850	`TOTL 9850.00A`
8729.53	[C I] 8727	`C 1 8727.00A`
4622.864	[C I] 4621	`C 1 4621.00A`
6097000.0	[C I] 610μm	`C 1 609.200m`
3703700.0	[C I] 369μm	`C 1 369.700m`
1576429.62	[C II] 157.7μm	`C 2 157.600m`

Table B.1 (cont'd)

Vacuum Wavelength (Å)	Line ID	Cloudy ID
2325.4	C II] 2326	`C 2 2325.00A`
2324.21	C II] 2326	`C 2 2324.00A`
2328.83	C II] 2326	`C 2 2329.00A`
2327.64	C II] 2326	`C 2 2328.00A`
2326.11	C II] 2326	`C 2 2327.00A`
1908.73	C III]	`C 3 1910.00A`
1906.68	[C III]	`C 3 1907.00A`
5201.705	[N I] 5200	`N 1 5200.00A`
6585.27	[N II] 6585	`N 2 6584.00A`
6549.86	[N II] 6549	`N 2 6548.00A`
5756.19	[N II] 5756	`N 2 5755.00A`
1218000.0	[N II] 122μm	`N 2 121.700m`
2053000.0	[N II] 205μm	`N 2 205.400m`
2142.3	N II] 2141	`N 2 2141.00A`
573300.0	[N III] 57μm	`N 3 57.2100m`
6302.046	[O I] 6302	`O 1 6300.00A`
6365.535	[O I] 6365	`O 1 6363.00A`
5578.89	[O I] 5578	`O 1 5577.00A`
631852.0	[O I] 63μm	`O 1 63.1700m`
1455350.0	[O I] 145μm	`O 1 145.530m`
3727.1	[O II] 3726	`O II 3726.00A`
3729.86	[O II] 3729	`O II 3729.00A`
7332.21	[O II] 7332	`O II 7332.00A`
7321.94	[O II] 7323	`O II 7323.00A`
2471.088	[O II] 2471	`O II 2471.00A`
1661.241	O III] 1661	`O 3 1661.00A`

Table B.1 (cont'd)

Vacuum Wavelength (Å)	Line ID	Cloudy ID
1666.15	O III] 1666	`O 3 1666.00A`
5008.24	[O III] 5007	`O 3 5007.00A`
4960.295	[O III] 4960	`O 3 4959.00A`
4364.435	[O III] 4364	`TOTL 4363.00A`
2321.664	[O III] 2321	`O 3 2321.00A`
883564.0	[O III] 88μm	`O 3 88.3300m`
518145.0	[O III] 52μm	`O 3 51.8000m`
128135.48	[Ne II] 12.8μm	`Ne 2 12.8100m`
155551.0	[Ne III] 15.5μm	`Ne 3 15.5500m`
360135.0	[Ne III] 36μm	`Ne 3 36.0140m`
3869.86	[Ne III] 3870	`Ne 3 3869.00A`
3968.59	[Ne III] 3968	`Ne 3 3968.00A`
3343.5	[Ne III] 3343	`Ne 3 3343.00A`
1812.205	[Ne III] 1815	`Ne 3 1815.00A`
4725.47	[Ne IV] 4720	`Ne 4 4720.00A`
2796.352	Mg II 2800	`Mg 2 2795.53A`
2803.53	Mg II 2800	`Mg 2 2802.71A`
348140.0	[Si II] 35μm	`Si 2 34.8140m`
10323.32	[S II] 10331	`S 2 1.03300m`
6732.673	[S II] 6732	`S II 6731.00A`
6718.294	[S II] 6717	`S II 6716.00A`
4069.75	[S II] 4070	`S II 4070.00A`
4077.5	[S II] 4078	`S II 4078.00A`
187130.0	[S III] 18.7μm	`S 3 18.6700m`
334800.0	[S III] 33.5μm	`S 3 33.4700m`
9533.2	[S III] 9533	`S 3 9532.00A`

Table B.1 (cont'd)

Vacuum Wavelength (Å)	Line ID	Cloudy ID
9071.1	[S III] 9071	`S 3 9069.00A`
6313.81	[S III] 6314	`S 3 6312.00A`
3722.75	[S III] 3723	`S 3 3722.00A`
105105.0	[S IV] 10.5μm	`S 4 10.5100m`
69852.74	[Ar II] 7μm	`Ar 2 6.98000m`
7137.77	[Ar III] 7138	`Ar 3 7135.00A`
7753.19	[Ar III] 7753	`Ar 3 7751.00A`
5193.27	[Ar III] 5193	`Ar 3 5192.00A`
3109.98	[Ar III] 3110	`Ar 3 3109.00A`
218302.0	[Ar III] 22μm	`Ar 3 21.8300m`
89913.8	[Ar III] 9μm	`Ar 3 9.00000m`
7334.17	[Ar IV] 7330	`Ar 4 7331.00A`
2669.951	[Al II] 2670	`Al 2 2670.00A`
2661.146	[Al II] 2660	`Al 2 2660.00A`
1854.716	[Al III] 1855	`Al 3 1855.00A`
1862.7895	[Al III] 1863	`Al 3 1863.00A`
143678.0	[Cl II] 14.4μm	`Cl 2 14.4000m`
8581.06	[Cl II] 8579	`Cl 2 8579.00A`
9126.1	[Cl II] 9124	`Cl 2 9124.00A`
5539.411	[Cl III] 5538	`Cl 3 5538.00A`
5519.242	[Cl III] 5518	`Cl 3 5518.00A`
606420.0	[P II] 60μm	`P 2 60.6400m`
328709.0	[P II] 32μm	`P 2 32.8700m`
12570.21	[Fe II] 1.26μm	`Fe 2 1.25668m`

BIBLIOGRAPHY

Abazajian, K. N., Adelman-McCarthy, J. K., Agüeros, M. A., et al. 2009, ApJS, 182, 543

Allen, M. G., Groves, B. A., Dopita, M. A., Sutherland, R. S., & Kewley, L. J. 2008, ApJS, 178, 20

Anders, E., & Grevesse, N. 1989, Geochim. Cosmochim. Acta, 53, 197

Anders, P., & Fritze-v. Alvensleben, U. 2003, A&A, 401, 1063

Asplund, M., Grevesse, N., Sauval, A. J., & Scott, P. 2009, ARA&A, 47, 481

Baldwin, J. A., Phillips, M. M., & Terlevich, R. 1981, PASP, 93, 5

Bayliss, M. B., Rigby, J. R., Sharon, K., et al. 2014, ApJ, 790, 144

Belfiore, F., Maiolino, R., Maraston, C., et al. 2016, MNRAS, 461, 3111

Berg, D. A., Skillman, E. D., Henry, R. B. C., Erb, D. K., & Carigi, L. 2016, ApJ, 827, 126

Berg, D. A., Skillman, E. D., Marble, A. R., et al. 2012, ApJ, 754, 98

Bertelli, G., Bressan, A., Chiosi, C., Fagotto, F., & Nasi, E. 1994, A&AS, 106, 275

Binette, L., Magris, C. G., Stasińska, G., & Bruzual, A. G. 1994, A&A, 292, 13

Bloecker, T. 1995, A&A, 299, 755

Bressan, A., Marigo, P., Girardi, L., et al. 2012, MNRAS, 427, 127

Brinchmann, J., Charlot, S., White, S. D. M., et al. 2004, MNRAS, 351, 1151

Brown, T. M., Smith, E., Ferguson, H. C., et al. 2008, ApJ, 682, 319

Bundy, K., Bershady, M. A., Law, D. R., et al. 2015, ApJ, 798, 7

Byler, N., Dalcanton, J. J., Conroy, C., & Johnson, B. D. 2016, ArXiv e-prints, arXiv:1611.08305

—. 2017, ApJ, 840, 44

Cardelli, J. A., Clayton, G. C., & Mathis, J. S. 1989, ApJ, 345, 245

Charlot, S., & Fall, S. M. 2000, ApJ, 539, 718

Charlot, S., & Longhetti, M. 2001, MNRAS, 323, 887

Choi, J., Conroy, C., & Byler, N. 2017, ApJ, 838, 159

Choi, J., Conroy, C., Moustakas, J., et al. 2014, ApJ, 792, 95

Choi, J., Dotter, A., Conroy, C., et al. 2016, ApJ, 823, 102

Christensen, L., Laursen, P., Richard, J., et al. 2012, MNRAS, 427, 1973

Cid Fernandes, R., Stasińska, G., Mateus, A., & Vale Asari, N. 2011a, MNRAS, 413, 1687

—. 2011b, MNRAS, 413, 1687

Conroy, C. 2013, ARA&A, 51, 393

Conroy, C., Gunn, J. E., & White, M. 2009, ApJ, 699, 486

Contini, T., Treyer, M. A., Sullivan, M., & Ellis, R. S. 2002, MNRAS, 330, 75

Cordier, D., Pietrinferni, A., Cassisi, S., & Salaris, M. 2007, AJ, 133, 468

Crowther, P. A. 2007, ARA&A, 45, 177

de Jager, C., Nieuwenhuijzen, H., & van der Hucht, K. A. 1988, A&AS, 72, 259

Ding, J., Cai, Z., Fan, X., et al. 2016, ArXiv e-prints, arXiv:1612.00902

Dopita, M. A., Kewley, L. J., Heisler, C. A., & Sutherland, R. S. 2000, ApJ, 542, 224

Dopita, M. A., & Sutherland, R. S. 1995, ApJ, 455, 468

Dopita, M. A., Sutherland, R. S., Nicholls, D. C., Kewley, L. J., & Vogt, F. P. A. 2013, ApJS, 208, 10

Dopita, M. A., Fischera, J., Sutherland, R. S., et al. 2006, ApJS, 167, 177

Dotter, A. 2016, ApJS, 222, 8

Du, X., Shapley, A. E., Martin, C. L., & Coil, A. L. 2016, ArXiv e-prints, arXiv:1612.06866

Ekström, S., Georgy, C., Eggenberger, P., et al. 2012, A&A, 537, A146

Eldridge, J. J. 2012, MNRAS, 422, 794

Eldridge, J. J., Stanway, E. R., Xiao, L., et al. 2017, ArXiv e-prints, arXiv:1710.02154

Erb, D. K., Pettini, M., Shapley, A. E., et al. 2010, ApJ, 719, 1168

Esteban, C., García-Rojas, J., Carigi, L., et al. 2014, MNRAS, 443, 624

Feltre, A., Charlot, S., & Gutkin, J. 2016, MNRAS, 456, 3354

Ferland, G. J., & Netzer, H. 1983, ApJ, 264, 105

Ferland, G. J., Porter, R. L., van Hoof, P. A. M., et al. 2013, Rev. Mexicana Astron. Astrofis., 49, 137

Fioc, M., & Rocca-Volmerange, B. 1999, ArXiv Astrophysics e-prints, astro-ph/9912179

Galleti, S., Bellazzini, M., Buzzoni, A., Federici, L., & Fusi Pecci, F. 2009, A&A, 508, 1285

Garnett, D. R. 1990, ApJ, 363, 142

Georgy, C., Ekström, S., Granada, A., et al. 2013, A&A, 553, A24

Giavalisco, M., Koratkar, A., & Calzetti, D. 1996, ApJ, 466, 831

Girardi, L., Bressan, A., Bertelli, G., & Chiosi, C. 2000, A&AS, 141, 371

Gomes, J. M., Papaderos, P., Kehrig, C., et al. 2016, A&A, 588, A68

Grevesse, N., Asplund, M., Sauval, A. J., & Scott, P. 2010a, Ap&SS, 328, 179

—. 2010b, Ap&SS, 328, 179

Grevesse, N., & Noels, A. 1993, in Origin and Evolution of the Elements, ed. N. Prantzos, E. Vangioni-Flam, & M. Casse, 15–25

Groves, B. A., Dopita, M. A., & Sutherland, R. S. 2004, ApJS, 153, 9

Gutkin, J., Charlot, S., & Bruzual, G. 2016, MNRAS, 462, 1757

Halpern, J. P., & Steiner, J. E. 1983, ApJ, 269, L37

Heckman, T. M. 1980, A&A, 87, 152

—. 1981, ApJ, 250, L59

Heckman, T. M., Robert, C., Leitherer, C., Garnett, D. R., & van der Rydt, F. 1998, ApJ, 503, 646

Henry, R. B. C., Edmunds, M. G., & Köppen, J. 2000, ApJ, 541, 660

Hernández-Pérez, F., & Bruzual, G. 2014, MNRAS, 444, 2571

Herwig, F. 2000, A&A, 360, 952

Hillier, D. J., & Lanz, T. 2001, in Astronomical Society of the Pacific Conference Series, Vol. 247, Spectroscopic Challenges of Photoionized Plasmas, ed. G. Ferland & D. W. Savin, 343

Hirschmann, M., Charlot, S., Feltre, A., et al. 2017, MNRAS, 472, 2468

Ho, L. 1999, in Astrophysics and Space Science Library, Vol. 234, Observational Evidence for the Black Holes in the Universe, ed. S. K. Chakrabarti, 157

Ho, L. C. 2008, ARA&A, 46, 475

—. 2009, ApJ, 699, 638

Holden, B. P., van der Wel, A., Rix, H.-W., & Franx, M. 2012, ApJ, 749, 96

Huang, W., Gies, D. R., & McSwain, M. V. 2010, ApJ, 722, 605

James, P. A., & Percival, S. M. 2015, MNRAS, 450, 3503

Johansson, J., Woods, T. E., Gilfanov, M., et al. 2016, MNRAS, 461, 4505

Jones, E., Oliphant, T., Peterson, P., et al. 2001–, SciPy: Open source scientific tools for Python

Kalirai, J. S., Saul Davis, D., Richer, H. B., et al. 2009, ApJ, 705, 408

Kauffmann, G., Heckman, T. M., White, S. D. M., et al. 2003a, MNRAS, 341, 33

Kauffmann, G., Heckman, T. M., Tremonti, C., et al. 2003b, MNRAS, 346, 1055

Kaviraj, S., Schawinski, K., Devriendt, J. E. G., et al. 2007, ApJS, 173, 619

Kehrig, C., Monreal-Ibero, A., Papaderos, P., et al. 2012, A&A, 540, A11

Kewley, L. J., & Dopita, M. A. 2002, ApJS, 142, 35

Kewley, L. J., Dopita, M. A., Sutherland, R. S., Heisler, C. A., & Trevena, J. 2001, ApJ, 556, 121

Kewley, L. J., & Ellison, S. L. 2008, ApJ, 681, 1183

Kewley, L. J., Groves, B., Kauffmann, G., & Heckman, T. 2006, MNRAS, 372, 961

Kormendy, J., & Ho, L. C. 2013, ARA&A, 51, 511

Koski, A. T., & Osterbrock, D. E. 1976, ApJ, 203, L49

Kroupa, P. 2001, MNRAS, 322, 231

Kudritzki, R.-P., & Puls, J. 2000, ARA&A, 38, 613

Kudritzki, R.-P., Urbaneja, M. A., Gazak, Z., et al. 2012, ApJ, 747, 15

Langer, N. 1998, A&A, 329, 551

Leitherer, C., Tremonti, C. A., Heckman, T. M., & Calzetti, D. 2011, AJ, 141, 37

Leitherer, C., Schaerer, D., Goldader, J. D., et al. 1999, ApJS, 123, 3

Leja, J., Johnson, B. D., Conroy, C., van Dokkum, P. G., & Byler, N. 2017, ApJ, 837, 170

Lejeune, T., Cuisinier, F., & Buser, R. 1997, A&AS, 125, astro-ph/9701019

Levesque, E. M. 2015, STSci Newsletter

Levesque, E. M., Kewley, L. J., & Larson, K. L. 2010, AJ, 139, 712

Levesque, E. M., Leitherer, C., Ekstrom, S., Meynet, G., & Schaerer, D. 2012, ApJ, 751, 67

Levesque, E. M., & Richardson, M. L. A. 2014, ApJ, 780, 100

Mainali, R., Kollmeier, J. A., Stark, D. P., et al. 2017, ApJ, 836, L14

Maraston, C. 2005, MNRAS, 362, 799

Maraston, C., Nieves Colmenárez, L., Bender, R., & Thomas, D. 2009, A&A, 493, 425

Marigo, P., Bressan, A., Nanni, A., Girardi, L., & Pumo, M. L. 2013, MNRAS, 434, 488

Marigo, P., Girardi, L., Bressan, A., et al. 2008, A&A, 482, 883

McGaugh, S. S. 1991, ApJ, 380, 140

McIntosh, D. H., Wagner, C., Cooper, A., et al. 2014, MNRAS, 442, 533

Meynet, G., & Maeder, A. 2000, A&A, 361, 101

Miller Bertolami, M. M. 2016, A&A, 588, A25

Mollá, M., García-Vargas, M. L., & Bressan, A. 2009, MNRAS, 398, 451

Morton, D. C. 1991, ApJS, 77, 119

Moy, E., Rocca-Volmerange, B., & Fioc, M. 2001, A&A, 365, 347

Nakajima, K., Schaerer, D., Le Fevre, O., et al. 2017, ArXiv e-prints, arXiv:1709.03990

Nugis, T., & Lamers, H. J. G. L. M. 2000, A&A, 360, 227

O'Connell, R. W. 1999, ARA&A, 37, 603

Pagel, B. E. J., Edmunds, M. G., Blackwell, D. E., Chun, M. S., & Smith, G. 1979, MNRAS, 189, 95

Pandya, V., Greene, J. E., Ma, C.-P., et al. 2017, ApJ, 837, 40

Papaderos, P., Gomes, J. M., Vílchez, J. M., et al. 2013, A&A, 555, L1

Pauldrach, A. W. A., Hoffmann, T. L., & Lennon, M. 2001, A&A, 375, 161

Paxton, B., Bildsten, L., Dotter, A., et al. 2011, ApJS, 192, 3

Paxton, B., Cantiello, M., Arras, P., et al. 2013, ApJS, 208, 4

Paxton, B., Marchant, P., Schwab, J., et al. 2015, ApJS, 220, 15

Peimbert, M. 1967, ApJ, 150, 825

Pettini, M., & Pagel, B. E. J. 2004, MNRAS, 348, L59

Pietrinferni, A., Cassisi, S., Salaris, M., & Castelli, F. 2004, ApJ, 612, 168

Pilyugin, L. S., & Thuan, T. X. 2005, ApJ, 631, 231

Rauch, T. 2003, A&A, 403, 709

Reimers, D. 1975, Memoires of the Societe Royale des Sciences de Liege, 8, 369

Reines, A. E., Nidever, D. L., Whelan, D. G., & Johnson, K. E. 2010, ApJ, 708, 26

Rigby, J. R., & Rieke, G. H. 2004, ApJ, 606, 237

Rix, S. A., Pettini, M., Leitherer, C., et al. 2004, ApJ, 615, 98

Rosen, A. L., Krumholz, M. R., & Ramirez-Ruiz, E. 2012, ApJ, 748, 97

Rosenfield, P., Johnson, L. C., Girardi, L., et al. 2012, ApJ, 755, 131

Rosenfield, P., Marigo, P., Girardi, L., et al. 2014, ApJ, 790, 22

Salim, S., Rich, R. M., Charlot, S., et al. 2007, ApJS, 173, 267

Sarajedini, A., Bedin, L. R., Chaboyer, B., et al. 2007, AJ, 133, 1658

Sargent, W. L. W., & Searle, L. 1970, ApJ, 162, L155

Sarzi, M., Falcón-Barroso, J., Davies, R. L., et al. 2006, MNRAS, 366, 1151

Sarzi, M., Shields, J. C., Schawinski, K., et al. 2010, MNRAS, 402, 2187

Schaller, G., Schaerer, D., Meynet, G., & Maeder, A. 1992, A&AS, 96, 269

Schawinski, K., Kaviraj, S., Khochfar, S., et al. 2007, ApJS, 173, 512

Schiavon, R. P., Rose, J. A., Courteau, S., & MacArthur, L. A. 2004, ApJ, 608, L33

Schmidt, K. B., Huang, K.-H., Treu, T., et al. 2017, ApJ, 839, 17

Schombert, J. M. 2016, AJ, 152, 214

Senchyna, P., Stark, D. P., Vidal-García, A., et al. 2017, MNRAS, 472, 2608

Shapley, A. E., Steidel, C. C., Pettini, M., & Adelberger, K. L. 2003, ApJ, 588, 65

Singh, R., van de Ven, G., Jahnke, K., et al. 2013, A&A, 558, A43

Smith, L. J., Norris, R. P. F., & Crowther, P. A. 2002, MNRAS, 337, 1309

Smith, N. 2014, ARA&A, 52, 487

Stanway, E. R., Eldridge, J. J., & Becker, G. D. 2016, MNRAS, 456, 485

Stark, D. P., Richard, J., Siana, B., et al. 2014, MNRAS, 445, 3200

Stark, D. P., Richard, J., Charlot, S., et al. 2015, MNRAS, 450, 1846

Stasińska, G., Vale Asari, N., Cid Fernandes, R., et al. 2008, MNRAS, 391, L29

Steidel, C. C., Strom, A. L., Pettini, M., et al. 2016, ApJ, 826, 159

Steidel, C. C., Rudie, G. C., Strom, A. L., et al. 2014, ApJ, 795, 165

Stroe, A., Sobral, D., Matthee, J., Calhau, J., & Oteo, I. 2017a, MNRAS, 471, 2558

—. 2017b, MNRAS, 471, 2575

Taniguchi, Y., Shioya, Y., & Murayama, T. 2000, AJ, 120, 1265

Telford, O. G., Dalcanton, J. J., Skillman, E. D., & Conroy, C. 2016, ApJ, 827, 35

Thomas, D., Maraston, C., Bender, R., & Mendes de Oliveira, C. 2005, ApJ, 621, 673

Thuan, T. X. 2008, in IAU Symposium, Vol. 255, Low-Metallicity Star Formation: From the First Stars to Dwarf Galaxies, ed. L. K. Hunt, S. C. Madden, & R. Schneider, 348–360

Trager, S. C., Faber, S. M., Worthey, G., & González, J. J. 2000, AJ, 120, 165

Tremonti, C. A., Heckman, T. M., Kauffmann, G., et al. 2004, ApJ, 613, 898

van Zee, L., Salzer, J. J., & Haynes, M. P. 1998a, ApJ, 497, L1

van Zee, L., Salzer, J. J., Haynes, M. P., O'Donoghue, A. A., & Balonek, T. J. 1998b, AJ, 116, 2805

Vassiliadis, E., & Wood, P. R. 1994, ApJS, 92, 125

Vazdekis, A., Sánchez-Blázquez, P., Falcón-Barroso, J., et al. 2010, MNRAS, 404, 1639

Veilleux, S., & Osterbrock, D. E. 1987, ApJS, 63, 295

Vidal-García, A., Charlot, S., Bruzual, G., & Hubeny, I. 2017, MNRAS, 470, 3532

Vink, J. S., de Koter, A., & Lamers, H. J. G. L. M. 2000, A&A, 362, 295

—. 2001, A&A, 369, 574

Walcher, J., Groves, B., Budavári, T., & Dale, D. 2011, Ap&SS, 331, 1

Weiss, A., & Ferguson, J. W. 2009, A&A, 508, 1343

Westera, P., Lejeune, T., Buser, R., Cuisinier, F., & Bruzual, G. 2002, A&A, 381, 524

Woods, T. E., & Gilfanov, M. 2014, MNRAS, 439, 2351

Worthey, G., Faber, S. M., Gonzalez, J. J., & Burstein, D. 1994, ApJS, 94, 687

Yan, R., & Blanton, M. R. 2012, ApJ, 747, 61

Yi, S. K., Yoon, S.-J., Kaviraj, S., et al. 2005, ApJ, 619, L111

York, D. G., Adelman, J., Anderson, Jr., J. E., et al. 2000, AJ, 120, 1579

Zetterlund, E., Levesque, E. M., Leitherer, C., & Danforth, C. W. 2015, ApJ, 805, 151

VITA

Eleanor Beryl Byler was born in Massapequa, NY in 1989 to loving parents, Eric and Tess. She graduated from Palo Alto High School in 2007 with the intent of studying art and math at New York University. In her first semester at NYU, Eleanor took an introductory astronomy course to fulfill a graduation requirement, forever altering her life trajectory. Eleanor transferred to Wellesley College in 2008, where she graduated with a degree in physics in 2011. She went on to pursue her PhD in astronomy at the University of Washington, which she completed in in 2017. Eleanor is looking forward to next working at the Australian National University in Canberra, Australia as a postdoctoral fellow at the Research School of Astronomy & Astrophysics.